

QUENCH TESTS OF LHC MAGNETS WITH BEAM: STUDIES ON BEAM LOSS DEVELOPMENT AND DETERMINATION OF QUENCH LEVELS

THIS IS A TEMPORARY TITLE PAGE
It will be replaced for the final print by a version
provided by the service académique.

Thèse n. 6116 2014
présenté le 24 Janvier 2014
à la Faculté des Sciences de Base
programme doctoral en Physique
École Polytechnique Fédérale de Lausanne
pour l'obtention du grade de Docteur ès Sciences
par

Agnieszka Priebe

acceptée sur proposition du jury:

Prof. Dr. Georges Meylan, président du jury
Prof. Dr. Minh Quang Tran, EPFL co-directeur de thèse
Dr. Mariusz Sapinski, CERN co-directeur de thèse
Prof. Dr.-Ing. Mathias Noe, rapporteur
Prof. Dr. Leonid Rivkin, rapporteur
Dr. Luca Bottura, rapporteur

Lausanne, EPFL, 2014



ÉCOLE POLYTECHNIQUE
FÉDÉRALE DE LAUSANNE

Good decisions come from experience.
Experience comes from making bad decisions.
— Mark Twain

To my beloved family...

Abstract

The application of superconducting materials in the field of high energy accelerator physics not only opens the doors to the generation of the magnetic fields unattainable to normal conductors but also demands facing new challenges. A transition from the superconducting state, which is characterized by a resistance-free flow of the electric current, to the normal conducting state is called quenching. This process might be extremely dangerous and even lead to destruction of a magnet superconducting coil if no protecting actions are taken. Therefore, the knowledge of a magnet quench level, i.e. amount of energy which causes the transition to the resistive state, is crucial for the safety and operational efficiency of the accelerator. Regarding that, specific thresholds are incorporated to dedicated quench prevention systems in order to suppress the origin of detected energy perturbation, for example beam losses, or mitigate the consequences of the quenching process by dissipating the energy stored in the magnetic field and extracting electric currents from the magnet circuit.

The coils of Main Magnets of the Large Hadron Collider (LHC) are made of superconducting cables based on niobium-titanium. These cables can carry the electrical current of up to 13 kA. The generated magnetic field of 8.33 T will allow governing protons at unprecedented energy of 7 TeV. However, an operation in such a critical environment follows a risk of beam losses high enough to provoke magnet quenching. This is due to the fact that the total stored energy of the beam will reach 362 MJ while the quench level of a superconducting cable at high current is in the order of millijoules. Therefore, the LHC is equipped with the Beam Loss Monitoring (BLM) system surveying a level of ionization radiation along the machine. Understanding the mechanism of quenching allows setting BLM thresholds so that beams are extracted from the LHC if the losses exceed certain safety value. This prevents magnets from undergoing the transition to the resistive state due to beam losses.

In this thesis, the experimental studies on the LHC Main Magnet quench levels are presented. These include finding and testing a method of inducing beam losses which would meet the demands of quench test specifications, i.e. particular loss duration and appropriate loss rate (a number of particles lost in the unit of time). Two cases varying in loss timescale and, therefore, mechanisms of heat transport in a superconducting system were investigated. In the fast loss regime in the order of milliseconds, a quench level is defined by heat capacity of the cable and the liquid helium, which the cable is immersed in. In contrast, a quench level of a superconductor exposed to steady state losses lasting for seconds is determined by the efficiency of heat evacuation to liquid helium bath.

Since currently no measurements of energy deposited by lost particles can be provided inside

the superconducting coils, the quench levels were assessed using Monte Carlo simulations. The conditions of the dedicated experiments were recreated in Geant4 code. In order to optimize time needed to simulate various loss scenarios, an approximation method of weighting point-like losses with coefficients corresponding to an estimated loss pattern was applied. The accuracy of this technique was validated by comparing simulated radiation of secondary particle shower outside magnet cryostats to the BLM signals measured during the quench tests. In addition, complementary calculations of quench levels were provided using QP3 heat transfer code.

The quench levels assessed in these studies provide important information for the optimization of BLM thresholds. This will allow limiting an uncertainty margins used nowadays and therefore avoiding unnecessary beam dumps when still assuring reliable machine protection.

KEYWORDS: quench level, beam-induced quench, superconducting magnets, quench test, fast losses, steady state losses, Beam Loss Monitors, BLM, magnet protection, Geant4 simulations

Résumé

L'utilisation de matériaux supraconducteurs dans le domaine de la physique des accélérateurs à haute énergie permet la génération de champs magnétiques inatteignables pour des conducteurs habituels, mais requiert de faire face à de nouveaux défis. Une transition de phase depuis l'état supraconducteur, caractérisé par une résistance nulle à la circulation du courant électrique, vers un état de conduction habituel (résistance non nulle) s'appelle le "quench". Ce processus pourrait être extrêmement dangereux pour les bobines supraconductrices des aimants et même provoquer leur destruction si aucune mesure de protection n'est prise. En conséquence, la connaissance du niveau de quench d'un aimant, c'est-à-dire la quantité d'énergie pouvant causer la transition de phase vers un état résistif, est cruciale pour la sécurité et l'efficacité opérationnelle de l'accélérateur. Dans ce but, des seuils spécifiques ont été incorporés à plusieurs systèmes de prévention des quench pour supprimer l'origine des perturbations énergétiques détectées, comme par exemple les pertes de faisceau ; ou pour atténuer les conséquences du processus de quench, en dissipant l'énergie contenue dans le champ magnétique et en extrayant les courants du circuit électrique de l'aimant.

Les bobines des aimants principaux du Grand Collisionneur de Hadrons (Large Hadron Collider, LHC) sont constitués de câbles supraconducteurs faits de Titane - Nodium. Ces câbles peuvent transporter un courant électrique de près de 13 kA. Le champ magnétique généré, de 8.33 T, permettra de diriger des protons circulant à une énergie sans précédent de 7 TeV. Cependant, opérer dans un environnement aussi critique créé un risque de pertes de faisceau suffisamment importants pour provoquer un quench des aimants. Ceci est dû au fait que l'énergie totale du faisceau atteindra 362 MJ, alors que le niveau de quench d'un câble supraconducteur à haute intensité est de l'ordre du millijoule. En conséquence, le LHC est équipé d'un système de moniteurs de perte de faisceau (Beam Loss Monitors, BLM) qui mesure le niveau de radiation ionisante tout au long de l'accélérateur. La compréhension des mécanismes de quench permet de régler les seuils des BLMs de façon à ce que les faisceaux soient extraits du LHC si les pertes dépassent certaines valeurs considérées comme sûres. Ceci empêche les aimants de subir une transition vers un état résistif due aux pertes de faisceau.

Dans cette thèse, les études expérimentales des seuils de quench des aimants principaux du LHC sont présentées. Ces études incluent la recherche et le test d'un moyen de créer les pertes de faisceau correspondantes aux spécifications des tests de quench, c'est-à-dire la durée des pertes et leur fréquence (nombre de particules perdues par unité de temps). Deux cas ont été étudiés, différenciés par l'échelle de temps des pertes et donc les mécanismes de transport de la chaleur dans un système supraconducteur. Durant le régime de pertes rapides (de l'ordre

de quelques millisecondes) le niveau de quench est défini par la capacité thermique du câble et du dû à l'hélium liquide, dans lequel le câble est immergé. A l'inverse, le niveau de quench d'un supraconducteur exposé à des pertes de régime permanent (qui durent plusieurs secondes) est déterminé par l'efficacité de l'évacuation de la chaleur par le bain d'hélium liquide.

Actuellement, comme aucune mesure de l'énergie déposée dans les bobines supraconductrices par les particules perdues n'est disponible, les niveaux de quench ont été estimés par des simulations Monte Carlo. Les conditions des expériences ont été recréées par un code Geant4. De façon à optimiser le temps de calcul nécessaire à la simulation des différents scénarios de pertes, une méthode d'approximation de pertes ponctuelles par des coefficients correspondants à une structure de pertes estimée a été appliquée. La précision de cette technique a été validée en comparant les radiations simulées de gerbes de particules secondaires en dehors des cryostats des aimants avec le signal des BLMs mesuré durant les tests de quench. De plus, des calculs complémentaires des niveaux de quench ont été fournis par le code de transfert de chaleur QP3.

Les niveaux de quench estimés dans ces études ont fourni des informations importantes pour l'optimisation des seuils des BLMs. Ils vont permettre de limiter les marges d'incertitude utilisées actuellement, et par conséquent d'éviter des suppressions de faisceau non nécessaires tout en conservant une protection de la machine fiable.

MOTS-CLÉS : niveau de transition de phase supraconductrice, quench dû au faisceau, aimants supraconducteurs, tests de quench, pertes de faisceau rapides, pertes de faisceau en régime permanent, moniteurs de pertes de faisceau, BLM, protection des aimants, simulations Geant4.

Zusammenfassung

Die Anwendung von supraleitenden Materialien auf dem Gebiet der Beschleuniger für die Hochenergiephysik eröffnet die Türen zur Erzeugung von bisher unerreichbaren Magnetfeldwerten, bringt aber auch neue Herausforderungen mit sich. Der Übergang vom supraleitenden Zustand, der durch den widerstandsfreien Fluss des elektrischen Stroms gekennzeichnet ist, zu dem normalleitenden Zustand, wird als Quench bezeichnet. Dieser unerwünschte Prozess kann sogar zur Zerstörung von einem supraleitenden System führen, wenn keine Schutzmaßnahmen ergriffen werden. Deshalb ist die Kenntnis des Quenchlevels eines Magneten, d. h. die Energiemenge, die den Übergang zum widerstandsbehafteten Zustand bewirkt, entscheidend für die Sicherheit und die Effizienz des Beschleunigers. Um mit dem Quench von Magneten umzugehen, werden in speziellen Systemen Schwellenwerte verwendet, die die auslösenden Effekte von erkannten Energiestörungen, wie Strahlverluste, unterdrücken oder die Folgen eines Quenches mildern. Dies wird erreicht, indem die in dem Magnetfeld gespeicherte Energie in Wärmeenergie überführt wird.

Die Hauptmagnete des Large Hadron Colliders (LHC) basieren auf Niob-Titan Filamenten und können einen elektrischen Strom von bis zu 13 kA bei 1,9 K unter nominellen Bedingungen leiten. Das erzeugte Magnetfeld von 8,33 T erlaubt es, Teilchenstrahlen mit einer bisher nicht erreichten Energie von 7 TeV abzulenken. Der Betrieb der Magnete birgt das Risiko, dass Strahlverluste hoch genug sein können, um einen Quench zu provozieren. Die gesamte gespeicherte Energie im Strahl beträgt 362 MJ, während das Quenchniveau eines supraleitenden Kabels bei hohen Strömen lediglich Millijoule beträgt. Daher wird der LHC mit Strahlverlustmonitoren (BLM) ausgestattet, welche die ionisierende Strahlung ausserhalb der Magnete entlang des Beschleunigers messen. Das genaue Verständnis des Mechanismus eines Quenches ermöglicht die Ermittlung von BLM-Schwellenwerten, so dass Strahlen aus dem LHC extrahiert werden, wenn die Verluste bestimmte Sicherheitswerte überschreiten. Dies verhindert den Übergang der Spulen der Magnete in den widerstandsbehafteten Zustand durch Strahlverluste.

In dieser Arbeit werden die phänomenologischen Untersuchungen zu den Quenchniveaus der LHC-Hauptmagnete dargestellt. Dazu gehören die Suche und Erprobung eines Verfahrens zur Erzeugung von Strahlverlusten, welche die Anforderungen der Quenchtestspezifikationen, insbesondere die Verlustdauer und die adäquate Verlustrate, erfüllen. Zwei Fälle mit unterschiedlicher Verlustzeitskala und somit verschiedenen Wärmetransportmechanismen im supraleitenden System wurden untersucht. Im Falle von kurzzeitigen Verlusten in der Größenordnung von Millisekunden wird das Quenchniveau durch die Wärmekapazität der Kabel und des flüssigen Heliums definiert. Im Gegensatz dazu wird das Quenchniveau bei

einem Sekundenlangen Strahlverlust bestimmt durch die Effizienz des Wärmeentzugs aus den Kabeln, die von flüssigem Helium umgeben sind.

Da noch keine Messungen der Energiedeposition durch verlorene Teilchen in den supraleitenden Spulen existieren, wurden die Quenchlevel mit Hilfe von Monte-Carlo-Simulationen untersucht. Die gut definierten Bedingungen der durchgeführten Experimente wurden in Geant4 Code nachgebildet. Um die Simulationszeit der verschiedenen Verlustszenarien zu optimieren, wurde ein Näherungsverfahren angewandt, welches lokalen Teilchenverlusten dem Verlustmuster entsprechende Koeffizienten zuteilt. Die Genauigkeit dieser Methode wurde durch den Vergleich von simulierten Teilchenschauern außerhalb der Magnetkryostaten mit den BLM-Signalen während der Quenchtests validiert. Ergänzende Berechnungen des Quenchniveaus wurden mit einem QP3-Wärmeübertragungscode durchgeführt.

Die Quenchlevel aus dieser Studie liefern wichtige Informationen für die Optimierung der BLM Schwellenwerte. Dies ermöglicht die Reduktion der Unsicherheitsspannen und damit die Vermeidung unnötiger Strahlextraktionen.

STICHWÖRTER: Quenchlevel, strahlinduzierter Quench, supraleitende Magnete, Quenchtest, schnelle Strahlverluste, stationäre Strahlverluste, Strahlverlustmonitore, BLM, Magnetschutz, Geant4 Simulationen

Acknowledgments

Like a butterfly flapping its wing can induce a hurricane, even a small interaction might be sufficient to change one's life. Initial conditions, history, environment and people who we meet affect us and participate in the process of becoming who we are currently. However, the dominant contribution usually comes from our close ones. Therefore, first of all I would like to express my greatest gratitude to my beloved family: my mom Katarzyna Priebe, grandma Krystyna Rybarska, grandpa Stanisław Rybarski and my sister Magdalena Priebe who have always provided me love, believed in me and supported me in making my dreams come true. It is also your merit that I have become the person who I am now. Thank you for that! In addition, I would like to give a big smile to my twin sister, who was and is my point of reference. Many times, our “little” competition was the strongest motivation and driving force for me (... well, for her too ...).

I would like to thank my fiancée, Rafał Noga for his love and that I could rely on him in difficult moments. His objective attitude was also valuable to me and has allowed me to see the World from a new, different perspective.

I would like to show my appreciation to my supervisors, Prof. Dr. Minh Quang Tran and Dr. Mariusz Sapiński, who supervised my doctoral studies. I would like to thank them for the guidelines and effort they made in correcting this thesis. I am also grateful to the section leader of Beam Loss Monitoring section, Dr. Bernd Dehning for enabling me to perform my studies at CERN.

The quench tests conducted in 2013 would not be possible without the cooperation of many excellent experts. Especially, I would like to thank Tobias Baer, Daniel Valuch and Wolfgang Hoefle for their great involvement and professionalism.

A big thank you goes to Vera Chetvertkova for providing the beam tracking simulations in MadX, Arjan Verweij and Bernhard Auchmann for the help with QP3 code and cross-checking my calculations, Anton Lechner and Nikhil Shetty for sharing their Fluka results, which I could use for the comparison with my Geant4 data. Special thanks belong to Eduardo Nebot Del Busto for his kind help in solving problems related to programming.

I would like to show my gratitude to Christoph Kurfuerst and Aurelien Marsili for translating

Acknowledgments

the abstract of this thesis into German and French, respectively. Thank you guys!

Besides the scientific development, the time spent here was also the wonderful opportunity for hiking and discovering the beauty of the Swiss and French Alps. I was lucky to share these moments with Rafal, Magda and my A-Team - Sophie Mallows, Juan Herranz Alvarez, Jose Luis Sirvent Blasco and Eleftherios Fadakis. I have really enjoyed our trips!

I will also always remember nice and funny chats with my two colleagues, Christoph Kurfuerst and Mateusz Dąbrowski, who have used to be my office mates and R3 company as well.

Last, but not least I would like to thank all other colleagues, who I had a pleasure to meet at CERN and work with. I have learnt a lot during these three years and I am very grateful to them for sharing their knowledge and experience.

CERN, 20 December 2013

Agnieszka Priebe

Podziękowania

Niczym trzepot skrzydeł motyla może wywołać huragan, tak nawet małe oddziaływanie może wystarczyć, aby zmienić czyjeś życie. Zarówno warunki początkowe, historia, środowisko, jak i ludzie, których spotykamy, wpływają na nas i biorą udział w procesie kreowania ludzi, jakimi się w końcu stajemy. Nie mniej jednak, dominujący udział zazwyczaj pochodzi od naszych bliskich. Dlatego, przede wszystkim chciałabym podziękować mojej ukochanej rodzinie: mojej mamie Katarzynie Priebe, mojej babci Krystynie Rybarskiej, mojemu dziadkowi Stanisławowi Rybarskiemu i mojej siostrze Magdalenie Priebe, którzy zawsze zapewniali mi miłość, wierzyli we mnie i wspierali w dążeniu do realizacji moich marzeń. To również Wasza zasługa, że stałam się osobą, którą jestem dzisiaj. Dziękuję Wam za to! Ponadto, chciałabym przesłać duży uśmiech mojej siostrze bliźniaczce, która była i jest moim punktem odniesienia. Niejednokrotnie nasza „mała” rywalizacja była dla mnie największą motywacją i siłą napędową (... cóż, dla niej również ...).

Chciałabym podziękować mojemu narzeczonemu, Rafałowi Nodze za jego miłość i za to, że mogłam na nim polegać w trudnych chwilach. Jego obiektywna postawa była dla mnie bardzo wartościowa i pozwoliła mi dojrzeć świat z nowej, innej perspektywy.

Chciałabym wyrazić moją wdzięczność moim promotorom, Prof. Dr. Minh Quang Tran i Dr. Mariuszowi Sapińskiemu, którzy sprawowali pieczę nad moim doktoratem. Chciałabym im podziękować za wskazówki i trud włożony w korektę mojej pracy. Jestem również wdzięczna kierownikowi sekcji Beam Loss Monitoring, Dr. Berndowi Dehningowi za umożliwienie mi odbycia studiów w CERNie.

Quench testy przeprowadzone w 2013 roku nie byłyby możliwe bez współpracy wielu świętych ekspertów. Chciałabym zwłaszcza podziękować Tobiasowi Baer, Danielowi Valuchowi i Wolfgangowi Hoefle za ich wielkie zaangażowanie i profesjonalizm.

Specjalne podziękowania należą się Verze Chetvertkovej za wykonanie symulacji orbity wiązki w MadX, Arjanowi Verweijowi i Bernhardowi Auchmannowi za pomoc z kodem QP3 i sprawdzenie wyników moich obliczeń oraz Antonowi Lechnerowi i Nikhilowi Shetty'emu za udostępnienie swoich wyników z Fluki, które mogłam użyć do porównania z moimi rezultatami z Geant4. Specjalne podziękowania należą się Eduardo Nebot Del Busto za jego życzliwą pomoc w rozwiązywaniu problemów związanych z programowaniem.

Podziękowania

Chciałabym wyrazić moją wdzięczność Christophowi Kurfuerstowi i Aurelienowi Marsili za przetłumaczenie streszczenia niniejszej pracy odpowiednio na niemiecki i francuski. Dzięki chłopaki!

Poza rozwojem naukowym, czas spędzony tutaj był dla mnie również wspaniałą okazją do wędrówek i odkrywania piękna szwajcarskich i francuskich Alp. Miałam szczęście dzielić te chwile z Rafałem, Magdą i moją Drużyną A - Sophie Mallows, Juanem Herranzem Alvarezem, Jose Luisem Sirventem Blasco i Eleftheriosem Fadakisem. Naprawdę bardzo podobały mi się nasze wycieczki!

Zawsze będę też pamiętać miłe i zabawne pogawędki z dwojgiem moich kolegów, Christophe'm Kurfuerstem i Mateuszem Dąbrowskim, z którymi również dzieliłam biuro, i którzy dotrzymywali mi towarzystwa w R3.

Na końcu chciałabym podziękować wszystkim pozostałym koleżankom i kolegom, których miałam przyjemność poznać w CERNie, i z którymi pracowałałam. Wiele się nauczyłam w przeciągu tych trzech lat i jestem im bardzo wdzięczna za dzielenie się ze mną swoją wiedzą i doświadczeniem.

CERN, 20 grudnia 2013

Agnieszka Priebe

Contents

Abstract (English/Français/Deutsch)	v
Acknowledgments	xi
Podziękowania	xiii
Acronyms	xxvii
Glossary	xxxi
1 Introduction	1
1.1 CERN	1
1.2 Accelerating particles at CERN - a journey from the red bottle to the experiments	1
1.3 The Large Hadron Collider	3
1.4 Basic concepts of superconductivity	5
1.5 LHC main magnets	10
1.5.1 Transfer matrix formalism	11
1.5.2 Design of the LHC Main Magnets	13
1.6 LHC magnet protection systems	15
1.6.1 Introduction	15
1.6.2 Quench Protection System	19
1.6.3 Beam Loss Monitoring System (BLM)	22
1.6.4 Operational statistics	27
1.7 Beam losses	28
1.7.1 Regular and irregular losses	28
1.7.2 Classification of beam losses by loss duration	29
1.7.3 UFOs	30
1.8 Methodology of inducing controlled beam losses	30
1.8.1 Three corrector orbit bump	31
1.8.2 Transverse Damper (ADT)	34
2 Overview of the beam induced LHC Quench Tests	39
2.1 Ultra fast losses	40
2.1.1 Q6 Quench Test 2011	40
2.1.2 Q6 Quench Test 2013	41

Contents

2.1.3	Injection&Dump Quench Test on arc LHC Main Magnets	41
2.2	Fast losses	41
2.2.1	Wire Scanner Quench Tests 2010	42
2.2.2	Fast Loss Quench Test 2013 on MQ12.L6	44
2.3	Steady state losses	44
2.3.1	3.5 TeV Collimation Quench Test with protons 2011	44
2.3.2	3.5 Z TeV Collimation Quench Test with lead ions 2011	45
2.3.3	4 TeV Collimation Quench Test with protons 2013	46
2.3.4	450 GeV Steady State Loss Quench Test 2010	47
2.3.5	3.5 TeV Steady State Loss Quench Test 2010 on MQ.14R2	49
2.3.6	4 TeV Steady State Loss Quench Test 2013 on MQ.12L6	49
2.4	Strategy of assessing quench levels	50
2.5	Summary of the beam induced Quench Tests	51
3	Geant4 simulations	55
3.1	Motivation of using Geant4 code	55
3.2	Introduction to Geant4	55
3.3	Code description	55
3.3.1	Physics list	56
3.3.2	Magnetic field	56
3.3.3	Magnet representation	57
3.3.4	Sensitive Detector	59
3.4	Strategy of simulating BLM signals	59
3.4.1	BLM response functions	60
3.4.2	Contribution of secondary particles to the total BLM signal	61
3.5	Strategy of determining loss patterns	63
3.6	Error origins	66
3.7	Summary of the Geant4 simulation strategy	67
4	4 TeV Fast Loss Quench Test 2013	69
4.1	Motivation	69
4.2	Preparation to the Quench Test	69
4.3	ADT Fast Loss Test at 450 GeV (26.03.2012)	70
4.4	ADT Fast Loss Test at 450 GeV and 4 TeV (22.06.2012)	71
4.5	ADT combined with MKQ Fast Loss Test (13.10.2012)	74
4.6	Installing the additional equipment	76
4.7	ADT setting test (30.01.2013)	77
4.8	Description of the Fast Loss Quench Test	79
4.9	Analysis of the experimental data	80
4.9.1	Characteristic of the beam and induced beam losses	80
4.9.2	Validation of BLM thresholds with experimental data	86
4.10	Geant4 simulations	88
4.10.1	Loss pattern studies	89

4.10.2 Energy deposition inside a superconducting coil	91
4.10.3 BLM signals	96
4.10.4 Quench levels obtained with QP3 heat transfer code	99
4.10.5 Comparison between Geant4 and Fluka simulations	104
4.10.6 Quench levels - Geant4, Fluka and QP3 results	110
4.10.7 Final summary and conclusions	111
5 3.5 TeV Steady State Loss Quench Test 2010	113
5.1 Motivation	113
5.2 Description of 3.5 TeV Steady State Loss Quench Test 2010	113
5.3 Analysis of the experimental data	114
5.3.1 Studies of beam intensity loss	114
5.3.2 Beam position measurements	118
5.3.3 BLM signals and loss evolution	119
5.3.4 Development of the beam loss and onset of the quench	120
5.4 Analysis of the Geant4 simulations	123
5.4.1 Evolution of applied methods for assessing the loss pattern	125
5.4.2 Presentation of GQM results	127
5.4.3 Summary of assessing quench levels	134
6 4 TeV Steady State Loss Quench Test 2013	137
6.1 Motivation	137
6.2 Description of the Steady State Loss Quench Test	138
6.3 Analysis of the experimental data	140
6.3.1 Characteristic of the beam losses	140
6.3.2 Development of the beam loss and onset of the quench	145
6.3.3 Validation of BLM thresholds	146
6.4 Results of Geant4 simulations	148
6.4.1 Loss pattern studies	149
6.4.2 Energy deposition inside a superconducting coil	150
6.4.3 BLM signals	154
6.4.4 Quench levels obtained with QP3 heat transfer code	158
6.5 Final conclusions	158
7 Summary and final conclusions	161
8 Future perspectives	167
A Technical drawings	169
B Response functions	175
Bibliography	186
Curriculum Vitae	187

Contents

List of publications	193
-----------------------------	------------

List of Figures

1.1	CERN accelerator complex	2
1.2	Diagram of the LHC	4
1.3	Critical surface of NbTi	5
1.4	Meissner effect	6
1.5	Types of superconductors - magnetization curves	7
1.6	Diagram showing the principle of the BSC theory	8
1.7	Quench level	10
1.8	Diagram of a beam transfer line	13
1.9	Cross-sections of the MB and MQ	14
1.10	The LHC Superconducting cable	15
1.11	Energy stored in the beam as a function of beam momentum in the case of various accelerators	16
1.12	Material damage test at 450 GeV	17
1.13	The LHC Beam Dump	18
1.14	QPS: Diagram of the LHC MB electrical circuit	20
1.15	QPS: Diagram of the LHC MQ electrical circuit	20
1.16	QPS: Diagram of the LHC MB circuit in the case of quenching	21
1.17	Diagram of an ionization chamber	23
1.18	Design of BLM	24
1.19	BLM locations in the LHC arcs	25
1.20	A diagram of processes assigned to the FPGA of the BLM system	26
1.21	A diagram of a three corrector orbital bump	31
1.22	A simplified block diagram of the transverse feedback system	35
1.23	A diagram of the LHC Transverse Damper	36
1.24	Influence of the transverse damper on injection errors	37
1.25	Impact of the transverse damper gain on damping vertical oscillations	37
2.1	Wire Scanner Quench Test 2011: Final results	43
2.2	Wire Scanner Quench Test 2011: Measured and simulated BLM signals	43
2.3	Proton Collimation Quench Test 2011: Tune functions in time.	45
2.4	Proton Collimation Quench Test 2011 and 2013:Comparison	46
2.5	Proton Collimation Quench Test 2013:Losses	47
2.6	450 GeV Main Magnet Quench Test 2010: Beam intensities	48

List of Figures

2.7	450 GeV Main Magnet Quench Test 2010: Signal in BLMs	48
2.8	Strategy of assessing quench levels	50
3.1	Magnetic field map of the MQ at 3.5 TeV	57
3.2	Geant4 simulations: MQ coil division into recording unit cells	60
3.3	BLM response functions	61
3.4	Angular distribution - calculating contributions of available response functions	63
3.5	Distribution of the normalized simulation-experiment similarity estimator - symmetrical case	66
3.6	Diagram of the Geant4 simulation strategy	68
4.1	ADT Fast Loss Test at 450 GeV: Beam and loss characteristics obtained using different ADT modes	70
4.2	ADT Fast Loss Test at 450 GeV and 7 TeV: Final results	72
4.3	ADT Fast Loss Test at 450 GeV and 7 TeV: Correspondence between BPM and BLM measurements	73
4.4	ADT Fast Loss Test at 450 GeV and 7 TeV: Time constants of beam oscillations for injection and nominal energies	74
4.5	ADT Fast Loss Test at 450 GeV and 7 TeV: Comparison of ADT-induced losses with results of WS Quench Test 2010 and UFO losses	75
4.6	ADT Fast Loss Test at 450 GeV and 7 TeV: Integrated BLM signals of ADT-induced losses, WS-induced losses and UFO losses	75
4.7	ADT combined with MKQ Fast Loss Test: Loss durations	76
4.8	LHC half-cell 12L6: diagram of BLM locations	77
4.9	MQ.12L6 and its vicinity before installation of mobile monitors	78
4.10	MQ.12L6 and its vicinity after installation of mobile monitors	78
4.11	Diagram of the procedure applied during the Fast Loss Quench Test (15.02.2013)	81
4.12	Fast Loss Quench Test 2013: Loss structure	82
4.13	FLQT 2013: Radiation along the magnets (RS06)	84
4.14	FLQT 2013: comparison of longitudinal propagation of secondary particle shower for different bunches	85
4.15	Fast Loss Quench Test 2013: Final summary	86
4.16	Fast Loss Quench Test 2013: BLM signals vs. thresholds when no quenching occurred	87
4.17	Fast Loss Quench Test 2013: BLM signals vs. thresholds during the MQ quench	87
4.18	Fast Loss Quench Test 2013: Geant4 magnet representation	89
4.19	Fast Loss Quench Test - Loss patterns	90
4.20	Fast Loss Quench Test 2013: angle	92
4.21	Fast Loss Quench Test 2013: Geant4 simulations - longitudinal energy density distribution inside a coil	93
4.22	Fast Loss Quench Test 2013: Geant4 simulations - radial maximum energy density distribution in SC coil	95

4.23 Fast Loss Quench Test 2013: Geant4 simulations (Case 73) - coil cross-section in the plane where the maximum energy density was deposited	95
4.24 Fast Loss Quench Test - Color maps of energy density in coils	96
4.25 Fast Loss Quench Test 2013: Geant4 simulations - Quenching volume as a function of considered criteria	97
4.26 Fast Loss Quench Test 2013: Geant4 simulations - secondary particle distribution along the magnets	98
4.27 Fast Loss Quench Test 2013: Geant4 simulations (Case 73) - Angular distributions of particles recorded by BLMs	98
4.28 Fast Loss Quench Test 2013: Geant4 simulations (Case 73) - Angular contribution of particles to the signals recorded by BLMs	99
4.29 Fast Loss Quench Test 2013: Geant4 simulations (Case 73) - Contribution of secondary particles to the BLM current	100
4.30 Fast Loss Quench Test 2013: Geant4 simulations (Case 73) - Current generated in BLMs by secondary particles	100
4.31 Fast Loss Quench Test - a comparison of measured and simulated BLM signals	101
4.32 Fast Loss Quench Test 2013: Geant4 simulations - error estimations of the simulated BLM signals	102
4.33 Fast Loss Quench Test 2013: QP3 input distributions	103
4.34 Fast Loss Quench Test 2013: QP3 input distributions	105
4.35 Fast Loss Quench Test 2013: BLM signals - comparison of Geant4 and Fluka results	108
4.36 Fast Loss Quench Test 2013: BLM signals - comparison of Geant4 and Fluka results	109
4.37 Fast Loss Quench Test 2013: BLM signals - correspondence between BLM signals obtained with Geant4 and Fluka simulations.	109
5.1 Steady State Quench Test 2010: Diagram of the three corrector orbital bump.	115
5.2 Steady State Loss Quench Test 2010: beam intensity	116
5.3 Steady State Loss Quench Test 2010: Beam radiation along the LHC	116
5.4 Steady State Loss Quench Test 2010: Comparison of losses on the target and collimator	117
5.5 Beam position measurements provided by the BPMs. Zero on x-axis corresponds to the moment of the beam dump. Although the bump was imposed in the vertical plane (the violet line) the deflection of beam orbit in the horizontal plane was observed (the pink curve) as well.	118
5.6 Steady State Loss Quench Test 2010: Locations of BLMs	119
5.7 Steady State Quench Test 2010: BLM signals in time (RS09)	121
5.8 Steady State Quench Test 2010: Longitudinal radiation distribution based on RS09 measurements	121
5.9 Steady State Quench Test 2010: Radiation distribution in space and time (BLM signals)	122
5.10 Steady State Quench Test 2010: Loss evolution in time	122

List of Figures

5.11 Steady State Quench Test 2010: Summary plot of BLM and QPS signals at the moment of quenching	124
5.12 Steady State Quench Test 2010: β -function at 3.5 TeV	126
5.13 GQM results - Evolution of $\Sigma_{\mu, \sigma_r, \sigma_l}^{norm}$ as a function of σ_l	128
5.14 GQM results - Evolution of $\Sigma_{\mu, \sigma_r, \sigma_l}^{norm}$ as a function of σ_r	129
5.15 GQM results - distribution of $\Sigma_{\mu, \sigma_r, \sigma_l}^{norm}$ as a function of σ_l and σ_r	130
5.16 Steady State Quench Test 2010: Loss pattern obtained using GQM	130
5.17 Steady State Quench Test 2010: Energy density distribution in the SC coil and the number of secondary particles reaching the pseudo-detectors	132
5.18 Steady State Quench Test 2010: Radial distribution of energy density along the most exposed bin.	132
5.19 Steady State Quench Test 2010: Ratios between simulated and measured BLM signals for the best fitting scenario.	133
5.20 Steady State Quench Test 2010: Time dependent loss pattern evolution.	133
5.21 Steady State Quench Test 2010: Time dependent loss pattern evolution - 3D. . .	134
6.1 Diagram of the procedure applied during the Steady State Loss Quench Test (16.02.2013).	138
6.2 Steady State Loss Quench Test 2013: ADT excitation function	139
6.3 Steady State Loss Quench Test 2013: Beam intensity	141
6.4 Steady State Loss Quench Test 2013: Bunch by bunch intensity measurements .	141
6.5 Steady State Loss Quench Test 2013: BLM signals	143
6.6 Steady State Loss Quench Test 2013: Loss pattern	143
6.7 Steady State Loss Quench Test 2013: Comparison of longitudinal radiation profiles resulting from two excitations.	144
6.8 Comparison of longitudinal BLM signals along magnets between SSLQT 2013 and FLQT 2013	144
6.9 Steady State Loss Quench Test 2013: Final results	145
6.10 Steady State Loss Quench Test 2013: BLM signals vs. thresholds when no quenching occurred	147
6.11 Steady State Loss Quench Test 2013: BLM signals vs. thresholds during quenching	147
6.12 BLM threshold as a function of loss scale	148
6.13 Steady State Loss Quench Test - Loss pattern	149
6.14 Steady State Loss Quench Test 2013: Geant4 simulations - longitudinal energy density distribution inside a coil	150
6.15 Steady State Loss Quench Test 2013: Geant4 simulations - radial maximum energy density distribution in a SC coil	151
6.16 Steady State Loss Quench Test 2013: Geant4 simulations - coil cross-section in the plane where the maximum energy density was deposited	151
6.17 Steady State Loss Quench Test - Color maps of energy density in coils	152
6.18 Steady State Loss Quench Test 2013: Geant4 simulations - Quenching volume as a function of considered criteria	153

6.19 Steady State Loss Quench Test 2013: Geant4 simulations - secondary particle distribution along the magnets	154
6.20 Steady State Loss Quench Test 2013: Geant4 simulations - Angular distributions of particles recorded by BLMs	155
6.21 Steady State Loss Quench Test 2013: Geant4 simulations - Contribution of different response functions to the total signal	156
6.22 Steady State Loss Quench Test 2013: Geant4 simulations - Current generated in BLMs by secondary particles	156
6.23 Steady State Loss Quench Test 2013: Geant4 simulations - Contribution of secondary particles to the BLM signal	157
6.24 Steady State Loss Quench Test - a comparison of measured and simulated BLM signals	157
6.25 Steady State Loss Quench Test 2013: Geant4 simulations - error estimations of the simulated BLM signals	158
6.26 Steady State Loss Quench Test 2013: QP3 input distributions	159
A.1 Technical drawing: MQ cross-section	170
A.2 Technical drawing: MB cross-section	171
A.3 Technical drawing: SSS-MB Interconnection	172
A.4 Technical drawing: MB-SSS Interconnection	173
A.5 Technical drawing: Layout of LHC cell Q12	174
B.1 BLM response functions for various particle types and impacting angles	176

List of Tables

1.1	BLM integration time windows	27
2.1	Ion Collimation Quench Test 2011: Summary. BLM signals compared to the quench levels for different limiting locations.	46
2.2	450 GeV Main Magnet Quench Test 2010: Summary	49
2.3	Summary of the beam induced Quench Tests	53
4.1	Fast losses in the LHC: summary	74
4.2	FLQT: Beam and loss parameters	83
4.3	Fast Loss Quench Test 2013: Summary - measured BLM signals compared to the expected BLM values at quench for different integration times.	88
4.4	Fast Loss Quench Test 2013: Comparison of loss patterns	91
4.5	Fast Loss Quench Test 2013: Maximum energy density in the SC coil	93
4.6	Fast Loss Quench Test 2013: Energy deposited in the coil - final results	94
4.7	Fast Loss Quench Test 2013: Fast Loss Quench Test 2013: QP3 results - E_{peak} in the coil	104
4.8	Fast Loss Quench Test 2013: Fast Loss Quench Test 2013: QP3 results - E_{avg} in the coil	105
4.9	Fast Loss Quench Test 2013: Quench level as a function of time and number of lost protons (QP3 results)	106
4.10	Fast Loss Quench Test 2013: Quench levels	107
4.11	Fast Loss Quench Test 2013: BLM signals - Comparison between Geant and Fluka results	110
4.12	Fast Loss Quench Test 2013: BLM signals - Comparison between Geant and Fluka results	110
4.13	Fast Loss Quench Test 2013: Comparison between Geant4 and Fluka simulations	112
5.1	Steady State Loss Quench Test 2013: Summary of quench limits obtained with different simulation approaches	135
6.1	Steady State Loss Quench Test 2013: Summary - measured BLM signals compared to the expected BLM signals at quench for different integration times.	146
6.2	SSLQT and FLQT 2013: Maximum energy density in the SC coil	151

List of Tables

7.1	Summary of the beam induced Quench Tests 2013	163
-----	-----------------------------------------------	-----

Acronyms

AD	Antiproton Decelerator
ADC	Analog to Digital Converter
ADT	Transverse Dumper
ALICE	A Large Ion Collider Experiment
ATLAS	A Toroidal LHC Apparatus
B1H	Beam 1 in horizontal plane
B2V	Beam 2 in vertical plane
BCS	Bardeen, Cooper, Schrieffer theory
BIS	Beam Interlock System
BLM	Beam Loss Monitor
BLN	Brookhaven National Laboratory
BPM	Beam Position Monitor
CDD	CERN Drawing Directory Server
CERN	European Organization for Nuclear Research
CFC	Current to Frequency Converter
CLIC	Compact Linear Collider
CMS	Compact Muon Solenoid
CNGS	CERN Neutrinos to Gran Sasso
CTF3	CLIC Test Facility 3
DCUM	CUMulative Distance
DESY	Deutsches Elektronen-Synchrotron (German Electron Synchrotron)
DB	Data Base
DC	Direct Current
DS	Dispersion Suppressor
EE	Energy Extraction
FBCT	Fast Beam Current Transformer
FLQT	Fast Loss Quench Test
FWHM	Full Width at Half Maximum
FPGA	Field Programmable Gate Array
GEANT4	GEometry ANd Tracking (Monte Carlo code)
HERA	Hadron-Elektron-Ringanlage (Hadron-Electron Ring Accelerator)
IC	Ionization Chamber
IP	Interaction Point

Acronyms

IR	Insertion Region
ISOLDE	Isotope Separator On Line DEvice
LEIR	Low Energy Ion Ring
LEP	Large Electron–Positron Collider
LHC	Large Hadron Collider
LHCb	Large Hadron Collider beauty
LHCf	Large Hadron Collider forward
LINAC2	LINear ACcelerator 2
LS1	Long Shutdown 1
MAD-X	Methodical Accelerator Design version X
MB	Main Dipole
MBRB	Twin Aperture Separation Dipole
MCBH	Arc Orbit Corrector in MSCBA(B,C,D), Horizontal
MCBV	Arc Orbit Corrector in MSCBA(B,C,D), Vertical
MSCBB	Dipole Corrector in Arc SSS. External aperture consists of MS+MCBV and internal aperture is made of MS+MCBH. External aperture is defocusing.
MD	Machine Development
MDT	Superconducting Magnet Design and Technology
MF	Monitor Factor
MKD	Ejection dump kicker
MKQ	Magnet Kicker for Q (Tune Kicker)
MQ	Main Quadrupole
MQE	Minimum Quench Energy
MO	Octupole lattice corrector in arc SSS
MP	Machine Protection
MPP	Machine Protection Panel
MPS	machine Protection System
MQT	Tuning (or short trim) quadrupole corrector in arc SSS
MS	Arc sextupole lattice corrector associated to MCBH or MCBV in MSCBA(B C,D)
nTOF	neutron Time-Of-Flight
OP	OPeration
PM	Post Mortem
PS	Proton Synchrotron
QPS	Quench Protection System
QT	Quench Test
QTSAG	Quench Test Strategy Analysis Group
QTSWG	Quench Test Strategy Working Group
QL	Quench Level
RF	Radio Frequency
RHIC	Relativistic Heavy Ion Collider
RS	Running Sum
SBF	Safe Beam Flag

SC	SuperConducting
SEM	Secondary Emission Monitor
SPS	Super Proton Synchrotron
SSLQT	Steady State Loss Quench Test
SSS	Short Straight Section
TC	Threshold Comparator
THEA	Thermal, Hydraulic and Electric Analysis
TOTEM	TOtal Elastic and diffractive cross section Measurement
UFO	Unidentified Falling Objects
WS	Wire Scanner

Glossary

<i>ADT</i>	- see <i>Transverse Damper</i>
<i>Beam</i>	- a group of particles used in an accelerator; a beam might constitute of one or many bunches
<i>Beam dump</i>	- a part of an accelerator where a beam can be deposited without damaging it
<i>Beta function</i>	- a beam optical periodic function (one of Twiss parameters) which changes along an accelerator
<i>BLM</i>	- Beam Loss Monitor, a detector installed in the LHC tunnel (for example on a magnet cryostat or mobile stands) for measuring radiation of secondary particles
<i>Bunch</i>	- a package of many particles traveling inside an accelerator
<i>Bunch train</i>	- a group of bunches which are injected together to a machine from its preaccelerator
<i>Dipole</i>	- a magnet constituting of two poles; according to Lorenz force, it bends a trajectory of charged particles
<i>Emittance</i>	- a property of a particle beam; it is an area limited by position and angle of a particle; in the case of a bunch constituting of many particles, the emittance is defined as the averaged value of areas enclosed by these particles ; it is constant along an accelerator
<i>Geant4</i>	- a C++ code describing a transport of particles and their interactions with the matter; it is based on Monte Carlo methods
<i>Machine Development</i>	- a special time period in a machine operation devoted to the studies of its components (capability and maintenance)

Glossary

<i>MAD-X</i>	- stands for Methodical Accelerator Design, a code used for simulating behaviour of particle accelerators, describing beam dynamics and optimizing beam optics; in the case of beam-induced Quench Tests MAD-X was used for assessing loss patterns of excited particles
<i>Nominal bunch</i>	- a package of $(1.1 - 1.7) \cdot 10^{11}$ protons which are needed to reach nominal luminosity of $L = 10^{34} \text{ cm}^{-2} \text{ s}^{-1}$ at the values of beta function in the collision point $\beta* = 0.55 \text{ m}$
<i>Pilot bunch</i>	- a package of $(2 - 5) \cdot 10^9$ protons which is injected to the LHC before high intensity bunches; a loss of a pilot bunch at injection energy (450 TeV) assures that no magnet quenching will occur
<i>QP3</i>	- a heat transfer code developed at CERN; it estimates quench behaviour and provides calculations of maximum and average energy which deposition in a superconducting cable leads to quenching
<i>QPS</i>	- Quench Protection System, a system for detecting quenching of superconducting elements and providing an active protection
<i>Quench</i>	- a transition from the superconducting (resistance free current flow) to the normal conducting state (resistant current flow)
<i>Quench level</i>	- amount of energy which causes the transition of a superconducting component to the resistive state (quenching)
<i>Quench test</i>	- an experiment devoted to quenching a superconducting element
<i>Quadrupole</i>	- a magnet which is built of four poles; it is used for focusing a charged particle beam in the transverse plane (horizontal or vertical)
<i>Three corrector orbit bump</i>	- a technique of changing particle beam position using three correctors; it is used for hitting magnets during experiments in LHC arc sections
<i>Transverse Damper (ADT)</i>	- a system used for damping beam oscillations in standard operation mode; it was used for inducing beam losses during the quench tests

1 Introduction

1.1 CERN

European Organization for Nuclear Research, CERN,¹ is one of the leading research centres in the World. It was founded in 1954 and currently (year 2013) has 20 member states. The laboratory is located on the Franco-Swiss border close to the city of Geneva.

Approaching the technology frontiers in development of sophisticated instruments allowed performing experiments never done before. This resulted in several breakthroughs among which, the most prominent are the discovery of Z and W bosons (1983, Nobel prize for C. Rubbia and S. van der Meer in 1984), creating first atoms of anti-hydrogen² (1995) and discovery of Higgs boson (2012).

The variety in CERN's scientific domain is broad - from studying fundamental particles, producing antimatter and engineering to software development. Nevertheless, what makes it the most recognizable nowadays is the largest and the highest-energy accelerator in the World - the Large Hadron Collider (LHC).

1.2 Accelerating particles at CERN - a journey from the red bottle to the experiments

The LHC will deliver particles with unprecedented energy of 7 TeV to experiments where they will collide. However, due to the magnitude of ultimate energy, the LHC cannot work as a standalone machine. Therefore, a system of pre-accelerators is required to provide beam energy increase in intermediate steps.

¹The acronym CERN stands for *Conseil Européen pour la Recherche Nucléaire* (i.e. *European Council for Nuclear Research*). This provisional organization was established in 1952. Although the European Organization for Nuclear Research was founded two years later, the former acronym is used till nowadays.

²An anti-hydrogen is an atom constituting from one antiproton (particle alike proton but with the negative charge) and one positron (i.e. antielectron, particle alike electron but with the positive charge).

Chapter 1. Introduction

A story of particles³ heading to the LHC starts in the red bottle filled with gaseous hydrogen. In order to strip electrons from the H₂ atoms, a so-called duoplasmatron (an ion source) is used. As the result of applied electric field, 50 keV protons are obtained and extracted to the first and the last linear accelerator (LINAC2, Fig. 1.1) on their way. At the end of the machine, particle energy reaches the value of 50 MeV. Then, they are injected to the first circular structure - the Proton Synchrotron Booster (PSB). This four-ring accelerator increases a number of protons delivered to the Proton Synchrotron (PS) by a factor of 100 when comparing to direct transferring from the LINAC2. At this level, the beam energy is enlarged to 1.4 GeV. Bunches are guided to a 628 m long structure of 277 room-temperature PS electromagnets where their structure is modified (a so-called bunch splitting) and the protons reach the energy of 25 GeV. This is followed by leading them to the SPS (Super Proton Synchrotron) where they travel through the same path as they predecessors 40 years earlier when contributing to the discovery of W and Z bosons. Finally, after reaching the energy of 450 GeV, protons are injected through two transfer lines (TI2 and TI8) in the opposite directions to their final destination - the LHC. Eight radio-frequency (RF) cavities operating at 4.5 K provide the total accelerating voltage of 16 MV per beam at 400 MHz. Around 9600 LHC magnets (most of them superconducting) will allow controlling beams at the nominal energy of 7 TeV. At the last stage, the particles collide in one of the four dedicated experiments: ALICE (A Toroidal LHC Apparatus), ATLAS (A Large Ion Collider Experiment), CMS (Compact Muon Solenoid) or LHCb (Large Hadron Collider beauty). Besides that, there are two other experiments: TOTEM (TOTal Elastic and diffractive cross section Measurement) and LHCf (Large Hadron Collider forward).

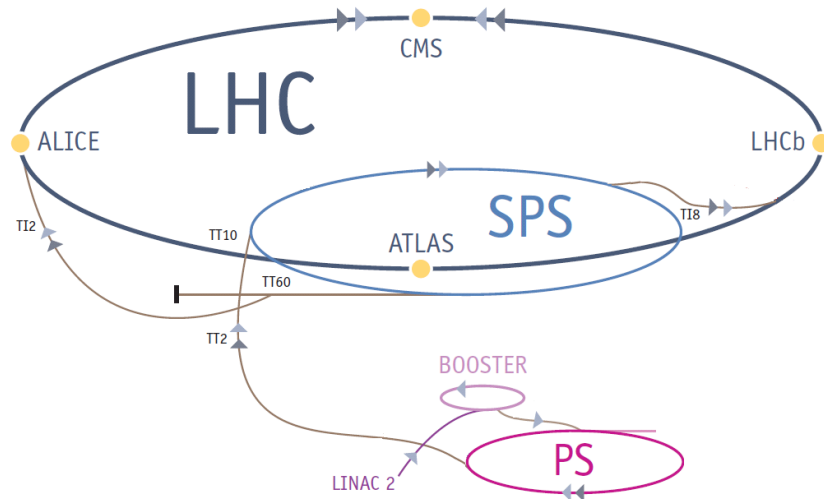


Figure 1.1 – CERN accelerator complex [1]. LINAC 2 - linear accelerator, PS - proton Synchrotron, SPS - Super Proton Synchrotron, LHC - Large Hadron Collider, TT2 and TT8 - transfer lines, ATLAS, ALICE, CMS, LHCb - experiments.

³Two types of particles are currently used in the LHC - protons and lead ions. However, since the experiments presented in the thesis were performed using protons, only these particles are considered here.

1.3 The Large Hadron Collider

Design of the LHC The LHC (Large Hadron Collider) is the highest-energy accelerator ever built⁴ which at nominal energy will provide unprecedented beam energy of 7 TeV. This 27 kilometer in circumference structure is located on average 100 m below the ground level⁵ depending on the geological feature between Jura mountains and Lake Geneva. The LHC is housed in the same tunnel, where previously the LEP (Large Electron–Positron Collider) was installed. The diagram of the LHC is presented in Fig. 1.2. The machine is subdivided into eight arc sections and eight insertion regions (straight sections). Each arc section is built of 23 regular ≈ 107 m long arc cells (so-called FODO cells⁶) which are made of two half-cells (like in Fig. A.5). Three ≈ 15 m long Main Dipoles (MBs, see Section 1.5) and one ≈ 6 m long Straight Section (SSS) constitute a single half-cell [2]. A SSS consists of one Main Quadrupole (MQ) and several corrector magnets [3]. A structure of insertion regions varies depending on the position along the LHC and its role, i.e. injecting beams from transfer lines TI2 and TI8, beam collisions in experimental areas, beam extracting line in Point 6, collimation regions for beam cleaning in Interaction Regions (IR3 and IR7), RF cavities in IR4. A very important part of the LHC is so-called beam dump - the only place where high energy particles can be safely deposited in case of failures or decrease in beam quality.

Particle beams circulate inside vacuum pipes with pressure of $(10^{-14} - 10^{-13})$ atm [4] which is equivalent to $(10^{-11} - 10^{-10})$ mbar. This has to be provided in order to prevent interactions of particles with gas atoms and correlated losses.

LHC proton beam Hadrons, i.e. particles constituting of quarks held by strong forces, circulating in the LHC are formed into bunches, i.e. packages constituting of $(1.1 - 1.7) \cdot 10^{11}$ protons at nominal conditions. This is a direct consequence of accelerating fields of RF cavities⁷ [5]. The bunches will be 7.55 cm long at 7 TeV [6]. A distance between each of 2808 bunches is around 7.5 m [7] which corresponds to 25 ns spacing. A transverse bunch size, σ , varies along the machine with respect to the following equation

$$\sigma(s) = \sqrt{\epsilon \cdot \beta(s) + D^2(s)\delta^2}. \quad (1.1)$$

The transverse emittance, ϵ , is an area enclosed by a particle phase space defined by a position and an angle. According to Liouville's theorem, the emittance remains constant along an accelerator if the conservative forces act on the particles [5]. Here, β refers to the optical periodic function (one of Twiss parameters), which changes along a ring. $D(s)$ is the dispersion

⁴Although the LHC is housed in the old LEP (Large Electron–Positron Collider) tunnel, its performance allows achieving the collision energy almost 28 times larger than in the case of its predecessor.

⁵This value varies from 50 m to 175 m below the ground level.

⁶FODO cell is a periodic lattice consisting of one Focusing quadrupole, O - nothing, i.e. drift space/bending magnet, one Defocusing quadrupole and O - nothing, i.e. drift space/bending magnet.

⁷Continuous beams can be managed only when using DC (Direct Current) accelerating fields or when no acceleration is needed [5].

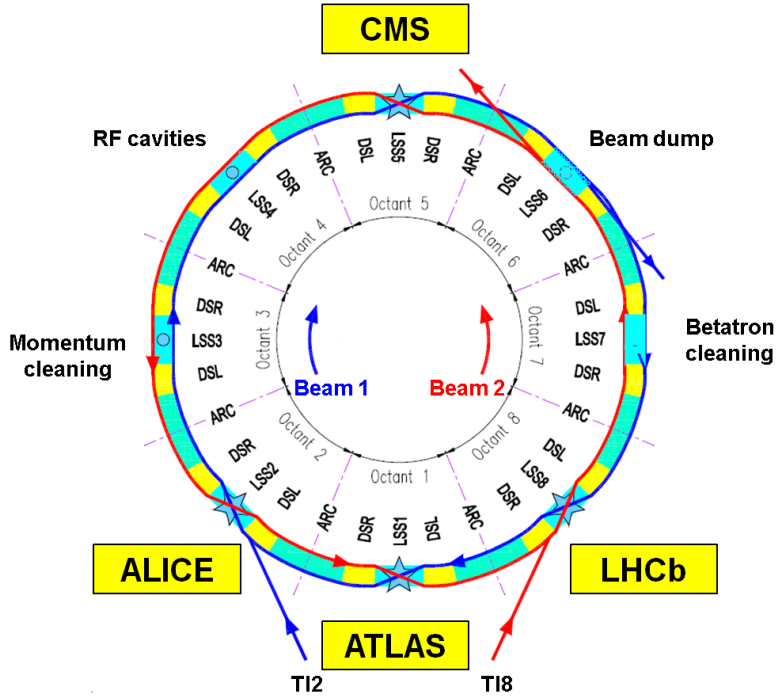


Figure 1.2 – Diagram of the LHC [2]. Particles are injected from the SPS to the LHC through two transfer lines, TI2 and TI8. Beam 1 circulates clockwise and Beam 2 travels counterclockwise. The LHC is divided into eight arc sections and eight insertion sections. Collimation systems are installed to intercept particles occupying a space beyond an acceptance regions. Beam dump allows particle beams to be safely extracted from the machine in case of machine failures or decrease of beam quality. Beams collide in the dedicated interaction points: ATLAS, ALICE, CMS and LHCb.

function (also dependent on the longitudinal position of the beam) and δ is the momentum spread of the beam.

The beam size needs to be kept as small as possible in the interaction points where two beams collide. This is due to the fact, that the beam size is one of the parameters determining the luminosity of a collider and, therefore, its performance. The additional decrease of the beam size before the Interaction Points (IP) is provided by inner triplets⁸ (so-called beam squeezing). Considering head on collision of two beams with the same transverse sizes, σ_x and σ_y in the horizontal and vertical planes, the peak luminosity is defined as

$$L = \frac{n_b N_1 N_2 f}{4\pi\sigma_x\sigma_y}, \quad (1.2)$$

where N_1 and N_2 represents populations of particles per bunch, n_b is a number of colliding bunches and f is the revolution frequency. In the case of LHC, where $f = 11.245$ kHz,

⁸Inner triplets are three low-beta quadrupole magnets located symmetrically before the IPs in order to decrease a beam size.

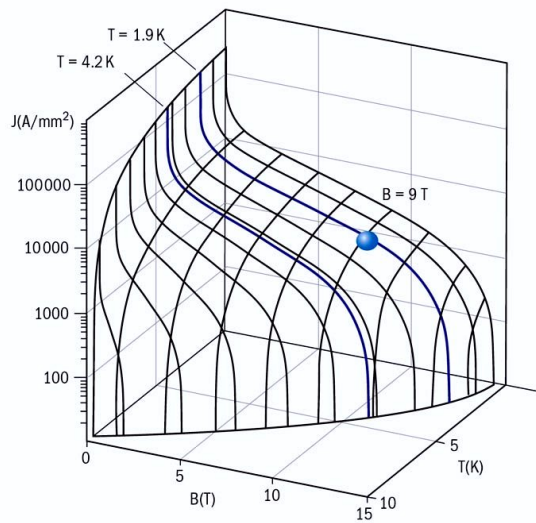


Figure 1.3 – Critical surface of NbTi [8]. The superconducting state is determined by three characteristic quantities - critical temperature T_C , critical current density J_C and critical magnetic field B_C . If any of these is exceeded, a transition to the normal conducting state, i.e. quenching, occurs.

$\sigma_x = \sigma_y = 16.7 \mu\text{m}$ at $\beta^* = 0.55 \text{ m}$ (beta function at the interaction point), the luminosity at the nominal energy is $L \approx 10^{34} \text{ cm}^{-2}\text{s}^{-1}$.

1.4 Basic concepts of superconductivity

The phenomenon of superconductivity is an excellent example of a quantum mechanics effect which manifests macroscopic properties. Its history dates back to 1908 when Heike Kamerligh Onnes succeeded in liquefaction of helium. This opened the door to studying material properties at temperatures of several Kelvins. Three years later, for the first time the state characterized by vanishing resistance was observed in pure mercury at 4.2 K. Further examinations revealed that in some materials an electric current can flow without power dissipation under certain conditions. Later it was discovered that not only the low temperature (T) but also the current density (J) and magnetic field (B) determine the existence of the superconducting (SC) state. Each superconductor is described by so-called critical surface (Fig. 1.3) which sets a boundary between the superconducting state and the normal conducting state. A material remains in the resistance free state as long as none of the quantities (T , J , B) exceeds its critical value (T_C , J_C , B_C). Otherwise, quenching, i.e. a transition to the normal conducting state, occurs.

Besides being perfect conductors, the superconductors turned out to exhibit perfect diamagnetism. Experiments performed in 1933 by Meissner and Ochsenfeld showed that the magnetic field was expelled not only if a superconductor cooled down below T_C was exposed

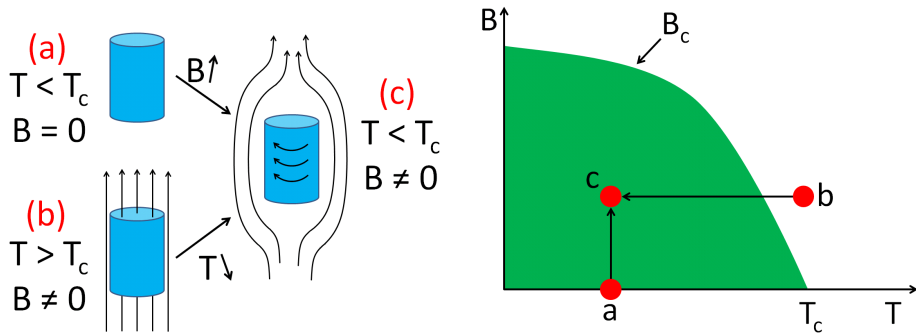


Figure 1.4 – Meissner effect. Regardless of the history of events leading to state c , i.e. case a , when a superconductor is at $T < T_c$ and then is located in $B > 0$, or case b , when the superconductor is in external B -field at $T > T_c$ and then is cooled down below T_c , the magnetic field is expelled from the superconductor's interior.

to the magnetic field (Fig. 1.4, case (a)). The same effect was achieved when a superconductor with initial temperature $T > T_c$ was located in the magnetic field and then was cooled down below the critical value (case (b)). As the first case could be explained by the properties of perfect conductors, the other one stayed beyond the physics described by classical Maxwell's equations [9]. The exclusion of the magnetic field from the interior of SC material is called Meissner effect and implies that the resistance-free state can be destroyed if $B > B_c$ [10].

In 1935, Heinz and Fritz London proposed phenomenological approach to the Meissner effect assuming the existence of "super-electrons". This lead to the definition of the London penetration depth given by

$$\lambda_L = \sqrt{\frac{m}{\mu_0 n_s e^2}}, \quad (1.3)$$

where m_e denotes electron mass, n_s is the density of super-electrons, e -electric charge and $\mu_0 = 4\pi \cdot 10^{-7} (V \cdot s)/(A \cdot m)$ is the vacuum permeability. The physical interpretation of λ_L is that actually the magnetic field lines can enter a superconducting material but only to a certain depth. Therefore, the current is allowed to flow exclusively⁹ in a thin layer limited to about $(10^{-8} - 10^{-7})$ m [9], [11].

Type I and type II superconductors

Constraining current flow to a very small region inside a superconductor makes an application of these materials very limited. Fortunately, besides type I superconductors characterized only by Meissner (the magnetic field free) phase, there are also type II superconductors where additional mixed phase (also known as Shubnikov phase) occurs (Fig. 1.5). If such a material is in $B < B_{c1}$ the magnetic field is expelled the same as in the case of type I superconductors.

⁹This applies to type I superconductors.

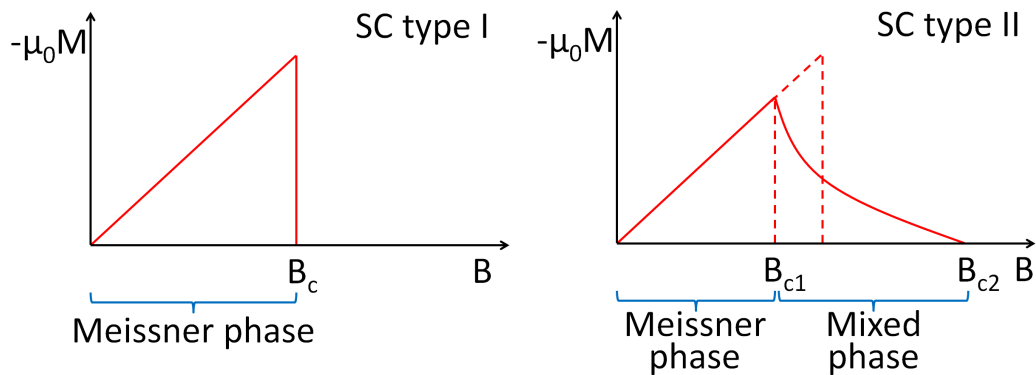


Figure 1.5 – Magnetization curves of type I (left plot) and type II superconductors (right plot). Description in the text.

However, if $B_{c1} < B < B_{c2}$ the magnetic field lines enter the material in the form of flux tubes around which the super vortex current can flow. This property finds a great use in designing accelerating cavities and high field magnets and, therefore, high energy accelerators, fusion reactors and medicine.

The criterion used for distinguishing superconductor's type relies on Ginzburg-Landau parameter. This is defined as a ratio of the London penetration depth (λ_L) and the coherence length ξ [12], i.e. the boundary over which the density of supercurrent carriers decays to zero:

$$\kappa = \frac{\lambda}{\xi}. \quad (1.4)$$

and

$$\text{if } \kappa < \frac{1}{\sqrt{2}} \rightarrow \text{type I superconductors (Pb, Hg, Sn, Al, etc.)} \quad (1.5)$$

$$\text{if } \kappa > \frac{1}{\sqrt{2}} \rightarrow \text{type II superconductors (PbIn, Nb, NbTi, Nb}_3\text{Sn, YBCO, etc.).} \quad (1.6)$$

Introduction to the BCS theory

In 1957, John Bardeen, Leon Neil Cooper, and John Robert Schrieffer proposed a theory (BCS) postulating that a flow of Cooper pairs, not single electrons as in normal conductors, is responsible for vanishing resistance in superconductors. The Cooper pairs are nothing else as objects constituting of two bounded electrons, which posses the same magnitude of momentum but the opposite sign (direction). Although single electrons are fermions, i.e. they have a half-integer spin, their condensation results in total integer spin. Therefore,

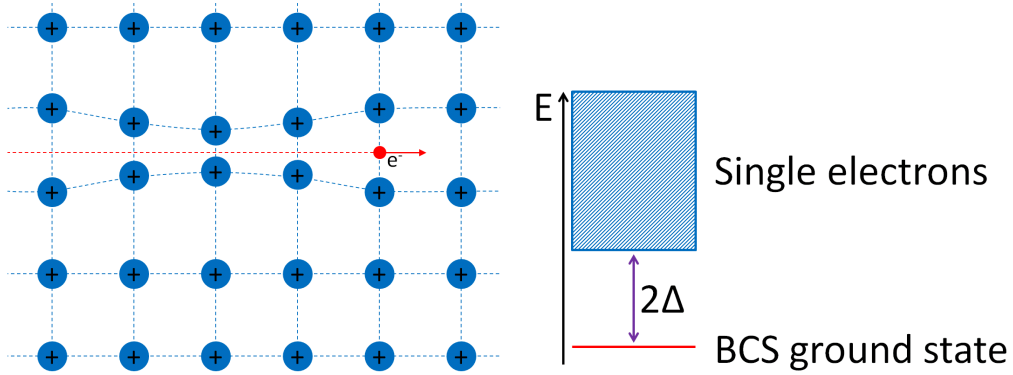


Figure 1.6 – Diagram showing the principle of the BSC theory. Left plot: a negatively charged electron passing through a lattice of positive ions induces lattice vibrations. Therefore, another electron will experience effectively greater attractive potential there and will follow the same path as the first one. Right plot: BCS ground state is separated from the single electron state by the energy gap of 2Δ . This energy has to be provided in order to break a Cooper pair into single free electrons.

Cooper pairs behave like bosons¹⁰ and prefer occupying the same quantum state. The origin of creating Cooper pairs lies in the existence of attractive force between two electrons. This is due to an exchange of phonon - a quasiparticle - with a lattice of positively charged ions (left picture in Fig. 1.6). The first electron passing through the lattice causes its vibrations. However, due to inertia of the ions, this deformation is delayed with respect to the motions of the electron and spread over the distance of around (100 – 1000) nm. Consequently, another electron experiences the strongest attractive potential in the region of accumulated positive charges along the path of the first electron and, therefore, follows this way. The reason why the phenomenon of the superconductivity is observed only in low temperatures is the fact that binding energy of two electrons constituting a Cooper pair is small, around (0.1 – 1) meV, and delivering energy sufficient to excite this object results in breaking the pair into two free electrons. Vanishing resistance in superconductors is directly related to the presence of energy gap (right picture in Fig. 1.6), i.e. energy needed to excite a Cooper pair, which is equivalent to breaking it to single electrons. The magnitude of energy gap is given by

$$E_g(0) = 2\Delta = 3.528k_B T_C, \quad (1.7)$$

where k_B is the Boltzmann constant ($1.38 \cdot 10^{-23}$ J/K). The resistance in normal conductors originates from scattering processes - on impurities and thermal vibrations of the lattice. However, in the case of superconductors, a Cooper pair does not experience scattering. This is applies if the kinetic energy of Cooper pairs is less than the energy gap.

¹⁰In contrast to bosons (atoms or He nuclei), Cooper pairs are much more extended objects, i.e. a distance between electrons is around (100 – 1000) nm. Moreover they exist only in the BCS ground state [9].

Quenching

A transition from the superconducting state, where resistance is zero, to the normal conducting state with non-zero resistance is called quenching. This process occurs when at least one of the characteristic critical parameters (T_C , B_C or J_C) is exceeded. Following a sudden increase of electrical resistivity, Joule heating causes warming up of the superconductor and further expansion of the quenching zone.

As it was already mentioned breaking a Cooper pair is related to depositing energy greater than $E_g(0)$. The liberated single electrons suffer from scattering which is the source of resistance. Nevertheless, considering superconducting cables used in a magnet coil production the situation becomes much more complicated. This is because of additional aspects, like a size of superconductor filaments (see Section 1.5.2), insulation type, design of a cable, etc., which start playing a role.

High current flowing through SC cables might induce through electromagnetic forces a superconductor's movement of several micrometers. This might be equivalent to releasing frictional energy of around 1 mJ/g [13] which is high enough to cause quenching. Tests performed at CERN showed that quench levels of the same type magnets provided by the same manufacturer varied significantly [4]. Most of the first magnet quenches occurred at around (70 – 90)% below the critical surface. However, it was reported that providing so-called training allowed approaching the quench levels to the critical surface. During this process, magnet quenches appeared at operating with higher and higher fields.

Magnet quenches can be also induced by energy perturbation. Regarding superconducting accelerators, this might originate from beam losses. However, in this case not only the magnitude of deposited energy but also the loss duration matters. Hence, because of various timescales of heat transport mechanisms, the following regimes can be distinguished [14], [15]

- short losses (loss duration up to around 0.1 ms) - Q_L is given by the enthalpy of a dry cable; the loss duration is so short that the heat does not propagate from the superconducting strands to the liquid helium, which is inside the cable,
- intermediate losses (loss duration of 1 ms to 1 s) - Q_L depends on the liquid helium, which a cable is immersed in, due to its great heat capacity,
- steady state losses (loss duration longer than 1 s) - Q_L is determined by the efficiency of heat evacuation by liquid helium from a magnet coil.

Fig. 1.7 presents quench levels of the LHC MQ magnets obtained with the algorithm presented in [14] as a function of time and beam energy. Quenching might result in damaging superconducting components of an accelerator. Therefore, in order to provide a safe operation of the machine, adequate detecting and protecting mechanisms have to be incorporated to the system. More in this topic can be found in Section 1.6.

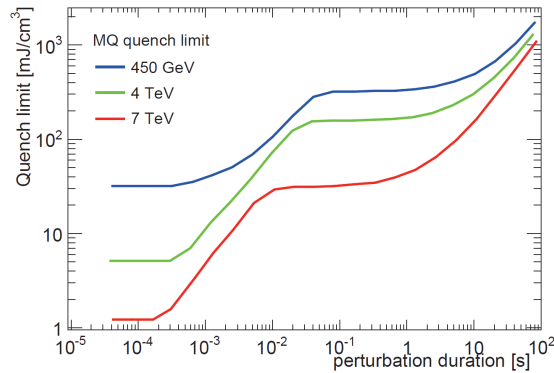


Figure 1.7 – Quench levels of the LHC Main Quadrupole as a function of the magnitude and duration of energy perturbation [16]. The agent responsible of a superconductor transition to the normal conducting state is a loss of beam with energy of 450 GeV (blue line), 4 TeV (green line) and 7 TeV (red line). Quench levels of more complex structures, i.e. magnet coils, depend not only on the properties of used superconductor. Considering the duration of energy deposition to a superconductor longer than around 1 ms, superfluid helium dominantly contributes in the heat evacuation.

1.5 LHC main magnets

A majority of any circular accelerator structure is constituted by magnets. This allows governing beam behaviour as a natural consequence of the fundamental interactions between the induced magnetic fields and electric charges. In this section, the basics of magnet physics are presented. In addition, a description of the LHC main magnet design is provided.

A number of magnet poles and their configuration determine a role of the component in beam controlling. Dipoles are the magnets which provide bending of a beam trajectory. This is feasible due to the fact that charged particles passing through the magnetic field experience the Lorenz force. In order to keep particles on a closed orbit a condition of equilibrium state with the centrifugal force has to be conserved. Therefore, the magnetic field, B determines a curvature, ρ , of particles traveling with energy E [5]:

$$\frac{1}{\rho} [m^{-1}] = 0.2998 \frac{B[T]}{\beta E[GeV]} . \quad (1.8)$$

In this equation¹¹, β is a ratio of velocity of particles to the speed of light and for the relativistic case $\beta \approx 1$. However, using only dipole magnets would not be sufficient for operating an accelerator properly. This is because a beam constitutes of billions of particles possessing the same charge. If no external forces acted on them, this would result in spreading out and loosing particles on an aperture. Therefore, a focusing system needs to be incorporated to guide the particles back to their initial orbit. This is provided by magnets, called quadrupoles,

¹¹In other chapters, β might refer to β -function of particles circulating in an accelerator.

which are built of four poles. The main property of quadrupoles is the presence of the gradient of the magnetic field g . This implies that the particles diverged more from the magnet center experience stronger forces. The focusing strength of a magnet, k , is expressed by the following formula

$$k [m^{-2}] = 0.2998 \frac{g [Tm^{-1}]}{\beta E [GeV]} \quad (1.9)$$

and is correlated with a focal length f , i.e. a distance from the focal point where the particles are focused, by

$$\frac{1}{f} = kl, \quad (1.10)$$

where l is a length of particle path inside the magnet. However, quadrupoles posses such a feature that they focus a beam transversely in only one plane and defocus it in the perpendicular one. Hence, in order to deflect the beam towards the centre in both planes, a system of alternate magnets has to be applied (so called FODO-lattice). Higher order magnets are used in addition to improve beam quality and remove errors. For instance, sextupoles are installed close to quadrupoles to reduce chromaticity effects, i.e. errors coming from a particle energy distribution and, therefore, a focal point spread due to quadrupole focusing [17].

1.5.1 Transfer matrix formalism

The matrix formalism is a very useful tool which allows describing a particle trajectory along an accelerator. Although in the nature, physical fields cannot change abruptly, in this approximation it is assumed that focusing, which originates in dipoles, $\frac{1}{\rho_0}$, and quadrupoles, k_0 , is constant over a magnet length

$$K = \frac{1}{\rho_0^2} + k_0 = \text{const.} \quad (1.11)$$

Therefore, a particle transverse motion is expressed by Hill's equation

$$u'' + Ku = 0, \quad (1.12)$$

where u is a generalized variable standing either for the horizontal, x , or the vertical, y , direction. This differential equation has two principal solutions with respect to the longitudinal position, s :

$$\text{if } K > 0: C(s) = \cos(\sqrt{K}s) \text{ and } S(s) = \frac{1}{\sqrt{K}} \sin(\sqrt{K}s) \quad (1.13)$$

and

$$\text{if } K < 0: C(s) = \cosh(\sqrt{|K|}s) \text{ and } S(s) = \frac{1}{\sqrt{|K|}} \sinh(\sqrt{|K|}s). \quad (1.14)$$

Therefore, they can be used in the matrix formalism giving the following correlation

$$\begin{bmatrix} u(s) \\ u'(s) \end{bmatrix} = \begin{bmatrix} C(s) & S(s) \\ C'(s) & S'(s) \end{bmatrix} \begin{bmatrix} u_0(s) \\ u'_0(s) \end{bmatrix}, \quad (1.15)$$

where $u_0(s)$ and $u'_0(s)$ represent initial values of a particle position and angle, respectively.

Considering drift space (i.e. region with zero magnetic field) and weak dipole magnets ($\frac{1}{\rho_0^2}$, $k_0 = 0$, $K = 0$), the particle trajectory can be written as

$$\begin{bmatrix} u(s) \\ u'(s) \end{bmatrix} = \begin{bmatrix} 1 & s - s_0 \\ 0 & 1 \end{bmatrix} \begin{bmatrix} u_0(s) \\ u'_0(s) \end{bmatrix}. \quad (1.16)$$

Taking into account the length of the drift space $l = s - s_0$, the transformation matrix is given by

$$\mathbf{M}_d(l|0) = \begin{bmatrix} 1 & l \\ 0 & 1 \end{bmatrix}. \quad (1.17)$$

In the case of quadrupoles, the $K = k_0$ because $\frac{1}{\rho_0} = 0$. Since k_0 can be either positive or negative, a quadrupole works either as focusing (Eq. 1.18) or defocusing (Eq. 1.19) element:

$$\begin{bmatrix} u(s) \\ u'(s) \end{bmatrix} = \begin{bmatrix} \cos\psi & \frac{1}{\sqrt{k_0}} \sin\psi \\ -\sqrt{k_0} \sin\psi & \cos\psi \end{bmatrix} \begin{bmatrix} u_0(s) \\ u'_0(s) \end{bmatrix} \text{ if } k_0 = |k_0| > 0 \text{ and } \psi = \sqrt{k_0}(s - s_0) \quad (1.18)$$

or

$$\begin{bmatrix} u(s) \\ u'(s) \end{bmatrix} = \begin{bmatrix} \cosh\psi & \frac{1}{\sqrt{|k_0|}} \sinh\psi \\ -\sqrt{|k_0|} \sinh\psi & \cosh\psi \end{bmatrix} \begin{bmatrix} u_0(s) \\ u'_0(s) \end{bmatrix} \text{ if } k_0 = -|k_0| < 0 \text{ and } \psi = \sqrt{|k_0|}(s - s_0). \quad (1.19)$$

For practical reasons, these can be simplified by the thin lens approximation which uses assumption that the total quadrupole length, $l = s - s_0$, is much less than its focal length f and tends to zero ($l \ll f$, $l \rightarrow 0$) fulfilling condition that

$$\frac{1}{f} = k_0 l = \text{const.} \quad (1.20)$$

Consequently, since $\psi = \sqrt{k_0}l \rightarrow 0$, Eq. 1.18 and Eq. 1.19 are expressed as

$$\begin{bmatrix} u \\ u' \end{bmatrix} = \begin{bmatrix} 1 & 0 \\ -\frac{1}{f} & 1 \end{bmatrix} \begin{bmatrix} u_0 \\ u'_0 \end{bmatrix}, \quad (1.21)$$

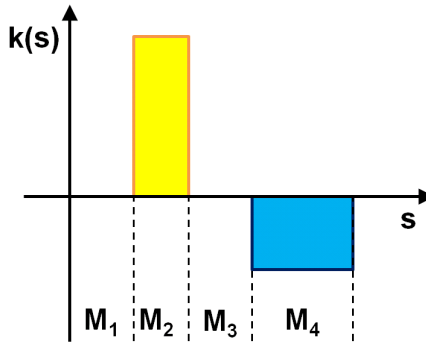


Figure 1.8 – Diagram of a beam transfer line. \mathbf{M}_1 and \mathbf{M}_3 represent transformation matrices of drift space regions, \mathbf{M}_2 is a matrix for a focusing quadrupole and \mathbf{M}_4 for a defocusing quadrupole.

where for the focusing quadrupole

$$\frac{1}{f} = k_0 l > 0 \quad (1.22)$$

and for the defocusing quadrupole

$$\frac{1}{f} = k_0 l < 0. \quad (1.23)$$

A position of a particle can be studied simply by multiplying transformation matrices \mathbf{M}_i of accelerator components. For the situation presented in Fig. 1.8, the total transformation matrix is given by

$$\mathbf{M} = \mathbf{M}_4 \mathbf{M}_3 \mathbf{M}_2 \mathbf{M}_1. \quad (1.24)$$

1.5.2 Design of the LHC Main Magnets

The majority of the 27-km long LHC accelerating system¹² is filled with bending and focusing magnets. For a construction of 15-meter long Main Dipoles (MBs) and 3-meter long Main Quadrupoles (MQs) the concept of 2-in-1 structure was applied (Fig. 1.9). This enabled installing two apertures for both beams circulating in the opposite directions in single magnets, which means that the yoke, helium vessel and helium bath, shrinking cylinder, cryostat are common. In the LHC, there are 1232 MBs and 392 MQs installed¹³.

One of the most important aspects of the LHC Main Magnets is the fact that they are based on the technology of superconducting cables. This allows reaching high magnetic fields of

¹²More than 90% of all LHC arcs [4].

¹³There are 1232 MB in the LHC - 1104 in the lattice and 128 in the Dispersion Suppressor (DS). Among 392 MQs, 360 are installed in the lattice and 32 in the DS [18].

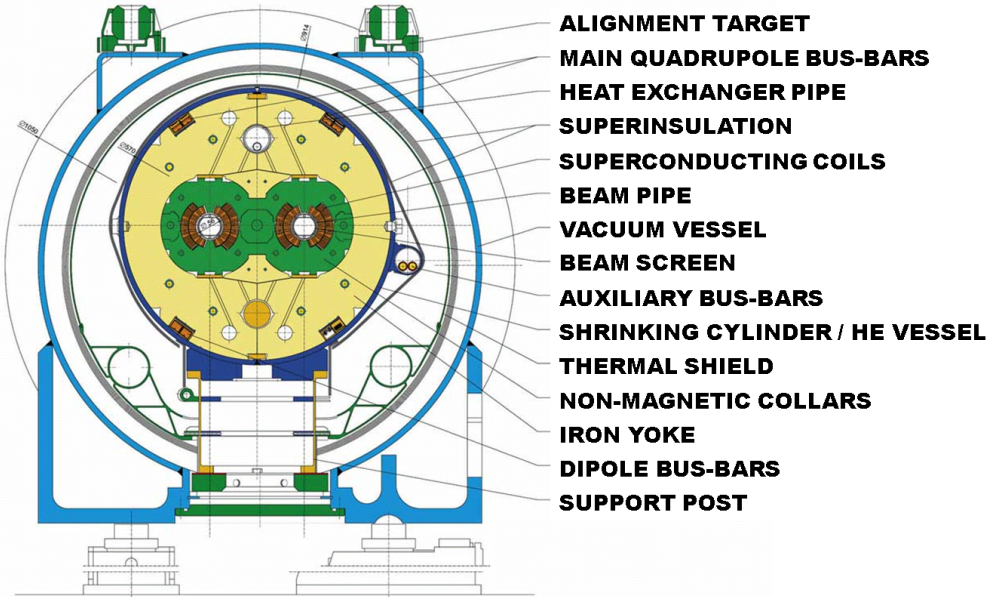


Figure 1.9 – Cross-sections of the Main Dipole [19]. The magnet design is based on 2-in-1 concept which allows both beams to be guided inside single magnets. Description in the text.

up to 8.33 T and gradients of 223 T/m in the case of the MB and MQ¹⁴, respectively. As a consequence of that, proton beams with energy of up to 7 TeV can be controlled. On the designing stage of the machine, it was decided to use niobium-titanium (NbTi) alloys. However, pure superconductors could not be applied since they are unstable and easily undergo transition to the normal conducting state. This is mainly due to flux jumps from the pinning centres and accompanied heating [13]. Moreover, this energy is sufficient to cause an increase of the material's temperature above its critical value. Therefore, thousands¹⁵ of thin NbTi filaments with a diameter of (6-7) μm were embedded into a copper matrix (Fig. 1.10). This solution not only provides mechanical stability but also, due to the excellent thermal and electrical conductivity of copper, allows returning of a temporarily quenching filament to the superconducting state. In addition, the chosen stabilizer has to withstand a current density of 1000 A/mm² which usually flows through the superconductor [4]. After coating, around 1 mm in diameter single strands [20] are twisted and form Rutherford cables (bottom picture in Fig. 1.10). In order to achieve desired magnetic field distribution and remove higher order components, copper wedges were inserted between cables when constructing magnet coils. Since high currents in the order of up to 13 kA induce strong forces affecting a position of the coils, a counteracting mechanism was needed. This was provided by installing austenitic steel collars around the coils (Fig. 1.9). The next stage of the magnet construction is represented by a yoke surrounding the collars. The purpose of introducing this element lies in the fact that the

¹⁴The MQs in the LHC have the peak magnetic field of 6.85 T [20].

¹⁵Around 8900 filaments are used to create one strand of MB inner layer cable. In the case of MB outer layers and MQ layers, around 6500 filaments are used.

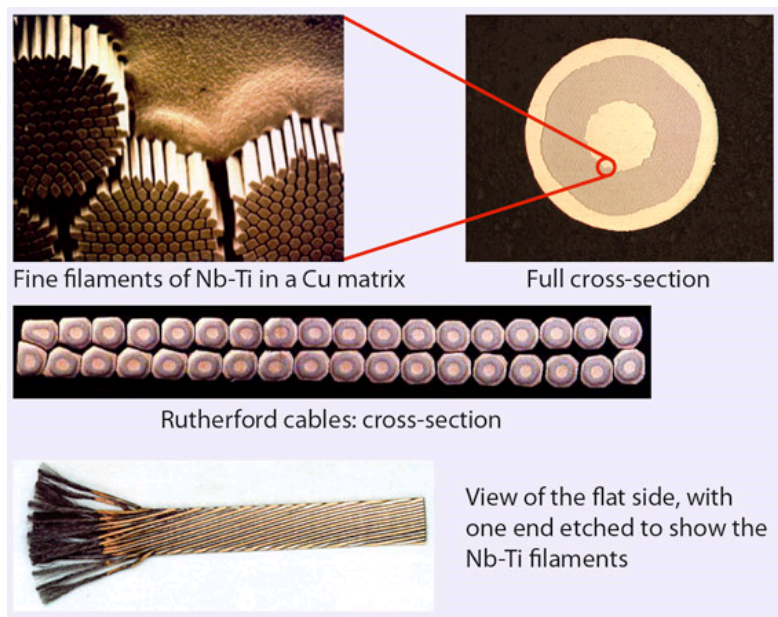


Figure 1.10 – The LHC Superconducting cable [21].

magnetic fields should be confined in order to protect electronics mounted in the proximity of the magnets and enlarge magnetic field in the central part of the magnet [4]. All elements described by now constitute so-called cold mass which is immersed in the superfluid helium at temperature of 1.9 K and housed inside a helium vessel. Finally, the entirety is inserted into a cryostat where the vacuum of about 10^{-9} atm is ensured to separate the cold environment from the room temperature tunnel.

Each LHC arc half FODO cell is made of three Main Dipoles, one Main Quadrupole and several corrector magnets. This gives more than 53 m long unit.

1.6 LHC magnet protection systems

1.6.1 Introduction

The LHC design has crossed the technological frontiers set by the previous accelerators to provide beam energy up 7 TeV. The total electromagnetic energy stored in the superconducting magnets will reach an unprecedented value of 10 GJ (Fig. 1.11) at nominal operation conditions. Each circulating beam consisting of $3 \cdot 10^{14}$ particles will carry the stored energy of 362 MJ [22], two orders of magnitude greater than in the case of Tevatron. Therefore, handling the machine operation under the circumstances is challenging not only in terms of delivering beams with quality specified by the demands of the experiments but also regarding probable failures. This is due to the fact that any uncontrolled release of this magnitude energy can be destructive to the accelerator components.

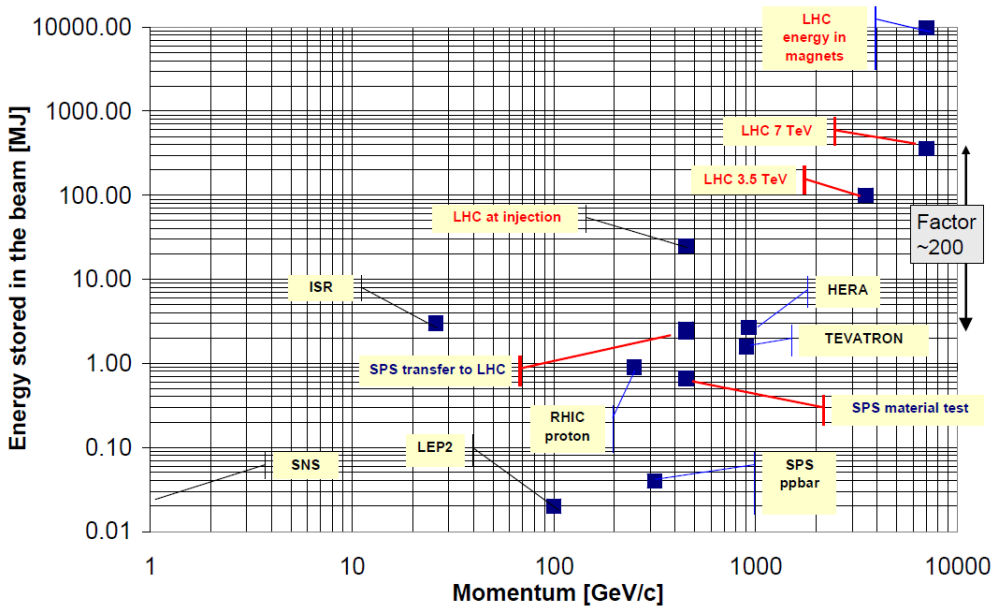


Figure 1.11 – Energy stored in the beam as a function of beam momentum in the case of various accelerators [22]. The LHC stores 10 GJ in the SC magnets and 362 MJ in each of 7 TeV circulating beams.

A series of studies have been performed before the LHC start-up to estimate consequences of a direct beam impact on the matter. The experiment demonstrating material damages caused by 450 GeV (6.4% of the LHC nominal energy) SPS beam losses was performed in 2004 [23]. A 30-centimeter structure consisting of 108 metal plates (copper, stainless steel and zinc; dimensions of the plates were $6\text{ cm} \times 6\text{ cm} \times 2\text{ mm}$) was exposed to irradiation (Fig. 1.12). Evaporating and melting of the material was observed depending on beam intensities. Depositing around $8 \cdot 10^{12}$ protons resulted in drilling a hole with several millimeter in radius in the penetrated material.

Another interesting studies devoted to assessing implications of the worst case scenario, i.e. accidental release of the total 7 TeV proton beam are presented in [24]. A loss of 100 bunches (out of 2808 which will be used in the LHC) onto a solid copper target was simulated with Fluka program. The obtained results were combined with BIG-2 code¹⁶ which allowed hydrodynamic and thermodynamic response of the material to be modeled. This revealed that depositing less than 4% of the nominal LHC beam would cause development of a shock wave moving a material from the impacted region outwards. Hence, bunches arriving later would experience less material due to the local density decrease and would be able to penetrate it deeper. The penetration depth in the copper block was estimated to be between 10 m and 40 m.

¹⁶BIG-2 is a two-dimensional code concerning semi-empirical equation of state. It is used for describing material changes occurring during its heating and expanding.

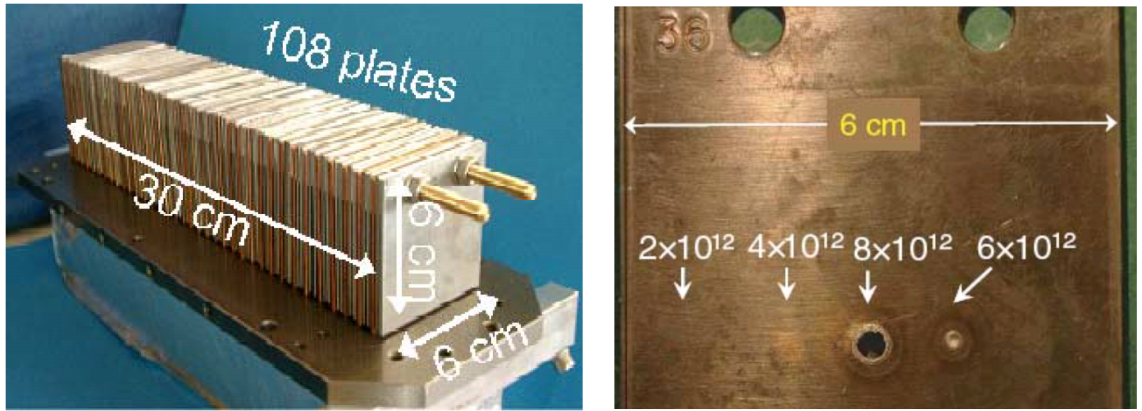


Figure 1.12 – Material damage test at 450 GeV: SPS beams with different intensities were deposited on a metal block consisting of copper, steel and zinc plates (the left plot [23]). A dependency of beam intensities on a damage level is presented on the right plot [22].

These two examples perfectly illustrate that the machine equipment is under a real threat of damage. Therefore, a reliable Machine Protection System (MPS) continuously surveying the machine and beam parameters, detecting failures, diagnosing and appropriately reacting is essential for providing safe operation conditions.

Three top priorities of the LHC MPS are [25]:

- protecting the LHC components from damaging by beams,
- preventing quenches of SC magnets,
- avoiding unnecessary beam dumps.

These requirements are met by incorporating many subsystems capable to absorb beam energy (absorbers and collimation system), measure particle losses (Beam Loss Monitoring System), detect transition of superconducting components to the normal conducting state (Quench Protection System), estimate beam transverse location (Beam Position Monitoring) and many others. If any of these systems registers abnormal beam or machine behaviour exceeding the predefined safety margins, the information is sent to the Beam Interlock System (BIS). The beam permit loop is aborted and, as the consequence, beam dumping is initiated. This means that the beam is extracted from the accelerator to the Beam Dump Absorber Block (TDE) - the only place which can accept such high energy density. The core of the TDE is built of a 7.7 m long, 0.7 m in diameter graphite block [26] (Fig. 1.13, the left plot) shielded against radiation by about 900 tons of iron and concrete [27]. Although this structure is designed to withstand temperatures up to around 1000°C, two systems of orthogonally deflecting dilution kickers (MKB) provide beam sweeping into *e*-shape to spread the beam energy (Fig. 1.13, the right plot).

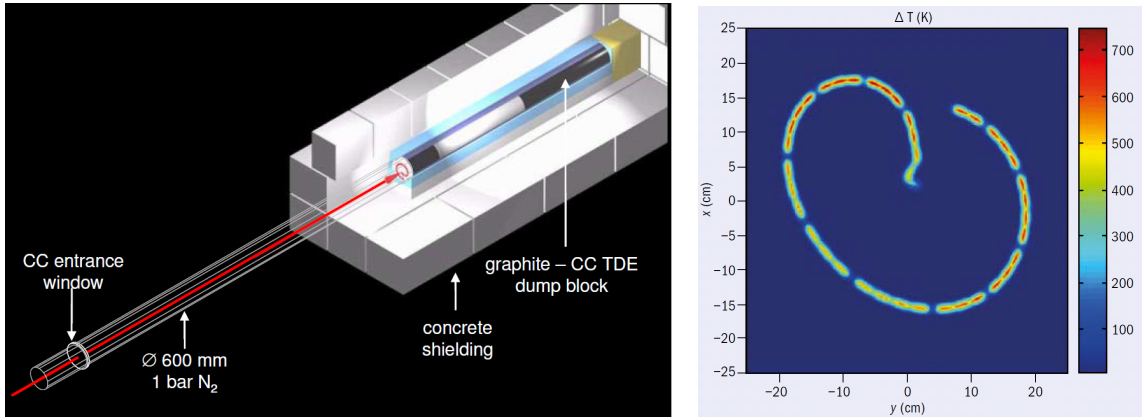


Figure 1.13 – The LHC Beam Dump. Left plot: the TDE carbon composite (CC) core is housed in the concrete shielding. Over-pressured nitrogen prevents the heated block from firing [28]. The right plot: the calculated temperature increase map in the case of depositing 7 TeV nominal beam. The energy stored in the beam (362 MJ) will result in rise of the block temperature by $\approx 750^\circ\text{C}$ [25].

Among many systems belonging to the MPS, there are three complementary and independent systems playing a dominant role in protecting the SC magnets against quenching. At the first stage passive components intercept particles, which lie outside a certain transverse acceptance region and, otherwise, could be lost somewhere in the cold regions. This is done by applying collimators which constitute dynamic aperture limitation. They protect machine from beam losses, which are always present and cannot be avoided. However, a whole spectrum of failures can occur at any step of the acceleration process leading to accidental losses (Section 1.7.1). Therefore, Beam Loss Monitors are installed along the LHC in the locations with highest probability of loosing particles. This system has the property that allows beam to be extracted from the machine before quenching of SC components appears. The mechanism of the BLM system is based on measuring the radiation dose of the secondary particles showers outside magnet cryostats. Hence, if the acquired signals exceed specified thresholds, the BLM system initiate beam dumping. The Quench Protection system reacts in the case when a superconducting material enters the normal conducting state. In this scenario, not only beam losses¹⁷ but also the energy stored in the magnetic field are dangerous to the quenching magnet. Therefore, the QPS assures the safe magnet quenching by extracting the beam through the BIS and additionally by firing quench heaters to dissipate energy over entire volume of the superconductor. The detailed description of the QPS system actions is given in the following section.

¹⁷Remember that only one billionth (millijoules) of the total stored beam energy (362 MJ) is sufficient for inducing a magnet quench while the energy stored in a Main Dipole circuit is 1.22 GJ.

1.6.2 Quench Protection System

Quenching

The basic condition of existence the superconducting state is that all the characteristic parameters, i.e. the current density, temperature and magnetic field, stay below the critical values (see Section 1.4). This provides resistance-less flow of current. However, if the critical surface of a superconducting material is exceeded, the transition to the normal conducting state occurs. In this situation, electrical resistivity rises rapidly leading to Joule heating. This is followed by increase of the magnet temperature causing further expansion of the quenching zone.

Energy stored in the electromagnetic field

Powering of the LHC magnets is divided into eight independent and symmetrical sectors. Each such a sector contains one circuit of 154 Main Dipoles (RB) and two circuits of 47 or 51 (depending on a location) Main Quadrupoles (RQF and RQD; focusing and defocusing magnets, correspondingly). Moreover, there are other circuits dedicated to corrector magnets. Overall, including both superconducting magnets and normal conducting magnets, the LHC consists of 1612 various electrical circuits. Concerning the case of the nominal beam energy of 7 TeV, the energy stored in one RB circuit is around 1.22 GJ and 20 MJ per each main quadrupole circuit [29]. In the event of one magnet quenching, the magnetic energy of all connected magnets would be dissipated in this resistive magnet if no protecting actions were taken [30]. This would certainly result in destroying it. Therefore, a system devoted to preventing the damages resulting from superconductor quenching is needed.

Quench detection and protection

The Quench Protection System (QPS) is based on a principle of measuring voltage occurring when a superconducting element undergoes the transition to the normal conducting state. An analog Wheatstone bridge is applied in order to compare continuously the voltage across two apertures (U_1, U_2) of a Main Dipole [31] (Fig. 1.14). In the case of Main Quadrupoles (Fig. 1.15), the voltage examination concerns a comparison of two coils of the same aperture. This is due to the fact that the focusing and defocusing circuits are powered separately [32]. The QPS condition determining magnet quenching¹⁸ is that the absolute value of the voltage difference exceeds 100 mV for time longer than 10 ms. If quenching is detected, the QPS initiates beam abort permit and the beam is extracted from the machine. In addition, power converters are switched off. Triggering quench heaters provides dissipation of energy stored in the magnetic field over the entire volume of the coil. These elements are made in the form of austenitic stainless steel strips embedded in polyimide-epoxy glue [33] and are attached to outer layers of SC coils. The power is supplied to the quench heaters by discharging aluminum electrolytic

¹⁸The QPS system concerns all superconducting components of the LHC. A strategy of detecting quenching, setting thresholds and taking appropriate actions varies depending on SC elements. Details regarding insertion region magnets, inner triplets and corrector magnets can be found in [31].

Chapter 1. Introduction

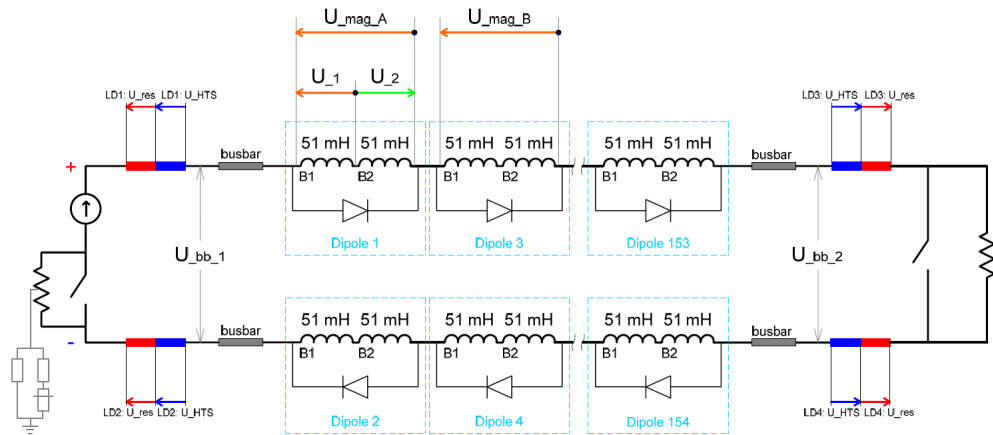


Figure 1.14 – QPS: Diagram of the LHC MB electrical circuit. Courtesy of Alexandre Erokhin.

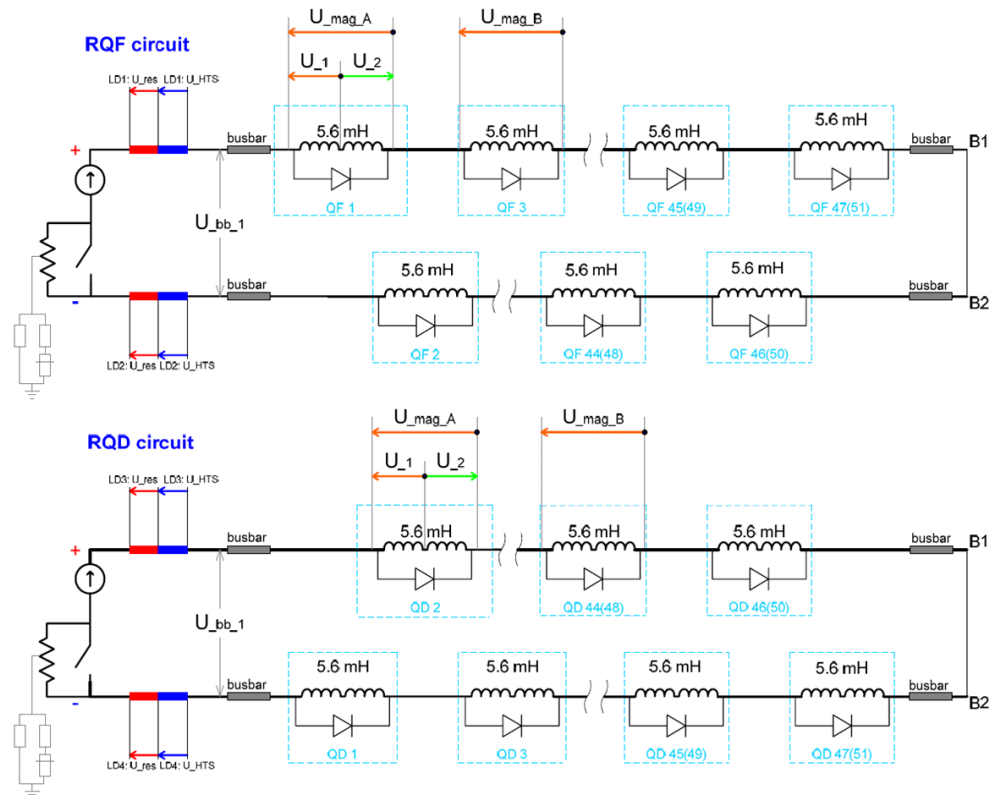


Figure 1.15 – QPS: Diagram of the LHC MQ electrical circuit. Courtesy of Knud Dahlerup-Petersen.

capacitors which is triggered by a thyristor. Each power supply consists of two sets of three capacitors connected in series which gives 7.05 mF of total capacitance [34]. The capacitors operate at nominal voltage of ± 460 V with respect to the ground giving around 2.9 kJ of stored energy per Quench Heater Discharge System (DQHDS) unit. The application of quench heaters allows the energy concentrated in a hot spot to be spread, thus providing protection of this magnet. However, the magnets are connected in series and the overall energy of the circuit is too large. Therefore, the idea of by-passing current from quenching magnet was introduced. This is done by incorporating high-current silicon cold diodes parallel to the magnet coils [32]. In the event of quenching the SC coils, a threshold voltage of the diode (about 6 V [29]) is exceeded and the current flows through the diode instead of the quenching magnets. This causes discharging of the magnet over internal resistance. Nevertheless, such diodes have to be protected since they are not able to accept the energy of all magnets belonging to the same circuit without destruction. Thus, the Main Magnet circuits are equipped with energy extraction systems which enable extracting the current from chains of magnets. Due to the magnitude of the energy stored, there are two identical Energy Extraction (EE) systems in the case of Main Dipole circuits - one located in the mid-point of the electrical circuit and the other EE placed in the vicinity of the power converter. The Main Quadrupole circuits (RQF, RQD) require only a single EE per circuit [35]. Circuit breakers and dump resistors are the main components of each EE system. The powering of the circuit is permitted if all four branches of the 4 kA DC breakers are closed, three branches are needed for a safe operation of the breakers. The switches are opened for extracting the current to the dump resistors if two branches are opened. The extraction resistors have to withstand large power loads. Thus, they have to be made of a material characterized by low inductance and a low temperature coefficient¹⁹. For both main circuits the dump resistors consist of stainless steel body. Cooling is provided by a forced air-to-water heat exchangers. The time constants of the exponential current decay are adjusted so that the quenching due to the eddy currents (so-called quench back) are prevented. For the currents of 13 kA and inductance of all dipoles in one sector

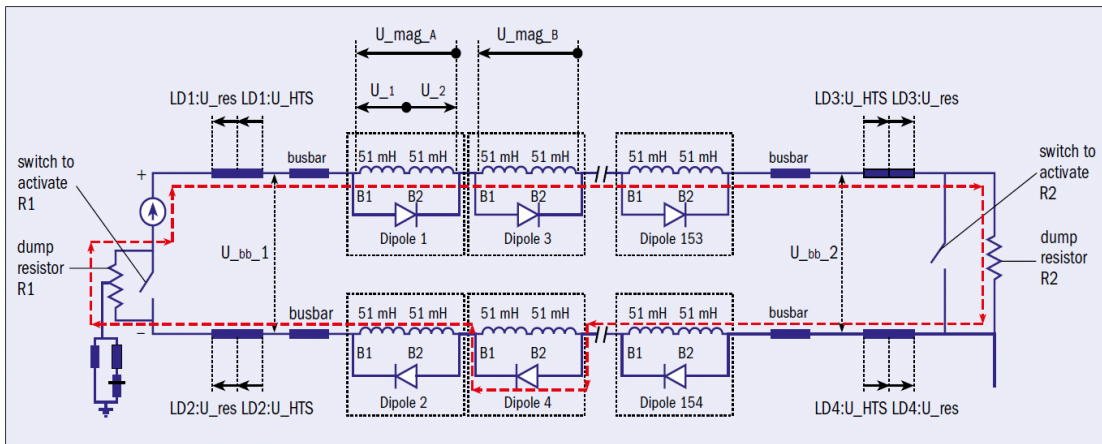


Figure 1.16 – QPS:Diagram of the LHC MB circuit in the case of quenching [36].

¹⁹In the case of the LHC Main Dipole circuits, dump resistors reach the temperature of up to 350 °C.

$L = 15.1$ H, the time constant is around 104 s. In the case of quadrupoles ($L = 0.26$ H) the time constant was calculated to be around 40 s [37].

Fig. 1.16 presents the actions of the QPS system in the case of quenching of Dipole 4. The current (red dotted line) by-passes the resistive magnet and flows through a cold diode. The entire circuit is discharged thanks to open switches and guiding the current to the dump resistors.

The described system is so-called old QPS (iQPS)²⁰ and it protects SC coils when asymmetrical quenching occurs (voltage drop $\Delta U > 0$). Unfortunately, it fails in the case of symmetrical quenches, i.e. in the situation when a resistive zone develops identically in both compared superconducting parts and $\Delta U = 0$. This happened during magnet training in sector 5-6 in June 2008 and was caused by a heat exchange between neighbouring magnets. Therefore, a new QPS system (nQPS) was developed. In contrast to iQPS, the total voltage drops are compared between separate magnets - four neighbouring dipoles and two quadrupoles [38]. The voltage detection threshold is twice as big as in the case of iQPS (200 mV, the same detection time of 10 ms) in order to recognize an origin of a dump event.

1.6.3 Beam Loss Monitoring System (BLM)

The Beam Loss Monitoring (BLM) system is one of the most crucial and critical elements of the LHC MPS providing continuous surveillance of particle losses along the machine. It was designed to meet three main requirements [39]:

- protecting magnets and other accelerator components from damages originating in beam losses,
- preventing superconducting coils from quenching due to energy deposition (local heating) of lost particles,
- enabling beam diagnostics, i.e. studies on local aperture limitations, beam orbit distortions and particle oscillations.

The driving mechanism of the BLM system is based on measuring radiation dose using ionization chambers²¹. Due to various phenomena (see Section 1.7.1) primary particles are lost on an aperture and interact with mater of accelerator components. As a consequence, a hadronic shower of secondary particles develops and propagates in all directions. If a registered signal exceeds a certain threshold, the BLM system breaks a beam permit loop and the Beam Interlock System (BIS) initiates beam dumping.

²⁰In this chapter only systems directly related to coils of the arc Main Magnets are presented. Considerations of bus bars, splices, corrector magnets etc. are beyond the scope of this thesis.

²¹The BLM system uses several methods of detecting radiation of secondary particles - ionization chambers (IC BLMs), secondary emission monitors (SEMs), diamond detectors. However, in these studies only IC BLMs are presented since only their measurements were used for the Quench Tests analysis.

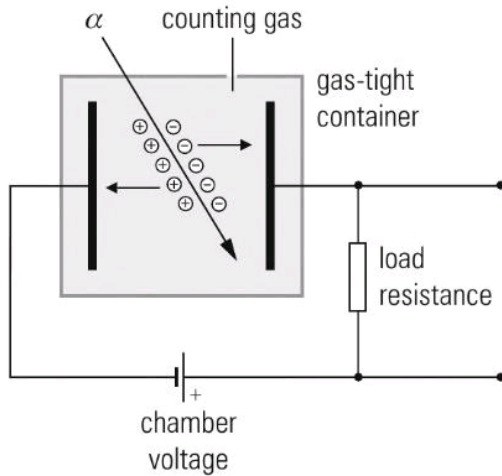


Figure 1.17 – Diagram of an ionization chamber [40]. A charged particle passing through a detector ionizes gas molecules. Positively charged ions are attracted to a cathode with the negative polarity while free electrons are collected on an anode with the positive polarity. A drift of charges constitutes the ionization current. Resistance is incorporated to the circuit in order to allow low currents to be measured indirectly.

Principle of ionization chambers

The ionization chamber is the simplest gas-filled detector built of electrodes embedded in a tight container (Fig. 1.17). A charged particle passing through the ionization chamber can ionize neutral gas molecules if its energy is greater than specific ionization potential. A pair consisting of a positively charged ion and a negatively charged free electron is created. In order to induce movements of the charges the electric field is imposed - the ions are attracted to a cathode with the negative polarity while the electrons are collected on an anode with the positive polarity. Measuring this generated electric current is the basic principle of ionization chambers. Nevertheless, its magnitude is very low (in the order of 10^{-12} A). Therefore, an active amplification has to be provided to measure it indirectly. This is done by incorporating electrometers or dynamic capacitors into the electric circuit [41]. Ionization chambers measure only the charges coming directly from a gas ionization by incident particles. This means that no multiplication processes are involved which distinguishes ICs from other gas detectors.

Design of IC BLMs

A BLM is a 50-centimeter long cylindrical detector with a diameter of 9 cm. 61 parallel aluminum electrodes (thickness of 0.5 mm, diameter of 75 mm, spaced by 5.75 mm; Fig. 1.18) are housed inside a stainless steel tube with the wall thickness of 2 mm. The interior of the chamber is filled with gaseous nitrogen, N_2 , with overpressure of 100 mbar. A bias voltage of 1.5 kV was implemented between electrode plates to induce movement of ions and electrons and enables charge collection. After installing the ICs in the LHC, the response of the mon-



Figure 1.18 – Design of BLM - an internal structure which is housed in a cylinder [44].

itors is checked with a radioactive source, i.e. caesium ^{137}Cs [42], [43] in order to verify the correctness of connecting the cables to appropriate channels of the electronics.

Locations

The BLMs are located along the LHC in the places where the losses are expected to occur first or have the highest magnitude. This particularly applies to:

- collimators [45], where the aperture is limited in order to cut off transverse beam tails,
- quadrupoles, where the β -function reaches maximum values,
- inner triplet magnets²², where the high radiation occurs due to the proximity of collision points [46].
- dispersion suppressors,
- beam dumps, where total beam intensity is deposited during beam extraction from the machine.

Recording specific losses and distinguishing losses coming from both beams are the main criteria taken into account when deciding on monitor placement. Each arc Main Quadrupole (MQ) is equipped with six horizontally-mounted monitors (Fig. 1.19, yellow bars) outside magnet cryostat. Three detectors are devoted to surveying losses of beam 1 and three others detect losses coming from beam 2. However, a so-called cross-talk appears, i.e. monitors record losses of the opposite beam. The cross-talk signals are approximately five times smaller than the signals coming from the observed beam.

Electronics

The ionization chambers measure radiation of secondary particles. The generated current is evaluated by the BLM analog front-end electronics which, for arc magnets, is located below quadrupoles. Since the system specification required measuring a wide dynamic range varying

²²A sequence of three superconducting magnets installed just before the interaction points is called an inner triplet. These magnets provide final squeezing of beams before collisions.

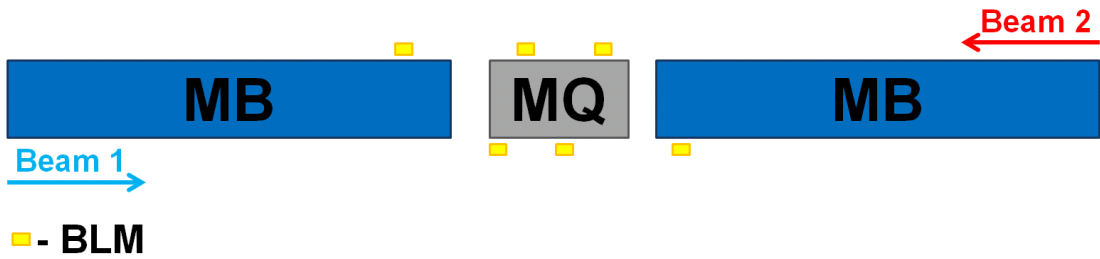


Figure 1.19 – A diagram of the BLM locations in the LHC arcs. Each arc MQ (the grey bar) is equipped with six BLMs (the yellow bars). Three monitors observe losses coming from beam 1 and three others survey losses of beam 2. A direction of beam trajectories is indicated by arrows. The blue bars represent MBs. The diagram is not to scale.

from 10 pA to 1 mA (eight orders of magnitude), a specially designed Current to Frequency Converter (CFC) was applied. Its mechanism is based on the balanced charge integration and allows the ionization chamber signal to be converted into proportional frequency in ranges from 0.05 Hz to 5 MHz [47]. In addition, an Analog to Digital Converter (ADC) was incorporated to improve the response time of the CFC to low currents [48] and increase the dynamic range [47]. The signal is integrated over a $40 \mu s$ long time window and transmitted using redundant high speed optical links to the module called BLETC (Beam Loss Electronics for Threshold Comparator). This is done every $40 \mu s$. The BLETC is installed on the surface and provides signal processing, i.e. collecting, analyzing and comparing the acquired data with threshold tables. The backbone of the BLM system is the FPGA (Field Programmable Gate Array) where the decision process whether the beam should be removed from the machine is taken [49]. Fig. 1.20 shows the schematic overview of the FPGA components. Up to 16 channels can be treated in parallel by a single module. For each detector the recorded data is verified and signals coming from the CFC and ADC are merged. An analyzing method of Successive Running Sum (SRS) generates history of BLM signals in 12 integration time windows [50]. These values are continuously computed and compared to the corresponding pre-defined thresholds in the Threshold Comparator (TC). In the case of detecting unacceptable radiation dose, the system communicates with the Beam Interlock System (BIS) requesting for the beam abort.

BLM signals are stored in the on-line logging database with the frequency of 1 Hz which enables tracing beam loss evolution and studying history of various events. Moreover, in the case of beam dumping, the data with resolution of $40 \mu s$ is recorded in 82 ms long BLM Post Mortem²³ (PM) buffer which is stored forever. This allows investigating signals 78 ms before and 4 ms after the dump.

Running Sums

A signal from the BLM is delivered to the FPGA card every $40 \mu s$ and added to a register. This

²³The BLM Post Mortem can also provide 1.7 s long debugging expert data [51].

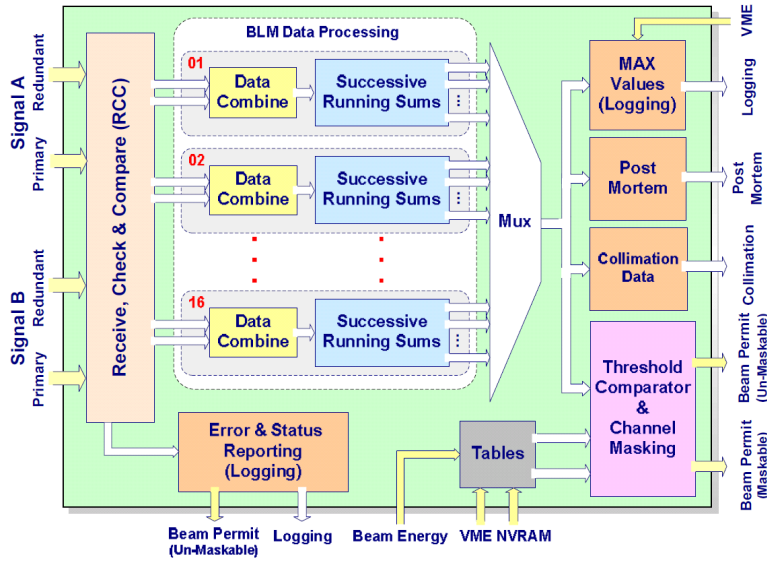


Figure 1.20 – A diagram of processes assigned to the FPGA of the BLM system [52].

value is subtracted after n cycles. The time difference between these two actions defines the integration time of moving sum window (Running Sum, RS). In the other words, this means that a certain window contains m signals recorded within $40 \mu\text{s}$. When a new signal arrives, the oldest one is removed from the register [49]. The value of m is characteristic for each RS.

A summary of all Running Sums available in the BLM system is given in Table 1.1.

Thresholds

The BLM thresholds are calculated with respect to the estimated quench levels [54]. A loss of a single proton with energy of E_{beam} results in measuring the BLM signal $Q_{BLM}(E_{beam})$. Depending on beam energy and loss duration, Δt , there are different total numbers of protons, $N_p(E_{beam}, \Delta t)$, which can be safely deposited on an aperture without inducing quenching of a superconductor:

$$T(E_{beam}, \Delta t) = Q_{BLM}(E_{beam}) \cdot N_p(E_{beam}, \Delta t) = Q_{BLM}(E_{beam}) \cdot \frac{Q_L(E_{beam}, \Delta t)}{E_{coil}(E_{beam}, \Delta t)} \quad (1.25)$$

$E_{coil}(E_{beam}, \Delta t)$ is the energy deposited in a magnet coil and $Q_L(E_{beam})$ is the quench level at given beam energy. $T(E_{beam}, \Delta t)$ is the BLM Master threshold which includes a margin three times the estimated quench level. Due to uncertainties in threshold computation, a monitor factor MF is introduced. Usually, $MF=0.1$ but this value can be change up to 1. Therefore the Applied Thresholds, which are implemented to the electronics, are defined as:

$$t(E_{beam}, \Delta t) = MF \times T(E_{beam}, \Delta t) \quad (1.26)$$

Table 1.1 – BLM integration time windows. Source: [53].

Signal name	Time windows		Refreshing		Data formats		Comments
	Number of 40 μ s steps	Duration [ms]	Number of 40 μ s steps	Duration [ms]	FPGA or VME	Measurement & Logging DB (rate: 1 Hz) [Gy/s]	
RS01	1	0.04	1	0.04	Maximum of sum values observed from the last readout	Maximum of sums normalized to window length	X
RS02	2	0.08	1	0.04			X
RS03	8	0.32	1	0.04			X
RS04	16	0.64	1	0.04			X
RS05	64	2.56	2	0.08			X
RS06	256	10.24	2	0.08			X
RS07	2048	81.92	64	2.56			X
RS08	16384	655.36	64	2.56			X
RS09	32768	1310.72	2048	81.92	Last calculated sums observed in the last readout	Last calculated sum normalized to window length	X
RS010	131072	5242.88	2048	81.92			
RS011	524288	20971.52	16384	655.36			
RS012	2097152	83886.08	16384	655.36			X

Each of approximately 4000 BLM detectors²⁴ installed along 27 km of the LHC ring is characterized by a set of 384 threshold values. All 12 integration time intervals varying from 40 μ s to 83.89 s and 32 energy levels covering the range from 450 GeV to 7 TeV are taken into account in so-called threshold tables. This gives about $1.5 \cdot 10^6$ BLM thresholds in total[56] which need to be handled in order to provide a safe and efficient (avoiding unnecessary dumps) operation of the machine. Knowing quench levels (see Section 1.4) of LHC superconducting magnets is the key to assessing appropriate BLM thresholds. Monte Carlo simulations have been used for modeling the response of the magnets to energy deposition considering various loss scenarios. The obtained results were verified during dedicated experiments and standard LHC operation. This method allows approaching the optimal BLM settings.

1.6.4 Operational statistics

The operational experience with the MPS system confirms its good performance. In the period of three years (2010-2013) around 1500 beam dumps were successfully carried out at energies above 450 GeV. However, unnecessary dumps constituted around 15 % of these events reducing the LHC availability for physics, i.e. delivering particles to the experiments. Until the LHC Long Shutdown 1 (February 2013), no beam induced quenches have been observed during operation with circulating beams. This is mainly due to the fact that the

²⁴The LHC BLM system comprise of 3592 ionization chambers and 289 secondary emission monitors [55].

LHC operated at a half of its nominal energy. Moreover, the provided beam quality was very good and the collimation system ensured efficient beam cleaning. Besides that, the absence of beam induced quenches proves that the BLM thresholds are low enough to initiate beam extracting from the ring before a magnet transition to the normal conducting state is initiated.

1.7 Beam losses

Beam losses are natural phenomena occurring in accelerators. They might come from applied conceptual solutions (collimators), imperfections or failures of machine components. Probably the most unavoidable losses come from cleaning process, during which collimation system intercepts transverse beam tails. This leads to development of secondary particle shower propagating in the beam direction. On the other hand, although high level technologies are applied for positioning the accelerator elements, some misalignment might occur due to influence of strong forces originating in high currents. Such mismatching might influence a distribution of the magnetic field lines and, therefore, particle motion. Moreover, there is a wide spectrum of possible failures related to powering, material quality and data processing which might affect beam behaviour. These effects are potentially critical, in particular, when operating with high stored energies (both in beams and electric circuits) and high intensity beams since even small initial perturbations might lead to serious consequences.

Good knowledge of mechanisms provoking beam losses enables designing appropriate protection systems against damages and quenching. These systems either reduce impact of beam losses onto superconducting components (by intercepting disturbed particles in the dedicated regions) or prevent further developing of the losses (by removing beams from the accelerator). Depending on chosen benchmarks, beam losses are mainly classified with respect to their nature (regular and irregular losses) and loss duration (ultra fast, very fast, fast and steady state regimes).

1.7.1 Regular and irregular losses

The regular (normal) beam losses are unavoidable aspect of the machine operation. They are always present and mostly correlated to

- beam dynamics (beam scattering processes, particle diffusion or various beam instabilities)
- variations in machine operation (changes in tune, orbit, phenomena occurring during ramping, squeezing and collisions [57])

The regular losses might occur at any stage of the machine operation [58] - from injection, through ramping, squeezing to final colliding. For instance, ineffective damping of injection oscillations might result in loosing particles during the first several turns. In addition, protons

staying outside RF buckets are also lost during beam energy ramping. This is mainly due to phase errors, noise and instabilities. The timescale of the flash of transient losses is in the order of 1 s [59]. Finally, collisions in the interaction points are the source of steady particles losses.

The effects of the regular losses can be reduced by means of applying passive protection, i.e. collimators and absorbers. Cutting off beam transverse tails allows limiting beam emittance and prevents losses of particles with high amplitude oscillations in SC regions which could lead to magnet quenching. Therefore, beam aborts are avoided and beam parameters can be corrected [60]. Moreover, in the LHC the Transverse Damper (see Section 1.8.2) provides damping beam oscillations.

Failures or improper operation of machine components contribute to irregular (abnormal) beam losses. In this case, not only quenching of the superconducting magnets can be induced, but also accelerator components can be destroyed if an appropriate protection is not applied. The most critical failure scenarios are:

- Asynchronous dump - this event is defined as a lack of synchronization between 15 dump kickers (MKD) with the 3 μ s beam abort gap,
- Erratic dump (single module pre-fire) - it occurs when one of MKDs is pre-triggered randomly and soon later other 14 kicker modules are simultaneously re-triggered almost certainly out of phase with respect to the beam abort gap [61],
- Flash-over of the LHC injection kicker
- UFOs (see Section 1.7.3)
- undetected orbit bump (resulting for example from human error).

In order to avoid damages caused by beam losses, collimators and absorbers are located in the places where the machine failures are the most probable. Moreover, losses are monitored by fast Beam Loss Monitors (Section 1.6.3) which, in the case of detecting abnormal rise in radiation, initiate the beam abort system actions. This allows the beam to be extracted to the beam dump within 2-3 turns, i.e. (178-267) μ s.

1.7.2 Classification of beam losses by loss duration

There is no uniform criterion of specifying strictly the time ranges and they vary depending on literature [62], [14], [15], [63]. However, from the machine protection point of view, beam loss types are distinguished as follows:

- Ultra-fast losses (one turn, i.e. 89 μ s) occurring due to injection and ejection kicker failures,

- Very fast losses (< 5 ms) related to D1 warm (normal conducting) magnet failure, UFOs (see the next section)
- Fast losses (> 5 ms) appearing due to hardware errors,
- Steady state losses (several seconds) occurring close to aperture limitations (collimators) and collision points (debris radiation).

Nevertheless, regarding the protection of LHC superconducting coils, another time-dependent aspect is taken into account - the capability of transporting heat. This classification is given in Section 1.4 and physics behind it is explained.

1.7.3 UFOs

In the LHC, UFOs (Unidentified Falling Objects) refer to dust macroparticles moving across the vacuum chamber [64]. Interactions of UFOs with particle beams (beam scattering, secondary particle shower production) cause fast beam losses in the order of 10 LHC turns (≈ 1 ms). Although, the UFO-induced losses are characterized by a Gaussian profile in time, asymmetries in the loss shape can be observed due to beam dumping mechanism [65].

The first²⁵ UFO was registered in July 2010. Since then UFOs have appeared in different locations around the LHC, however numerous events were observed in the vicinity of MKIs (Magnet Kickers for Injection). For example, within one year (between July 2010 and August 2011) 13 out of 35 beam dumps were related to UFO losses in this region [66]. Intensive studies on MKI UFOs revealed that they are up to $100 \mu\text{m}$ large, positively charged Al_2O_3 compounds which detach from the ceramic beam screen support tubes surrounding the beams [67], [68]. However, the nature of the UFOs occurring in the cold magnets remains unknown.

Existence of UFOs was considered as a significant limitation when handling higher energy beams after the LHC upgrade (fall 2015). Therefore, the UFOs were the subject to investigations during 2013 Quench Test slot.

1.8 Methodology of inducing controlled beam losses

In general, the existence of particle losses is an undesirable phenomenon which occurs during the standard LHC operation. However, many machine tests and experiments require controlled beam losses in order to validate machine settings (positions of collimator jaws, BLM thresholds, aperture measurements) or understand physical mechanisms (development of magnet quenching). The objectives of the tests, location along the LHC ring and the specification of correlated beam loss features, i.e. loss type (primary/secondary particles), beam size, beam intensity, loss duration determine which method can be applied for provoking beam losses.

²⁵Further detailed analysis has shown that small UFOs had appeared earlier.

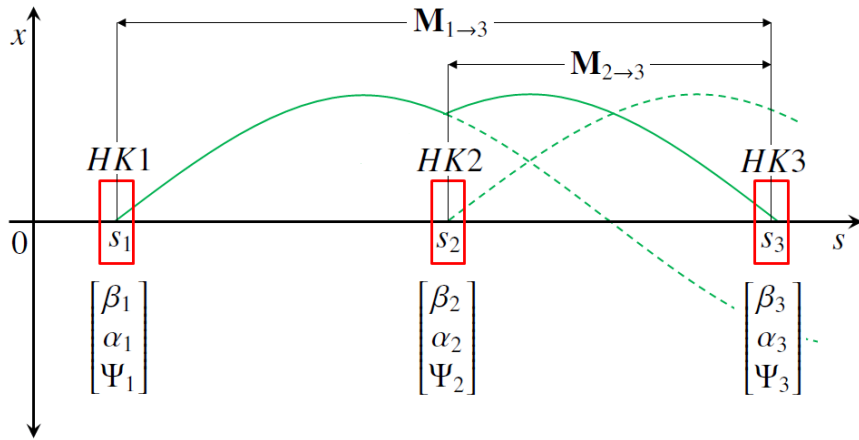


Figure 1.21 – A diagram of a three corrector orbital bump. Particles traveling along s -axis are distorted in the transverse plane due to the magnetic field of the corrector magnets HK1, HK2, HK3. Zero on the x -axis represents the ideal beam orbit.

In this section two methods, which played a crucial role for performing Quench are presented. A standard procedure for changing beam trajectory in the LHC involves a three corrector orbit bump technique. Its principle is based on changing the magnetic field in corrector magnets which results in determining a new orbit for traveling particles. This method was used for tests done in 2010. At that time, a dynamic mode was applied which means that the bump amplitude increased in time. Three years later, the Transverse Damper, known also as the ADT, was combined with the static (i.e. with fixed bump amplitude) three corrector orbit bump in order to create beam losses with strictly defined parameters (loss duration, loss rate). Implementing two modes of the ADT during the dedicated experiments, allowed obtaining fast losses for UFO studies and real steady state losses with almost constant loss rate.

1.8.1 Three corrector orbit bump

Local orbit bumps provide a controlled and well-specified transverse beam displacement in an isolated region of an accelerator [69], [70], [71]. This means that the rest part of the beam orbit remains unaffected by the implemented changes. A basic principle of corrector orbit bumps relies on using additional small corrector (steering) magnets. The applied magnetic field causes beam distortion from its initial orbit. The simplest case of this technique is represented by so-called 180° bump (π -bump). Only two correctors are sufficient to change a transverse beam position, x , by applying an angle, x' , in one place and revert to the beam initial parameters at another location. However, this solution imposes constraints on the distance between two steering magnets which has to be adjusted so that the phase advance is equal $\Psi = \pi$. This matching is barely possible when designing a real machine. Therefore, a method providing freedom in positioning correctors is required.

The idea of the three corrector orbit bump is presented in Fig. 1.21. Beam transverse motion²⁶ is presented as a function of longitudinal position given by s -coordinate. A particle traveling along the initial orbit experience deflecting field of corrector HK1 at the position s_1 . Hence, the trajectory from point s_1 to s_3 is expressed by [69]

$$\mathbf{X}_{1 \rightarrow 3} = \mathbf{M}_{1 \rightarrow 3} \cdot \begin{pmatrix} 0 \\ \kappa_1 \end{pmatrix}, \quad (1.27)$$

where $\mathbf{M}_{1 \rightarrow 3}$ is the transfer matrix and κ_1 is the bending angle (strength) of HK1. The position of steering magnet HK3 can be freely chosen, regardless of the position of HK1. Thus in position s_3 the beam is characterized by the separation x_2 and angle x'_3 . Since the dispersion has to vanish, an additional corrector with strength κ_2 is used in point s_2 (HK2). If only this magnet acted on the beam, the beam motion would be defined according to

$$\mathbf{X}_{2 \rightarrow 3} = \mathbf{M}_{2 \rightarrow 3} \cdot \begin{pmatrix} 0 \\ \kappa_2 \end{pmatrix} \quad (1.28)$$

where $\mathbf{M}_{2 \rightarrow 3}$ is the transfer matrix from point s_2 to point s_3 . Combining Eq. 1.27 and Eq. 1.28 gives the following trajectory vector

$$\begin{aligned} \mathbf{X}_3 &= \mathbf{M}_{1 \rightarrow 3} \cdot \begin{pmatrix} 0 \\ \kappa_1 \end{pmatrix} + \mathbf{M}_{2 \rightarrow 3} \cdot \begin{pmatrix} 0 \\ \kappa_2 \end{pmatrix} \\ &= \begin{pmatrix} a_{11} & a_{12} \\ a_{21} & a_{22} \end{pmatrix} \cdot \begin{pmatrix} 0 \\ \kappa_1 \end{pmatrix} + \begin{pmatrix} b_{11} & b_{12} \\ b_{21} & b_{22} \end{pmatrix} \cdot \begin{pmatrix} 0 \\ \kappa_2 \end{pmatrix} \\ &= \begin{pmatrix} a_{12} \cdot \kappa_1 & b_{12} \cdot \kappa_2 \\ a_{22} \cdot \kappa_1 & b_{22} \cdot \kappa_2 \end{pmatrix}. \end{aligned} \quad (1.29)$$

After passing the bump, the particle has to return to its initial orbit (otherwise the bump is not closed). Therefore, the strength κ_3 of the third corrector is adjusted so that the particle angle is compensated

$$\mathbf{X}_3 = \begin{pmatrix} 0 \\ -\kappa_3 \end{pmatrix}. \quad (1.30)$$

The correlation between corrector strengths is obtained by merging equations 1.29 and 1.30

$$\begin{aligned} a_{12}\kappa_1 + b_{12}\kappa_2 &= 0 \\ a_{22}\kappa_1 + b_{22}\kappa_2 &= -\kappa_3. \end{aligned} \quad (1.31)$$

The matrix elements a_{ij} and b_{ij} can be calculated by using the transfer matrix dependent on

²⁶The basics of the matrix formalism are presented in 1.5.1.

Twiss parameters β, α [72]

$$\mathbf{M} = \begin{pmatrix} \sqrt{\frac{\beta}{\beta_0}}(\cos \Psi + \alpha_0 \sin \Psi) & \sqrt{\beta \beta_0} \sin \Psi \\ \frac{(\alpha_0 - \alpha) \cos \Psi - (1 + \alpha_0 \alpha) \sin \Psi}{\sqrt{\beta \beta_0}} & \sqrt{\frac{\beta}{\beta_0}}(\cos \Psi - \alpha \sin \Psi) \end{pmatrix}. \quad (1.32)$$

where zero index corresponds to the initial conditions. Thus, having the value of κ_1 specified, the other magnet strengths can be derived according to

$$\kappa_2 = -\frac{a_{12}}{b_{12}}\kappa_1 = -\sqrt{\frac{\beta_1}{\beta_2}} \frac{\sin(\Psi_3 - \Psi_1)}{\sin(\Psi_3 - \Psi_2)} \kappa_1 \quad (1.33)$$

and

$$\begin{aligned} \kappa_3 &= -a_{22}\kappa_1 - b_{22}\kappa_2 \\ &= \kappa_1 \sqrt{\frac{\beta_1}{\beta_3}} \left\{ \frac{\sin(\Psi_3 - \Psi_1)}{\tan(\Psi_3 - \Psi_2)} - \cos(\Psi_3 - \Psi_1) \right\} \end{aligned} \quad (1.34)$$

where β_s denotes the β -function and Ψ_s is the phase advance at the location of HK s . Index s refers to the longitudinal position of the correctors ($s=1, 2, 3$).

As it is demonstrated, the three corrector orbit bump allows matching corrector strengths and providing closed orbit bumps regardless of the corrector positions. Despite the fact that the slope of the bump cannot be controlled (as when using four steering coils), this technique finds application in correcting orbits locally.

During Quench Tests in the LHC arc sections, three corrector orbit bumps are applied in order to deposit beam energy on a quadrupole located next to the middle corrector. The LHC correctors work in Parabolic-Linear-Parabolic (PLP) mode²⁷ reaching the maximum linear current increase rate of 0.5 A/s. This corresponds to the gain of $\approx 1\%$ of their maximum current every second. Therefore, at the beam energy of 4 TeV, the maximum kick is about 150 μ rad which corresponds to the maximum current. Therefore, the correlated bump speed is $\approx 1.5 \mu$ rad/s. At the energy of 450 GeV the correctors are able to deflect a beam by $\approx 10 \mu$ rad/s which corresponds to a speed of bump amplitude at the targeted quadrupole of ≈ 1.8 mm/s [73].

The dynamic bumps, applied during 2010 Quench Tests, provided beam losses with the time constant in the order of several seconds, as required. However, due to the operation in PLP mode, it was not possible to control the speed of the bump (done automatically by the control system). During this experiment a loss rate increased nonlinearly in time. Hence, in 2013 a static orbit bump was combined with the transverse damper white noise excitation to provide

²⁷Parabolic-Linear-Parabolic (PLP) mode means that the current, and therefore the magnetic field, in a magnet is increased smoothly in order to reduce beam orbit perturbations and beam excursion. This is followed by the linear component and finally smooth reaching the ultimate current value. The obtained function of the current in time is characterized by a sigmoid-like shape.

a real steady state regime, i.e. constant number of particles lost within certain time window. In addition, a static bump was used as a part of inducing fast losses for UFO studies. In this case additional beam excitation was implemented as well (see Chapter 4).

1.8.2 Transverse Damper (ADT)

The Transverse Damper, also referred as the ADT, is a feedback system playing an important role in a safe and efficient operation of the LHC. On one hand it reduces consequences of effects leading to beam size growth and therefore helps conserving beam emittance. On the other hand, it removes particles present beyond longitudinally specified regions, e.g. in an abort gap.

The ADT system covers a wide spectrum of applications:

- suppressing particle oscillations originating in errors related to injecting beams from the SPS to the LHC, i.e. kicker magnet errors, ripples of bending magnets and septa in the transfer lines.

The transverse beam emittance has to be preserved in order to fulfill conditions of reaching the nominal LHC luminosity during collisions of beams. However, a series of various error sources (steering errors, betatron mismatch, dispersion mismatch, energy errors, mechanical mismatch, coupling [74]) occur during transferring beams from the SPS to the LHC. Hence, the LHC Transverse Damper can deal with oscillation amplitudes of up to ≈ 4 mm (3.5σ , σ - initial RMS beam size) due to injection errors [75] within a damping time of around 50 turns (≈ 4.5 ms). The ADT provides beam deflection by maximum $2\ \mu\text{rad}$ per turn at the injection energy [76].

- stabilizing coupled bunch transverse instabilities²⁸ in the frequency range varying from 3 kHz to 20 MHz (higher frequency oscillations are reduced by natural Landau damping).
- cleaning the abort gap of LHC beams in order to enable a safe extraction from the machine.

Circulating LHC beams have high stored energy which, in the case of failures or degradation of beam quality, has to be safely and reliably removed from the accelerator. This is provided by special kicker magnets which deflect beams to extraction lines. No particles should be present (or more precisely, the number of particles should stay below the damage level) in the kicker magnet during its magnetic field rise time. Therefore, the LHC filling patterns contain a so-called abort gaps, i.e. $3\ \mu\text{s}$ long time slots, which are deliberately provided free of particles. Nevertheless, due to various mechanisms, the abort gap can be repopulated because of particles transferred into this region. The ADT ensures the abort gap cleaning by exciting unwanted particles. Due to oscillation amplitude increase, these particles are later lost on aperture limitations [78].

²⁸Coupled bunch instabilities occur when instabilities from one bunch propagate to other bunches along a bunch train (set of bunches) within subsequent revolutions [77].

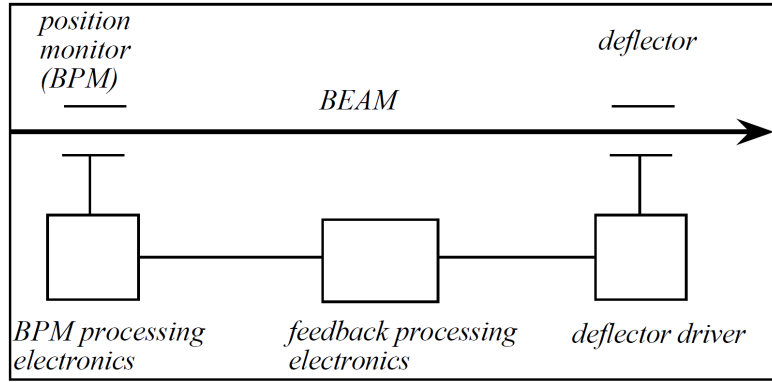


Figure 1.22 – A simplified block diagram of the transverse feedback system [80].

- exciting transverse beam oscillations for various measurements of beam parameters and machine settings - loss maps, aperture bottleneck studies, tune measurements, quench tests, etc.

The collimation system intercepts particles which stay beyond certain acceptance regions. This prevents loosing particles on superconducting magnets. Loss maps are performed in order to verify settings of the multistage beam cleaning process, i.e. alignment of collimator jaws with respect to the beam orbits. The ADT is used for controlled beam blow-up as an alternative method to crossing the third order resonance [79]. Moreover, the application of the ADT gives a big advantage over the other method due to the possibility of acting on single bunches instead of the entire beam. Since the ADT enables creating very controlled excitations, it was also used during Quench Tests in 2013 (See Chapters 4 and 6).

System description

The general principle of the transverse feedback system is presented in Fig. 1.22. The bunch position is measured by a Beam Position Monitor (BPM) and based on that the displacement from a closed orbit²⁹ is estimated [80]. The data is treated by a series of electronic processes, including the feedback system. Finally, the signal is sent to the power electronics which controls the behaviour of a deflector. This allows correcting the transverse momentum, i.e. the angle of the measured bunch by applying the corresponding electric field. The feedback has to be adjusted to the phase advance between the beam position monitor and the kicker on one hand and the bunch time of flight on the other hand. The LHC is equipped with four individual transverse damping systems - one per transverse plane (horizontal/vertical) and per circulating beam (beam 1/beam 2). The ADT operates in the bunch-by-bunch and turn-by-turn mode. The main components of this system are presented on the diagram in Fig. 1.23 [75]. A bunch transverse position is measured when passing through Pick-Ups (PU). These devices are 15-cm long and have an aperture of 49 mm. Each LHC ADT has two pick-ups

²⁹A closed orbit is a path along which particles of a circulating beam perform betatron oscillations [5].

Chapter 1. Introduction

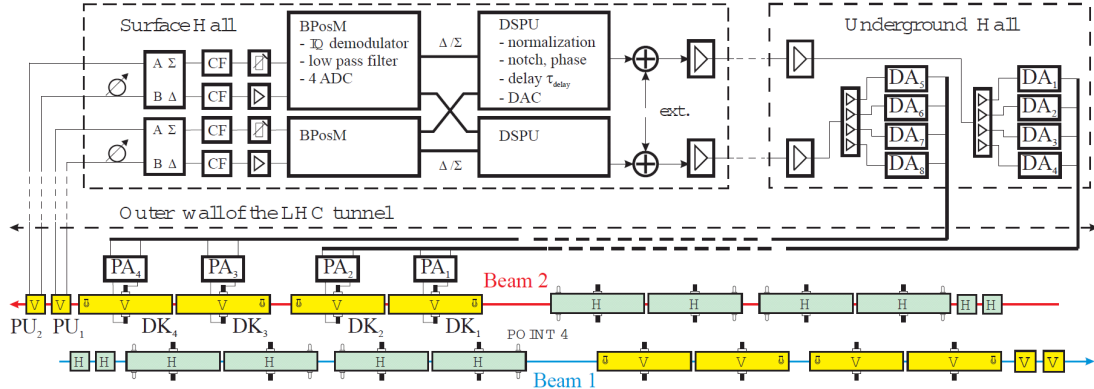


Figure 1.23 – A diagram of the LHC Transverse Damper [75]. DA - Driver Amplifier, DK - Damper Kicker, PA - Power Amplifier, PU - Pick-Up, CF - Comb Filter, DSPU - Digital Signal Processing Unit, BPosM - Beam Position Module, ADC - Analog to Digital Converter, DAC - Digital to Analog Converter.

per beam and plane (eight in total). The signals are sent to a hybrid located in the surface hall. At this stage data is merged and subtracted giving new signals, Σ and Δ , correspondingly. The Comb Filters (CF) are used for adding signals to the same signals delayed in time. This results in constructive and destructive interference generating wavelets at 400.8 MHz. Depending on the magnitude, the signals are sent either to attenuators (signals too high) or amplifiers (signals too low). In the Beam Position Module (BPosM) the data is digitized with the ADC and the normalized transverse beam positions Δ/Σ for single bunches are calculated with a FPGA [81]. In the DSPU (Digital Signal Processing Unit) [82], the signals are normalized proportionally to $\sqrt{\beta}$ at PU, rejecting closed orbits and converting the digital data to analog signal. Eight Driver Amplifiers (DA) with a power of 200 W are located in the underground hall and controlled by the incoming processed signal. In the final stage electrodes of the kicker are driven by wide band amplifiers. A large kick voltage is obtained when the amplifiers work at low frequencies due to the impedance of around 1 k Ω . The components of the kickers are located on both sides of Interaction Point 4 (IP4) in RF regions where the β -function reaches high values ($\beta \geq 100$ m). This is done to provide maximum efficiency of the ADT kickers.

Fig. 1.24 shows the normalized transverse beam positions (Δ/Σ) as a function of number of LHC turns (1 turn = $89\mu\text{s}$) recorded by two pick-ups. The violet line represents signals recorded in Q7 and the pink line - signals in Q9. Beam oscillations induced by injection errors decay but are not completely suppressed in the case when no external damping is applied (the left plot). Activating the ADT allows not only the oscillation amplitudes to be reduced but also to keep them relatively small and stable during the further operation.

The ADT gain

Depending on the applied ADT mode, the overall gain determines how much the particle oscillations are damped or induced. Several systems and signal processing blocks constitute

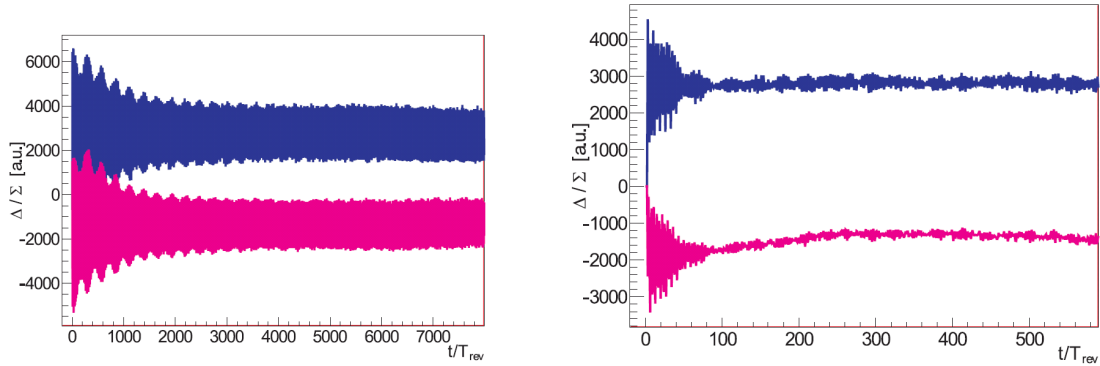


Figure 1.24 – Comparison of damping horizontal injection oscillations without (left plot) and with (right plot) transverse damper. Signals from two pick-ups (Q7 - top function, Q9 - bottom function) are reproduced from [75].

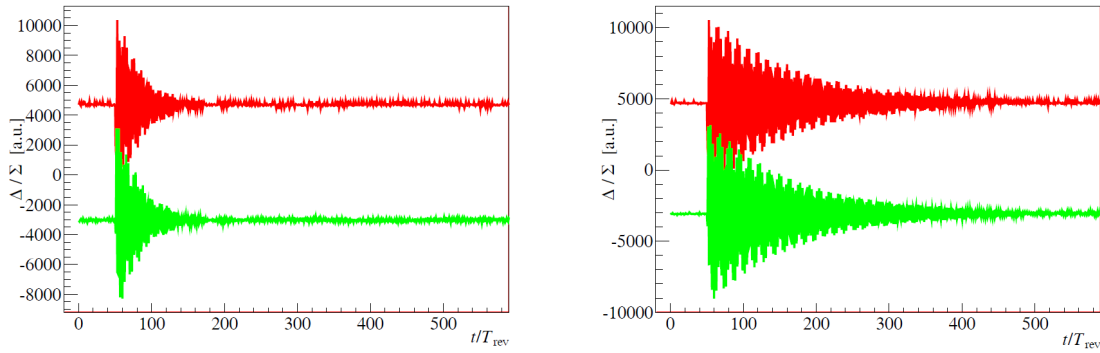


Figure 1.25 – Impact of the transverse damper gain on damping vertical oscillations induced by a tune kicker. Left plot: high gain, right plot: lower gain. Signals from two pick-ups (Q7 - top function, Q9 - bottom function) are presented [75].

the damping system and therefore contribute to the total gain. The LHC ADT gain is normalized so that a specified amplitude of bunch oscillations results in a corresponding kick voltage (100% gain). However, for the non-standard applications, like during the Quench Tests, not the linearity between these two features but the fastest possible beam excitation was required for single bunches. Therefore, by carefully modifying gains of chosen blocks of the data processing chain, it was possible to reach gains above the standard 100%. This means that the higher kicker voltage could be applied [83].

Depending on the ADT feedback loop gain, a control of the damping time is provided (Fig. 1.25). High gains result in fast reduction of the oscillations (left plot) when applying lower gains - in slower damping.

ADT modes

The LHC Transverse Damper system provides suppression of beam oscillations as a result of applying the feedback. Depending on the magnitude of beam displacement from the ideal

Chapter 1. Introduction

orbit, an appropriate angle change of the beam trajectory is imposed. In contrast to this performance, the ADT can work in three modes providing beam excitation:

- Coherent excitation - this mode is used for abort gap cleaning during which, the particles moved outside dedicated slots are excited. Due to increase of their amplitudes, these particles are lost on aperture limitations.
- White noise excitation - this mode is used for a controlled emittance blow-up providing beam losses for special experiments like Quench Tests or validating positions of collimators (loss maps).
- Feedback sign flip - this mode is never used during the standard LHC operation. Moreover it can be considered as a potential failure mode. Nevertheless, changing the sign of ADT response to beam oscillations has found a great application for inducing fast losses for UFO studies (see Section 1.7.3).

The ADT played a crucial role during the Quench Test MD slot in February 2013 recreating conditions of specified loss scenarios. Thanks to that, all experiments, during which the ADT system was used, terminated successfully delivering precious data needed for the LHC set-up after LS1³⁰.

³⁰Long Shutdown 1 (LS1) is a period devoted to maintenance and consolidation of the LHC components, injectors and experiments. LS1 is scheduled for approximately 1.5 year.

2 Overview of the beam induced LHC Quench Tests

A transition of a superconductor from the superconducting state to the normal conducting state is called quenching (see Section 1.4). This phenomenon can be induced by exceeding at least one of the characteristic parameters determining the critical surface (Fig. 1.3): the current density, magnetic field or temperature. In the case of accelerators, superconducting magnets are continuously affected by particle beam losses. In order to provide efficient protection of these devices the critical amount of energy, which could be deposited inside a superconductor, i.e. the quench level, needs to be estimated. Results of theoretical considerations [14] and simulations (Geant4, Fluka) have to be verified by means of experimental techniques. Therefore, so called Quench Tests (QTs) are performed. During such an experiment, abnormal conditions are deliberately imposed to disturb a beam and cause energy deposition on an aperture limitation. As a consequence of primary particle interactions with the matter, a cascade of secondary particles is generated and develops towards superconducting elements. Quench levels strongly depend not only on a superconductor coil design (SC material properties, ratio of copper to superconductor, insulation type etc.) but also on the loss duration (ultra fast, fast and steady state regimes). All these aspects have to be taken into account to fully understand the mechanism of quenching and provide an adequate protection. Therefore, various scenarios have to be considered.

In this chapter, an overview of beam-induced quench tests, which were done between the beginning of the LHC operation (September 2008) and LS1 (February 2013), is given. Experiments are classified depending on a beam loss duration due to different agents participating in heat evacuation from a superconductor-based system. The nomenclature of the quench tests is correlated to a name of a quenching element, a location where a test was performed or the main tool applied during an experiment:

- LHC arc main magnet QTs,
- wire scanner QTs,
- Q6 QTs,
- collimation QTs.

It needs to be stressed that no superconducting materials are used in the design of collimators and wire scanners. These elements are used for provoking beam losses. In these cases, the accelerator components, which undergo the transition to the normal conducting state, are usually downstream SC magnets.

2.1 Ultra fast losses

Beam losses in the order of nano- and microseconds are classified as ultra fast losses. In this timescale, the quench level is determined by the enthalpy of a dry superconducting cable. This is due to the fact that the loss duration is too short for the heat to propagate from the SC strands to the liquid helium which is present inside a cable. There were three experiments dedicated to ultra fast loss regime: two on Q6 magnet and one on arc magnets.

2.1.1 Q6 Quench Test 2011

Although the collimation system is designed so that beam losses are intercepted (see Section 1.3), a certain failure of injection kickers may be one of the origins of quenching the SC magnets located downstream the collimators. This happened in April 2011 when a batch¹ of 36 bunches was over-kicked by the MKI due to the vacuum degradation and grazed the collimators: the TDI and the TCLIB. As a consequence, scattered primary protons and developed secondary particle shower caused quenching of 11 magnets [84], [85].

The Collimation Quench Test was performed on 3rd July 2011 in order to verify a loss rate at magnet Q6.L8 depending on the TCLIB jaw positions. In addition, the quench level at this magnet was studied. Single proton pilot bunches of beam 2 were used in the Injection&Dump mode which means that the particles had the energy of 450 GeV. During the experiment, the aperture in the TCLIB was reduced in steps from 8.3σ to 1.3σ (≈ 1 mm). In addition, an offset of up to -3σ (towards beam) was introduced to catch the entire beam. Beam losses and voltage measurements were done for different bunch intensities ($1 \cdot 10^{10}$ protons, $2 \cdot 10^{10}$ protons, $3 \cdot 10^{10}$ protons) and currents (in 200 A steps up to 2200 A which corresponds to 5 TeV conditions) in Q6.L8 magnet.

The experiment terminated without quenching Q6.L8 although the BLM signals exceeded significantly the values expected at quench, i.e. by a factor of ≈ 8 at 450 GeV (200 A) and ≈ 40 at 5 TeV (2200 A)². This divergence comes from the fact that in this case, similarly to the wire scanner QT, the expected BLM signals at quench were defined according to a different loss scenario than was provided. This means that, the BLM thresholds are set with respect to results of experiments in arc magnets, where a beam hits magnet aperture directly. However, in the case of Q6 QT, beam affected the collimator and the secondary particles shower propagated through longer distance to reach the detectors located downstream.

¹A batch is a group of bunches.

²The expected BLM signal at quench for Q6.L8 was 5.8 Gy/s at 450 GeV and 0.46 Gy/s at 5 TeV [86].

2.1.2 Q6 Quench Test 2013

Q6 Quench Test 2013 was the repetition of the experiment performed in 2011. In order to succeed in quenching Q6.L8, it was decided to use bunches at 450 GeV with the intensity twice as big as previously ($6.5 \cdot 10^{10}$ protons). Indeed, hitting a collimator with such a bunch leaded to development a secondary particle shower with energy high enough to cause quench of the magnet located downstream the collimator. At that moment, Q6.L8 operated at the electric current of 2500 A which is equivalent to generating the magnetic field needed for 5.6 TeV beam. The QP3 computations predicted the quench level of the MQM (Insertion Region Quadrupole) to be 20 mJ/cm^3 and 16 mJ/cm^3 at currents of 2000 A and 2500 A, respectively. However, no quench occurred at 2000 A. The magnet quenched at 2500 A and according to Fluka simulation the quench level was around 30 mJ/cm^3 . Summing up, there was a factor of 2 difference between QP3 and Fluka results.

2.1.3 Injection&Dump Quench Test on arc LHC Main Magnets

The Quench Tests in the LHC arc Short Straight Sections (see Section 1.3) are performed to estimate the Main Quadrupole quench levels. These focusing magnets are considered to be in danger of quenching because of their localization in the places where β -function reaches maximum values. A three corrector orbit bump technique (see Chapter 1.8.1) was used to deflect beam trajectory and aim at a central magnet during the experiments done in 2010. Later in 2013, this method was enhanced by applying the ADT and the MKQ. All these experiments were done using direct proton losses. It should be stressed that current BLM thresholds are mainly based on results of these tests.

The first Quench Test with a three corrector orbit bump (see Section 1.8.1) after the 2008/2009 LHC break was performed between 18th and 19th September 2010. Bunches consisting of $(3 - 6) \cdot 10^9$ protons (beam 1) were individually delivered to the LHC in Injection&Dump mode (energy of 450 GeV). They were diverted from the nominal orbit towards quadrupole MQ.14R2 with a rising amplitude up to 24.3 mm in the horizontal plane. Although the beam screen³ aperture was 23.25 mm and the beam was certainly deposited on the magnet, no high losses were observed in the transient regime. Therefore, an increased bunch intensities of $(9 - 9.5) \cdot 10^9$ protons were applied. Due to electronics problem⁴, the experiment terminated without quenching with a bump amplitude of 22.8 mm.

2.2 Fast losses

Fast losses are the losses with a timescale of several milliseconds. In this case the enthalphy of a cable still plays a dominant role in quenching process. Moreover, the contribution from liquid helium bath is not negligible any more. In the LHC there were two quench tests dedicated to

³CDD drawings: LHCVSSB_0146, LHCVSSB_0147

⁴A communication with the old QPS system was lost, a controller needed to be restarted.

fast losses. During the first one, wire scanner was used for provoking beam losses. The other experiment was done in arc region and, therefore, a novel method of inducing fast losses, i.e. a combination of three corrector orbit bump technique with ADT sign flip mode, was applied.

2.2.1 Wire Scanner Quench Tests 2010

The observation of fast losses in the LHC in 2010 and 2011 and correlated beam dumps induced certain worries about LHC beam availability in the future when operating with higher beam energy. Not only beam extractions from the LHC triggered by exceeded BLM thresholds but mainly probable quenching of superconducting magnets could limit the machine operation. Therefore, it was decided to conduct the Wire Scanner (WS) Quench Test devoted to studying quench levels in the timescale of milliseconds. In addition, the obtained data was used to validate the QP3 heat transfer code [87].

The experiment was done on 1st November 2010 [88] in cell 05L4 using 3.5 TeV circulating beam 2. The beam constituted of 144 bunches with total intensity of $1.53 \cdot 10^{13}$ protons. A $34 \mu\text{m}$ in diameter carbon wire was moved into a beam. As a result of interactions between the wire and the beam, a cascade of secondary particles was generated [89]. This situation perfectly mimicked the processes occurring during UFO-induced losses (see Section 1.7.3). Every WS measurement consists of two scans - IN and OUT. The IN scans are taken when a wire is driven from its parking position through the beam. These scans were done with nominal speed of 1 m/s. The OUT scans are performed when the wire comes back to the initial point. During the WS QT, a speed of the wire OUT scans was decreased in steps from 1 m/s to 0.05 m/s. Due to the location of the Wire Scanner, a Twin Aperture Separation Dipole (MBRB)⁵ was the most exposed to the radiation of the secondary particles. Quenching of the MBRB occurred as a consequence of passing around $1.4 \cdot 10^{14}$ protons through a wire⁶ during approximately 10 ms (wire scan speed: 5 cm/s). Fig. 2.1 presents the final results of the experiment. The BLM signal (the blue line) is characterized by an irregular shape (three peaks). This might indicate that a wire started vibrating when going through the beam. The voltage measurement (the red curve) allowed the moment of MBRB quenching to be estimated (the green line). The sudden drop on quench heaters' voltage points the moment of the beam dump. The Fluka simulations [91], [92], [93] were provided [88], [94] in order to estimate the energy needed to induce MBRB superconductor transition to the normal conducting state. Fig. 2.2 shows the comparison of simulated and measured BLM signals. The agreement was in the order of 30 %. Studies of radial energy distribution showed that the energy density of around 10 mJ/cm³ was needed to quench the magnet. The QP3 code [87] calculations provided the value twice as big. This might result from different definition of the moment of quenching between Fluka and QP3 code.

⁵The MBRB (Twin Aperture Separation Dipole) is a special magnet operating at 4.5 K. It was built in Brookhaven National Laboratory [90], USA.

⁶Although about $1.4 \cdot 10^{14}$ protons passed through the wire, only about 10^{-4} of them probably were lost there [86].

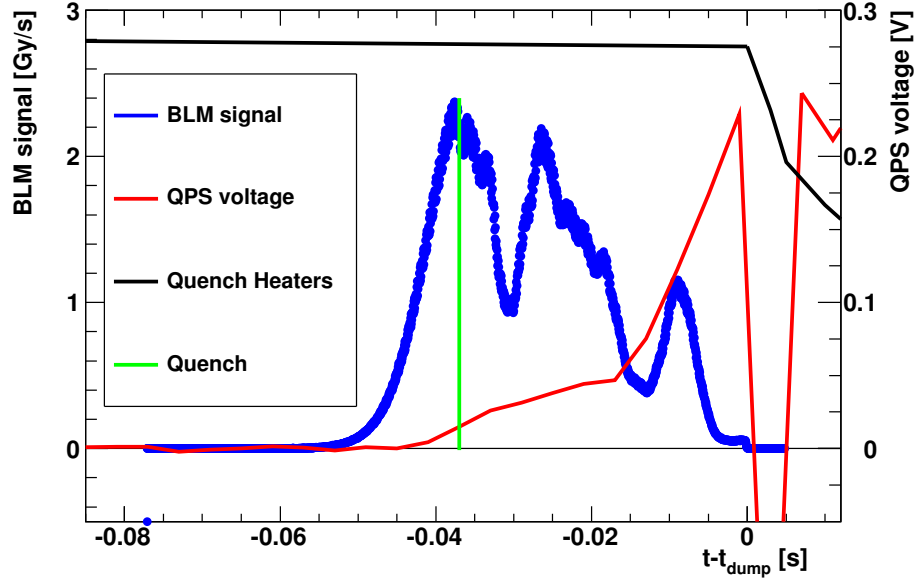


Figure 2.1 – Final Wire Scanner Quench Test results: the correlation between BLM and QPS system measurements. The blue line represents the beam losses in the most exposed BLM monitor, the red line - the voltage on the MBRB magnet, the black line - the voltage on the quench heaters. The green line points the moment of quenching, which was estimated from the first significant rise in voltage measured by the QPS [88].

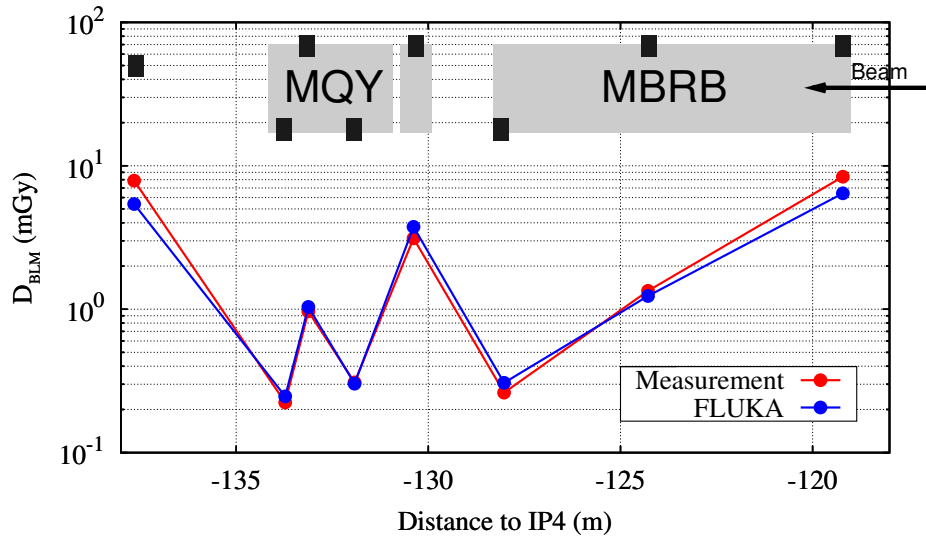


Figure 2.2 – Final Wire Scanner Quench Test results: Measured (the red dots) and simulated (the blue dots) BLM signals during quenching the MBRB [88].

The Wire Scanner Quench Test has provided the quench level estimates for the loss scenario considering an impact of secondary particles onto a magnet aperture. These studies are very important especially in the sense that BLM thresholds are set regarding direct beam losses [95].

2.2.2 Fast Loss Quench Test 2013 on MQ12.L6

An increasing interest in UFO losses and their real hazards to the LHC efficiency made the Fast Loss Quench Test to be the top priority of the 2013 MD slot. However, the previously applied method of inducing losses with a wire scanner was not available any more. This was due to the proximity of WS to the MBRB magnet which was distinguishing among other LHC magnets. In 2012, neither any fully functional spare MBRB magnets nor production lines were available at CERN. This means that in the case of damage of the MBRB installed inside the LHC, it would take around four years to provide replacement [96]. In addition, the MBRB was not a representative magnet for UFO studies since UFOs were observed everywhere and the MBRB is was a very rare magnet. Hence, it was decided to conduct the experiment in the arc region but to do so a new strategy of inducing fast losses needed to be invented.

The experiment was performed on 15th February 2013 at 4 TeV using beam 2 in the horizontal plane. MQ.12L6 quenched after depositing around $8.2 \cdot 10^8$ protons within 10 ms. This loss duration was feasible thanks to a novel technique of combining the three corrector orbital method with the ADT sign flip mode and MKQ excitation. Analysis revealed that the BLM signal at quench of a monitor installed on the MQ was ≈ 12 times higher than the expected value. Detailed proceedings of the experiment, Geant4 simulation results and data analysis are provided by the author and presented in Chapter 4.

2.3 Steady state losses

The loss duration of several seconds is considered as a steady state regime. In this timescale, a quench level of a superconductor is determined by the liquid helium capability of evacuating heat from a magnet coil. Six dedicated experiments were provided between 2010 and 2013 to assess a quench level in the cases of slow losses.

2.3.1 3.5 TeV Collimation Quench Test with protons 2011

The Dispersion Suppressor (DS) regions are considered as critical parts of the LHC ring due the highest losses originating in cleaning insertions, i.e. collimators, and experiments [97], [98]. Therefore, in order to investigate a response of the system to the designed load of 500 kW, the steady state loss quench test on the primary collimators (IR7) was performed on 5th May 2011. 74 BLM monitor thresholds were changed basing on loss maps [99] to avoid beam dumps triggered by the BLM system. The positions of collimator jaws were set to the default nominal

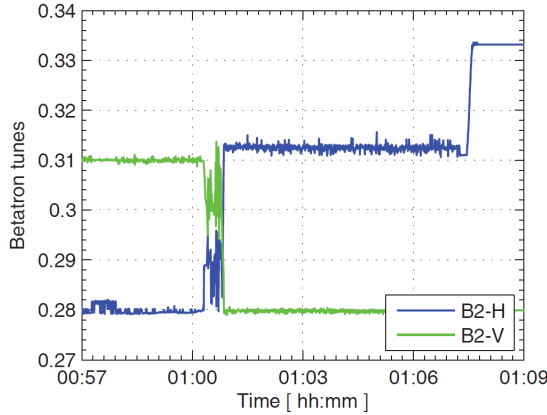


Figure 2.3 – Proton Collimation Quench Test 2011: Tune functions in time [97].

values. The horizontal tune Q_h was shifted close to $\frac{1}{3}$ (Fig. 2.3). Under this condition sextupole fields can cause third order resonances [72] leading to a beam oscillation amplitude rise and beam losses.

The tests were done with 3.5 TeV unsqueezed beams. Using beam 2 consisting of one train of 12 bunches and 4 individual bunches (total intensity $\approx 1.2 \cdot 10^{11}$ protons), a peak loss rate of $9.1 \cdot 10^{11}$ protons per second was obtained. This value corresponds to the power of 510 kW delivered to the primary collimators within 1 s, as intended. The loss rate on limiting magnet Q8.L7 (regarding the collimators for beam 2 cleaning) was estimated to be around 336 W and gave no quenching. The experiment proved that the collimation system is capable to safely withstand high beam losses as designed.

2.3.2 3.5 Z TeV Collimation Quench Test with lead ions 2011

The Proton Collimation Quench Test was followed by a similar test using lead ions (6th December 2011). The idea behind it was to verify estimated limitations related to ion beam intensities and critical locations. Since the collimation cleaning efficiency for ions is less than in the case of protons, the loss load was decreased by a factor of 100 (to 5 kW) [100]. This corresponds to the loss of 10^8 ions, i.e. $82 \cdot 10^8$ charges at 3.5 Z TeV within one second (Z is the atomic number of lead). The driving mechanism for inducing beam losses was the same as for the proton test (crossing the 3rd resonance, default machine setup, increasing BLM thresholds [101], switching off the ADT). Using $3.4 \cdot 10^{11}$ charges per beam (three trains of 12 bunches) peak losses of $1.1 \cdot 10^{11}$ charges per second (on Q11L7) were achieved for beam 1 and $4.9 \cdot 10^{10}$ charges per second (on Q09L7) in the case of beam 2. Table 2.1 contains final results of the experiment. The maximum ratios of the BLM signals to the assumed quench levels are given together with the locations and the integration times. All beam dumps were triggered by the BLM system due to the exceeded threshold values, meaning that no magnet quenched. The test showed that ion losses are faster than proton losses.

Table 2.1 – Ion Collimation Quench Test 2011: Summary - BLM signals compared to the quench levels for different limiting locations. Table based on [97], [100].

BLM signal/quench level [-]	Location	RS	Integration time [s]
2.4	Q08.L7	07	$81.92 \cdot 10^{-3}$
1.2	Q11.R7	07	$81.92 \cdot 10^{-3}$
1.7	Q08.L7	06	$10.24 \cdot 10^{-3}$
1.6	MB9.L7	09	1.3

2.3.3 4 TeV Collimation Quench Test with protons 2013

The 4 TeV Proton Collimation Quench Test was a part of the Quench Test slot in February 2013 at the end of LHC run before LS1⁷. The motivation of performing this test was the same as previously, i.e. studying leakage from the collimation to the dispersion region in IR7. The main difference between these two tests lay in the method of inducing beam losses - instead of crossing the 3rd order resonance, the ADT white noise excitation was applied to blow-up beams. This provided the loss duration of up to 14 s. In contrast to the 2011 tests, the collimation jaws of TCSG in IR7 and all collimation jaws in IR6 were retracted by 1 σ in order to generate the same loss rate using lower beam intensities [102].

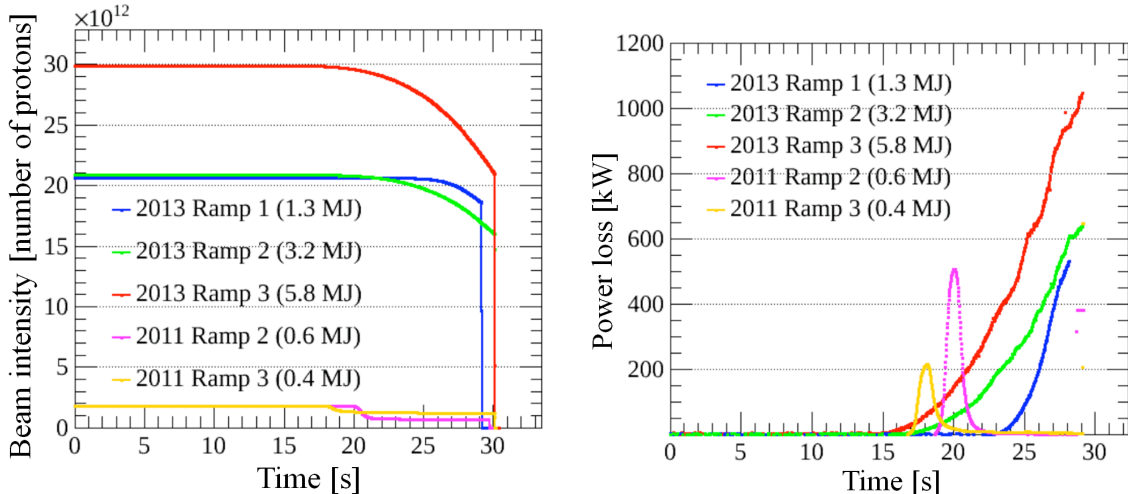


Figure 2.4 – Comparison of the Proton Collimation Quench Test performed in 2011 and 2013. Left plot: Beam intensity as a function of time. Right plot: Power loss in time. Courtesy B. Salvachua [103].

⁷ Initially it was planned to perform both, proton and ion, tests in order to repeat previous experiments at higher energies and longer loss durations. However, due to the issues related to the ion source (maintenance of an oven), the second experiment could not be done.

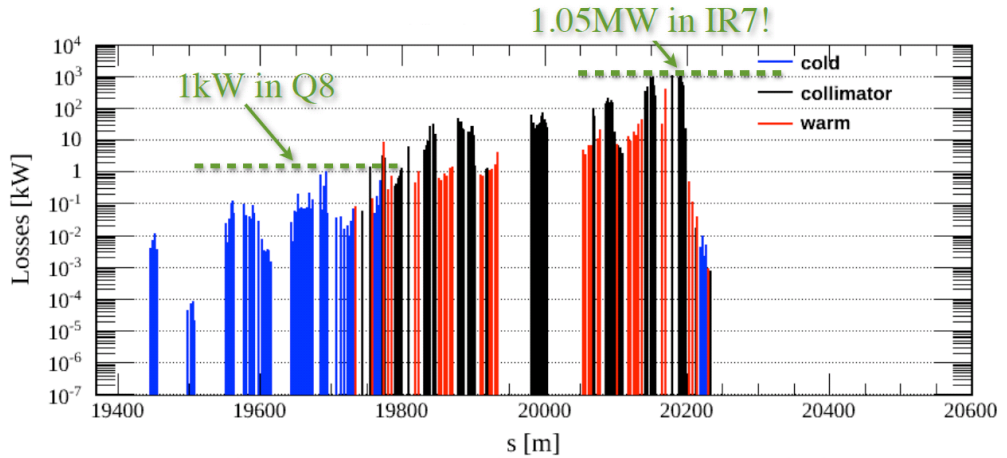


Figure 2.5 – Proton Collimation Quench Test 2013:Losses in DS IR7. Courtesy B. Salvachua [103].

Fig. 2.4 shows comparison of the Proton Collimation Quench Tests performed in 2011 and 2013. The red curves show beam intensity loss (left plot) resulting in the power loss of 1050 kW on collimator TCP.B6R7.B2 and approximately 1 kW in Q8 (Fig. 2.5). Although such high load was delivered, no quenching occurred. The BLM signal recorded by BLMQI.08L7.B2I10_MQ was greater than the estimated BLM signal at quench by a factor of 2.3 in RS09 (signal integration time of 1.3 s) and 5.1 in RS10 (signal integration time of 5.2 s). This issue is further discussed in Section 6.3.3.

2.3.4 450 GeV Steady State Loss Quench Test 2010

450 GeV Steady State Loss Quench Test 2010 was performed in arc half-cell 14R2 on 6th October 2010. In order to induce beam losses on the MQ, a beam with intensity of 10^{11} protons was deflected using three corrector orbit bump method. Depending on the focusing properties of the MQ.14R2, during the experiment beam 1 was used in the horizontal plane and beam 2 - in the vertical plane. The FBCT (Fast Beam Current Transformer) measurements (Fig. 2.6) show that in the case of tests with beam 2 all particles were deposited on the aperture when in the case of beam 1 - around 34% of initial intensity was dumped. BLM signals, in the moment when maximum signals occurred, are given in Fig. 2.7. The details of the MD slot are summarized in Table 2.2.

First two beam losses (B2V) triggered the QPS on bus bars to cause beam extraction. This was probably related to quenching the MQ. Later, as the result of losing $1.10 \cdot 10^{11}$ protons of beam 1 in the horizontal plane during around 1.5 s (the last case), the downstream Main Dipole (MB.C14R2) quenched⁸. The recorded BLM signal (0.039 Gy/s) was very close to the expected BLM signal at quench (0.041 Gy/s). The reason why the MB quenched instead of the MQ is

⁸Among six quench tests performed in arcs and using the three corrector orbit bump technique, only once (6.10.2010) quenching of the main dipole located downstream of the targeted quadrupole was observed.

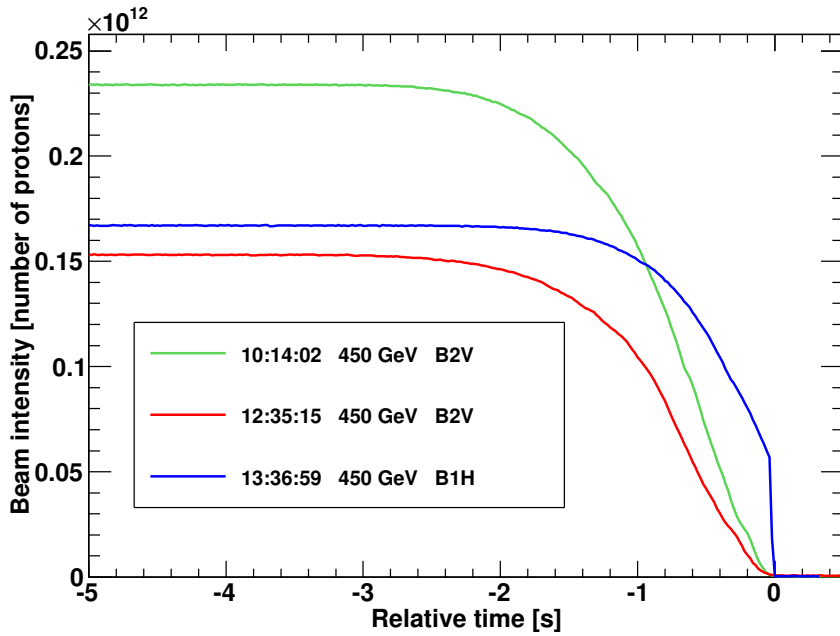


Figure 2.6 – 450 GeV Main Magnet Quench Test 2010: Beam intensities. Zero on the time axis corresponds to the moment of the beam dump.

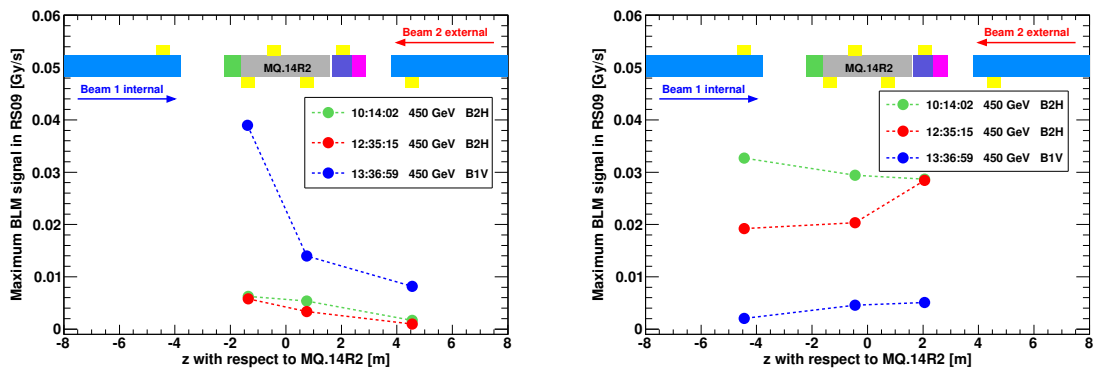


Figure 2.7 – 450 GeV Main Magnet Quench Test 2010: Maximum BLM signals observed during quenches (1.3 s integration time, RS09). Left plot - monitors observing beam 1 losses, right plot - monitors surveying beam 2 losses.

Table 2.2 – 450 GeV Main Magnet Quench Test (6.10.2010): Summary. Losses of beam 2 deflected in the horizontal plane resulted in quenching the MQ bus bars. Losses of beam 1 in the vertical plane caused quenching of the main dipole (MB.C14R2) located downstream the targeted quadrupole. $N_{protons_{initial}}$ - initial beam intensity, $N_{protons_{lost}}$ - number of lost protons, t_{loss} - loss duration from the moment when 5% of initial intensity was lost.

No	Time	Beam	Plane	$N_{protons_{initial}}$	$N_{protons_{lost}}$	t_{loss} [s]	Quenching part
1	10:13:58	2	Vertical	$2.43 \cdot 10^{11}$	$2.43 \cdot 10^{11}$	≈ 1.9	MQ.14R2
2	12:35:11	2	Vertical	$1.53 \cdot 10^{11}$	$1.53 \cdot 10^{11}$	≈ 2.0	MQ.14R2
3	13:37:00	1	Horizontal	$1.67 \cdot 10^{11}$	$1.10 \cdot 10^{11}$	≈ 1.2	MB.C14R2

probably due to a loss pattern, especially the loss orientation, and loss intensity. Two first attempts were done with the vertical losses so considering the situation geometrically, most of a secondary particle shower propagated to the region of MB magnets were no superconductor was present (coils are located horizontally). In the last case, the beam loss intensity was smaller than previously but provided in the horizontal plane. Therefore, it was possible to quench MB for which the threshold was apparently lower than in the case of the MQ.

2.3.5 3.5 TeV Steady State Loss Quench Test 2010 on MQ.14R2

Specific results of 450 GeV Steady State Quench Test were encouraging to repeat the experiment at nominal (for year 2010) energy of 3.5 TeV. The main objective of the test performed on 17th October 2010 was to validate current BLM thresholds based on simulations and measurements [104]. In order to induce beam losses, the three corrector orbit bump technique was applied in LHC half-cell 14R2. A 5.6 s long loss of approximately $1.1 \cdot 10^{11}$ protons of beam 2 deflected in the vertical plane caused quenching of the MQ. Detailed description, simulations and data analysis were prepared by the author and can be found in Chapter 5.

2.3.6 4 TeV Steady State Loss Quench Test 2013 on MQ.12L6

The outcomes from the 2010 QT at 3.5 TeV delivered very interesting information of quench behaviour. Based on that, the BLM system was updated (in terms of modifying BLM thresholds and implementing additional RS10 and RS11 into the logging data base). However, in order to verify BLM settings for the actual steady state losses (previous loss rate increased in time), the Quench Test at 4 TeV (16th February 2013) was performed by combining the three corrector orbit bump technique with the ADT white noise excitation. This solution ensured close to constant losses of about $3.1 \cdot 10^8$ protons per second. Beam 2 was distorted in the horizontal plane over about 20 s. The results confirmed the reliability of BLM thresholds in the steady state loss regime. The detailed case study is given by the author in Chapter 6.

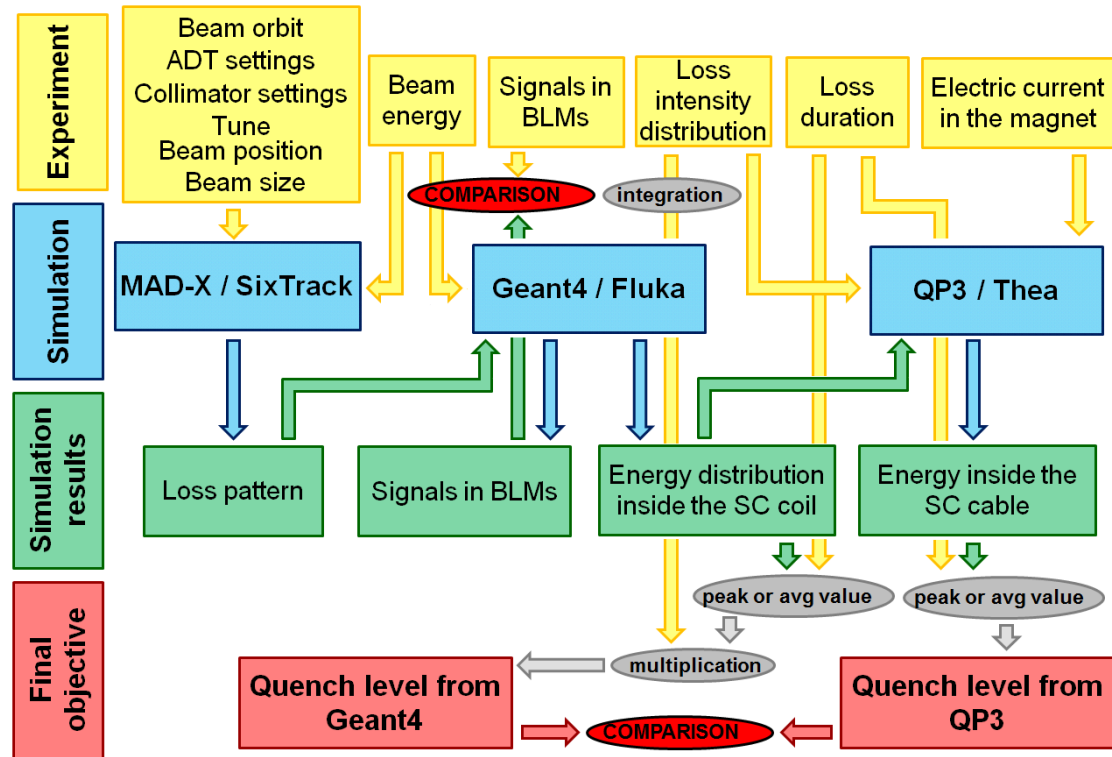


Figure 2.8 – Strategy of assessing quench levels. Description in the text.

2.4 Strategy of assessing quench levels

The Quench Tests presented in previous sections have delivered the data necessary for the further studies on loss patterns and quench levels in different loss timescales. The procedure of assessing quench levels is based on several correlated and complementary steps which are presented in Fig. 2.8. Yellow blocks represent measured observables and settings of accelerator components used during the experiments. According to the simulation methods (given in blue) and their results (shown in green), the following stages are distinguished:

- **MAD-X [105], [106] or SixTrack simulations [107]**

MAD-X and SixTrack simulate beam trajectory by recreating machine settings and their influence on beam behaviour. This includes the lattice specification (definition of magnetic elements: bending, focusing, etc.), tune, position of collimator jaws, ADT parameters and applied bumps. In addition, a beam size and an initial beam position are defined. As the result, the loss patterns, i.e. the distribution of lost particles along the aperture limitation is provided.

- **Geant4 [108], [109], [110] or Fluka [91], [92], [93]**

In Monte Carlo codes (Geant4 and Fluka), representation of accelerator components (magnets, collimators, etc.) is implemented together with the magnetic field maps

in order to simulate electromagnetic processes and interactions of primary particles with matter. These simulations might use loss patterns obtained from MAD-X/SixTrack either directly (specification in the code) or indirectly on the stage of further analysis (see Chapter 3). Based on the experimental conditions (beam type, beam energy, target, impact angle), Geant4/Fluka provide energy distribution in magnet superconducting coils and signals in BLMs. Depending on loss timescale, and therefore different agents contributing in heat evacuation from the coil, and number of particles lost during the experiment, quench levels can be calculated. The values of computed BLM signals are compared to the measured observables.

- **QP3** [87] or **Thea** [111], [112]

QP3 and Thea are the programs for calculating the energy gain of a superconducting cable, which is needed to induce its transition from the superconducting state to the normal conducting state at the current used during an experiment. As an input, the normalized loss distribution (experimental data) is used together with the normalized radial distribution of energy deposited inside a coil (results from Monte Carlo simulations). Depending on the loss duration either peak energy (fast losses) or average energy (slow losses) has a meaning of quench level.

Concluding, the quench levels are obtained in two ways but the QP3/Thea computations depend on the input from Geant4/Fluka simulations. The agreement between these results gives the confidence in the correctness of the obtained quench levels. The performed studies revealed that in the steady state regime, the quench levels resulting from different simulation techniques are consistent. Nevertheless, in the fast loss case, significant discrepancies have been observed. This requires further investigations but the most likely is related to the fact that the models used in QP3/Thea were not yet validated with experimental data in the timescale of milliseconds.

2.5 Summary of the beam induced Quench Tests

Among all LHC quench tests performed between 2010 and 2013, six of them terminated in magnet quenching and two others - in quenching of the MQ bus bars. Table 2.3 summarizes performed experiments regarding the test type, the applied method of inducing beam losses, the loss location, the energy, the number of lost particles and the particle impact on magnets.

The most important conclusion coming from the experiments is that the quench level is not only determined by the superconductor properties and the design of the coil but also by the loss duration. In addition, BLMs signals strongly depend on the loss scenario, i.e. primary or secondary particle impact onto the magnets.

Understanding the mechanisms of

- beam losses,

Chapter 2. Overview of the beam induced LHC Quench Tests

- the propagation of the secondary particle shower along the various parts of the accelerator system ,
- magnet quenching process

allows LHC interlocks to be precisely adjusted in order to prevent machine damages and unreasonable beam dumps. Moreover, the thorough knowledge of the quench levels enables pushing the machine to its design limits resulting in an efficient luminosity productions for experiments like ATLAS and CMS.

The author's contribution to that process was to plan and conduct arc Main Magnet Quench Tests (in the cooperation with the BLM experts, operation team, ADT team and collimation team), provide Geant4 simulations and analysis.

Table 2.3 – Summary of the beam induced Quench Tests: 3COB - three corrector orbit bump, 3OR - 3rd order resonance, ADT_{SF} - ADT Sign Flip mode, ADT_{WN} - ADT White Noise excitation, p - protons, Pb^+ - lead ions, * - if there were more than one tests, at least one terminated with quenching.

Name	Type	Method	Location	Energy [TeV]	Particles	Impact on magnets	Quench*
Main Magnet QT	Ultra fast	3COB	14R2	0.45	p	direct	yes
	Fast	3COB+ ADT_{SF} +MKQ	12L6	4	p	direct	yes
		3COB	14R2	0.45	p	direct	yes
	Steady State	3COB	14R2	3.5	p	direct	yes
		3COB+ ADT_{WN}	12L6	4	p	direct	yes
Wire Scanner QT	Fast	wire scanner	05L4	3.5	p	indirect	yes
Collimation QT	Ultra fast	closed collimators	06.L8	0.45 - 5	p	indirect	yes
	Steady State	collimators+3OR	06R7	3.5	p	indirect	no
		collimators+3OR	06R7	3.5	Pb^+	indirect	no
		collimators+ ADT_{WN}	06R7	4	p	indirect	no

3 Geant4 simulations

3.1 Motivation of using Geant4 code

The Quench Tests on LHC magnets do not provide any information about density of energy deposited inside the superconducting coils directly. This is due to the fact that no detectors allowing this kind of measurements are currently (year 2013) installed in the machine. However the quench levels can be estimated by using particle shower physics simulation codes like Geant4 and FLUKA. The idea behind it is to correlate the energy deposition inside the SC coils (unknown) with the secondary particle radiation outside the magnet cryostat. The simulated BLM signals are compared to the experimental values. Agreement between these values specify uncertainty of the estimated quench level.

3.2 Introduction to Geant4

The Geant4 name comes from "GEometry ANd Tracking". This object orientated (C++) toolkit based on Monte Carlo methods has been developed to fulfill demands of complex nuclear physics experiments which required simulations of particles passing through matter [108], [109], [110]. The structure of the code is very complex - it includes representation of a system (i.e. geometry of magnets, detectors, etc.), material definitions, characterization of the fundamental particles (i.e. specification of mass, charge, spin, parity, life time, decay types, etc), implementation of the electric and magnetic fields, description of interaction types and their products (secondary particles), particle tracking.

3.3 Code description

The very complex structure of Geant4 code is based on complete specification of particles and their types of their interactions, the distribution of the magnetic field inside a magnet and representation of magnet system. The accuracy of implementation these conditions determine proper production of a secondary particle shower (as the consequence of primary

particle interactions with matter) and its development. Moreover, the way of recording energy deposited by particles has to be defined in order to obtain results with desired resolution. In this section one of the most important elements of Geant4 are presented. Each part contains a short introduction and description of applied settings used for Quench Test simulations.

3.3.1 Physics list

In the Physics list all particles which are expected to be important in the simulated process are defined. This concerns their fundamental properties (mass, charge, spin, constituting subparticles if applicable, lifetime, etc.) Additionally, type of interaction, which particles undergo, are specified.

The Quark Gluon String with Bertrini cascade model (QGSP_BERT) was implemented to the Geant4 Physics List for the Quench Test simulations. The decision of choosing QGSP_BERT was based on the fact that this list is the most recommended for this type of simulations [113]. The QGSP_BERT list contains following models[110]:

- **Quark Gluon String model** describing interactions of mesons (pions π , kaons K) and barions (neutrons n and protons p) with nuclei for energies greater than 12 GeV,
- **Low-Energy Parametrized (LEP) model** concerning interactions of π, K, n, p with nuclei in energy range from 9.5 GeV to 25 GeV,
- **Bertini (BERT) cascade model** considering intra-nuclear cascades,
- **parametrized (LEP + HEP) models** taking into account all other hadrons (namely hyperons).

In addition High Precision neutron transport was implemented. This was provided since the amount of materials considered in simulations might significantly influence the scattering processes.

3.3.2 Magnetic field

A distribution of the magnetic field has to be defined in order to impose an adequate motion of a charged particle inside magnetic elements. Based on the provided data points, Geant4 calculates the particle trajectories. The obtained curves are broken into linear chord segments which well approximate the movement of the charged particles.

The magnetic field maps were obtained from ROXIE calculations [114] and implemented to the Geant4 code for both, the MQ and MBs. The field mesh, i.e. distance between two simulated data points, for the MQ was 4.59 mm and 5.19 mm in the case of the MB map. These field maps were done for the central coil parts, i.e. where cables are parallel to the beam axis.

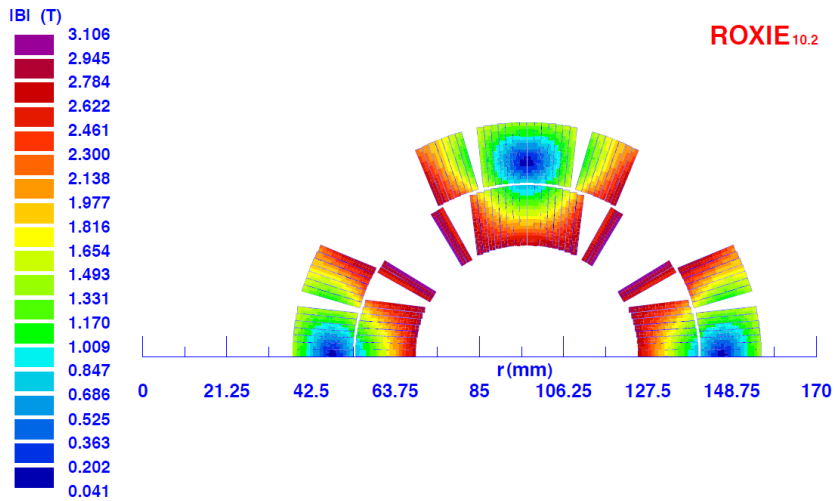


Figure 3.1 – Magnetic field map of the MQ at 3.5 TeV from ROXIE simulations [114]. Zero on x -axis corresponds to the centre of a cold mass, or in other words - the middle point between two apertures of a single magnet.

However, the situation gets more complicated at the endings of the coils where cables are bended. The magnetic field cannot terminate abruptly. Therefore, a smooth linear decay of its lines was implemented in order to take into account magnet fringe fields. Fig. 3.1 shows the magnetic field generated by the MQ at current of 5.94 kA which is needed for operation with 3.5 TeV beam. The external cables of the coils provide the highest magnetic field values.

3.3.3 Magnet representation

The environment, in which particles travel and interact, i.e. the mechanical components of a machine, have to be described. In Geant4 code, an object representation is built in four subsequent stages:

- **defining materials** - an atomic number, atomic mass (in the case of chemical elements), number of elements (in the case of compounds) and density have to be specified,
- **creating a geometrical volume** - a shape and size of a magnet element in the three-dimensional space are defined,
- **creating a logical volume** - the material type, which the element is made of, is imposed onto the geometrical volume,
- **creating a physical volume** - the logical volume is inserted in the 3D environment of the simulations, called "World".

This means that a physical volume cannot exist if three precedent steps are not provided. Obviously, separate parts of a complex system have to be organized in space in such a way

that they exactly represent the simulated case.

The magnet representation was introduced to Geant4 code from scratch by the author. This process has required massive time load due to the complexity of the magnet structure and spread of information in various data bases. The implementation of the magnet representation was based mainly on technical drawings (CERN Drawing Directory - CDD), the LHC Design Report and consultations with magnet and vacuum experts. Since the accelerator structure is very sophisticated, being built out of many complex-shape elements, a compromise between accuracy of the model and computing time had to be found. Although some simplifications were applied, the magnet representation was constructed in details. The introduced elements are listed below:

- **LHC tunnel**

a tunnel concrete floor, tunnel walls, cryogenic distribution line (QRL),

- **MQ ensemble**

a MQ cryostat, a vacuum vessel, thermal shielding, inertia tube (helium vessel), iron yoke (lamination), austenitic steel collars, superconducting coils (internal and external), endings of the coils with epoxy stabilizers, beam pipes (cold bores), beam screens, end plates, end flanges, internal epoxy connections, insulating washers, end caps, a simplified MQT magnet, a MSCBB yoke, MS laminations, MS shrinking rings, MS epoxy stabilizers, MS coils, MCB epoxy stabilizers, MCB coils,

- **MB ensemble**

a MB cryostat, a vacuum vessel, thermal shielding, inertia tube, iron yoke, austenitic steel collars, superconducting coils (internal and external), endings of the coils with epoxy stabilizers, beam pipes, beam screens, end plates, end flanges, a lyra side, end spacers, copper wedges, beam screen supports, MCS caps for magnetic shielding, MCS magnetic shielding, MCS clamps, a MCS cylinder, MCS laminations, MCS lamination slit tubes, MCS coils,

- **Interconnection between MQ and MB**

beam screens, nested bellows, a vacuum vessel, cooling tubes exits, asymmetrical conical clamps of a SSS side, upstream cooling tubes, asymmetrical conical clamps of a MB side, plug-in modules (PIN) of a SSS-MB side, beam pipes, thermal shielding, MQ end plates,

- **Interconnection between MB and MQ**

sliding bellows, a vacuum vessel, MB rotatable flanges, a MB lyra side, beam screens, downstream cooling tube exits, asymmetrical conical clamps, beam screen nested bellows, beam pipes, PIN modules of a MB-SSS, beam position monitors (BPMs), BPM supports, MQ end plates, beam screen supports,

- **Beam Loss Monitors**

two long pseudo-detectors along the entire "World".

Instead of simulating exact BLMs, it was decided to implement two long pseudo-detectors along magnet cryostat. Their horizontal and vertical positions are exactly the same as in the case of the physical BLMs. This solution provided information on the secondary particle radiation not only in the locations of the detectors installed in the LHC, but also beyond these regions. Therefore, thanks to the studies of 2010 experiments, it was possible to determine the most interesting places (regarding the maximum radiation or the steepest slope of the radiation distribution) where new mobile monitors should be mounted for 2013 Quench Tests.

Additionally, separate elements were defined to reconstruct complex shapes of the endings which are different than central parts (for example, superconducting coils). The characterization of media (vacuum, air, liquid helium), in which a certain element was immersed, was provided as well. The geometries of the sophisticated elements were approximated by simpler submodules resulting in introducing more than 1120 physical volumes to the Geant4 code.

3.3.4 Sensitive Detector

Applying the so-called "Sensitive Detector" (SD) allows particle energy deposition to be localized and measured. The idea behind this is based on specifying a shape of a virtual object which is subdivided into smaller pieces. The whole structure is incorporated onto a mechanical element (for example a part of a magnet) from which information (like deposited energy) should be acquired.

In the Geant4 simulations provided for Quench Test studies the SD grid was applied onto the MQ superconducting coils (only inner coils) since estimating the quench levels was the main objective of these studies. The sensitive volume was divided into 108 000 unit cells in the case of 2013 QT simulations and 81 000 recording unit cells regarding 2010 QT in order to obtain required resolution of determining deposited energy density. Fig. 3.2 shows steps of segmenting the coils - $\Delta z = 9.83$ mm, $\Delta\phi = 9^\circ$, $\Delta\rho = 3.85$ cm (2013 QT; $\Delta\rho = 5.13$ cm for 2010 QT). The binning was chosen so that the longitudinal dimension is much smaller than the nuclear interaction length¹. The transverse size was imposed in the way which allowed the energy deposition across a cable to be interpolated.

3.4 Strategy of simulating BLM signals

Besides assessing the energy deposited inside SC coils, it is also important to ensure a reference signal which could be compared to the measured observables from an experiment. In the case of the performed Quench Tests, the beam loss monitor data was used for validating the accuracy of simulations. Generally, there are two methods of estimating BLM signals in Monte Carlo simulations. The first one is based on direct scoring energy inside an ionization chamber which leads to generating the corresponding current. However, this method requires high statistics of simulated events and a complex representation of a detector has to be simulated

¹The nuclear interaction length in Nb is ≈ 18 cm, for Ti ≈ 28 cm and for Cu ≈ 15 cm.

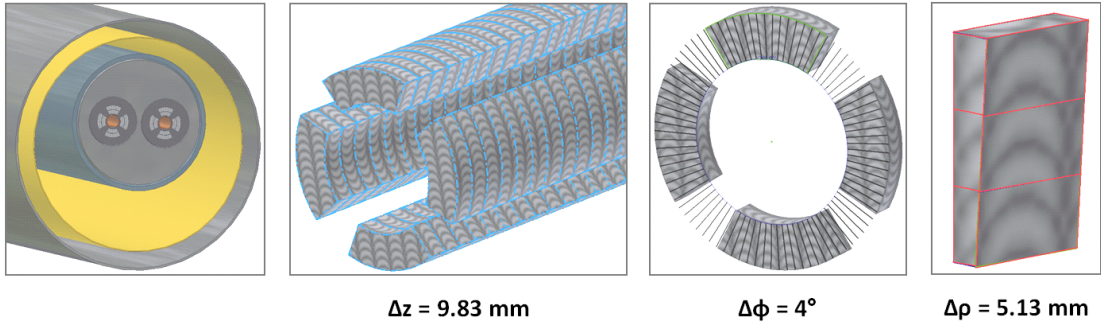


Figure 3.2 – Geant4 simulations. The very left picture shows cross-section of the implemented MQ representation. Other pictures: the segmentation of the MQ superconducting coil into 81 000 recording unit cells (for 2010 Quench Test, cell 14R2). Applied binning $n_z = 300$, $n_\phi = 90$, $n_\rho = 3$. Visualization was done in Autodesk Inventor based on the magnet representation introduced to the Geant4 code.

separately. The other solution, which was applied in these studies, relies on so-called response functions of the detectors. These functions were prepared for various particles, energies and impacting angles. In contrast to the previous solution, here signals are obtained faster with lower particle statistics. Moreover, it allows estimating the radiation dose relatively easy in any place outside a magnet system.

3.4.1 BLM response functions

A response of ionization chambers to various conditions (types of incoming particles, wide range of energies, various impacting angles) was studied in [115], [116], [117], [118], [119]. The main objective was estimating systematic errors coming from Geant4 simulations and validating the results using experimental data. The Geant4 BLM representation consisted of aluminum electrodes, connecting rods, plates (top, bottom and aluminum), an outer cylinder, insulators and an electronic box. The sensitive volume was imposed on a nitrogen gas (at 1.1 bar at temperature of 20°) which filled the space between the electrodes.

The total energy deposited in a detector is proportional to a number of particles, which cause the ionization of gas molecules when passing through the medium of the detector. This correlation was used to estimate the BLM detector response to the primary particle exposition. Every gas is characterized by so-called W -factor which specifies the energy needed to produce an ion-electron pair. In the case of nitrogen, $W=34.8\pm0.2$ eV. Only charges reaching the electrodes contribute to the generated signal. Thus, in the simulations the appropriate electric field map was implemented to recreate impact of bias voltage applied in the physical detectors. In addition, results of using two physics lists, QGSP and QGSP-BERT-HP, were compared.

The simulations were done in a wide range of energies of incoming particles - from 1 keV

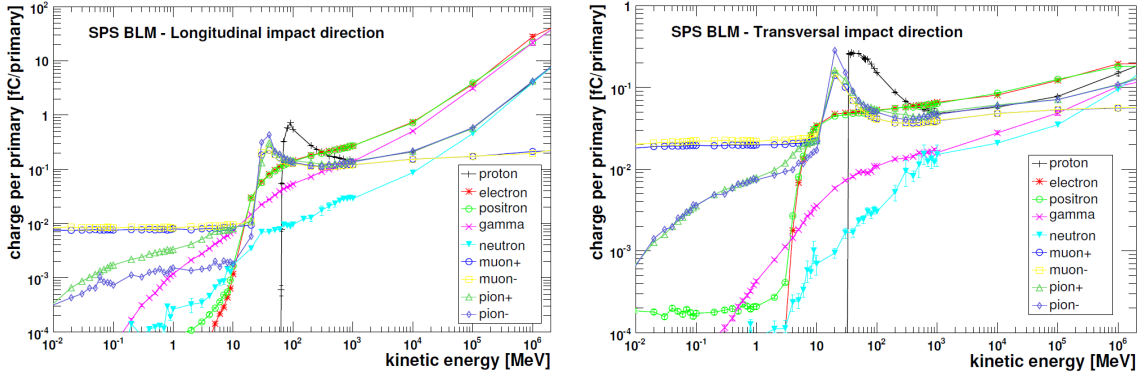


Figure 3.3 – BLM response functions based on Geant4 simulations [115]. Left plot: particle beam hit detector in the longitudinal plane. Right plot: particle beam hit detector in the transverse plane.

to 10 TeV with the statistics of 10^5 and 10^3 primary particles for low and high energy cases, correspondingly. An impact of p^+ , e^- , e^+ , γ , π^+ , π^- , μ^+ , μ^- and n was investigated.

Depending on an angle of an incoming beam, the wall thickness "seen" by the particles is different. These particles, which come with small angles, have to go through longer distance in the wall than those ones, which arrive with angles close to 90° . Therefore, the BLM response functions were provided for various particle impacting angles (see Appendix B).

Fig. 3.3 shows two BLM response functions depending on the particle distribution position: the results of the longitudinal impact direction is presented on the left and the transverse impact direction on the right. The factor of two in the signal amplitudes was explained by the difference in paths which the particles pass through (the BLM length was approximately a factor 2.4 larger than its width).

Although the BLM response functions were obtained for SPS BLMs, they can also be applied for LHC BLMs due to the similar designs of these detectors.

3.4.2 Contribution of secondary particles to the total BLM signal

Interactions of a primary particle beam with matter results in developing a secondary particle shower which propagates in all directions. However, only five response functions are available (0 deg, 15 deg, 30 deg, 60 deg, 90 deg) from the previous BLM studies. Using one response function for all incoming particles would result in incorrect results. Therefore, it was decided to apply a combination of all response functions with appropriate weights. In order to specify a contribution of certain response functions, for each BLM detector an angular distribution was provided.

The angular distribution represents a particle population as a function of angle at which a

particle reaches the detector. It is calculated using the following correlation:

$$\alpha = \arccos\left(\frac{p_z}{p_{total}}\right) = \arccos\left(\frac{p_z}{\sqrt{p_x^2 + p_y^2 + p_z^2}}\right). \quad (3.1)$$

Particle momenta in x, y, z - directions are given by p_x , p_y , p_z , correspondingly. The angular distributions (Fig. 3.4) with binning of 180 were divided into nine non-equal ranges. The border lines were chosen to be in the middle of the distances between two neighbouring values for which the response functions are known. Moreover, it was taken into account that particles coming with angle α are indistinguishable from particles coming with $(180^\circ - \alpha)$. Therefore, they are described by the same response functions. A contribution of each range to the BLM signal was introduced by calculating ratios of integrals over $(\alpha \pm \Delta\alpha)$ range to the total integral over entire range $(0, \pi)$ I_{total} :

$$w_i = \frac{I_{(\alpha \pm \Delta\alpha)}}{I_{total}} \quad (3.2)$$

The final simulated BLM signal is expressed in charges (in aC) collected on the detector electrode plates. It is derived by folding the particle fluences $N_{j,k}$ by the corresponding response functions $R_{i,j,k}$:

$$Q = \sum_{i=15^\circ, \dots, 165^\circ} \left(w_i \cdot \sum_{j=p, n, e^-, \gamma, \dots} \sum_k R_{i,j,k} N_{j,k} \right) \quad (3.3)$$

The first sum over i takes into account all available response functions for angles $i = 15^\circ, 30^\circ, 45^\circ, 60^\circ, 90^\circ, 120^\circ, 135^\circ, 150^\circ, 165^\circ$. The second sum is over all simulated particles, $j = p^+, \gamma, e^-, e^+, \pi^+, \pi^-, n$. The last component corresponds to k which is the energy range.

Physical BLMs return signals in Gy/s (see Section 1.6.3). In order to compare simulated values with the experimental data, signals have to be converted to Gy using :

$$S_{BLM}[\text{Gy}] = Q[\text{aC}] \cdot \frac{10^{-18}}{5.4 \cdot 10^{-5} [\text{C Gy}^{-1}]} \quad (3.4)$$

Value of $5.4 \cdot 10^{-5}$ was calculated for N_2 gas using the W -factor equal 34.8 eV. The dose absorbed by the detector (in Gy) can be obtained by multiplying S_{BLM} by a loss duration (specific BLM integration time, RS).

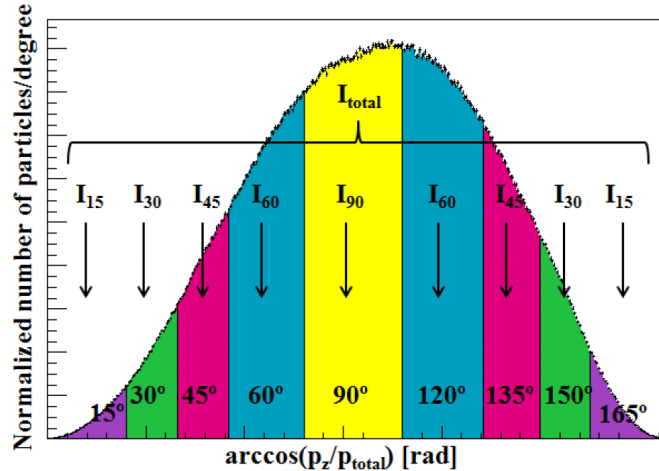


Figure 3.4 – Angular distribution - calculating contributions of available response functions. Description in the text.

3.5 Strategy of determining loss patterns

The main objective of performing Geant4 simulations of the Quench Tests is estimating quench levels of the LHC superconducting magnets. The general procedure of correlating BLM signals with energy deposition inside the superconducting coils consists of two main stages:

1. Geant4 simulation level

- (a) Inputs:
 - i. representation of the LHC arc half-cell where the experiment was performed (14R2 in the case of 2010 QTs and 12L6 in the case of 2013 QTs),
 - ii. experimental conditions (particle type, beam energy, beam impacting angle, the magnetic fields in the magnets),
- (b) Outputs: a ROOT file including information on:
 - i. energy deposition inside SC coils (with resolution depending on the coil binning),
 - ii. characterization of the secondary particle shower reaching two long pseudo-detectors located outside the magnet cryostats - information on a particle type, particle energy, particle moment and a population of specific particles.

2. ROOT analysis level

- (a) Inputs:
 - i. ROOT file
 - ii. experimental observables (beam intensity, BLM signals, a loss duration)

- iii. BLM response functions
- (b) Data processing:
 - i. creating a 3D histogram of energy deposited inside the coil,
 - ii. creating around 91 histograms with energy spectra (for each BLM, seven histograms of different secondary particles spectra are provided),
 - iii. creating 13 histograms with angular distributions for each BLM,
 - iv. calculating contributions of various angle ranges of incoming particles to the total signals of all BLMs (Fig. 3.4),
 - v. weighting energy spectra proportionally to the previously calculated coefficients,
 - vi. folding energy spectra with the corresponding response functions.
- (c) Outputs: a ROOT file including information on:
 - i. the final BLM signals in Gy
 - ii. a longitudinal energy density distribution along a cell where maximum value was recorded
 - iii. a radial energy deposition distribution for the most exposed bin; this function is later used as an input to the QP3 heat transfer code
 - iv. simulation validation in the form of a plot presenting ratio between measured and simulated BLM signals
 - v. a value of the normalized simulation-experiment similarity estimator (see Eq. 3.5)

Experimental methods allow many parameters (incoming particle angle, radiation outside magnet cryostats, moment of quenching, loss duration, beam size, etc.) to be precisely measured. However, a loss pattern, i.e. distribution of particles deposited on an aperture limitation (beam screen) along z -axis remains unknown. In 2010, when the first Quench Test at 3.5 TeV was done, there were no available techniques to deduce how the beam was lost. Therefore, it was decided to simulate many (70-80) point-like losses along targeted magnets (in steps of 0.1 m) and weighting results with calculated coefficients corresponding to an assumed loss pattern. This provided flexibility of considering various loss scenarios without necessity of repeating the very time-consuming simulation process.

In order to efficiently find the best fitting (to measured observables) case, an algorithm with a working name Geanto-Quencho-Meter (GQM) was developed by the author. The idea behind it was as follows:

- Since a particle beam has the Gaussian shape, a projection of losses onto a beam screen would also have Gaussian-like distribution².

²During the quench tests, a significant part of the beam was lost on the magnet aperture. Therefore, the Gaussian distribution could be applied in the Geant4 simulations. However, this approach is not valid in the case of a beam halo.

- Strong focusing forces act on charged particles inside quadrupoles. Thus, the loss pattern can possess an asymmetry.
- Weights are calculated for all simulated loss locations depending on an assumed loss scenario; a sum of all coefficients is equal 1.
- All histograms (particle spectra for all BLMs, energy deposition in coils, angular distribution for each BLM, etc.) are summed up with appropriate weights.
- Particle spectra are folded with the response functions (depending on angular contribution).
- BLM signals are calculated.
- For each considered loss scenario, a normalized simulation-experiment similarity estimator is calculated $\Sigma_{\mu, \sigma_r, \sigma_l}^{norm}$. This parameter expresses a comparison of n measured BLM signals BLM_i^{meas} with simulated values BLM_i^{sim} and is defined as

$$\Sigma_{\mu, \sigma_r, \sigma_l}^{norm} = \sum_{i=1}^n \left(\frac{BLM_i^{sim} - BLM_i^{exp}}{BLM_i^{sim}} \right)^2 \quad (3.5)$$

Index μ refers to a position of the maximum of the Gaussian distribution, σ_r and σ_l are size of the right and left half-Gaussians, correspondingly. The number of BLMs depends on the locations where the experiments were done: $n=6$ for cell 14R2 and $n=13$ for cell 12L6. The smaller $\Sigma_{\mu, \sigma_r, \sigma_l}^{norm}$, the better agreement between the measured and simulated values is obtained.

- The program searches for the minimum value of $\Sigma_{\mu, \sigma_r, \sigma_l}^{norm}$ in the specified ranges of $(\mu, \sigma_r$ and $\sigma_l)$. This value estimates the best fitting loss pattern.

Additionally, an option of introducing defined loss pattern was introduced to the GQM. This allows, for example, results of orbit simulations (MAD-X) to be directly used without affecting Geant4 files.

A typical distribution of normalized simulation-experiment similarity estimators as a function of μ for the symmetric case ($\sigma_r = \sigma_l$) is given in Fig. 3.5. In this case (based on 2010 QT data) the best fitting results would be obtained for the loss scenario with $\mu = 0.5$ m from the center of MQ.14R2. The changes of $\Sigma_{\mu, \sigma_r, \sigma_l}^{norm}$ as a function of σ_r and σ_l for a fixed μ can be seen in Fig. 5.15.

It has to be stressed, that although the presented method was developed in order to reduce simulation time (i.e. not simulating every assumed loss scenario separately), the process is very time-consuming. Simulating a single loss location with the statistics of around 2500 events (corresponding to single primary protons) takes around 4 days using lxbatch cluster (CERN). In parallel four different simulations can be run which gives around 70 days of continuous

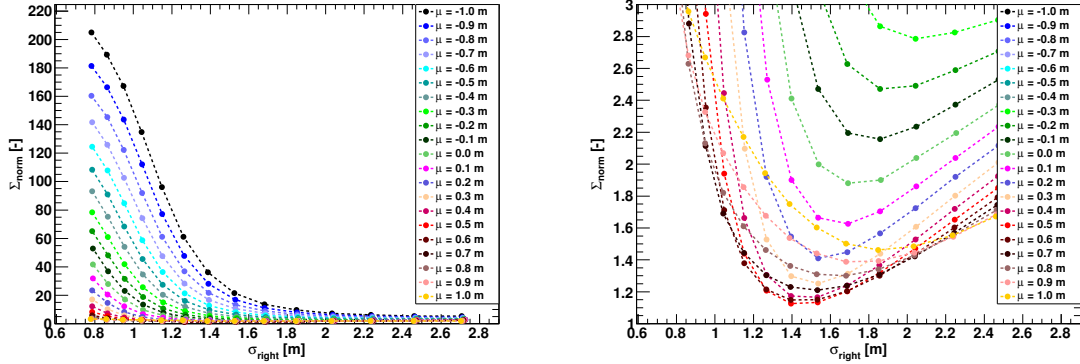


Figure 3.5 – A distribution of normalized simulation-experiment similarity estimators as a function of a location of the maximum Gaussian shape. Data of 2010 QT are presented assuming a symmetrical distribution of lost protons.

simulations in total. Since simulations are terminated after 140-200 events, they cannot be sent to lxbatch in a single step but have to be spread over 20-30 lower statistics cases. Different random seeds were used to assure that the various simulated samples were not biased. Before using GQM all files of single loss locations were checked and faulty assigned data was rejected. Creating around 105 histograms takes around 16 s. Taking into account 2500 events per loss location, it gives 40 000 s, i.e. more than 11 hours per loss location. Having 70 loss location, the total pre-analysis takes 32 days if done in row. The final stage of data analysis with final (70-80) files takes from around 10 minutes (in the case of using pre-defined loss pattern) to several tens hours (in the case of searching for the best fitting loss pattern; depending on number of considered scenarios).

3.6 Error origins

Although the Geant4 simulations were supposed to be done in the way so that the experimental conditions were recreated, there are several probable origins of errors.

- Material definition

The complex structures were approximated by a pseudo-material which density was calculated from the percentage contributions of their components. For example, the MQ superconducting coils were implemented in the form of uniform material (no "cable in helium bath"-structure). This material consisted of Cu (62.80%), Ti (15.13%), Nb (17.07%) and He (5%). The calculated weighted density was around 7.78 g/cm^{-3} .

- Geometry

Certain simplifications were applied in order to reduce simulation running time. All major elements are implemented but small elements (like screws) were neglected.

- Response functions

Currently (summer 2013) there are no response functions which would cover entire the angle range ($0^\circ, 360^\circ$). The proposed solution for calculating contributions of all available data sets seems to be the best possible option. However, it is still a subject of error origin.

- Simulating point-like losses

As it was already mentioned, the strategy of simulating many point-like losses was applied in order to limit very time consuming simulations. In other words, the idea was to possess a set of data which later can be quickly used for various loss scenarios. The step between neighbouring simulated loss locations is $\Delta z = 0.1$ m, which is less than the average distance between two nuclear interactions (≈ 0.15 m) in typical metals (Fe, Cu)[14]. Nevertheless, no transverse particle beam distribution is considered in these studies.

- Secondary particle cut-off

In the Geant4 simulation 1 mm long cut off was applied regarding secondary particle production. It was done in order to limit CPU time needed for tracking particles which have too little energy to cause producing new secondaries. Nevertheless, it was found to be important statistically [95]. In addition, all particle trackings were stopped in the case of reaching the longitudinal positions: $z < -7$ m and $z > +7$ m with respect to the MQ centre. Neither BLMs nor other sensitive volumes are located outside these limits.

3.7 Summary of the Geant4 simulation strategy

The summary of the assessing quench levels and the corresponding BLM signals when using Geant4 simulations is presented in Fig. 3.6. The core of the simulations contains the magnet representation (the LHC Design Report, technical drawings, specifications), the magnetic field maps (ROXIE) and the choice of the adequate physics processes. The experiment is simulated by introducing a specific particle type, its energy, impacting angle, position and the orientation of beam losses. Imposing a loss pattern (either simulated in MAD-X or found relying on defined assumptions) allows obtaining energy deposited inside a superconducting coil. In order to calculate a quench level, the number of particles lost during the test has to be taken into account. Combining energy spectra of secondary particles outside magnet cryostats with monitor response functions gives the final BLM signals. These values can be compared to the measured observables, which allows validating the accuracy of obtained quench levels.

The presented algorithm of performing Geant4 simulations was tested considering a simple, infinitely long MB magnet (interconnection regions omitted) [95]. Later, it was decided to extend the studies to the case of much shorter MQ magnet with the interconnections MB-SSS and SSS-MB.

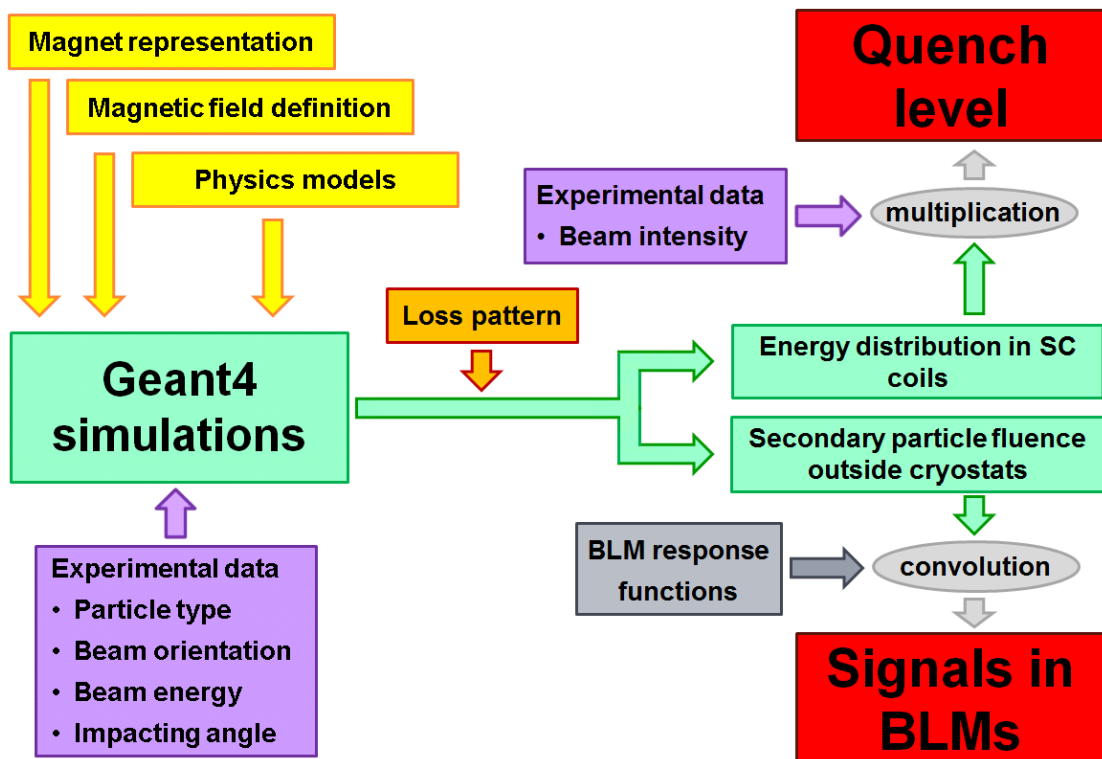


Figure 3.6 – Diagram of the Geant4 simulation strategy. Description in the text.

4 4 TeV Fast Loss Quench Test 2013

4.1 Motivation

The fast beam losses in the order of 1 ms are expected to be a potential major luminosity limitation for higher beam energies (6.5 TeV - 7.0 TeV) after LHC Long Shutdown 1 (LS1). Therefore studying quench behaviour at the nominal energy of 4 TeV in the UFO loss (see Section 1.7.3) regime was the main motivation for this experiment. Assessment of the superconducting coil quench level would allow the current theoretical models to be revised, following the BLM thresholds to be recalculated. These updates would ensure still safe LHC operation together with reducing a number of undesired beam dumps caused by the UFO events.

4.2 Preparation to the Quench Test

The preparation of the Quench Test started in early 2012, shortly after it was suggested to conduct a series of meetings devoted to a knowledge transfer between experts from the Superconducting Magnet Design and Technology (MDT) section, the BLM team, the QPS team, the Collimation section and the Machine Protection Panel (MPP). During six meetings of the Quench Test Strategy Working Group (QTSWG)[120], the results of previous experiments were carefully discussed in order to plan the Quench Test slot in the end of LHC run (February 2013).

Fast Loss Quench Tests could not be done any more using the Wire Scanner (see Section 2.2.1), as in November 2010, due to its location in the vicinity of the MRRB magnet (see Section 2.2.2). Thus, a new method of inducing losses in the order of milliseconds was needed to be found. It was proposed to use the LHC Transverse Damper (ADT, see Section 1.8.2) in a non-standard operation mode. The idea behind this was to create and amplify beam oscillations instead of reducing them. Between March 2012 and January 2013, a series of experiments were conducted to determine the ADT potentials and limitations. They are presented in Sections 4.3-4.7 and the final quench test is described in Section 4.8.

4.3 ADT Fast Loss Test at 450 GeV (26.03.2012)

The main aim of the experiment done on 26.03.2012 was to study the ADT as a system for inducing the fast losses in the order of one millisecond. Two ADT modes, the coherent excitation and the sign flip mode, were tested using proton pilot bunches at 450 GeV to characterize beam loss properties, i.e. the temporal loss shape and the loss duration. The beam was manipulated in such a way that the losses occurred on the LHC collimators. Therefore, the test was safe in terms of the machine protection.

A comparison of the losses and beam oscillations resulting from testing different ADT modes is given in Fig. 4.1. The experiment showed that the most adequate results for the final quench test were obtained when using the ADT sign flip method at the maximum gain. The smallest amount of initial losses, i.e. the losses occurring before the peak value, indicates the possibility of having a very short deposition of the primary particles onto the aperture. Moreover, the BPM (Beam Position Monitor) measurement analysis (Fig. 4.1, right plot) revealed that the beam amplitude rose the most regularly during this excitation. The shortest losses were obtained within six LHC turns ($\sim 550 \mu\text{s}$) at the injection energy which proved this method to be a good option for the UFO-like loss studies. Nevertheless, due to the fact that the higher the beam energy is, the more rigid the beam becomes, additional investigations were required to determine the ADT-induced loss duration at the nominal energy (4 TeV).

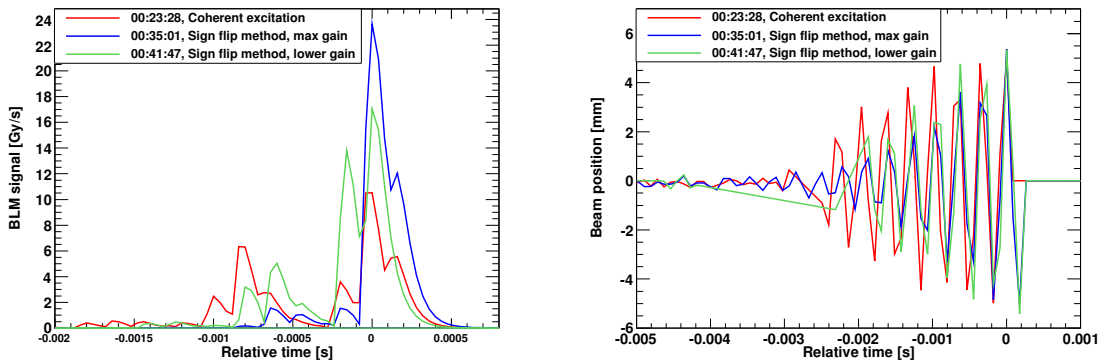


Figure 4.1 – Results of the ADT preparation test (26.03.2012). Left plot: the temporal loss distributions obtained using different ADT modes. The ADT sign flip mode at the maximum gain (blue line) provides the smallest amount of initial losses - losses occurring before the highest peak. Right plot: the beam transverse oscillations as a function of time. The most steady and close to linear increase of the beam amplitudes was observed when exciting the beam with the sign flip mode at the maximum gain. Zero in the time axis corresponds to the moment when the maximum value in BLM or BPM measurements was reached.

4.4 ADT Fast Loss Test at 450 GeV and 4 TeV (22.06.2012)

The second experiment, devoted to the preparation of the final Quench Test, was focused on the following aspects:

- Creating the conditions of the fast (~ 1 ms) proton beam losses which were the most similar to the Quench Test foreseen in winter 2013 (before LS1) at 4 TeV
- Studying the ADT system as a tool for inducing fast beam losses
- Investigating the impact of the phase advance between the source of losses (the transverse dampers) and the targets (the primary collimators)

The test was based on exciting a proton beam by the ADT and observing induced losses on the LHC primary collimators. In order to provide beam losses only on one side of the aperture, the collimator jaws were set asymmetrically. The tests were done at injection and nominal energies considering various combinations of beams and excitation planes, for instance: beam 1 excited in the horizontal plane.

During the first part of the MD, pilot bunches were individually excited in one plane using 100% of the ADT gain. Beam behaviour and loss properties were studied in order to find the most optimal configuration to be applied during the Quench Test 2013. There were three the most significant parameters determining this:

- a beam loss duration (the shortest losses are preferable),
- a beam loss amplitude (with respect to amplitudes of the initial losses occurring before the maximum value; the higher the better),
- beam loss confinement (losses should not occur beyond the targeted region).

Based on the criteria given above, beam 2 excited in the horizontal plane (B2H) was chosen to be the most suitable candidate (Fig. 4.2) compromising the required features. Specifically, this was due to the fact that among other configurations (beam 1/beam 2-horizontal/vertical plane) in this case the highest beam position amplitude was achieved and the maximum loss velocity occurred. Although the loss duration was shorter when exciting beam 1 in the vertical plane (B1V) than beam 2 in the horizontal plane, this option was disqualified due to other low parameters. The efficiency of exciting a beam in a specific plane depends on a physical condition of the corresponding ADT amplifiers (four amplifiers per beam and per plane) and the β -function at the location of the ADT [121].

A sufficiently high beam distortion from the ideal orbit results in particle losses which are measured by BLMs. A correspondence between beam oscillations and temporal loss pattern is important in understanding the processes of propagating a secondary particle shower through a magnet system. Since BLMs record data every $40\ \mu s$ and BPMs deliver signals every LHC revolution ($89\ \mu s$), these two systems are not synchronized in time. First of all, in order to

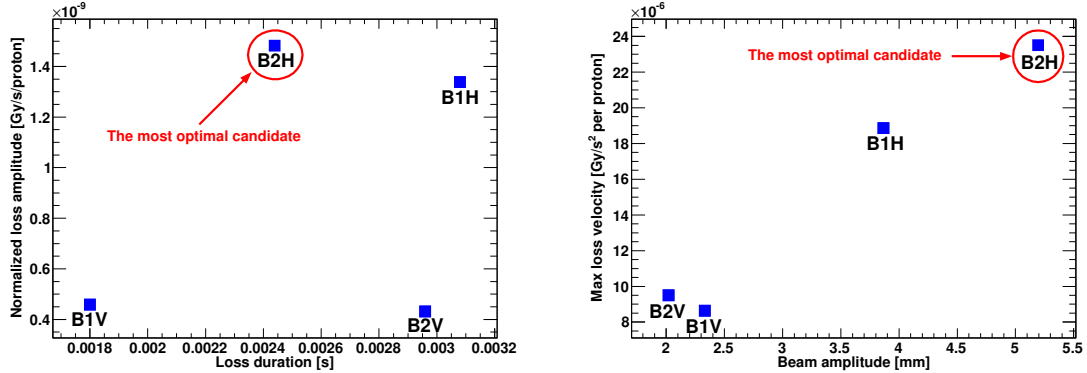


Figure 4.2 – Final results of the 450 GeV ADT Fast Loss Test (22.06.2012). Four cases are presented considering both beams (beam 1/beam 2) and both excitation planes (horizontal/vertical). During the experiment individual bunches were affected in only one plane. B1H denotes beam 1 excited in the horizontal plane, B2V - beam 2 excited in the vertical plane etc. A superposition of desired beam and loss properties determined B2H to be the optimal candidate for the future Quench Test.

arrange the corresponding measurement points, the number of BLM records was reduced to the number of BPM data. These BLM points were selected which occurred the closest in the timescale to the BPM points (details are presented in [122]). There are several criteria of adjusting measurements on the same timescale. The most common method uses the moment of the beam dump. Nevertheless, in the case when no dump occurs, the synchronization based on the correlation coefficient can be applied[122]. If x_{BPM_i} and y_{BLM_i} are measured values, \bar{x}_{BPM} and \bar{y}_{BLM} are the means of the respective BPM and BLM samples, the correlation coefficient can be written as [123]

$$r_{x_{BPM}, y_{BLM}} = \frac{\sum_{i=1}^n (x_{BPM_i} - \bar{x}_{BPM})(y_{BLM_i} - \bar{y}_{BLM})}{\sqrt{\sum_{i=1}^n (x_{BPM_i} - \bar{x}_{BPM})^2 (y_{BLM_i} - \bar{y}_{BLM})^2}} \quad (4.1)$$

A value of $r_{x_{BPM}, y_{BLM}}$ is bounded in the range of (-1,1) and its sign determines a type of correlation. The positive one ($r_{x_{BPM}, y_{BLM}}=1$) has a meaning of increasing linear relationship between variables and the negative one ($r_{x_{BPM}, y_{BLM}}=-1$) represents a decreasing linear dependency. If the considered signals were independent of each other, then the correlation coefficient would be equal zero ($r_{x_{BPM}, y_{BLM}}=0$). Probing various shifts (multiplications of LHC half-turns, i.e. 44.5 μ s) between the BLM and BPM signals ensures finding the most linear (synchronized) configuration, i.e. $r_{x_{BPM}, y_{BLM}}$ reaching the value which is the closest to 1. Fig. 4.3 presents the correspondence between the BLM (blue line) and BPM (red line) signals for 4 TeV B2H at the location of BPM.6R7.B2 obtained when exciting the beam with 200% ADT gain. The beam oscillation amplitudes reflect in the radiation peaks above certain threshold. However, in the final stage only the BLM signal can be observed. This is due to the beam intensity decay in time and BPM sensitivity which lower limit is around $5 \cdot 10^7$ protons at 450 GeV [83].

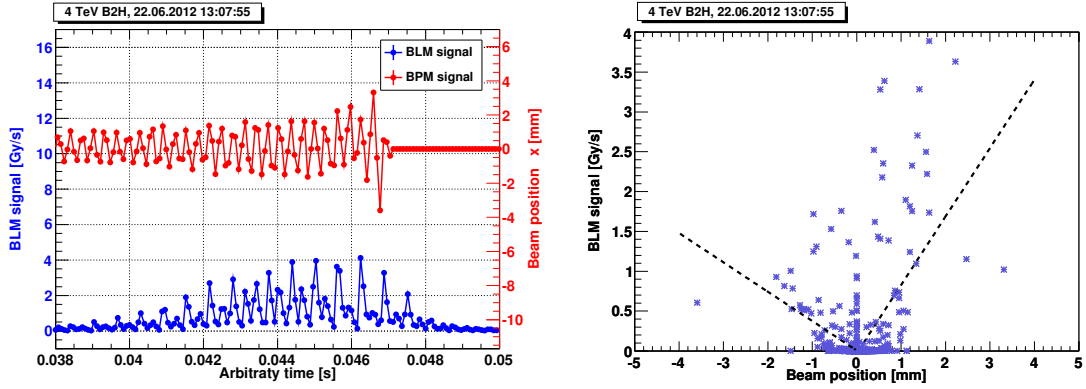


Figure 4.3 – Correspondence between the beam oscillations induced by the ADT sign flip mode at 200% gain (the red curve) and the radiation dose measured by the BLM (the blue curve). The synchronization between BPM and BLM systems based on finding the maximum of $r_{x_{BPM}, y_{BLM}}$ (nine turn shift with respect to the synchronization based on fitting to the signal maxima). The dotted lines represent linear fit functions for the positive ($x_{BPM} > 0$) and negative ($x_{BPM} < 0$) beam position measurements.

It was already mentioned that the higher the beam energy is, the more rigid and difficult to manipulate it becomes. Fig. 4.4 shows the beam positions when applying the ADT sign flip excitation for the cases of injection and nominal energies. Although the 4 TeV beam was treated with four times larger ADT gain than the 450 GeV beam, it is characterized by amplitudes approximately twice as small. The rise time, i.e. the parameter characterizing a response of a system to a time-dependent input, was calculated using

$$x_{beam}(t) = Ae^{\frac{t}{\tau}} + b \quad (4.2)$$

where $x_{beam}(t)$ is a beam transverse position, A (p1) and b (p2) are the fit parameters. The parameter b has the meaning of the beam position offset. During the excitations, the time constants reached values $\tau_{450\text{GeV}} = (2.50 \pm 0.01) \cdot 10^{-3}$ s and $\tau_{4\text{TeV}} = (6.30 \pm 0.03) \cdot 10^{-3}$ s for the cases of 450 GeV and 4 TeV beams, respectively.

The induced beam losses on collimators were compared to the losses created during the Wire Scanner Quench Test and three UFO losses (Fig. 4.5 and Fig. 4.6). The Transverse Damper provided around 7.5 times faster losses with respect to the WS operating at the wire velocity of $5 \frac{\text{cm}}{\text{s}}^1$. Nevertheless, the loss duration was still approximately one order of magnitude greater than UFO-induced losses. Based on integrated signals, it was found that a certain region in the case of the ADT-induced losses could be steep enough to correspond to the UFOs.

¹Obviously, the wire movement to $10 \frac{\text{cm}}{\text{s}}$ would significantly reduce the loss duration. A repetition of this test was proposed with greater beam intensity what could result in magnet quenching within about 1 ms. However, due to the risk of quenching the MBRB this experiment was not performed.

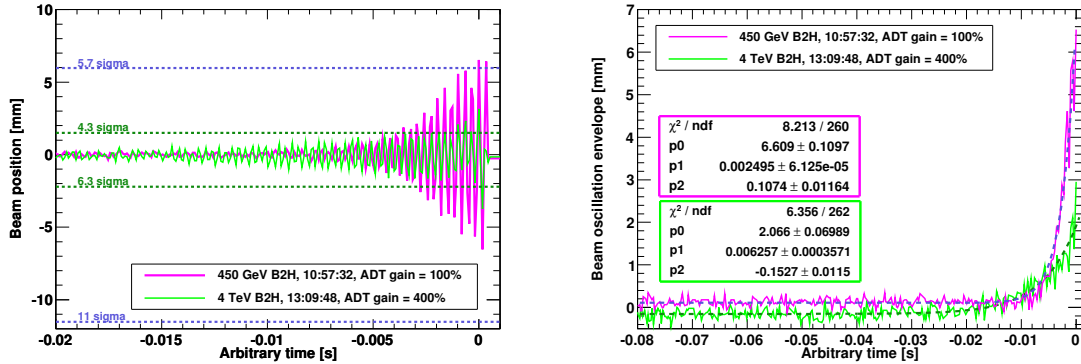


Figure 4.4 – Beam stiffness increase with energy (22.06.2012). The 450 GeV beam (magenta line) was treated with 100% of the ADT gain. In the case of the 4 TeV beam, 400% of the ADT gain was applied. BPM signals measured at the location of BPM.6R7.B2. Left plot: positions of the collimator jaws (TCP.C6R7.B2) are marked with dotted lines (450 GeV - purple line, 4 TeV - dark green line). Right plot: estimation of the time constants - beam envelopes fitted to the exponential functions.

The detailed proceedings and data analysis of the ADT Fast Loss Tests are presented in [124], [125] and [122].

4.5 ADT combined with MKQ Fast Loss Test (13.10.2012)

Although the ADT-induced losses were determined to be 7-8 millisecond long when loosing the beam on the collimators, it was expected that losses might be longer when depositing a beam on quadrupoles. This results from the strong focusing magnetic field acting on charged particles in the direction of the aperture centre. Therefore it was decided to apply a combination of two systems. ADT-induced beam oscillations were built on top of an initial

Table 4.1 – Summary of fast losses in the LHC. Complementary data for Fig. 4.5 and Fig. 4.7.

Name (loss origin)	Date	Beam energy	Beam	Plane	BLM monitor
ADT	2012-06-22 13:09:48	4 TeV	2	horizontal	BLMEI.06R7.B2I10_TCP.C6R7
WS	2010-11-01 15:40:03	3.5 TeV	2	horizontal	BLMEI.05L4.B2E10_MBRB
UFO1	2012-05-13 15:03:20	4 TeV	2	unknown	BLMQI.32L2.B2I20_MQ
UFO2	2012-08-03 06:28:57	4 TeV	1	unknown	BLMEI.05L2.B1E20_MKI.C5L2
UFO3	2010-08-23 13:50:38	3.5 TeV	2	unknown	BLMQI.22R3.B2E10_MQ
ADT+MKQ	2012-10-13 06:30:30	4 TeV	2	horizontal	BLMEI.06R7.B2I10_TCP.C6R7

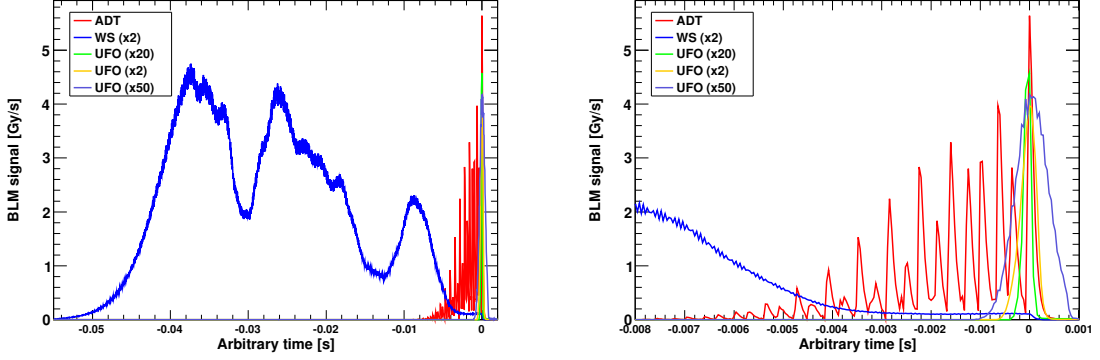


Figure 4.5 – Temporal loss distribution at 4 TeV. The UFOs are characterized by around 1 ms long Gaussian-like losses (green, yellow and bright blue lines). The ADT-induced losses posses a complex structure in the form of spikes and gaps in between (red line). The dark blue line represents losses measured during the WS Quench Test. Detailed information about the presented losses is given in Table 4.1.

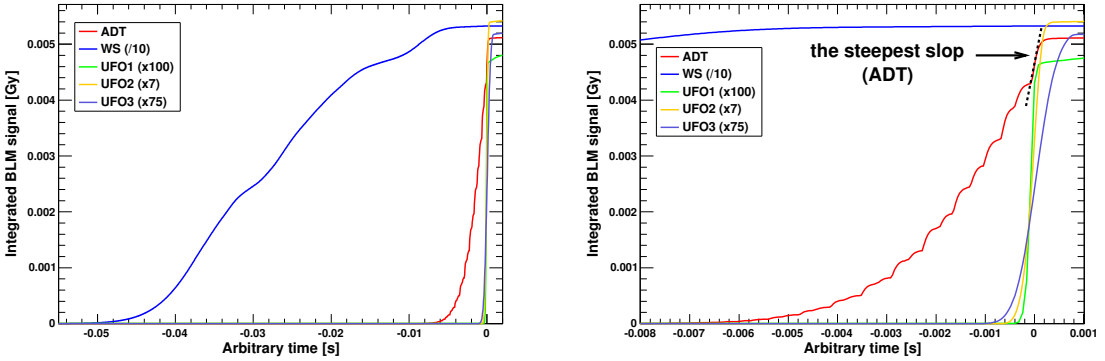


Figure 4.6 – Not instantaneous but integrated losses determine quenching of superconducting magnet coils. Here the integrated BLM signals from Fig. 4.5 are presented. A narrow range of the integrated ADT-induced losses overlaps with the slope of the UFO-induced losses.

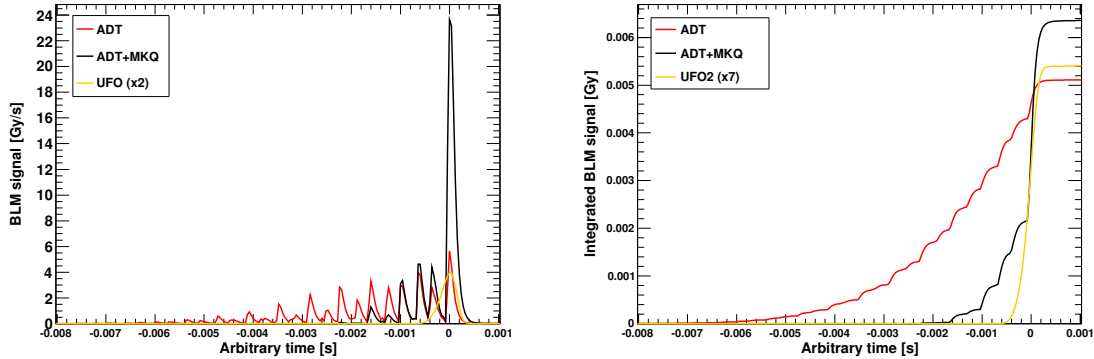


Figure 4.7 – Losses on the primary collimator TCP in the case of using only the ADT (red curve) and the combination of the ADT and the MKQ forces (black curve). The UFO-induced losses are represented by the yellow line. Detailed information about the presented losses is given in Table 4.1.

deflection of a beam trajectory provided by the tune kicker (MKQ). Although the MKQ effect on a beam was very small, it allowed specifying the exact moment for ADT to start the excitations. In addition, during the experiment the ADT excitation time window was increased in order to achieve faster beam losses. Thanks to the introduced modifications, the losses on collimators were created in the timescale of 2-3 milliseconds at 4 TeV Fig. 4.7.

The proceedings of the experiment are given in [126].

4.6 Installing the additional equipment

Fast Loss Quench Test 2013 required facing many challenges not only in terms of inducing 1 millisecond losses but also in dealing with very low intensity bunches (10^8 particles). In order to increase the spatial resolution of radiation measurements, seven additional beam loss monitors were installed in the close vicinity of MQ.12L6 in December 2012. This also allowed the beam loss pattern to be better estimated. Fig. 4.8 presents a diagram of the LHC region where the Quench Test was planned. The gray bar represents the Main Quadrupole (MQ) between two Main Dipoles (MBs, the blue bars). All arc quadrupoles are equipped with six standard BLMs (the yellow bars) - three of them survey losses originating from beam 1, three others register losses coming from beam 2. In addition, seven mobile monitors were located on beam 2 side (here, the internal part of the LHC ring). They are represented by the orange rectangles. Moreover, a diamond detector (the green bar) was attached to an ionization chamber at the end of MQ cryostat. Just before the Quench Test it was connected to a QPS oscilloscope to provide a synchronization between BLM and QPS systems². Pictures

²A synchronization between BLM and QPS systems is extremely important for understanding a development of quenching superconductor. The applied solution was expected to ensure this in the order of nanoseconds.

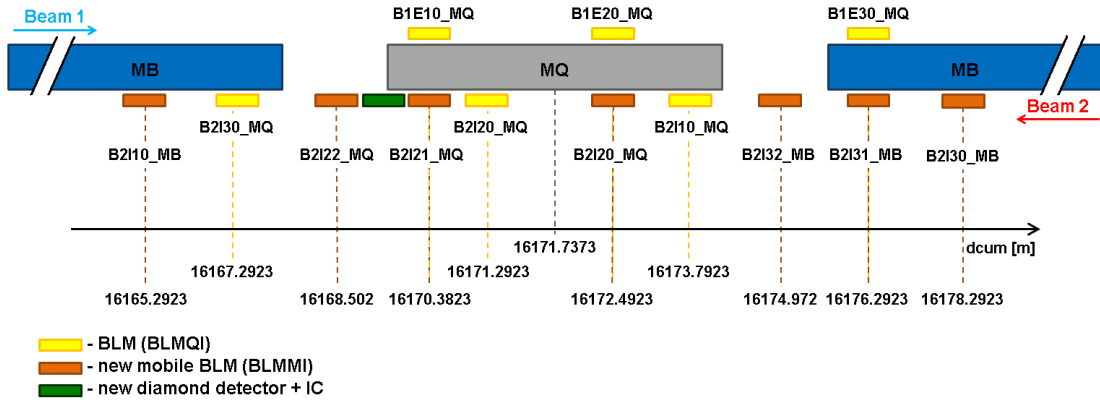


Figure 4.8 – Diagram of the LHC region where the Quench Tests were performed in 2013. The gray bar represents the Main Quadrupole (MQ). The Main Dipoles (MBs, the blue bars) are located on both sides of the MQ. Besides six standard Beam Loss Monitors (BLMs, the yellow bars), seven additional mobile monitors (the orange bars) were installed on the internal part of the LHC ring. The diamond detector was attached to the ionization chamber (the green bar) close to the end of the MQ. In the LHC 12L6 half cell, beam 1 travels in the external magnet aperture and beam 2 in the internal one. Dcum is the cumulative distance from Interaction Point 1, i.e. in the middle of ATLAS experiment.

of the LHC tunnel before the intervention are shown in Fig. 4.9. The final location of the mobile BLMs is presented in Fig. 4.10. The positions of the new monitors were established based on the results of the Steady State Quench Test performed in 2010 and Geant4 studies (longitudinal distribution of the secondary particle shower, Chapter 5). Movable stands (metal rods) were applied to ensure exact both, longitudinal, vertical and horizontal arrangement of all components - the mobile monitors were positioned on the same altitude as standard BLM and as close to the cryostats as possible.

4.7 ADT setting test (30.01.2013)

The last of the preparation tests was performed at 450 GeV two weeks before the final Quench Test and was devoted to setting the ADT to "ultra low intensity" parameters. This was required due to the operation with 10^8 proton bunches. The standard LHC BPMs cannot measure displacements of such low intensity bunches. Therefore the ADT pick-ups were used. This test was repeated just before the final experiment in order to estimate calibration of the ADT pick-ups' measurements with respect to those provided by the BPMs.

Moreover, the timing tables were prepared and tested at injection energy using $\approx 1 \cdot 10^9$ protons bunches. These tables are used in order to activate operation of various LHC systems which require accurate synchronization with an initial event. This involves mainly beam

However, during the experiment a communication with the scope was lost and no data could be recorded.

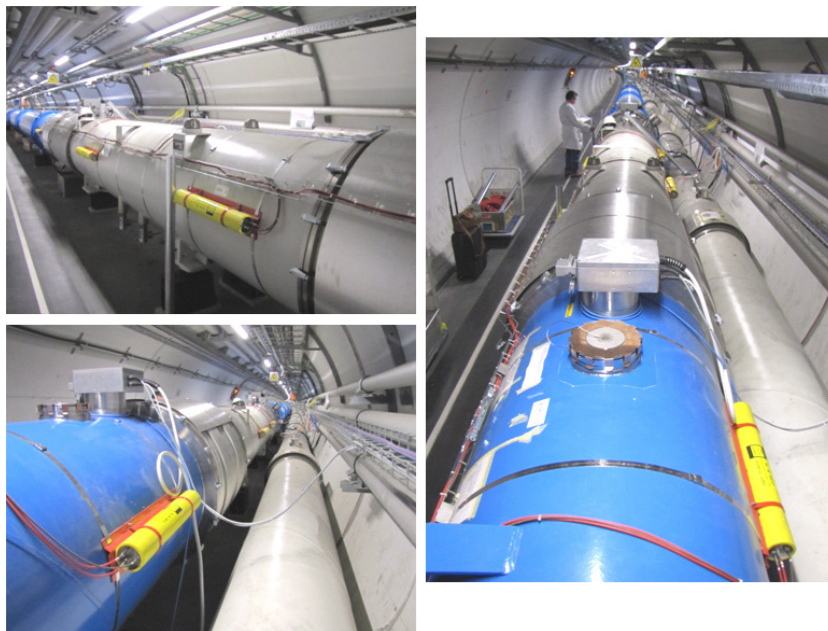


Figure 4.9 – Pictures of MQ.12L6 and its vicinity before the installation of the mobile monitors (Versonnex, France, December 2012).



Figure 4.10 – Pictures of MQ.12L6 and its vicinity after the installation of the mobile monitors. The mobile monitors were attached to the metal stands. The red arrow indicates the location of the diamond detector which was later connected to the QPS scope (Versonnex, France, December 2012).

manipulation and measurements. Since Post Mortem data is only saved when a beam dump is triggered, the BLM Study Buffer was used to obtain $80\ \mu\text{s}$ resolution BLM signal records. This synchronization with a MKQ kick and an ADT excitation is extremely important since the buffer length is limited to only 350 ms and missing this time window would result in loosing experimental data.

During the final part of this test, the connection of the new mobile monitors to the data acquisition systems was checked as well. In order to register BLM signals, a small bump with the amplitude of 15 mm was created on MQ.12L6.

4.8 Description of the Fast Loss Quench Test

Before the Quench Test special machine settings were applied in order to allow imposing the non-standard environment, i.e. beam distortions, increased BLM signals, opened collimators etc. This operation included:

- deactivating the ADT,
- setting BLM thresholds to the electronic maximum (23 Gy/s),
- masking BLMs on collimators, masking IR6 BPM interlock,
- setting the Safe Beam Flag³ to the relaxing settings,
- masking the collimation interlock, setting high resolution FBCT data acquisition.

Ten bunches with intensities of $(4 - 6) \cdot 10^9$ protons were injected from the SPS to the LHC (Fig. 4.11). They were separated by at least $5\ \mu\text{s}$ to ensure that protons from only a single bunch would be used during the final excitation (Injection Scheme⁴ Single_12b_8_8_8). Then, the beam energy was ramped up from 450 GeV to the nominal value of 4 TeV. The octupoles were set to zero and the chromaticity was decreased below 5 units providing the machine operation as linear as possible. This was required in order to reduce natural beam oscillation damping and reduce couplings between the horizontal and vertical planes[129]. A dynamic three corrector orbit bump on the Main Quadrupole in LHC half cell 12L6 was created in the horizontal plane. Its amplitude was increased until it reached the value of 21.61 mm when the losses were observed. In order to control a further bunch intensity reduction, the bump was decreased by 2 mm. This was followed by beam scrapping on the horizontal collimators which resulted in the bunch intensity decrease to about $(1.4 - 2) \cdot 10^9$ protons. The ADT was set to the "ultra low intensity" mode enabling operation with very low intensity bunches. Moreover, the horizontal and skew collimators were open to avoid any beam losses there. Based on the theoretical models, it was expected that several 10^8 protons at nominal energy are needed to induce magnet quenching. Therefore a single bunch was gated and slowly blown up in the

³The Safe Beam Flag (SBF) is the LHC setting mode when beam parameters are below the damage level. During an operation with SBF not all protection devices are necessary. The conditions for SFB depends on beam energy and beam intensities [127].

⁴According to the nomenclature of filling schemes [128], Scheme Single_12b_8_8_8 means that 12 single bunches were injected to the LHC and 8 pairs of bunches were expected to collide in IP1 (IP5), IP2 and IP8.

vertical plane using the ADT white noise excitation. This method allowed the bunch intensity to be slowly reduced since the dispersed particles (tails of the transverse Gaussian distribution) were lost on the collimators. The three corrector orbit bump was set back to 21.61 mm. Finally, the MKQ was activated⁵ which caused a small bunch deflection of approximately $0.7 \mu\text{rad}$. This was done to provide an initial bunch excitation which was further amplified using the synchronized ADT system in the sign flip mode. In the end, an optimization of the ADT gain and bunch intensity resulted in magnet quenching. It was already mentioned that the greater the ADT gain is, the faster the beam losses are. Thus, during the excitation of the first bunch ($1.9 \cdot 10^8$ protons), the maximum gain of 400% was applied. However, it resulted in reaching 42% of BLM electronic limit (23 Gy/s) in the $40 \mu\text{s}$ long integration time (RS01). During the second approach with the similar experimental conditions, the results were confirmed. The probability of dumping the beam by the BLM system without having the magnet quenched was high when using a greater intensity bunch. Therefore, it was decided to apply 200% of the ADT gain which is equivalent to prolongation the loss duration. Three bunches with different number of protons ($2 \cdot 10^8$, $4 \cdot 10^8$ and $8.2 \cdot 10^8$) were excited one after the other. The last one induced MQ.12L6 quenching.

The proposed experiment was approved before the Machine Development slot by the Machine Protection Panel (MPP) after careful analysis and consideration of experts' suggestions. The summarized details can be found in [130].

4.9 Analysis of the experimental data

4.9.1 Characteristic of the beam and induced beam losses

The loss properties have been analyzed based on the BLM and QPS system measurements. In this section the following aspects are studied:

- Temporal loss structure and loss duration (BLM)
- Loss pattern (BLM)
- Influence of losses onto the development of the resistive volume (correlation between BLM and QPS).

Loss structure and loss duration

During the experiment three last bunches with different intensities were excited individually using the same MKQ kick strength and the ADT gain (200%). The bunch-by-bunch measurements showed that all protons of the excited bunches were lost on the magnet, i.e. no particles from these bunches were extracted to the beam dump. In addition, the BLM measurements along the ring confirmed that the losses occurred only in the targeted region. This means that the experimental conditions were exactly the same in the case of the concerned bunches.

⁵In order to provide an exact sequence of events with specified time intervals, the "timing tables" were applied.

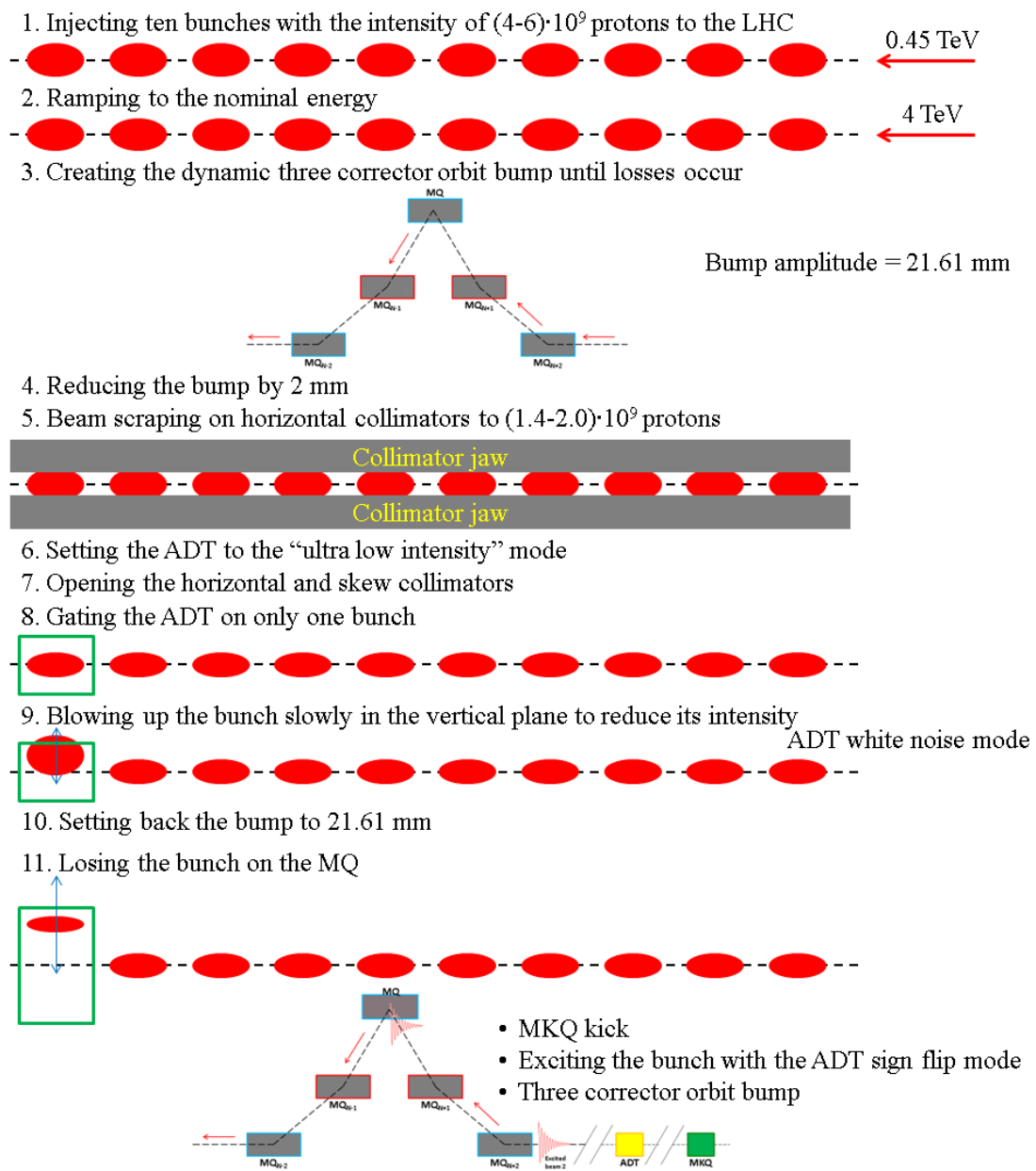


Figure 4.11 – Diagram of the procedure applied during the Fast Loss Quench Test (15.02.2013).

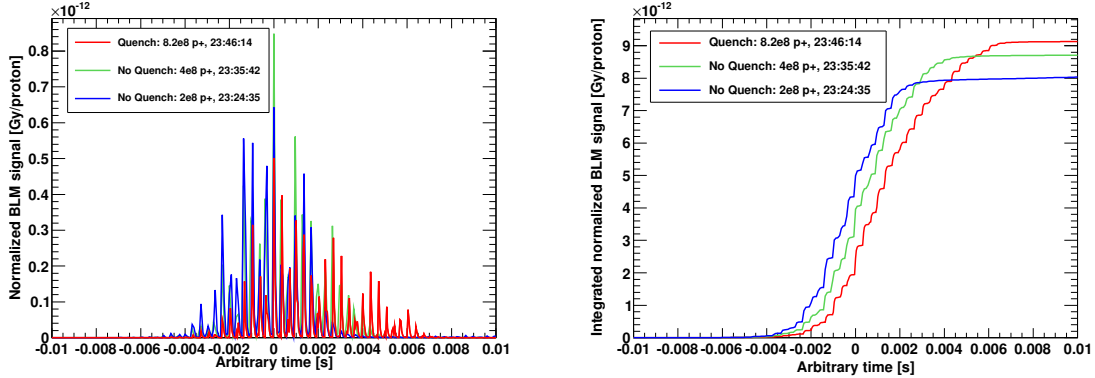


Figure 4.12 – Loss structure. Left plot: normalized BLM signals of individually excited bunches. Right plot: integrated normalized BLM measurements. Signal integration time: 40 μ s (BLM RS01) in the case of PM buffer (data recorded with quenching) and 80 μ s in the case of BLM Study Buffer (data recorded without quenching). The signals were normalized to one incident proton.

Therefore, taking into account that the radiation dose is proportional to the number of lost particles, it was expected that the radiation patterns measured by BLMs should also be the same or very similar when normalized to one incident proton. However, both the shape of the temporal loss distribution and the loss duration (Fig. 4.12, left plot) varied significantly. The losses of the 6th bunch (the red line) which ultimately caused MQ.12L6 quenching, were characterized by the maximum amplitude of the normalized BLM signal of $0.50 \cdot 10^{-12}$ Gy/proton. This is much smaller than in the case of two other bunch losses - $0.64 \cdot 10^{-12}$ Gy/proton (4th bunch - the blue line) and $0.85 \cdot 10^{-12}$ Gy/proton (5th bunch - the green line). In addition, the loss duration was extended over around 10 ms when in the other cases - 7 ms and 8 ms, correspondingly. It has to be stressed that, these given loss timescales are rough estimations since there is no precise criterion of estimating the BLM signal value which would indicate the beginning of losses. Due to the complex spiky loss structure consisting of sharp peaks and gaps in between it was not possible to fit any function giving a correct characteristic time⁶. The previous studies⁷ have shown that the integrated losses in time are the most important regarding quenching process in the fast regime. This applies when heat diffusion is short with comparison to the loss duration [131].

The right plot in Fig. 4.12 presents that although the losses of 6th bunch had relatively low maximum peak amplitude, overall they provided the highest total radiation dose in time. The observed differences in loss patterns measured using BLMs are not completely understood. The only factor known so far, which could be relevant, is related to the transverse shape of the

⁶The sigmoid shape function based on the Gauss error function was used. However, the correspondence between the data and the fit function was fairly poor.

⁷The impact of various heat dissipation shapes (rectangular, triangular, Gaussian and others) on the quench levels were tested using QP3 heat transfer code.

Table 4.2 – FLQT: Beam and loss parameters. I_0 - initial bunch intensity, I_l - loss intensity, t_l - loss duration, $L_{int,max}$ maximum of the BLM signal normalized to one incident proton, $L_{int,max}$ - maximum of the integrated BLM signal normalized per incident proton, σ_H - horizontal bunch size, σ_V - vertical bunch size.

Bunch	$I_0 = I_l$ [p]	$L_{norm,max}$ [Gy/p]	$L_{int,max}$ [Gy/p]	t_l [ms]	σ_H [μm]	σ_V [μm]
4 th	$2.0 \cdot 10^8$	$0.64 \cdot 10^{-12}$	$8.05 \cdot 10^{-12}$	7	123	1156
5 th	$4.0 \cdot 10^8$	$0.85 \cdot 10^{-12}$	$8.70 \cdot 10^{-12}$	8	134	1099
6 th	$8.2 \cdot 10^8$	$0.50 \cdot 10^{-12}$	$9.15 \cdot 10^{-12}$	10	129	830

bunches. The Wire Scanner measurements showed that, the 6th bunch possessed the smallest vertical size, σ_V among other bunches. In addition they have the smallest ratio between the vertical and the horizontal beam sizes. This indicates that the accumulation of protons in smaller space could result in locally higher energy density deposited in the superconducting coil which would be effective in inducing the magnet quenching. The parameters of the three bunches and correlated losses are summarized in Table 4.2.

Loss pattern

The installation of seven additional mobile BLMs in the vicinity of MQ.12L6 allowed the radiation dose pattern outside the magnets to be investigated with higher spacial resolution⁸. The BLM signals around the MQ.12L6 magnet for three bunches with increasing intensities (see Table 4.2) are shown in Fig. 4.13. The detector integration time of 10.24 ms (RS06) covers the entire loss duration of all considered losses and therefore was chosen for this comparison. In all cases the maximum signal was observed in B2I20 monitor (Fig. 4.8). According to the knowledge that the maximum BLM signal occurs around 1 m from the loss location, this indicates that the protons were lost in the first part (with respect to the beam motion) of the MQ magnet.

In Fig. 4.12 it was presented that the normalized BLM signals of three last bunches varied from each other despite the same experimental conditions. In order to check whether this tendency was conserved along the targeted region, the longitudinal distributions of normalized BLM signals per proton are given in the left plot in Fig. 4.14. Since the shape of the signals look very similar, the ratio of the normalized BLM signals of 6th bunch to the normalized BLM signals of 4th bunch (green line) and the ratio of the normalized BLM signals of 6th bunch to the normalized BLM signals of 5th bunch (blue line) were calculated. The results confirm that the losses propagated longitudinally in the same way (besides one point) and, thus, are characterized by the the same shapes. However, the difference in absolute values reaches

⁸Seven mobile monitors were installed only during the 2013 Quench Test slot. This increased a number of BLMs surveying beam 2 losses from three to ten giving required resolution. The Main Quadrupole (MQ.14R2) which was used as a target in 2010 was equipped in only three monitors per beam.

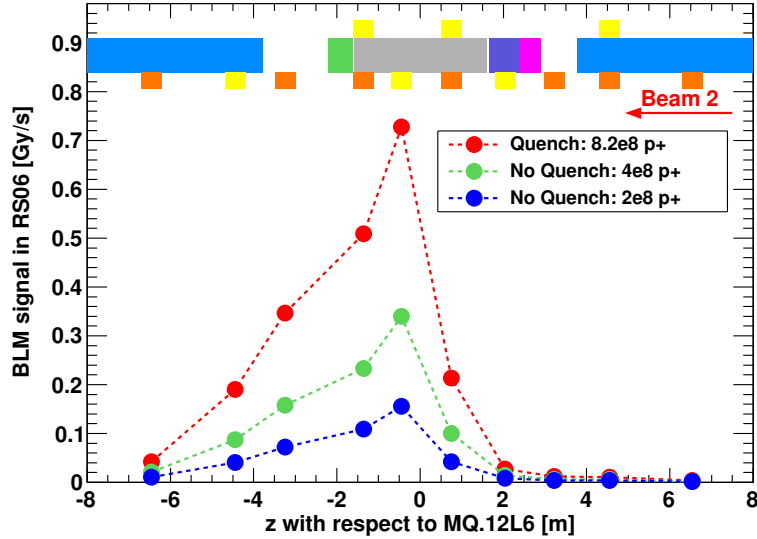


Figure 4.13 – FLQT 2013: Radiation along the magnets in the integration time of 10.24 ms (RS06). In all cases, the maximum of the loss occurred in B2I20. This indicates that the protons were lost in the first part of MQ. Beam 2 comes from the right.

up to 15% but is nearly constant for specific cases. This seems to confirm that the variations observed in Fig. 4.12 originated rather from the transverse than longitudinal effects.

Development of the beam loss and onset of the quench

Under standard LHC operation conditions, the BLM system would detect beam losses and initialize the beam abort. However, during the Fast Loss Quench Test, the BLM thresholds were increased to the electronic limit of 23 Gy/s in order to allow a resistive volume to develop in the superconducting coils. In the case of quenching, the QPS system decides whether the situation is safe or not. If the voltage difference between two parts of superconducting coils (U_{QS0}) is greater than 100 mV for time longer than 10 ms, the QPS system sends information to the beam abort system to extract the beam from the accelerator. At the same time, the quench heaters are triggered to dissipate the energy stored in the magnetic field over a whole volume of the superconductor. The detailed description of all protection actions assured by QPS is given in Section 1.6.2.

Although a correlation between BLM and QPS systems is extremely important for studying the quench phenomenon, these systems are not synchronized in time. Moreover, the resolution of the QPS data acquisition in PM is almost 13 times lower than in the case of BLM signals, i.e. the BLM signals are recorded every 40 μ s and QPS data is acquired every 5 ms. The idea of connecting the diamond BLM detector with the QPS oscilloscope was already mentioned. Nevertheless, the communication with the QPS scope was lost during the experiment. Therefore,

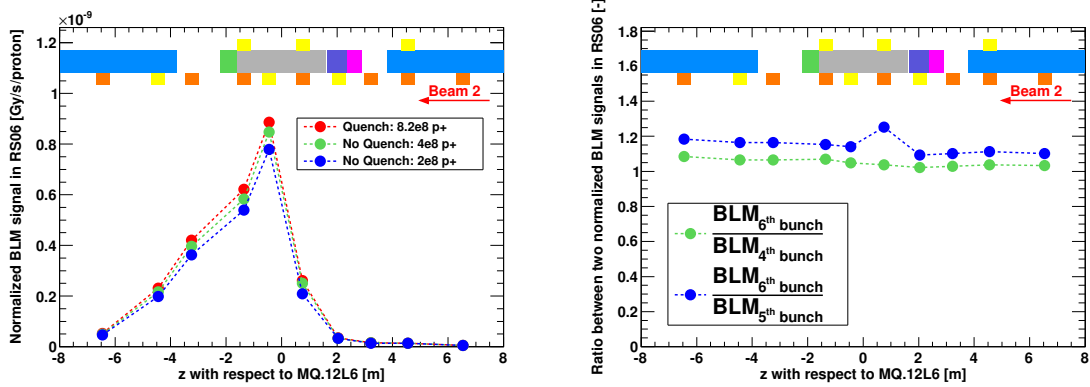


Figure 4.14 – FLQT 2013: comparison of longitudinal propagation of secondary particle shower for different bunches. Left plot: normalized BLM signals in RS06 per incident proton. Right plot: ratio of two signals presented in the left plot. Besides one point, the shape of the longitudinal distribution of radiation is conserved for all considered bunches. The absolute values vary up to 15%.

the BLM signals measured in half-cell 12L6 were synchronized with respect to the moment of the beam dump. The correctness of this method was verified using three other signals: one at the location of the MKD (Ejection Dump Kicker), which deflects a beam to the extraction line, one just before the beam dump and one located at the very end of the beam dump behind the graphite block. The U_QS0 characteristic was synchronized regarding the thresholds conditions but additional 5 ms were taken into account for activating the protection procedure. The final summary of the Fast Loss Quench Test results is given in Fig. 4.15. The green curve corresponds to the signal of the BLM monitor which was the most exposed to the radiation of secondary particle shower (BLMQI.12L6.B2I20_MQ). The QPS measurements are shown by the red and pink curves. The first one presents the development of the resistive volume on the internal quadrupole coil (U_QS0_INT), the other one provides information when warming of the coils started (the drop of the voltage on the quench heaters). The initial bunch intensity is known from the FBCT measurement and in the moment of quenching the $8.2 \cdot 10^8$ proton bunch was excited. Moreover, it is known that the full intensity was lost during the excitation and that the full intensity was lost in cell 12L6⁹. Taking into account proportionality of a BLM signal to a number of lost protons, an integrated BLM signal distribution can be recalculated to a lost proton distribution. It was calculated that approximately $5.4 \cdot 10^8$ protons (66% of the initial bunch intensity) induced a sudden increase in the U_QS0_INT signal, meaning the Main Quadrupole quenching. It was observed around 16 ms before the beam dump. However, an exact moment when quenching occurred cannot be precisely determined due to the QPS system resolution which is in the order of 5 ms. Therefore, the duration of the loss which lead to quenching is estimated to be 5-10 ms long.

⁹The three corrector orbit bump technique provides very localized losses. It was proved by previous quench tests[132].

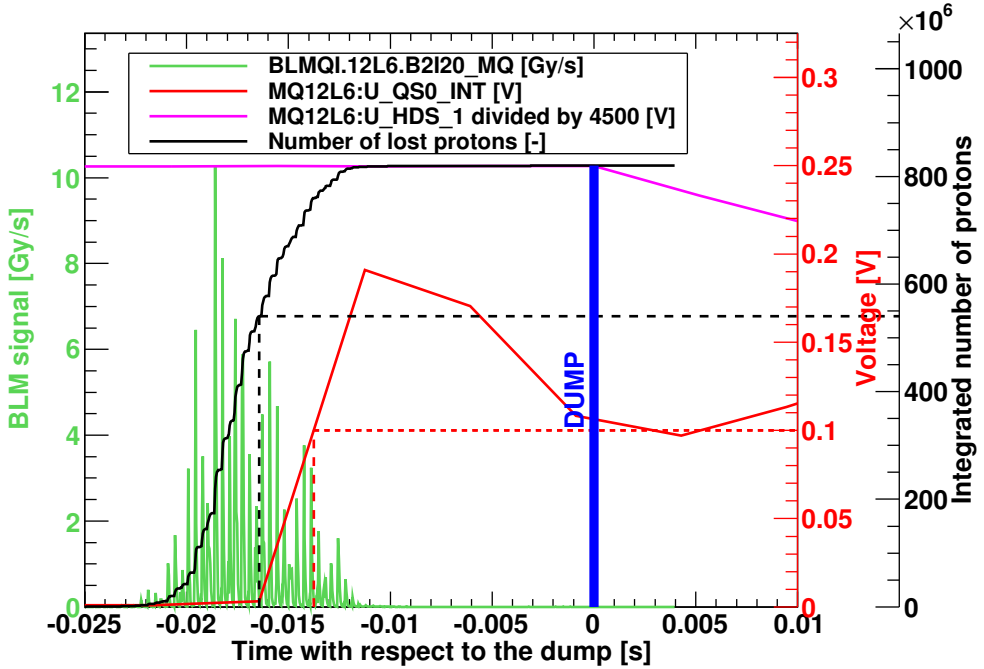


Figure 4.15 – Final summary of the Fast Loss Quench Test: the correlation between BLM and QPS system measurements. The green line represents the beam losses in the most exposed BLM monitor, the red line - the voltage difference between two parts of the MQ superconducting coil, the black line - the number of lost protons, the pink line - the voltage on the quench heaters. The black dotted lines point the moment of quenching and indicate the corresponding number of lost protons. The red dotted line marks the QPS threshold of 100 mV.

4.9.2 Validation of BLM thresholds with experimental data

BLM thresholds are the functions of the superconducting coil quench level which strongly depends on a loss duration. Since the loss causing the magnet quench lasted approximately 10 ms, only BLM running sums smaller than six (integration time up to 10.26 ms) can be analyzed here.

A revision of the nominal BLM thresholds (see Section 1.6.3) for proton beams operating at 4 TeV is given in Fig. 4.16 and Fig. 4.17. The green dots represent BLM thresholds for different signal integration times when the red dots correspond to the measured signals. The ratio between the BLM signals and the BLM thresholds are marked in the form of the blue dots. On the first plot, the situation when the ADT excitations caused losses of the 5th bunch with intensity of $4 \cdot 10^8$ protons is shown. Although the losses significantly exceeded the values which, under the typical LHC operation, would trigger the beam aborting system, no quenching occurred. The magnet transition to the normal conducting state was detected when the BLM losses in RS06 reached 40 times the threshold value (the second plot). Table 4.3

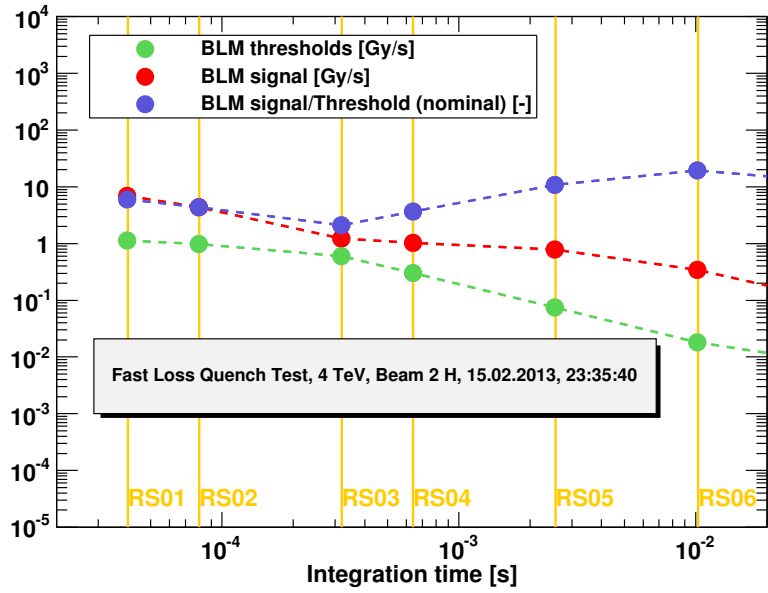


Figure 4.16 – FLQT 2013: The BLM signals (BLMQI.12L6.B2I20_MQ) measured during the ADT excitation of the bunch with the initial intensity of $4 \cdot 10^8$ protons (the red dots). The losses did not cause the transition to the normal conducting state. The green dots show nominal operating BLM thresholds for the 4 TeV proton beam. The ratio of the BLM signal and threshold is presented by the blue dots.

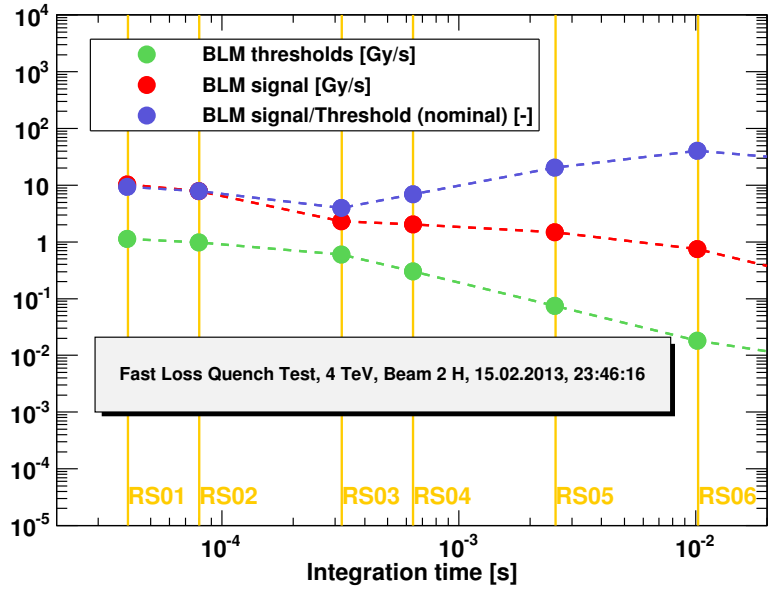


Figure 4.17 – FLQT 2013: BLM signals (BLMQI.12L6.B2I20_MQ) with respect to the nominal thresholds at 4 TeV in the case of the MQ quench at 4 TeV in 10 ms timescale. The loss reached the value 40 times greater than applied BLM threshold in RS06 (10.24 ms integration time).

Table 4.3 – Summary of the Fast Loss Quench Test. The ratios of BLM signals to the expected BLM values at quench are presented for five bunches used during the experiment. B - bunch number, Q - quench.

		Measured BLM signal/Expected BLM signal at quench [-]								
B	Lost p^+	ADT gain [%]	BLM loss integration time [s]							Q
			$40 \cdot 10^{-6}$	$80 \cdot 10^{-6}$	$320 \cdot 10^{-6}$	$640 \cdot 10^{-6}$	$2.56 \cdot 10^{-3}$	$10.24 \cdot 10^{-3}$		
2	$1.9 \cdot 10^8$	400	2.60	1.92	0.91	1.26	2.91	2.99		no
3	$2.0 \cdot 10^8$	400	2.15	1.75	0.86	1.27	2.93	3.06		no
4	$2.0 \cdot 10^8$	200	0.75	1.59	0.30	0.55	1.60	2.57		no
5	$4.0 \cdot 10^8$	200	1.78	1.30	0.63	1.05	3.20	6.60		no
6	$8.2 \cdot 10^8$	200	2.77	2.34	1.20	2.06	6.06	12.00		yes

contains the ratios of measured BLM signals to the expected BLM signals at quench for six BLM integration times (RS01-RS06) of all excited bunches. Among the bunches which did not provoke quenching (bunches 2 to 5), the maximum values are: 2.6 for $40 \mu s$ (RS01), 1.92 for $80 \mu s$ (RS02), 0.91 for $320 \mu s$ (RS03), 1.27 for $640 \mu s$ (RS04), 3.20 for $2.56 ms$ (RS05) and 6.60 in the case of $10.24 ms$ integration time (RS06). This means that either the quench levels are actually greater than the anticipated values¹⁰ or the energy deposited in the coil is smaller or the energy deposited in the BLM is greater than expected. In any case, according to obtained results, the thresholds of arc BLMs can be increased for the short running sums and the presented ratios indicate how large this change could be. Nevertheless for the understanding the actual reason of the observations, the Geant4 simulation has to be provided (see the following sections). The question how the new thresholds should be set for the future LHC operation after LS1, will be the objective of BLM Threshold Meeting Group to be held around spring-summer 2014. This will also concern the modification in BLM positions in the tunnel which is planned¹¹.

4.10 Geant4 simulations

The Fast Loss Quench Test 2013 was simulated using Geant4 version 9.3.p02. The detailed magnet representation of region 12L6, where the experiment was performed, was introduced to the code (for details see Chapter 3). Instead of considering exact BLM monitors, two long pseudo-detectors were implemented along the entire length of the magnets. This solution

¹⁰The anticipated quench levels are based on theoretical models, measurements and operational experience with the LHC beams.

¹¹It is planned to move central BLMs from arc MQs to the interconnection region between MBs and located them in the vertical position. This decision results from the probable occurrence of fast beam losses related to the UFOs in the cold parts of the LHC.

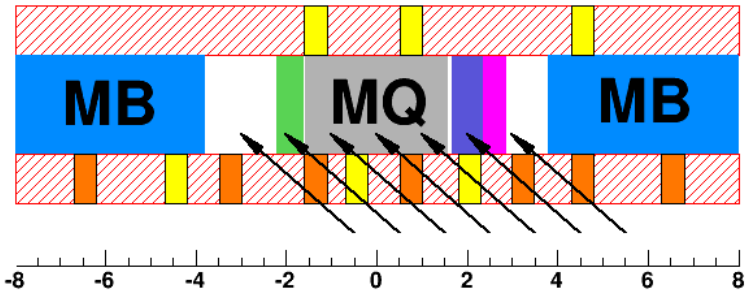


Figure 4.18 – Fast Loss Quench Test 2013: Geant4 magnet representation. The Main Quadrupole (MQ, grey bar) is located between two Main Dipoles (MBs, blue bars). The inter-connections between them are introduced in details but for the simplicity are not presented on the diagram. The green bar represents Short Trim Quadrupole Corrector magnet (MQT). The Arc Sextupole Lattice Corrector (MS, violet bar) and the Arc Orbit Corrector (MCBH, pink bar) constitute the Dipole Corrector in Arc Short Straight Section (MSCBB). Two long pseudo-detectors were simulated along the magnets (white-red hatched bars). The signals in BLMs physically installed in the tunnel were obtained by imposing constraints in x, y, z coordinates (standard BLMs - yellow bars, mobile monitors - orange bars). Black arrows indicate positions of point-like losses, the actual step is 0.1 m. Zero on z -axis corresponds to the MQ centre.

provided also information about secondary particle radiation beyond the regions which are covered by the actual ionization chambers. Signals in BLMs were obtained by imposing constraints in x, y, z coordinates regarding the positions of installed BLMs. 61 point like losses were simulated from $z = -3$ m to $z = 3$ m with respect to the MQ.12L6 centre with a step of 0.1 m (Fig. 4.18). This included whole region where particle losses were anticipated. Protons at 4 TeV hit on a surface of a beam screen with a fixed impacting angle¹² of 200 μ rad. Since beam 2 travels anticlockwise in the accelerator, also the particles were directed towards negative values on z -axis in the simulations. Moreover, in the considered sector, the orbit of beam 2 is located in the internal aperture. Therefore, the particles were lost on a beam screen in the horizontal plane outwards into to the centre of the LHC.

4.10.1 Loss pattern studies

A loss pattern is one of the major factors determining a BLM signal at quench. Therefore, it is extremely important to apply a precise distribution of lost particles along a targeted magnet to the simulations. Massive effort was made to simulate an orbit of particles excited during the Fast Loss Quench Tests [133]. Since the experiment was very complex, various scenarios were considered¹³ using MAD-X simulations:

¹²The choice of the impacting angle was based on the Steady State Quench Test 2010. The angle was calculated based on Beam Position Monitor measurements just before magnet quenching.

¹³Numbers 59, 61, 73 refer to iterations of considered loss patterns. It was decided to follow the original numbering to be consistent with analysis presented in numerous presentations.

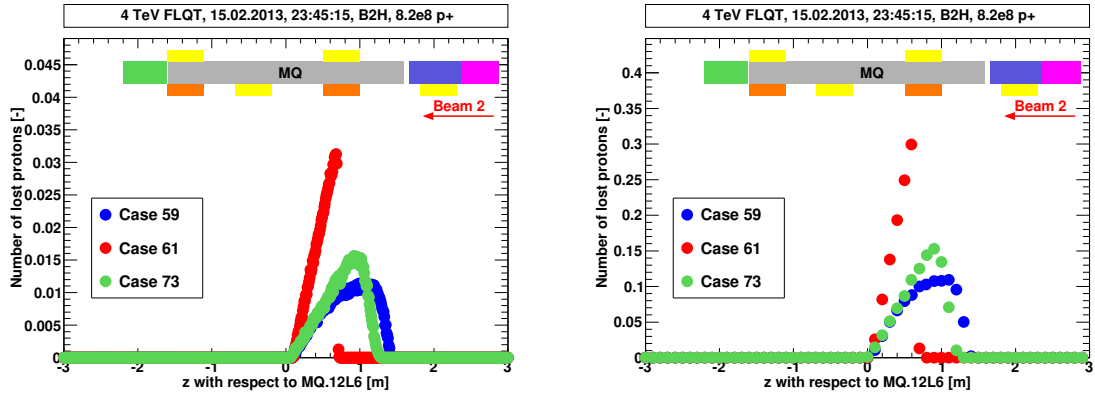


Figure 4.19 – Fast Loss Quench Test: Loss patterns. Left plot: normalized number of protons lost along the magnets with step of 0.01 cm (direct data from MAD-X). Right plot: normalized to 1 number of protons with step of 0.1 cm (recalculated input for Geant4 simulation analysis). Beam 2 comes from the right. Plots based on the data provided by [133].

- Case 59 - the bump was applied first and the tune was matched afterwards (this sequence of events was not done in the real experiment);
- Case 61 - 3rd order resonance was imposed by setting the horizontal tune to a values of 64.(3), next the bump was introduced (this case was studied to check how particles behave under extreme conditions, not done during the experiment);
- Case 73 - the tune was matched and the bump was applied later, in addition MQ errors were taken into account (the order of events is as in the experiment, this is the most probable loss scenario¹⁴).

Fig. 4.19 shows that, regardless of considered initial conditions, all simulated losses occurred in the first half (with respect to the beam motion) of the MQ magnet. In order to compare how the losses expanded in the presented three cases, the full width at half maximum (FWHM) was calculated. The maximum of lost particles appeared around 0.9 m before the centre of the MQ and the particle losses spread over 0.64 m. The corresponding values for two other cases are given in Table 4.4. Concluding, the obtained results show that the sequence of events, which a beam is treated with, determines a particle loss distribution regarding a shape and longitudinal size.

The loss patterns from MAD-X simulations were obtained with a mesh of 0.01 m along the aperture (statistics: 10^5 protons) when point-like losses were simulated with Geant4 every 0.1 m. Hence, the loss patterns were recalculated by rebinning histograms (the right plot in Fig. 4.19).

¹⁴Although Case 73 recreates the experimental conditions the most accurately, two other loss scenarios (Cases 59 and 61) are presented for comparison.

Table 4.4 – Fast Loss Quench Test 2013: Comparison of loss patterns. Longitudinal position of the maximum proton loss is given by z_{Lmax} with respect to MQ.12L6 centre.

	z_{Lmax} [m]	FWHM [m]
Case 59	1.1	0.93
Case 61	0.6	0.33
Case 73	0.9	0.64

At the moment of simulating the Fast Loss Quench Test with Geant4, the MAD-X simulations were still ongoing. The knowledge of impacting angles was limited to one value coming from previous experiments¹⁵. However, it was checked with Geant4 simulations that increasing an angle by up to around 500 μ rad has not introduced modifications in longitudinal energy distribution. Therefore, it was decided to implement a fixed angle to 2013 code.

MAD-X simulations revealed an angular spread of particles hitting the aperture. Fig. 4.20 shows the normalized number of lost protons and corresponding impacting angles as a function of longitudinal position along the magnets. A contribution of higher angles dominates in a region where the most particles were lost. In order to quantify a difference coming from neglecting angular spread in Geant4 simulations, a weighted average of impacting angles, $\bar{\alpha}$, was calculated using the following formula

$$\bar{\alpha} = \frac{\sum_{z=-3m}^{3m} \alpha_z \cdot l_z}{\sum_{z=-3m}^{3m} l_z} \quad (4.3)$$

The impacting angles are given by α_z and are correlated to the corresponding number of lost particles l_z . These values come directly from MAD-X simulations. The index z refers to the longitudinal position and it changes with a step of 0.1 m. The value of $\bar{\alpha}$ is $\approx 145 \mu$ rad is only a bit smaller than the one used in Geant4 simulations (200 μ rad). This, to some extend, confirms that an overall discrepancy between experimental (actually, simulated in MAD-X) and simulated in Geant4 conditions is small and should not affect the final results significantly.

4.10.2 Energy deposition inside a superconducting coil

Primary protons lost on a beam screen initiate a development of secondary particle shower which propagates in all directions. These particles which deposit their energy in the superconducting coils determine quenching. Therefore, in order to estimate the location of a hot spot where the maximum energy density, E_{max} , was deposited ($r_{E_{max}}, \phi_{E_{max}}, z_{E_{max}}$), the coil in Geant4 simulations was divided into 108'000 cells. In these cells, the energy deposited by secondary particles is registered. The size of the unit cells was chosen so that they are much smaller than a shower scale. Hence, each cell has dimensions of $\Delta\rho = 3.84$ mm, $\Delta\phi = 9^\circ$,

¹⁵The impacting angle was calculated from beam position measurements of Steady State Quench Test 2010.

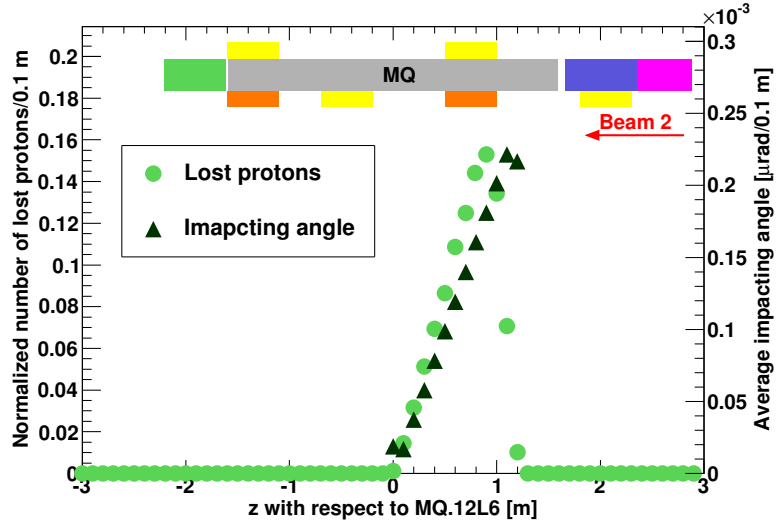


Figure 4.20 – Fast Loss Quench Test 2013: Angular distribution of incident particles are compared to the loss pattern (Case 73). Most of the protons hit the aperture with higher angles (data provided by [133]).

$\Delta z = 9.83$ mm in the polar coordinate system.

Fig. 4.21 presents the longitudinal distribution of energy density normalized per incident proton along the most exposed bin ($r = r_{Emax}, \phi = \phi_{Emax}$). In all considered cases the peak values occur in the center of the MQ, ≈ 0.3 m in Case 59, ≈ 0.1 m in Case 61, ≈ 0.3 m in Case 73 reaching values of $(2.8 \pm 0.2) \cdot 10^{-7}$ mJ/cm³, $(4.2 \pm 0.2) \cdot 10^{-7}$ mJ/cm³, $(3.2 \pm 0.2) \cdot 10^{-7}$ mJ/cm³ respectively (Table 4.5). These values are averaged over the volume of the most exposed cell¹⁶.

In the fast loss regime, i.e. milliseconds, the heat coming from the particle energy deposition do not have time to propagate through a cable. Therefore, a temperature gradient appears between inner and outer edges of the cable.

A contribution of the liquid helium in heat evacuation is negligible in the case of ultra fast losses in the order of microseconds and the enthalpy of the cable determines the quench level. However, in the case of fast losses, longer by three orders of magnitude, the dominant processes responsible for the heat transport are not well distinguished. Therefore, the quench level is defined as the energy deposited in the most exposed part of the coil, i.e. on its edge ($r = 28$ mm). In order, to calculate that value, the simulated radial distribution ($\phi = \phi_{Emax}, z = z_{Emax}$) of energy deposited in the coil is fitted to the power law function defined as

$$E(r) = p0 \cdot (r - p1)^{p2} \quad (4.4)$$

where $p0, p1, p2$ are the fit parameters (Fig. 4.22). The maximum energy density deposited

¹⁶Note that the volume of cells is not uniform and slightly increases with a distance from the coil centre. However, since E_{max} occurs always in the first exposed layer, the presented values are averages over the same volume.

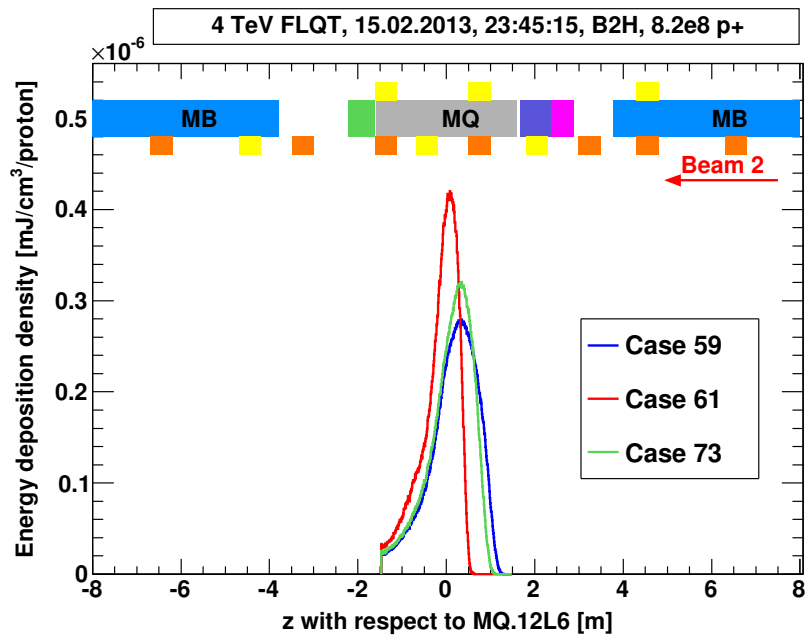


Figure 4.21 – Fast Loss Quench Test 2013: Geant4 simulations - longitudinal energy density distribution inside a coil. Regardless of the considered initial settings, all energy density peaks appear close to the MQ centre.

Table 4.5 – Fast Loss Quench Test 2013: Maximum energy density in the most exposed cell of SC coil, $z_{E\max}$ -position of the most exposed cell, $|z_{L\max} - z_{E\max}|$ - distance between the maximum energy density deposition and maximum of lost protons, E_{\max} - maximum energy density deposited in a single cell.

	$z_{E\max}$ [m]	$ z_{L\max} - z_{E\max} $ [m]	E_{\max} [mJ/cm³/proton]
Case 59	≈ 0.3	≈ 0.8	$(2.8 \pm 0.2) \cdot 10^{-7}$
Case 61	≈ 0.1	≈ 0.5	$(4.2 \pm 0.2) \cdot 10^{-7}$
Case 73	≈ 0.3	≈ 0.6	$(3.2 \pm 0.2) \cdot 10^{-7}$

Table 4.6 – Fast Loss Quench Test 2013: Energy deposited in the coil - final results. E_{peak} is the maximum energy density deposited in a surface of the SC, E_{avg} is the average energy density over 18 strands of the cable. The quench level in the fast loss regime (\approx ms) is obtained by multiplying E_{peak} by the number of protons which caused magnet quenching during the experiment.

	E_{peak} [mJ/cm ³ /proton]	E_{avg} [mJ/cm ³ /proton]
Case 59	$4.19 \cdot 10^{-7}$	$1.45 \cdot 10^{-7}$
Case 61	$6.38 \cdot 10^{-7}$	$2.15 \cdot 10^{-7}$
Case 73	$4.87 \cdot 10^{-7}$	$1.65 \cdot 10^{-7}$

on the edge of the coil, E_{peak} , was calculated to be $4.19 \cdot 10^{-7}$ mJ/cm³/proton in Case 59, $6.38 \cdot 10^{-7}$ mJ/cm³/proton in Case 61, $4.87 \cdot 10^{-7}$ mJ/cm³/proton in Case 73 (Table 4.6). By multiplying these values by a number of protons lost during the experiment, the quench level of the operational magnets can be calculated (see next sections). The average values of energy density along the cable are given for comparison and they are equal $1.45 \cdot 10^{-7}$ mJ/cm³/proton, $2.15 \cdot 10^{-7}$ mJ/cm³/proton, $1.65 \cdot 10^{-7}$ mJ/cm³/proton for the considered cases, respectively.

Another application of the radial energy density profile is related to QP3 code which concerns 18 strands of a MQ cable. In order to comprise an accuracy of the simulations, i.e. obtain sufficiently high transverse resolution of energy distribution in the coil, with optimization of the computing time (rational duration of the simulation process), a coil is divided radially into four layers in the Geant4 simulation. Therefore, the obtained fit parameters allow the Geant4 results based on only four layers to be recalculated to 18-strand case and implemented the QP3 code.

The transverse cross-section of the coil in the plane where the maximum energy density was deposited ($z = z_{E_{max}}$) is presented in Fig. 4.23. Most of the energy is confined in the central part of the targeted coil. A size of a superconductor, which underwent the transition to the normal conducting state, is another important aspect of quenching process. However, the minimum length/volume of the resistive zone depends on many parameters (magnetic field, applied current, cooling efficiency, temperature variations, initial heat pulse, cable twisting and correlated changes along the cable length [131]) and require calculations using numerical models which are beyond these studies.

Nevertheless, the Geant4 simulation results can be applied to estimate the importance of different coil parts in the quenching process. Plots in Fig. 4.24 present color maps of energy density in four simulated layers of the superconducting coil ($r = 0, 1, 2, 3$ [bin number]) in ϕ, z -coordinates. Black lines bound the regions satisfying the demand of $E_{thr} \geq f_{E_{max}} \cdot E_{max}$, where $f_{E_{max}}$ is a fraction of maximum energy density in the most exposed cell. The shape of the energy density distribution is slightly asymmetrical in the azimuthal plane and the

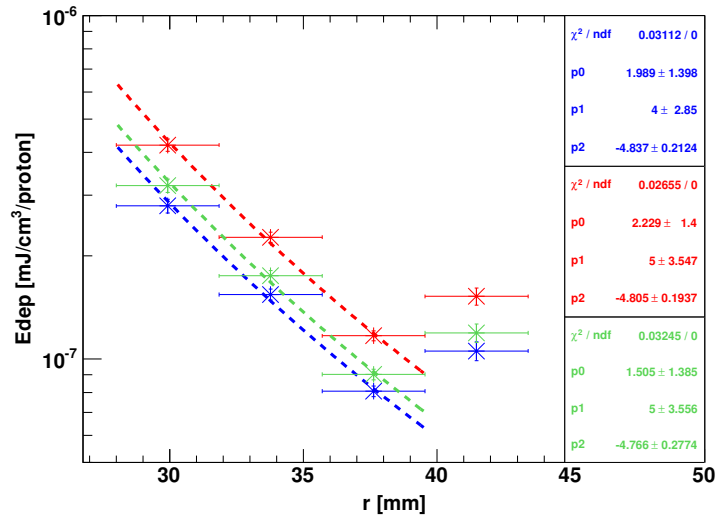


Figure 4.22 – Fast Loss Quench Test 2013: Geant4 simulations - radial maximum energy density distribution in SC coil ($\phi = \phi_{Emax}$, $z = z_{Emax}$). Energy density in the simulated radial bins was fitted to the power law (Eq. 4.4), last bin was neglected due to the simulation artifacts.

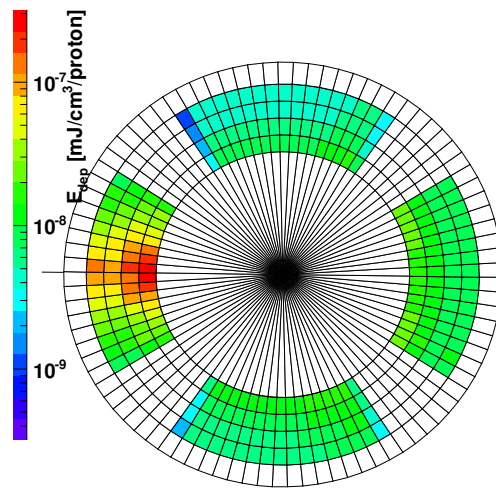


Figure 4.23 – Fast Loss Quench Test 2013: Geant4 simulations (Case 73) - coil cross-section in the plane where the maximum energy density was deposited.

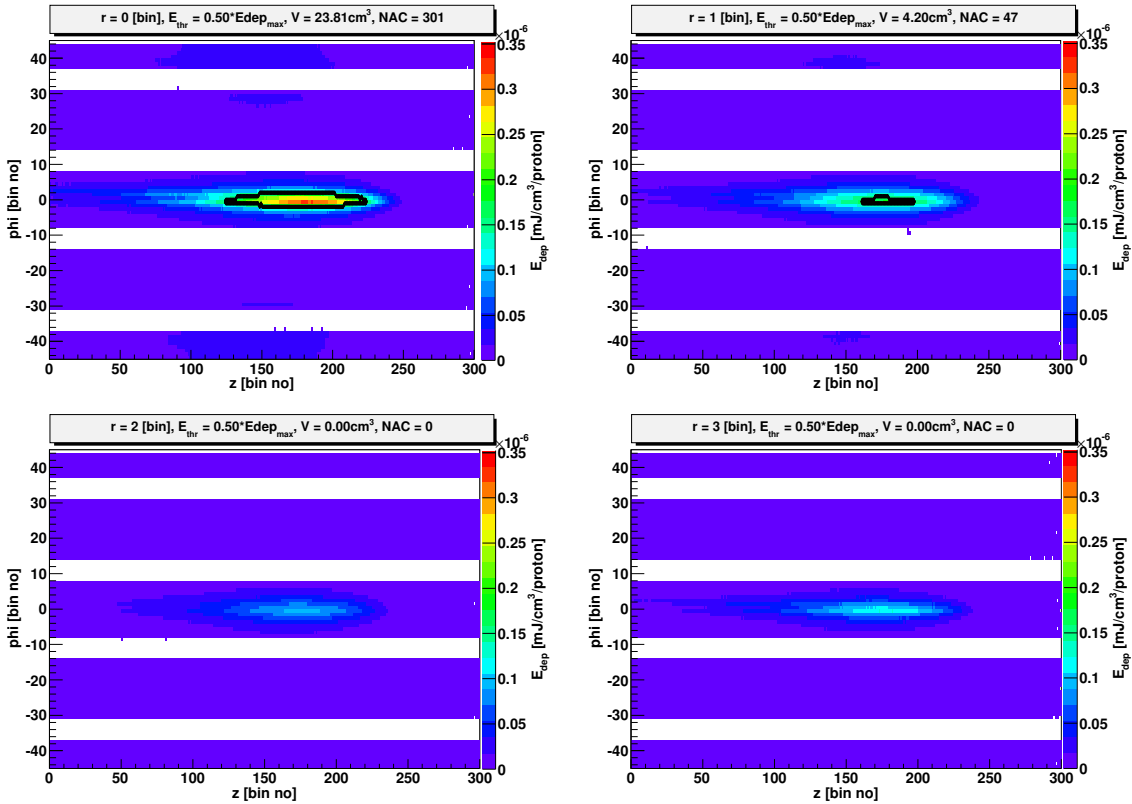


Figure 4.24 – Fast Loss Quench Test - Geant4 simulations (Case 73) - Color maps of energy density in four simulated coil layers. For simplicity r, ϕ - coordinates are expressed in bin numbers, beam comes from the right. Black lines limit the region defined by the threshold value $E_{thr} = f_{E_{max}} \cdot E_{max}$, here $f_{E_{max}} = 0.5$.

tail spreads over the entire coil length (in the case of $r = 0$ [bin] and $r = 1$ [bin]). Assuming a threshold value $E_{thr} = 0.5 \cdot E_{max}$, the obtained boundaries indicate that most active regions are concentrated in the first two coil layers. With this constraint, a Number of Active Cells, $NAC_1 = 301$ ($\approx 1.1\%$ all cells in the layer) in the first layer and $NAC_2 = 47$ ($\approx 0.2\%$ all cells in the layer), which correspond to the active volume of $V_1 \approx 24 cm^3$ and $V_2 \approx 4 cm^3$, correspondingly. The active volume size was checked for values of $f_{E_{max}}$ varying from 0.1 to 0.9 (left plot in Fig. 4.25). If $f_{E_{max}} > 0.5$ the total signal is confined totally inside the first, the most exposed layer ($r = 0$). Moreover, the volume size drops exponentially as a function of imposed energy threshold which is presented in the right plot of Fig. 4.25 for the case of the first layer ($r = 0$).

4.10.3 BLM signals

As it was already mentioned, instead of simulating exact BLMs which are located in the LHC, two long pseudo-detectors were implemented along the entire magnet length to the Geant4 code. This approach allowed studying the radiation also in the regions which were not

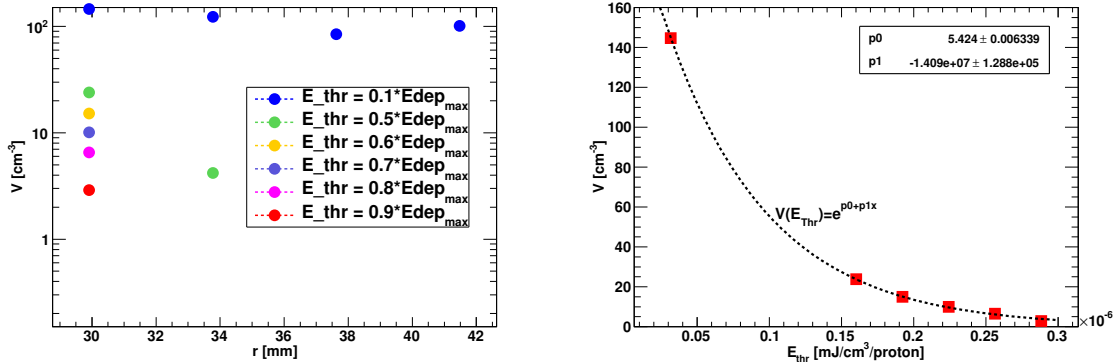


Figure 4.25 – Fast Loss Quench Test 2013: Geant4 simulations (Case 73) -Quenching volume as a function of considered criteria of energy magnitude. Left plot: Above the assumed threshold value of $0.5 \cdot E_{\text{max}}$ all energy is confined in the first, the most exposed layer of the coil. Right plot: the volume decreases exponentially as a function of imposed energy threshold, $E_{\text{thr}} =$ (results of the first layer).

covered by the detectors in the tunnel. The BLM signals were obtained by imposing position constraints onto the secondary particle coordinates which corresponded to the locations of the BLMs installed in the LHC tunnel.

Fig. 4.26 presents a longitudinal distribution of all secondary particles which reached the pseudo-detectors. Although the loss patterns differed significantly (Fig. 4.19) for various loss scenarios, the tendency of radiation spread is in general conserved. Among three peaks only the one appearing the closest to the maximum of lost particles is slightly shifted. The presence of these three peaks with different widths is related to the density of medium which particles pass through. The decay of the first peak seems to be natural - particles are stopped by the dense cold mass (alloys, steel). However, at the end of the MQ cryostat, where the MQT (green bar) is located, there is more lower density matter (epoxy stabilizers and liquid helium). Hence, the secondary particles can more easily travel outside the magnet (see Appendix A, Fig. A.5). Finally, the last peak is in the interconnection region which is constituted mainly of vacuum pipes and tubes filled with liquid helium.

BLM signals were obtained by folding particle energy spectra with BLM response functions. The detailed process is explained in Chapter 3. The angular distributions of all standard, i.e. not mobile, detectors are presented in Fig. 4.27. Although locations of angular distribution maxima (Fig. 4.27) depend on the distance of a monitor from the loss location both, longitudinally and transversely, on average (see method presented in Fig. 3.4) most of the particles enter monitors with angles between 60° and 120° (Fig. 4.28).

Fig. 4.29 presents the contribution of secondary particles (p^+ , e^- , e^+ , γ , π^+ , π^- and n) to the final BLM current. The highest signals are provided by γ , p^+ and n starting from the BLM

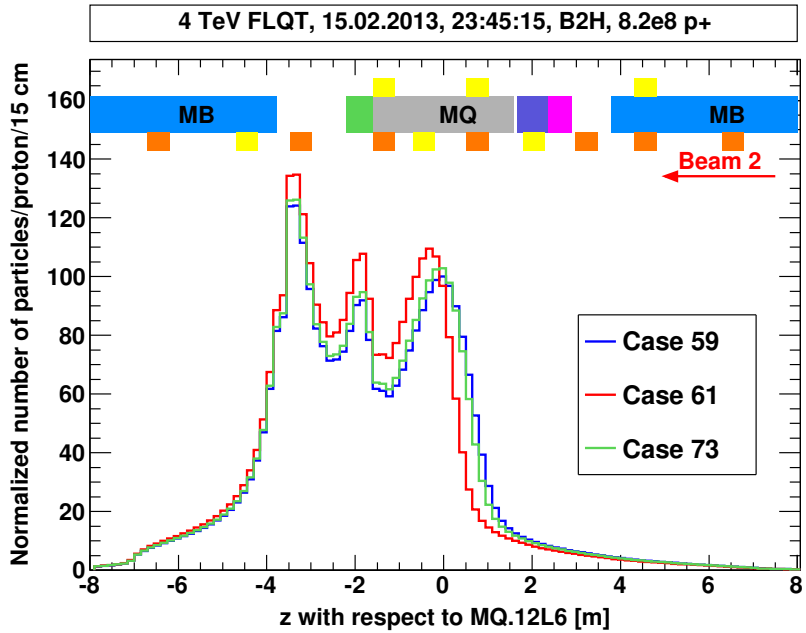


Figure 4.26 – Geant4 simulations - total secondary particle distribution along the magnets. Three peaks are the result of the difference in density of medium which particles pass through.

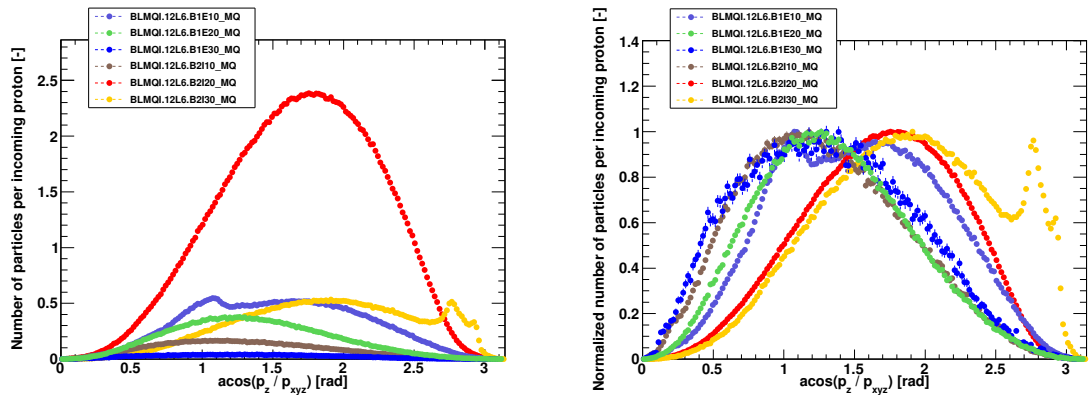


Figure 4.27 – Geant4 simulations (Case 73) - Left plot: angular distributions of particles recorded by standard BLMs. Right plot: normalized to 1 angular distributions of particles recorded by standard BLMs.

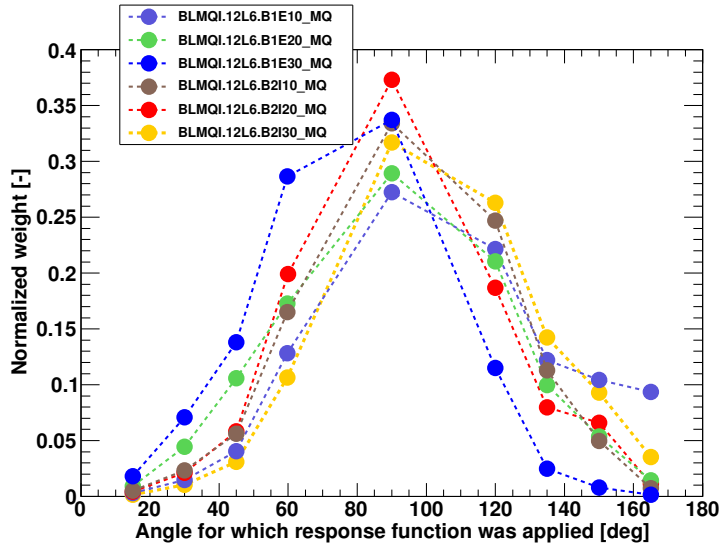


Figure 4.28 – Geant4 simulations (Case 73) - Angular contribution of particles to the signals recorded by BLMs.

located the closest to the loss location ($z \approx 1$ m) and reaching the maximum around 1 m from it ($z \approx 0$ m). Considering the percentage input of particles into the total BLM signal, gamma photons dominate over all particles constituting between 40% and 60% of the simulated radiation (Fig. 4.30). Effectively mainly gammas and backscattered neutrons reach upstream detectors.

A comparison of measured and simulated BLM signals is provided in Fig. 4.31 using 10.24 ms integration time (RS06). Left plots correspond to BLMs observing beam 1 losses (in this case cross-talk from beam 2 is observed) and right plots show results obtained for beam 2 monitors. The longitudinal shape of the simulated signals was obtained with good agreement with the corresponding measured values. However the Geant4 simulations provided signal underestimated by a factor of 2-3 (in the case of beam 2 monitors). In order to quantify the spread of results, histograms (with uncertainty of factor 0.1) are given in Fig. 4.32. In all cases the mean value is ≈ 0.4 and the RMS is ≈ 0.1 which indicate systematical error of the BLM signals simulated in Geant4.

4.10.4 Quench levels obtained with QP3 heat transfer code

Complementary to the Monte Carlo simulations, the QP3 heat transfer code [87] was used for computing the quench level in the millisecond loss timescale. However, since this program uses input from Geant4 simulations, the final results are not completely independent. The principle of the QP3 is based on calculating a quench level for a superconductor operating at certain current. In addition, the loss scenario is incorporated using a loss distribution in time and a shape of radial energy distribution. During the Fast Loss Quench Test 2013, the current

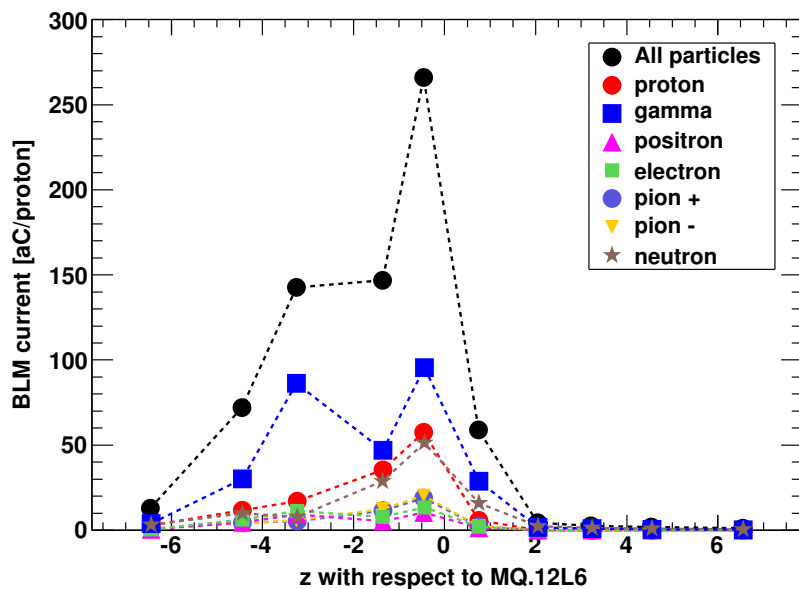


Figure 4.29 – Geant4 simulations (Case 73) - Contribution of secondary particles to the BLM current.

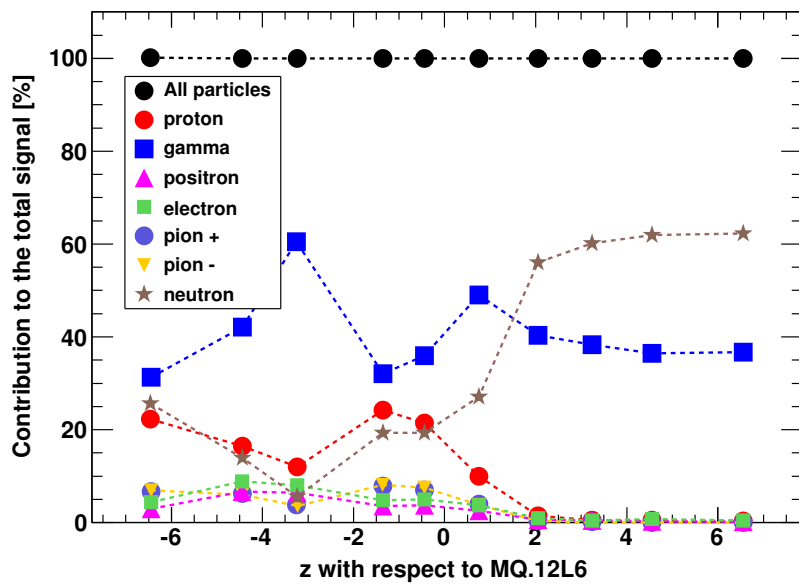


Figure 4.30 – Geant4 simulations (Case 73) - Current generated in BLMs by various secondary particles as a function of the longitudinal position of a monitor.

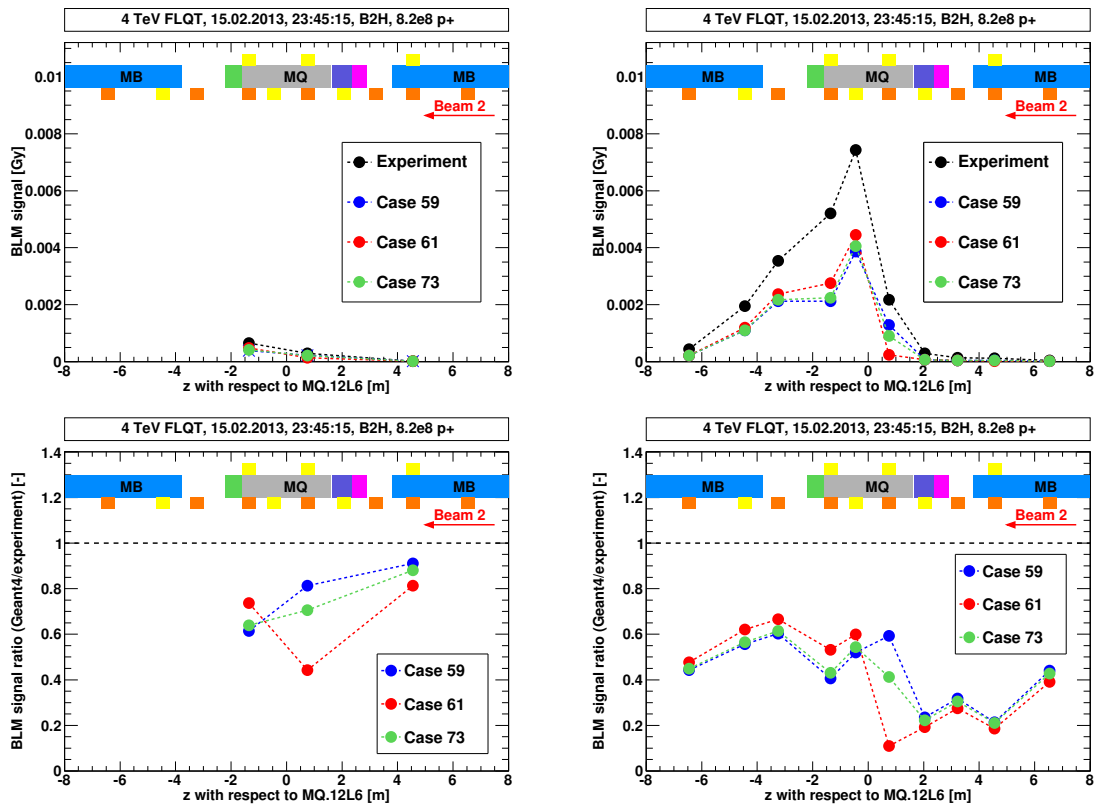


Figure 4.31 – Fast Loss Quench Test: a comparison of measured and simulated BLM signals. Geant4 simulations underestimated BLM signals by a factor 2-3 in the case of monitors surveying beam 2 losses.

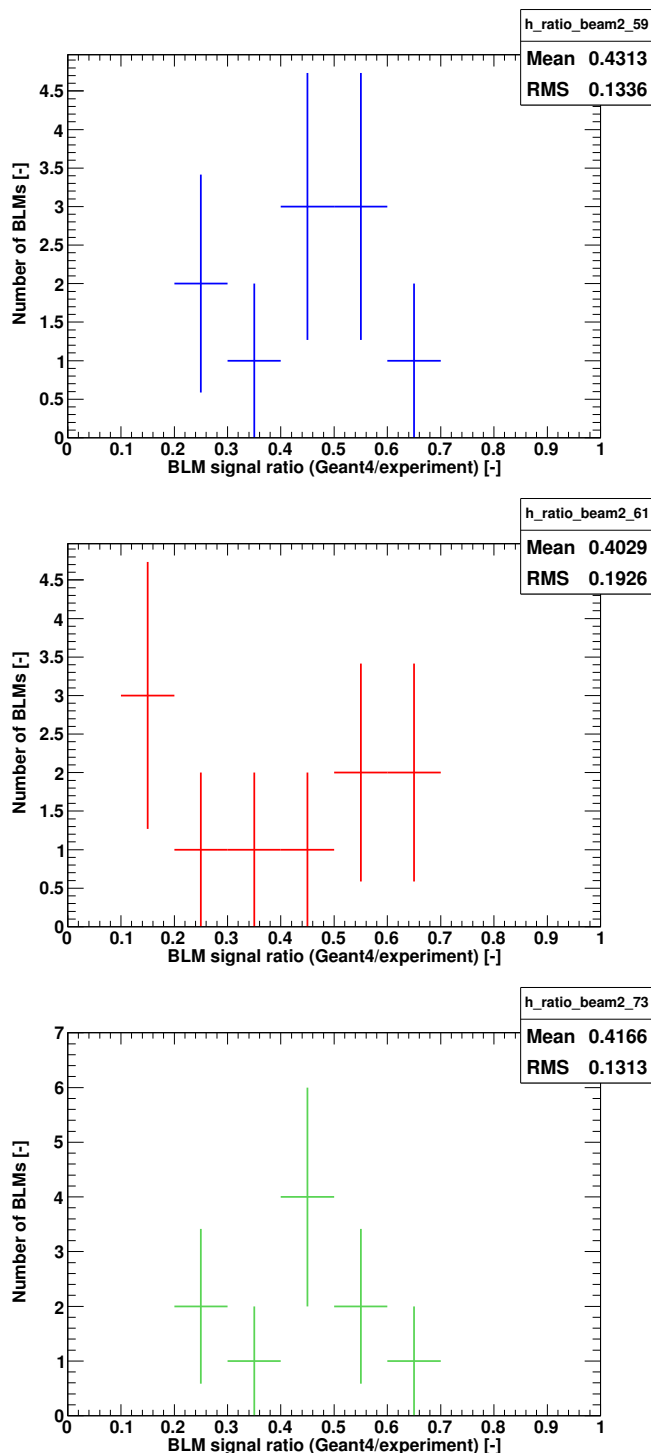


Figure 4.32 – Fast Loss Quench Test 2013: Geant4 simulations - error estimations of the simulated BLM signals.

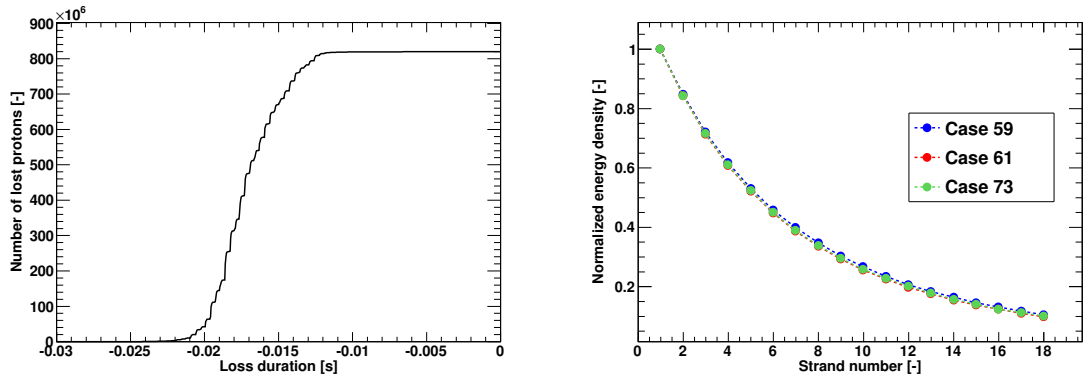


Figure 4.33 – Fast Loss Quench Test 2013: QP3 input distributions. Left plot: Intensity of lost protons, zero corresponds to the moment of the beam dump. Right plot: Normalized radial energy density distribution along a cable (18 strands) for different loss patterns (Case 59 - blue, Case 61 - red, Case 73 - green).

flowing in the circuit was approximately equal 6.38 kA (PM data). A number of lost protons in time (left plot of Fig. 4.33) was recalculated from the BLM signal of the monitor which was the most exposed to the radiation (B2I20). This could be done since the radiation is proportional to the number of lost protons. In addition, during the experiment collimators were opened, thus the particle losses occurred only on MQ.12L6. In order to obtain radial energy density distribution along 18 strands, as it is required when using the QP3, the Geant4 data was fitted to the power law. Based on the obtained function, the energy density was calculated in the centers of the cable strands. Finally the results were normalized to 1 as the QP3 considers the shape of the distribution, not the exact values. The obtained normalized radial distributions of three considered cases (59, 61, 73) are almost indistinguishable (right plot of Fig. 4.33). This reflects in the calculated maximum energy deposited inside a cable during quenching, E_{peak} (Table 4.7), and average energy over the cable, E_{avg} (Table 4.8). Although the final results are given for a loss of $4 \cdot 10^8$ protons, $5.4 \cdot 10^8$ protons, $8.2 \cdot 10^8$ protons, actually the value which is set in the QP3 code is the loss duration corresponding to the given intensity loss. This nomenclature was used for simplicity when comparing to Geant4 results. As it was already mentioned, in the case of fast loss regime, quench level is defined as the maximum energy, which in this case, was calculated to be $(28.7-28.8)$ mJ/cm³, $(35.9-36.0)$ mJ/cm³ and $(68.6-70.3)$ mJ/cm³ for the considered loss scenarios. The corresponding values of average energies are $(10.6-10.8)$ mJ/cm³, $(13.2-13.5)$ mJ/cm³ and $(25.8-26.0)$ mJ/cm³.

Geant4 simulations provide maximum energy deposited on the surface of a superconducting cable per incident proton. The quench level is obtained by multiplying this value by a number of protons lost on the magnet. In other words, quench level scales linearly with the intensity of the loss which lead to quenching during the experiment. In the case of QP3, the situation is different since a loss shape and loss duration determine quenching. The left plot in Fig. 4.34 presents quench levels corresponding to different numbers of impacting protons for the most

Table 4.7 – Fast Loss Quench Test 2013: Fast Loss Quench Test 2013: QP3 results - E_{peak} (maximum value of the deposited energy) in the coil.

Loss scenario	E_{peak} [mJ/cm ³]		
	Lower bound of quench level: $4 \cdot 10^8$ protons	Upper bound of quench level: $8.2 \cdot 10^8$ protons	Anticipated loss causing the quench: $5.4 \cdot 10^8$ protons
Case 59	28.7	68.6	35.9
Case 61	28.8	70.3	36.0
Case 73	28.8	70.3	36.0

probable Case 79. The QP3 results are shown as blue dots and Geant4 based values are given by the red dots. Note different scales for two methods. The QP3 calculations seem to be very sensitive on the loss duration and loss shape. However, the results do not project directly with respect to these parameters. The same data are presented as a function of loss duration in the right plot of Fig. 4.34. Since there is no precise criterion of defining which moment should be considered as the beginning of the loss, the loss intensities in time, $I_{loss}(t)$, were fitted to a sigmoid shape function given by the following equation

$$I_{loss}(t) = p_A \cdot \frac{1}{2} \left(1 + \frac{2}{\sqrt{\pi}} \int e^{\left(\frac{t-p_B}{\sqrt{2}p_C} \right)^2} dt \right). \quad (4.5)$$

Symbols p_A , p_B and p_C represent fit parameters. Equation 4.5 is the cumulative distribution, i.e. the integral, of the standard normal distribution and the parameter p_C corresponds to width of the Gaussian. Therefore, in this case multiplying p_C by 4 gives the time during which 95.5% of assumed protons were lost. The exact values are given in Table 4.9. It was decided to present the quench levels as the functions of both, the number of loss protons and loss duration since the first approach is relevant to the Geant4 simulations and the other one applies to QP3 calculations. Concluding, the quench levels obtained with QP3 code are around 5.7-9.5 times smaller than these ones obtained with Geant4 simulations. The origin of this discrepancy remains under investigation.

4.10.5 Comparison between Geant4 and Fluka simulations

A proper estimation of the quench level is critical for a safe and efficient machine operation. Therefore, independently two approaches of Monte Carlo simulations were developed within the Quench Test Analysis Working Group at CERN. In the following paragraphs a comparison between Geant4 and Fluka simulations are presented as well as their results.

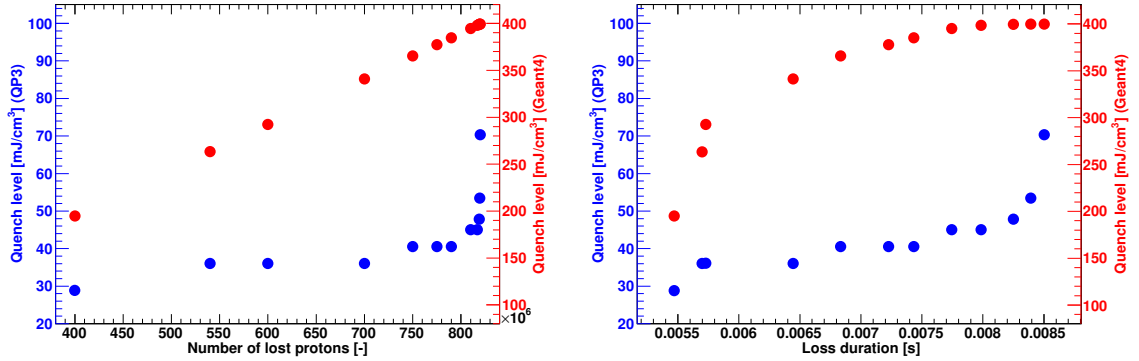


Figure 4.34 – Fast Loss Quench Test 2013: Quench levels obtained with Geant4 simulations (red dots) and QP3 heat transfer code (blue dots) for the most probable Case 79. left plot: in the case of Geant4, quench levels are obtained by multiplying E_{peak} by the number of protons which induce quenching. Right plot: the quench level obtained with QP3 code relies on loss duration and loss shape. Detail value are provided in Table 4.9.

Principles of simulating quench tests with Geant4 and Fluka

The first method was developed by the author using Geant4 in the time when no orbit simulations were available and the validation of assumed hypotheses of loss patterns needed to be done frequently and efficiently. Therefore, instead of simulating exact loss scenarios, a universal set of many point-like losses was provided with a longitudinal step of 0.1 m. The contributions of various loss locations were then weighted with correspondence to a loss pattern obtained from orbit studies (MAD-X data from [133]). In this method, a fixed impacting angle of lost particles was assumed and a transverse beam size was neglected. Although such an approach is less precise, it allowed considering various loss scenarios very quickly when the simulation process was done. This could be done since imposing loss distributions was provided on the stage of analysis, i.e. the histograms with data obtained for point-like losses

Table 4.8 – Fast Loss Quench Test 2013: Fast Loss Quench Test 2013: QP3 results - E_{avg} (average value of the deposited energy over entire cable length) in the coil.

Loss scenario	E_{avg} [mJ/cm ³]		
	Lower bound of quench level: $4 \cdot 10^8$ protons	Upper bound of quench level: $8.2 \cdot 10^8$ protons	Anticipated loss causing the quench: $5.4 \cdot 10^8$ protons
Case 59	10.8	25.8	13.5
Case 61	10.6	25.9	13.2
Case 73	10.7	26.0	13.3

Table 4.9 – Fast Loss Quench Test 2013: Quench level as a function of number of lost protons (Geant4 results) and loss duration (QP3 results) for Case 73. Details of Fig. 4.34.

Number of lost protons	Loss duration [ms]	Geant4 E_{peak} [mJ/cm ³]	Geant4 E_{avg} [mJ/cm ³]	QP3 E_{peak} [mJ/cm ³]	QP3 E_{avg} [mJ/cm ³]
$4.000 \cdot 10^8$	5.5	195	66	29	11
$5.400 \cdot 10^8$	5.7	263	89	36	13
$6.000 \cdot 10^8$	5.7	292	99	36	13
$7.000 \cdot 10^8$	6.4	341	116	36	13
$7.500 \cdot 10^8$	6.8	365	124	41	15
$7.750 \cdot 10^8$	7.2	377	128	41	15
$7.900 \cdot 10^8$	7.4	385	130	41	15
$8.100 \cdot 10^8$	7.7	394	134	45	17
$8.170 \cdot 10^8$	8.0	398	135	45	17
$8.190 \cdot 10^8$	8.2	399	135	48	18
$8.195 \cdot 10^8$	8.4	399	135	53	20
$8.200 \cdot 10^8$	8.5	399	135	70	26

were multiplied by the appropriate factors without changing the root files (Geant4 output files).

The other method was provided by [134], [135] using Fluka code. This approach concerned direct implementation of a loss pattern together with an angular spread to the simulations. The resolution of loss parameters (location, angles) was determined by the resolution of orbit simulations. In contrast to the Geant4 approach, this solution is more straightforward. However the loss pattern had to be known in advance and each time a new scenario has to be simulated.

Concluding, both simulation techniques, Geant4 and Fluka, has used loss distributions from orbit simulations but the way, how these distributions were implemented, was not the same. On top of that, the simulation conditions were different regarding details of magnet representation, resolution of recording energy deposited in the magnet coils and a method of obtaining BLM signals (Table 4.10).

Energy density deposited in the superconducting coils

Physical magnet coils consist of superconducting cables immersed in the helium bath. Each cable is made of 36 strands (in the case of Main Quadrupoles) and each strand is built of ≈ 6500 NbTi filaments incorporated into a copper matrix. A representation of such a complex structure would be extremely difficult to implement to Monte Carlo simulations. Therefore, it was substituted for a simplified uniform material in both Geant4 and Fluka codes. In the case of Geant4 simulations the weighted density of 7.78 g/cm³ was applied (62.8% Cu, 15.1% Ti,

Table 4.10 – Fast Loss Quench Test 2013: Comparison of quench levels obtained using various simulation techniques.

	Geant4 simulations	Fluka simulations
Simulation strategy	Imposing loss patterns by weighting point-like losses with corresponding coefficients	Loss patterns directly introduced to the simulations
Loss pattern resolution	0.10 m	0.01 m
Impacting angle	Fixed	Changing
Transverse size	Neglected	Introduced
Coil binning	n_r n_ϕ n_z	4 90 300
Signals in BLMs	Spectra of secondary particles folded with BLM response functions depending on angular distribution	Energy deposited in N_2 divided by the mass of the gas

17.1% Nb, 5% He) concerning the inner MQ coil and Fluka used the density of 6.95 g/cm^3 . Additionally, the simulated coils were divided into sub-units to enable determining a location and magnitude of hot spots precisely. Geant4 simulations has concerned binning of $n_r = 4$, $n_\phi = 90$, $n_z = 300$ when in Fluka division of $n_r = 8$, $n_\phi = 180$, $n_z = 31$ was implemented. Due to these non-equal bin sizes used in Geant4 and Fluka codes, the data was rebinned to $n_r = 4$, $n_\phi = 90$, $n_z = 30$ (Fig. 4.35) to compare energy density distributions along the most exposed cell. The maximum energy density occurs around 0.3 m from the centre of the MQ in the case of Geant4 simulations and around 0.6 m in the case of Fluka simulations. The corresponding mean values are 0.1 m and 0.3 m, the RMS is ≈ 0.5 m in both cases. This discrepancy probably results from differently implemented superconductor densities. Additional contribution might come from considering different impacting angles. It is worth reminding that the maximum values of energy density presented in Fig. 4.35 are not equal to peak energies on the edge of the coils. E_{peak} , which is later used for calculating the quench levels, is obtained from fitting data to power law and it is determined by the transverse energy distribution.

Signals in BLMs

The calculations of BLM signals were based on completely different techniques in the case of two considered simulations. Regarding Geant4 code, two long pseudo-detectors were implemented along the magnets. This has allowed obtaining not only the BLM signals but also studying radiation in the regions which were not covered by the physical monitors. Moreover, the signals were computed by folding various particle spectra with BLM response functions.

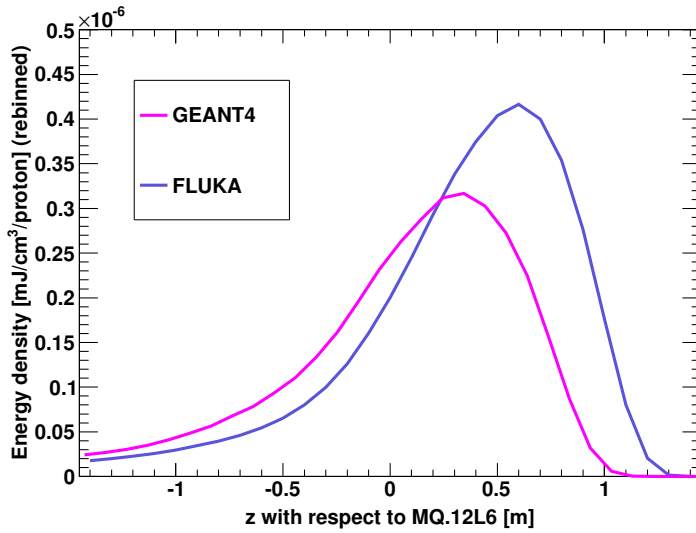


Figure 4.35 – Fast Loss Quench Test 2013: Comparison of energy density distributions along the most exposed bin obtained with Geant4 (the pink line) and Fluka (the violet line) simulations. The same coil binning was applied.

Since a reaction of an ionization chambers depends on an angle of incoming particles, the angular distributions were used for estimating contributions of different particle momenta. The decision of using this approach was based on the fact that it is faster and requires less statistics comparing to a direct conversion of energy deposited by particles in the gas filling a detector (as done in Fluka code).

Simulated BLM signals were validated with the corresponding measured values for both, Geant4 and Fluka, methods (Fig. 4.36). Geant4 data exhibits constant tendency of underestimating BLM signals (represented with dots) by a factor of 2-3. Moreover, this trend is conserved for all simulated signals. In contrast, Fluka results vary from positive to negative correlations with the highest variations in the positions of longitudinally external monitors.

Fig. 4.37 presents correspondence between Fluka and Geant4 simulations. The result of excluding two external points and fitting the data to a linear function indicates that the systematical error of using response functions is around 2. Besides that, Geant4 and Fluka simulations seem to be in good agreement.

In order to estimate accuracy between the simulations and measurements, the same procedure as in Fig. 4.32 was applied. Considering all ten monitors surveying beam 2 losses (Table 4.11) and the most probable loss scenario (Case 73), the mean value of ratios of Geant4-simulated and measured BLM signals was obtained to be 0.42 with RMS of 0.13. The corresponding values of Fluka simulations were 0.66 and 0.18. Taking into account only the central BLMs located downstream the loss location ($z = -4.445$ m to $z = 0.755$ m) Geant4 has given 0.53 ± 0.07

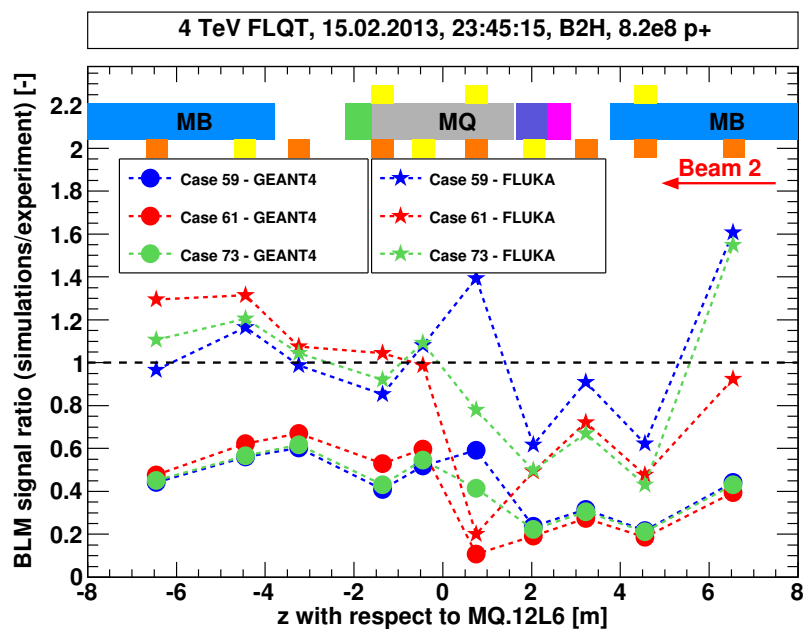


Figure 4.36 – Fast Loss Quench Test 2013: Ratios between simulated and measured BLM signals for beam 2 monitors. The dots represent Geant4 and stars - Fluka results.

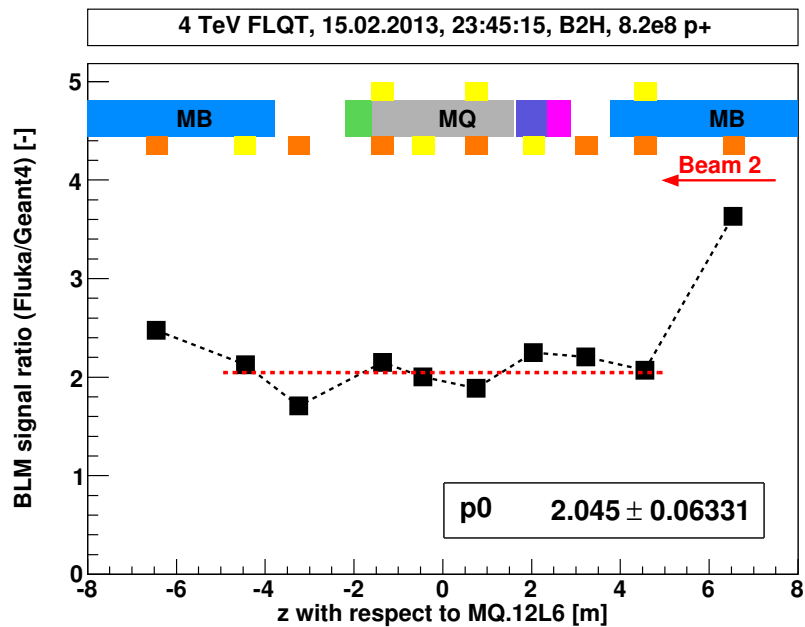


Figure 4.37 – Fast Loss Quench Test 2013: BLM signals - correspondence between BLM signals obtained with Geant4 and Fluka simulations.

Table 4.11 – Fast Loss Quench Test 2013: BLM signals - Comparison between Geant and Fluka results. The mean and RMS values are given for the calculated ratios of simulated to measured BLM signals (all beam 2 monitors).

	Geant4		Fluka	
	Mean [-]	RMS [-]	Mean [-]	RMS [-]
Case 59	0.43	0.13	0.80	0.15
Case 61	0.40	0.19	0.63	0.27
Case 73	0.42	0.13	0.66	0.18

Table 4.12 – Fast Loss Quench Test 2013: BLM signals - Comparison between Geant and Fluka results. The mean and RMS values are given for the calculated ratios of simulated to measured BLM signals (based on five BLMs located between $z = -4.445$ m and $z = 0.755$ m).

	Geant4		Fluka	
	Mean [-]	RMS [-]	Mean [-]	RMS [-]
Case 59	0.53	0.07	0.81	0.14
Case 61	0.50	0.20	0.59	0.39
Case 73	0.53	0.07	0.85	0.07

and Fluka 0.85 ± 0.07 . The same values of RMS for both simulation approaches indicate that although the absolute values are different, the accuracy is similar regarding signal variations. In view of the complexity of performed simulations and knowledge of the loss pattern, the obtained results are fairly good.

4.10.6 Quench levels - Geant4, Fluka and QP3 results

Since both Monte Carlo simulations provide results normalized per incident proton, the final quench level scales linearly with the number of protons lost during a dedicated experiment. However, the exact estimation of protons contributing to the MQ quenching during the Fast Loss Quench Test (2013) is not trivial. Although the BLM signal can be recalculated to the number of lost protons¹⁷ (Fig. 4.15), the resolution of QPS system limits the precision of assessing the moment of quenching to ± 5 ms. Moreover the synchronization between BLM and QPS is not perfect. Therefore, the following three cases were concerned for all studied loss patterns:

- loss of $4 \cdot 10^8$ protons which defines the experimental lower bound; with this intensity

¹⁷This can be done only if the loss was confined in the devoted region, i.e. no losses along the machine, especially on the collimators.

loss a resistive volume has not developed in the superconductor,

- loss of $8.2 \cdot 10^8$ protons which defines the experimental upper bound; all particles were lost on the magnet before QPS system initiated beam dumping due to magnet quenching (about 5 ms delay in effective reaction time),
- loss of $5.4 \cdot 10^8$ protons which corresponds to the last moment before sudden voltage increase on MQ.12L6; however this can be any value $\leq 8.2 \cdot 10^8$ protons since no data is available between these two neighbouring measurement points due to the resolution of QPS data acquisition. In addition to that, the voltage increase rather does not scale linearly with the number of lost protons.

Table 4.13 contains the summary of quench levels obtained with Geant4, Fluka and QP3 methods. Concerning the most probable loss scenario (Case 73) and the number of lost protons to be $5.4 \cdot 10^8$, the quench level was estimated to be ≈ 260 mJ/cm³ using Geant4, ≈ 270 mJ/cm³ using Fluka and (70 ± 40) mJ/cm³ when applying QP3 code. Although Geant4 and Fluka methods are based on different routines, they delivered consistent quench levels.

In addition to the Monte Carlo simulations, QP3 heat transfer code was used to calculate minimum quench energy. However, this Fortran program is dependent on a radial energy distribution along the most exposed cable which is derived from Geant4/Fluka simulations. Therefore, the QP3 results are biased by uncertainties and errors coming from Monte Carlo codes. The studies focused on determining the reason of the large discrepancy between the QP3- and Geant4/Fluka-estimated quench levels are ongoing.

4.10.7 Final summary and conclusions

Fast Loss Quench Test 2013 was planned precisely and performed successfully, i.e. terminated with magnet quenching. Detailed analysis of experimental observables and Geant4 simulations was provided. The quench level was estimated to be in the range of (200-400) mJ/cm³ at the magnetic field of about 2.7 T. Such wide range results from the uncertainty of assessing the number of lost protons which effectively initiated the MQ quenching. The quench levels obtained with QP3 heat transfer code exhibit large discrepancy with respect to both, Geant4 and Fluka, results. The origin of this difference remains under investigation but it is probably due to the fact that the theoretical data for the fast loss regime has never been validated with experimental observables in the case of QP3 code. Presented results are crucial for the future estimations of the BLM thresholds in the fast loss regime (milliseconds) for higher beam energies to be reached after LS 1. Applying new thresholds should approach the conditions allowing effective machine protection against UFO events and limiting unnecessary beam dumps. However, it has to be remembered that the provided quench levels were obtained for the case of primary beam losses on the aperture. In the case of UFOs, not only protons scattered on dust particles but also secondaries produced during the interactions between protons and dust particles hit the aperture. Therefore, the initial conditions regarding the

Table 4.13 – Fast Loss Quench Test 2013: Comparison of quench levels obtained with different simulation techniques: Geant4, Fluka and QP3. Note that QP3 does not consider a number of protons but the loss shape and loss duration. The given quench levels correspond to the loss pattern at the moment of loosing certain number of protons (see Table 4.9).

Method	Loss scenario	Quench level [mJ/cm ³]		
		Lower bound of quench level: $4 \cdot 10^8$ protons	Upper bound of quench level: $8.2 \cdot 10^8$ protons	Anticipated loss causing the quench: $5.4 \cdot 10^8$ protons
Geant4	Case 59	170	340	230
	Case 61	260	520	350
	Case 73	200	400	260
Fluka	Case 59	210	420	280
	Case 61	220	460	300
	Case 73	200	410	270
QP3	Case 59	30	70	40
	Case 61	30	70	40
	Case 73	30	70	40

particles lost on the aperture are different and the loss pattern is probably not the same as well. However, during the FLQT the loss duration, which is crucial quenching process, was achieved in the planned scale of millisecond (although 5-10 times longer than the UFO duration).

5 3.5 TeV Steady State Loss Quench Test 2010

5.1 Motivation

The main motivation of performing Steady State Quench Test 2010 was to validate the current BLM thresholds at nominal energies, estimate the quench levels at the timescale of seconds (steady state regime) and to study the correspondence between BLM and QPS systems.

In 2010, the BLM thresholds in the LHC were set according to the Geant4 simulations of MQ magnets [104]. These simulations were validated using data of magnet quenches at injection energy of 450 GeV (9th August 2008 and 7th September 2008, detailed description in [95]). However, they have never been tested at the nominal energy of 3.5 TeV. Moreover, these losses occurred in the fast regime and no data was available for the steady state case. Finally, the quench tests conducted at 450 GeV provided interesting results (6.10.2010, see Chapter 2), i.e. depending on the plane of inducing beam losses, different elements (MB or bus bars) quenched. Combining these three aspects resulted in the decision that behaviour of magnet system under the exposure to beam losses needed to be examined at high beam energies.

5.2 Description of 3.5 TeV Steady State Loss Quench Test 2010

The experiment was performed in cell 14R2 on 17th October 2010 [132], [136]. Since this was the first LHC quench test at the nominal energy and the current experience was based mainly on lower energy tests, precautionary solutions were required. First of all, the collimators were left un-touched at the nominal values¹ in order to ensure safe operation conditions. This means that the particles occupying space in the vacuum chamber beyond an acceptance region in the transverse plane were intercepted. Therefore, losses in remaining parts of the machine were prevented if a beam traveled along the nominal orbit (no disturbance sources). Secondly, modifications of the BLM thresholds in the vicinity of a targeted magnet were

¹During 2013 Quench Tests the mechanical aperture was increased at the location of collimators in order to avoid beam losses there. This operation allowed the number of protons lost on a quenching magnet to be calculated.

implemented very carefully. These changes were needed since during the standard LHC operation conditions, the BLM system would initiate beam extraction from the machine if losses exceeding certain thresholds were recorded. To avoid that, the BLM monitor factors were increased² by a factor of three (from 0.3 to 1.0) which corresponded to the values three times greater than the estimated quench levels. Depositing more particles in the dedicated region was allowed and hence quenching magnets. The resulting resistive volume in the superconducting coils was supposed to be detected by the QPS system.

Three pilot bunches with intensities of $(5\text{--}6)\cdot10^9$ protons were injected from the SPS to the LHC and their energy was ramped to 3.5 TeV. Since quenching the superconducting magnets was the main objective of this experiment, the three corrector orbit bump technique (see Section 1.9) was applied. This enabled particles to be distorted from their initial orbit and guided onto the target (Fig. 5.1). In addition, the dynamic mode was chosen to achieve steady state loss regime, i.e. loss duration in the order of seconds. This means that the magnetic field of corrector magnets was increased continuously in time so that the circulating particles experienced stronger deflecting forces each turn. Thus, the particles' amplitude rose in time as well. Of course, due to safety reasons, the bump was closed, i.e. behind the targeted magnet, the circulating protons were guided back to the initial orbit not to provoke losses elsewhere.

During the dedicated time slot, beam 1 was not available so it was decided to use beam 2 instead. The beam orbit was modified in the vertical plane due to the focusing properties of MQ.14R2 (focusing for beam 1 and defocusing for beam 2 in the horizontal plane). Although the quadrupole coils are symmetric (Fig. A.1), the beam screen shape is not. Therefore, some differences in quenching process were anticipated regarding the horizontal/vertical loss planes. In addition, since BLMs are located in the horizontal planes only (in the arcs), the signals from vertical losses would be much smaller than in the case of horizontal losses.

5.3 Analysis of the experimental data

5.3.1 Studies of beam intensity loss

As it was already mentioned, the knowledge of a number of protons deposited onto a targeted magnet is crucial for assessing the quench level. In this subsection a discussion devoted to the observed loss locations and their quantitative contribution to the total beam loss is presented.

The beam intensity distribution in time was measured with Fast Beam Current Transformers (FBCT) and is presented in Fig. 5.2. At the beginning of the experiment the total beam intensity of three bunches was equal approximately $1.85\cdot10^{10}$ protons. As the consequence of the applied dynamic bump, the particles were lost continuously. The shape of the loss exhibited a non-linear behaviour due to cutting transverse Gaussian³ of the beam on the aperture

²During the 2013 Quench Tests monitor factors were set to the electronic maximum of 23 Gy/s.

³An influence of cutting beam Gaussian tails on aperture limitations onto a loss shape was observed during Steady State Quench Test 2013 when a static bump was applied (see Chapter 6, Fig. 6.6). However, in 2013 QT

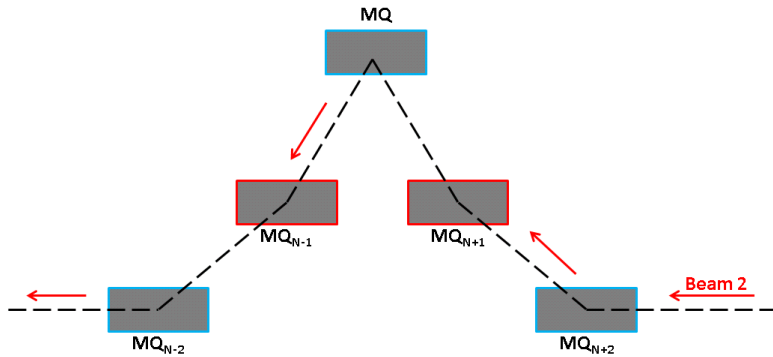


Figure 5.1 – Steady State Quench Test 2010: Diagram of the three corrector orbital bump. Corrector magnets used for changing the initial trajectory of the circulating particles are housed next to the Main Quadrupoles (MQs). Grey bars with blue frames represent magnets focusing in the vertical plane and these ones with the red frames - the magnets focusing in the horizontal plane. Beam 2 comes from the right and travels along the black dotted line. Due to the increasing magnetic field of the correctors, beam amplitude rose during the test. This finally resulted in particle deposition around the central MQ.

limitations. On top of that, the particles followed the parabolic-linear-parabolic (PLP) function of the dynamic dump[73] as the consequence of the characteristics of magnet currents. A sudden sharp decrease of the beam intensity represents the moment of beam dumping. This means that when quenching was detected, the QPS system initiated beam extraction from the machine in order to prevent further beam losses. Based on Fig. 5.2, it would be possible to calculate the number of lost protons on the target simply by subtracting the number of dumped protons ($\approx 0.75 \cdot 10^{10}$) from the initial beam intensity ($\approx 1.85 \cdot 10^{10}$). However, it could be done only if no losses occurred beyond the dedicated region or other losses were precisely controlled and measured.

In general, the three-corrector orbit bump is a very "clean" method which allows changing the beam orbit in a well-defined way within a limited region without affecting the other part of the machine. Nevertheless, during this quench test the collimators were partly closed, meaning that the particles were also lost there. Fig. 5.3 shows radiation measurements along the LHC - the highest losses appeared in two places - in the targeted region of MQ.14R2 and in IR7 where the collimation system is located. Although the BLM signal on a primary collimator was measured to be around 7.5 times smaller than the one on MQ.14R2 (Fig. 5.4), it represents significant contribution to the total beam losses. This is due to the different loss scenarios and density of materials involved in development of secondary particle showers⁴. Previous studies [138] has shown that a loss of approximately $1.2 \cdot 10^{12}$ protons on primary

around 58% of the beam was deposited which is more than only tails.

⁴The largest contribution to main magnet volumes come from collars and yokes which are made of steel (typical density of steel is [7.75-8.05] g/cm³). The LHC primary and secondary collimators [137] are mainly built of carbon fiber-reinforced carbon (typical density of CFC is [1.6-1.98] g/cm³).

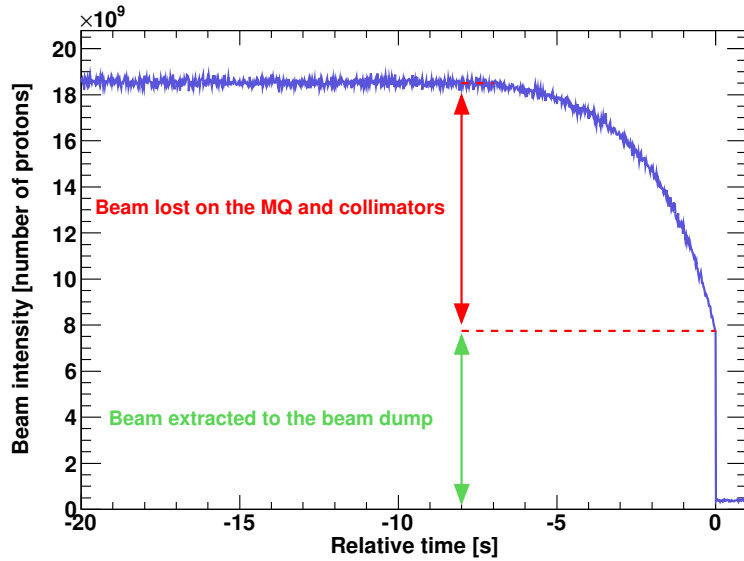


Figure 5.2 – Steady State Loss Quench Test 2010: beam intensity measurements provided by the FBCT. Zero on x-axis corresponds to the moment of the beam dump. The non-linear shape of intensity distribution results from cutting beam transverse Gaussian tails and the bump dynamic. During the experiment $\approx 1.1 \cdot 10^{10}$ protons were lost in total in MQ.14R2 vicinity and on collimators (see further analysis).

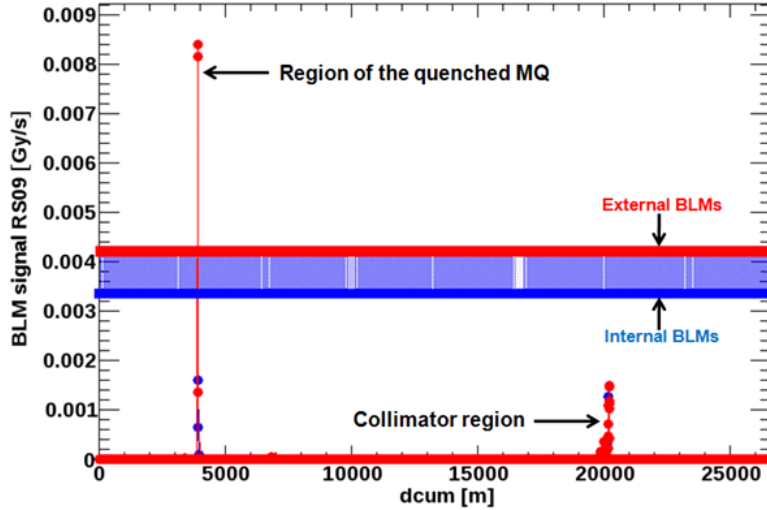


Figure 5.3 – Steady State Loss Quench Test 2010: Beam radiation along the LHC [132]. The three corrector orbit bump ensures very localized beam losses in the targeted region. However, particles were lost also in the collimator region due to the aperture limitations.

5.3. Analysis of the experimental data

collimators was needed to register BLM signal of 1 Gy. On the other hand, considering the most exposed BLM during Fast Loss Quench Test 2013 (see Chapter 4), it was calculated that BLM signal of 1 Gy corresponded to the loss of $\approx 1.1 \cdot 10^{11}$ protons on the MQ⁵. However, this value cannot be used directly for comparing signals at MQ and collimators since it was calculated for the case of horizontal losses when in 2010 the vertical loss was provided. Therefore, a factor, which was estimated to be between 2-3, was taken into account to compensate differences in BLM measurements resulting from losses in these perpendicular planes. Since the presented values were obtained for 4 TeV beam losses and SSLQT 2010 was done at 3.5 TeV, additional correction was needed. Studies presented in [139] show that the difference of 0.5 TeV between the considered values lead to a factor of ≈ 0.7 in BLM signals⁶. Combining all contributions mentioned above, it was roughly estimated that the observed BLM signal on the primary collimator ($1.13 \cdot 10^{-3}$ Gy/s) would be equivalent to a signal of about $(2.9-4.3) \cdot 10^{-3}$ Gy/s registered by a BLM mounted on the MQ⁷. This value corresponds to about (35-51)% of the signal on MQ.14R2 ($8.39 \cdot 10^{-3}$ Gy/s) measured during this experiment. Therefore, the final conclusion is that the exact number of particles lost on the MQ.14R2 during the Steady State Quench Test 2010 cannot be accurately assessed.

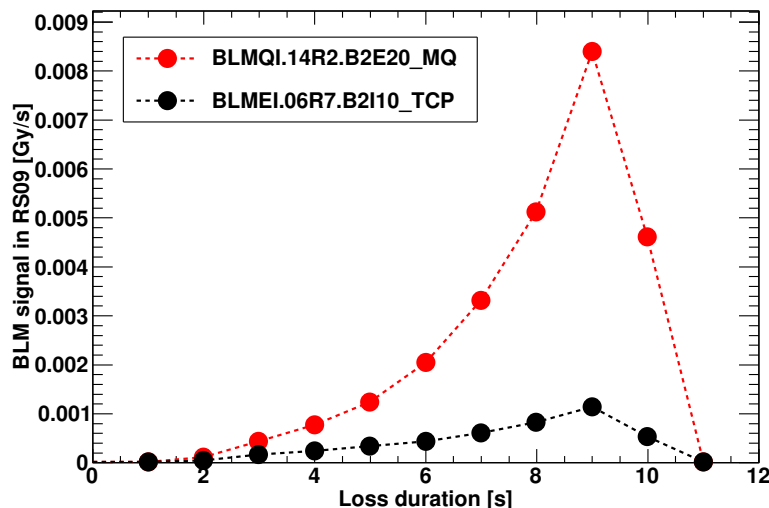


Figure 5.4 – Steady State Loss Quench Test 2010: Comparison of losses on the target and collimator. The red dots shows radiation dose measured by the most exposed BLM located on the MQ.14R2. The beam losses on a primary collimator TCP are presented by the black dots. BLM signals are given in 1.3 s integration time (RS09).

⁵During the experiment $\approx 8.2 \cdot 10^8$ protons were lost on MQ.12L6. This resulted in BLM signal of 0.73 Gy/s in 10.24 ms integration time (RS06). Therefore $\approx 1.1 \cdot 10^{11}$ protons corresponded to the signal of 1 Gy.

⁶Simulations presented in [139] show that a normalized detector signal was ≈ 0.25 in the case of 3.5 TeV beam losses and ≈ 0.35 in the case of 4 TeV.

⁷Losses on the secondary collimators were observed as well. However, they mainly constitute of secondary particles created on the primary collimators (multistage collimation system).

5.3.2 Beam position measurements

Beam position measurements were obtained using BPMs (Fig. 5.5). During the experiment, the maximum bump amplitude in the vertical plane was set to 15 mm but the MQ quenched earlier (at about 14.65 mm). Although the beam deflection was imposed only in the vertical plane (the violet curve), the changes were observed also in the horizontal plane (the magenta curve). There were several hypotheses trying to explain this additional contribution to the overall beam disturbance. The first idea concerned influence of the quadrupole field lines on the particles deviated from the ideal orbit. However, in the considered region the field changes were negligible [140], [114]. Another possibility was related to the accuracy of BPM measurements when operating with beams being close to the aperture limitations. Nevertheless, this has turned out to be around an order of magnitude smaller [141]. A probable failure of the used BPM was also taken into account but it was rejected by a detailed investigation performed by another BPM expert [142]. Therefore the presence of the horizontal beam deflection measurements remains unknown.

Measurements provided by neighbouring BPMs located the closest to the targeted magnet (MQ.14R2), allowed calculating impacting angles of incident protons. The beam position registered just before the beam dump corresponded to the angle of $202 \mu\text{rad}$. This value was later introduced to the Geant4 simulations.

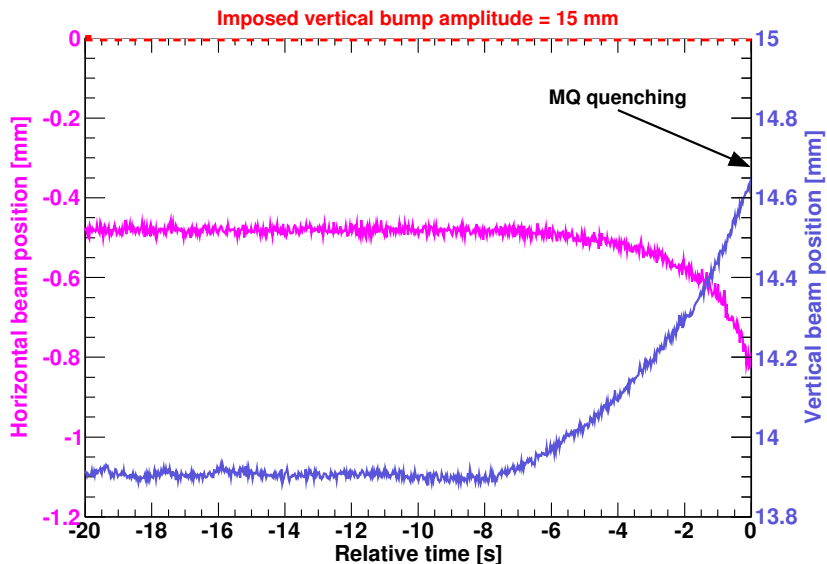


Figure 5.5 – Beam position measurements provided by the BPMs. Zero on x-axis corresponds to the moment of the beam dump. Although the bump was imposed in the vertical plane (the violet line) the deflection of beam orbit in the horizontal plane was observed (the pink curve) as well.

5.3.3 BLM signals and loss evolution

A loss pattern, i.e. a number of incident protons lost along the magnets, cannot be derived directly from the experiment since no such detectors are installed in the machine. However, Beam Loss Monitors (BLMs) located close to the positions, where the highest losses are anticipated, allow studying development of secondary particle shower originating from proton losses.

Fig. 5.6 shows the relative positions of six standard BLMs with respect to the arc Main Quadrupole centre. Three monitors survey losses related to beam 1 and three others - losses coming from beam 2. The first and the last monitors (for each beam) are installed close to the interconnection regions (MB-SSS⁸, SSS-MB). Over there increased radiation occurs due to the lower density environment (vacuum pipes, helium tubes) which particles need to pass through. Therefore, the particles can effectively travel much further than in the case of dense material components of the magnet cold mass. The positions of central detectors are adjusted so that the losses appearing in the MQ are registered. The origin of these losses is directly related to the beam optics and the presence of the β -function maximum. Due to the emittance conservation along the accelerator, this leads to the largest values of beam size.

A comparison of radiation dose measurements provided by BLMs in the vicinity of MQ.14R2 is presented in Fig. 5.7. Knowing that a peak of the secondary particles occurs around 1 m from the loss location, the highest signal of B2E20 confirms that the particles were lost in the region of MQ cryostat (in the MQ magnet and/or front correctors). On the other hand, low signal of B2E10 denies the presence of significant losses upstream the MQ and in the interconnection region SSS-MB. Very interesting information comes from B2E30 measurements. Although this monitor is located around 2.5 m downstream the end of the MQ cryostat, it registered roughly the same signal as B2E20. Such a configuration has not been found in 2013 Quench

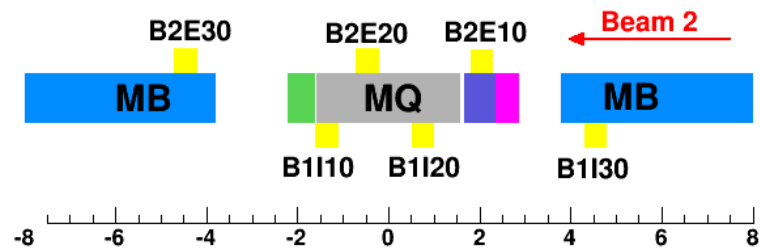


Figure 5.6 – Steady State Loss Quench Test 2010: Locations of BLMs. The Main Quadrupole (MQ, grey bar) is located between two Main Dipoles (MBs, blue bars). The MQ is represented by the green bar, the MS - violet bar, MCBV - the pink bar. BLMs are shown as yellow bars - three upper BLMs survey losses of beam 2, three others are devoted to monitoring beam 1 losses. In cell 14R2 beam 2 travels in the external aperture. The red arrow indicate direction of beam motion.

⁸SSS - Short Straight Section, see Chapter 1

Tests where correlations between the corresponding monitors were completely different and loss pattern studies revealed that the loss was very narrow (Fig. 6.13). The ratio between the middle and the last BLM was calculated to be $\frac{S_{B2E20}}{S_{B2E30}} \approx 1$ (also confirmed in RS12), when for the SSLQT 2013, $\frac{S_{B2I20}}{S_{B2I30}} \approx 2.5$ (from Fig. 6.6) and for the FLQT 2013, $\frac{S_{B2I20}}{S_{B2I30}} \approx 4$ (from Fig. 4.13). This indicates that the loss induced with the dynamic bump was widely spread over the length of the MQ. However, the beam screen shape asymmetry between the horizontal and vertical planes might also affect the shape of the secondary particle cascade. This could be due to the different distances between beam screen edges from the beam pipe surface (Fig. A.1) and thus, unequal amount of medium with low density (vacuum) which particles pass through. In addition, in the case of vertical losses, the BLMs are not located against the losses but aside of them, i.e. not on top/bottom of the magnet but on the right/left sides. The presented tendency in the correlation between corresponding BLM signals (S_{B2E20} and S_{B2E30}) is conserved up to 10% (1.0 ± 0.1) during the entire loss duration (right plot in Fig. 5.8). The shape of cross-talk registered by beam 1 monitors comes from the transverse distribution of the secondary particle shower (the left plot). However, interpretation of correlation between beam 1 and beam 2 BLM signals is difficult difficult to estimate. This is due to non-equal transverse distances from the loss location (both in the transverse and longitudinal planes) to monitors installed on the opposite sides of the MQ cryostat (difference of about 20 cm transversely).

Fig. 5.9 shows loss evolution in time and space for beam 1 (left plot) and beam 2 (right plot) monitors. Although relation between B2E20 and B2E30 signals stays almost constant, it does not apply to the correspondence with B2E10 measurements.

In order to estimate loss development in time, the ratios between consecutive BLM signals were calculated in the function of time (Fig. 5.10). The red dots represent $\frac{S_{B2E20}}{S_{B2E10}}$ and the blue squares show $\frac{S_{B2E30}}{S_{B2E20}}$. In contrast to the constant correlation between the middle and the last beam 2 monitor signals, ratio $\frac{S_{B2E20}}{S_{B2E10}}$ changes significantly in time exhibiting loss evolution. This is probably mainly because of the increasing in time magnetic field of the correctors (dynamic bump) which resulted in rise of impacting angles of incident protons. Therefore, the relative distance between loss location and these two monitors changed in time as well. Taking into account that the maximum radiation outside a magnet occurs around 1 m downstream the loss location it can be concluded that the loss of the primary particles moved in time from the first half of the magnet towards the front part of the magnet. In addition, lack of any major changes of $\frac{S_{B2E30}}{S_{B2E20}}$ during the loss duration implies that the loss length was much larger than the differences in loss locations resulting from angle decrease.

5.3.4 Development of the beam loss and onset of the quench

The energy deposited inside the superconducting coils by the lost protons cannot be derived directly from the experiment. However, using Monte Carlo simulations, it can be correlated with the corresponding radiation dose measured outside magnets with BLMs. On the other hand, the consequences of energy deposition can be observed in the form of developing

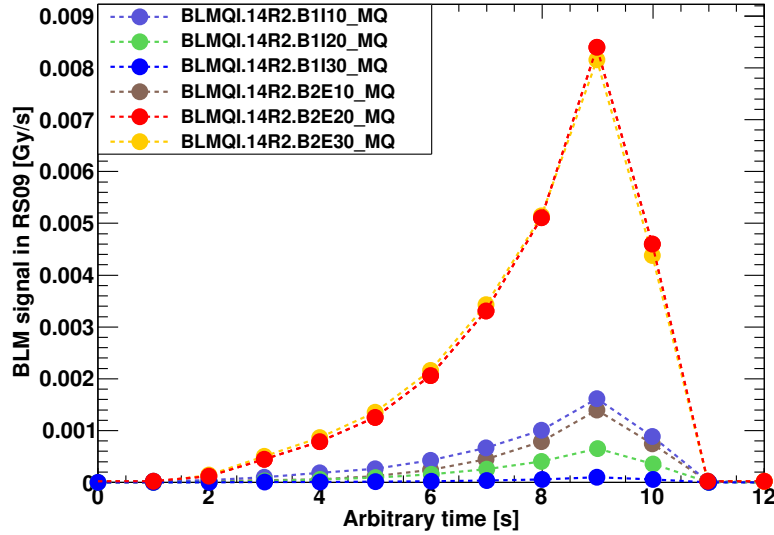


Figure 5.7 – Steady State Quench Test 2010: BLM signals in time (RS09). The highest radiation was measured by B2E20 and B2E30. These two signals are almost the same during the whole loss duration. Comparison with 2013 Quench Tests indicate that the loss was widely spread over the magnet length.

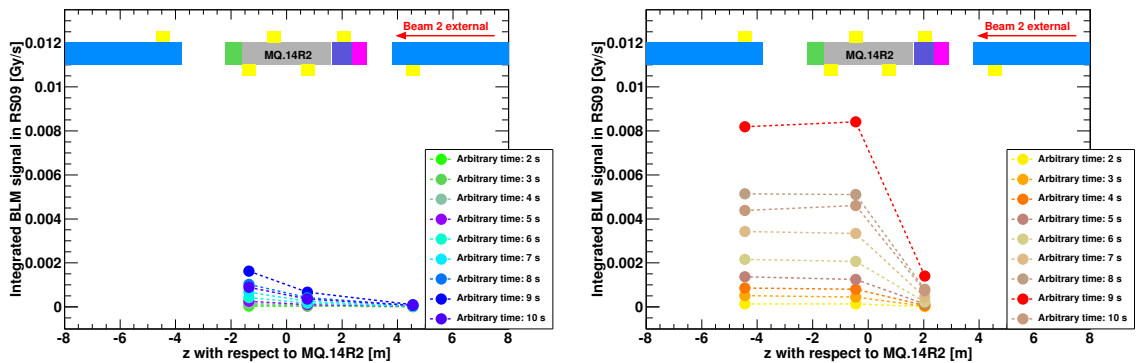


Figure 5.8 – Steady State Quench Test 2010: Longitudinal radiation distribution in consecutive time steps of 1 s is based on RS09 measurements. The ratio between B2E20 and B2E30 is conserved up to 10% (1.0 ± 0.1). The shape of cross-talk registered by beam 1 probably comes from the transverse distribution of the secondary particle shower. Left plot - signals measured by beam 1 monitors. Right plot - beam 2 BLM measurements.

Chapter 5. 3.5 TeV Steady State Loss Quench Test 2010

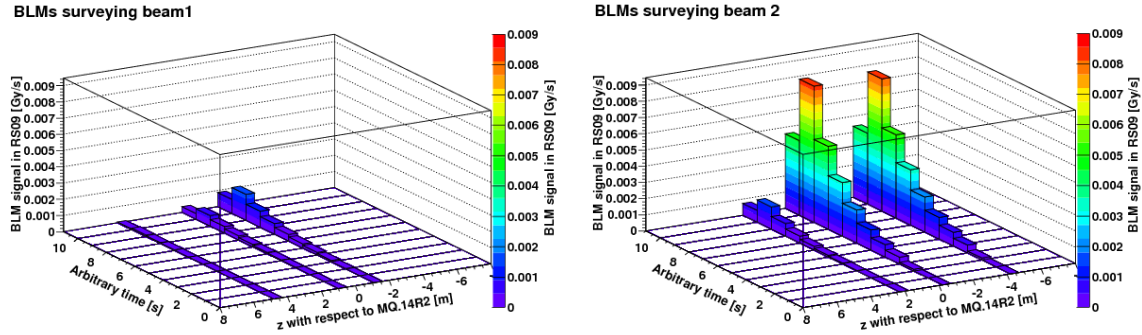


Figure 5.9 – Steady State Quench Test 2010: Radiation distribution in space and time (BLM signals in RS09).

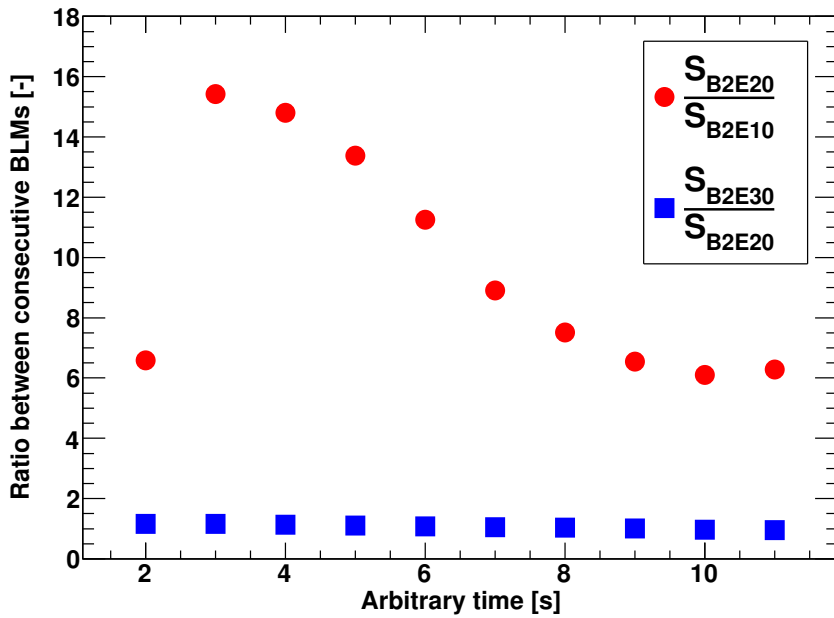


Figure 5.10 – Steady State Quench Test 2010: Loss evolution in time. The ratios between consecutive BLM signals are presented. The correlation between B2E20 and B2E30 signals remains constant and close to 1 during entire loss duration. The behaviour of $\frac{S_{B2E20}}{S_{B2E10}}$ exhibits development of the secondary particle shower in time.

resistive volume if one of the characteristic parameters, i.e. the temperature, exceeded the critical value. Therefore, it is important to study the correspondence between BLM and QPS observables in order to understand quenching process evolution. The accuracy of such a comparison is limited due to two main aspects:

- different time resolution of voltage and radiation measurements (the BLM system provides data every 40 μ s when QPS system acquires signals every 5 ms; therefore the QPS limits the overall synchronization between these two systems),
- lack of synchronization between BLM and QPS systems.

Fig. 5.11 presents correspondence between radiation dose measured by the most exposed BLM (B2E20, green curve), absolute value of voltage difference between two MQ.14R2 poles (U_QS0_EXT, red curve) and intensity loss (black curve) in time with respect to the moment of the beam dump (20:23:13, local time). The BLM signals are synchronized with respect to the moment of the beam dump. The first 78 ms of PM buffer contain radiation dose measurements before the beam extraction from the machine and the last 4 ms after include data acquired after the dump. The accuracy of this condition was verified by comparing B2E20 signal decrease at the moment of dumping with simultaneous increase of radiation at the position of the dump kicker (MKD) and the dump (not presented in the plot). The QPS signals were adjusted with respect to the condition of detecting quenching. This means 10 ms when the U_QS0_EXT was equal or greater than 100 mV. Additional 5 ms were taken into account for activating beam extraction and triggering quench heaters (pink curve).

Initially constant radiation (within the considered region; note that the loss lasted several seconds) dose suddenly started increasing at about $t \approx 50$ ms. However the resistive component occurred about 25 ms earlier and rose steadily till $t \approx 15$ ms. These two signals do not follow the same function which implies that the quench process is non-linear.

5.4 Analysis of the Geant4 simulations

Historically, the Geant4 simulations of 2010 Steady State Quench Test were provided before the simulations of 2013 Quench Tests (see Chapter 4). The difference between these simulations are mainly related to:

- magnet representation - the upstream MB and the interconnection SSS-MB were not implemented since it was assumed that the loss would occur in the MQ region,
- division of sensitive detector - the binning in radial plane was smaller, i.e. $\Delta n_r = 3$ ($\Delta n_r = 4$ in the case of 2013 simulations),
- position of the particle gun - particles hit the surface of the beam screen in the vertical plane and they were centered in the horizontal plane, impacting angle of 202 μ rad was applied,

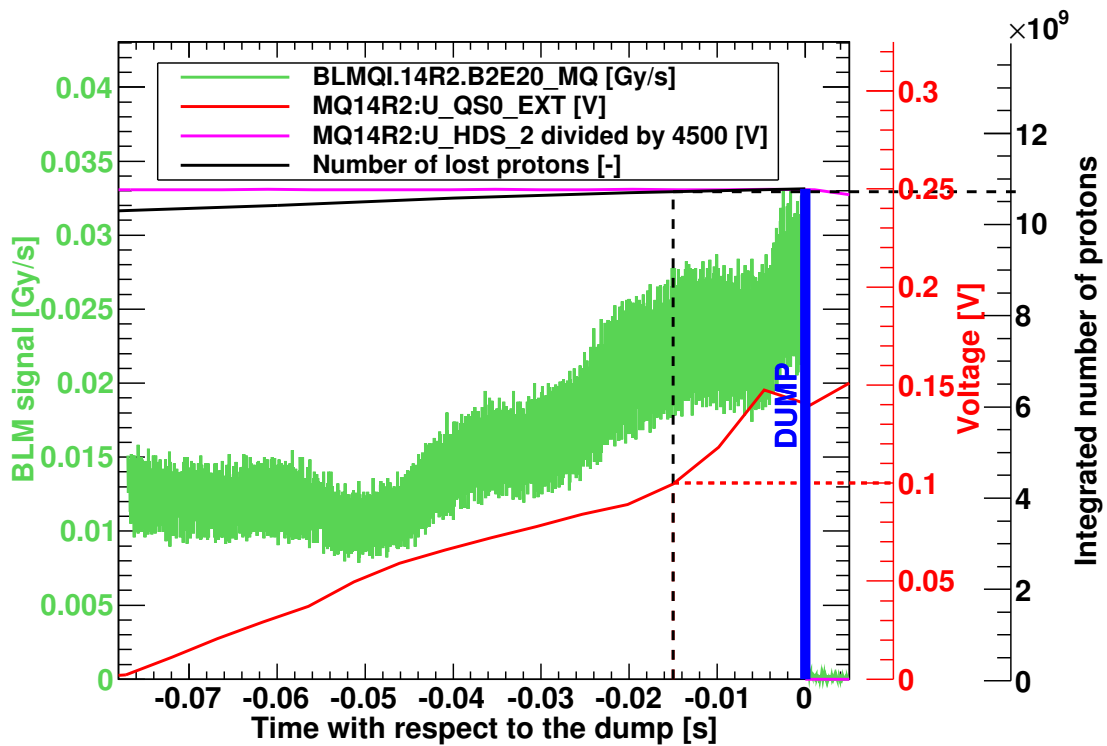


Figure 5.11 – Steady State Quench Test 2010: Summary plot of BLM and QPS signals at the moment of quenching. The green curve shows the radiation dose recorded by the most exposed BLM B2E20 within the last 78 ms before quenching. The voltage measured between two poles of MQ.14R2 is represented by the red curve. The number of total lost (on the magnet and collimators) protons is given by the black line. The pink line shows the voltage drop on the quench heaters as a part of magnet protection ensured by the QPS system.

- no secondary particle killing⁹ (in 2013 simulations, particles beyond the position of longitudinally external monitors were killed in order to decrease computing duration),
- vertically focusing magnetic field for 3.5 TeV beam.

Therefore, since different loss scenarios are considered in the case of 2013 QT (horizontal loss) and 2010 QT (vertical loss), geometrical asymmetries (the shape of the beam screen, locations of BLMs) and slightly changed simulation conditions have to be taken into account when comparing these two experiments.

In total 71 point like losses were simulated in the range from -4 m to 3 m with respect to the MQ.14R2 centre with step of 0.1 m. Since during the experiment no mobile monitors

⁹In Geant4 nomenclature, "killing a particle" means that a particle's track and correleted physics (i.e. energy, etc.) are deleted.

were installed, the simulations considered only six standard BLMs (on the stage of analysis; long pseudo-detectors were implemented to the code in the same way as in the case of 2013 simulations).

5.4.1 Evolution of applied methods for assessing the loss pattern

At the moment of performing the experiment (2010) and also in a few following years (until beginning of 2013), the knowledge of incident particle distribution when applying a three corrector orbit bump was limited to scientific hypotheses¹⁰. Since these ideas were based on several parameters (position of the loss maximum, loss spread, shape of the loss distribution) and they evolved many times, a fast and robust method was required to validate them. Therefore, it has been decided to simulate many point-like losses along the region, where the quench test was performed. The loss shape was imposed by weighting data by appropriate coefficients corresponding to an assumed loss shape. Since this was done on the stage of analysis, the Geant4 simulations were not affected and the data could be used many times without repeating a very time consuming process of simulations. A fixed angle, resulting from BPM measurements, was applied for all loss locations. The longitudinal beam size was taken into account indirectly through the loss shape. The transverse beam size was neglected.

The evolution of applied approaches leading to assessing the loss pattern can be observed in two publications written by the author. At the beginning a single point like loss in the centre of the MQ was considered [132]. The choice of the location was based on the presence of the β -function maximum. During the next step, a spread loss distribution substituted the single point-like loss method [136]. Two the most probable cases were considered - one in the centre of the MQ and the other one in the centre of the corrector magnet MCBV (due to the maximum bump amplitude). Moreover, it was assumed that the primary beam had a Gaussian shape and thus, the resulting loss on the beam screen plane should also exhibit similar properties. This means that if no external forces would act on the beam, the loss size would be a simple projection of the beam onto the surface of the beam screen as in the case of vertical losses inside MB magnets. The vertical beam size was measured with a Wire Scanner (WS) located in Point4 ($\sigma_{WS,ver} = 876 \mu\text{m}$). Knowing the value of β -function [143], [144] at the position of the apparatus ($\beta_{WS} = 404.55 \text{ m}$) the emittance was calculated by applying the following formula

$$\epsilon = \frac{\sigma_{WS,ver}^2}{\beta_{WS}} \quad (5.1)$$

Since emittance ($\epsilon = 1.9 \cdot 10^{-3} \mu\text{m}$) stays constant along an accelerator (no beam blow-up was anticipated during the test), it was possible to calculate beam sizes at the position of the MQ and MCBV. Taking into account $\beta_{MQ} = 184 \text{ m}$ and $\beta_{MCBV} = 176 \text{ m}$ (Fig. 5.12), the corresponding beam sizes were calculated to be $\sigma_{MQ,ver} = 591 \mu\text{m}$ and $\sigma_{MCBV,ver} = 577 \mu\text{m}$. Assuming the constant impact angle of $202 \mu\text{rad}$, this would result in directly projected

¹⁰Extensive studies on loss patterns started in fall 2012 in CERN Technology Department (mainly by [133] and were devoted to upcoming Quench Tests at 4 TeV (done in 2013).

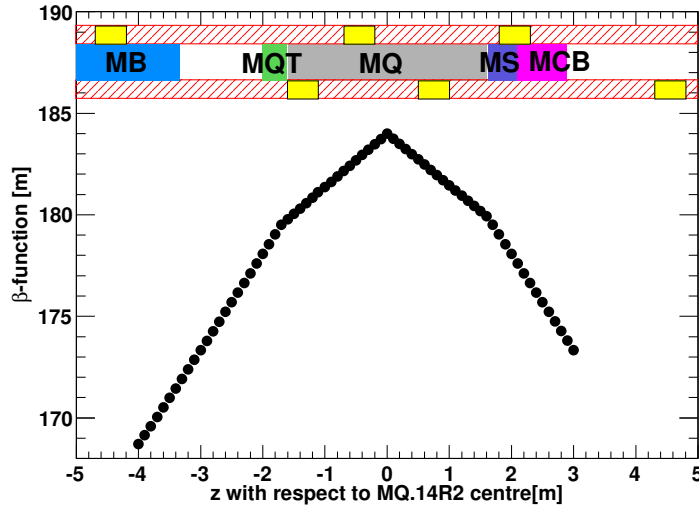


Figure 5.12 – Steady State Quench Test 2010: β -function at 3.5 TeV along the simulated region. In the MQ centre ($z_{MQ} = 0$ m) β -function reaches its maximum ($\beta_{MQ} = 184$ m). In the centre of the corrector magnet MCBV ($z_{MCBV} = 2.5$ m), $\beta_{MCBV} = 176$ m. Note that only the β -function values at the locations of magnets are taken from jmad. Remaining values were obtained from linear interpolation.

losses with sizes of $\sigma_{MQ,ver,loss} = 2.92$ m and $\sigma_{MCBV,ver,loss} = 2.86$ m, respectively. However, charged particles experience strong focusing fields when traveling through a quadrupole magnet. Therefore, the assumption of constant impact angle is not valid and the presented simple calculation cannot be applied any more. Since no direct beam size measurements could be done at the assumed loss locations, it was decided to use Eq. 3.5 for studying the correspondence between measured and simulated BLM signals the as the function of beam size changes. The thesis stated that the smaller $\Sigma_{\mu,\sigma_r,\sigma_l}^{norm}$ (μ -the mean of Gaussian distribution, σ_r and σ_l are standard deviations of the right and left parts of the normal distribution), the more probable the case is. Based on that, the estimated loss sizes were obtained to be $\sigma_{MQ,ver,loss} = 1.7$ m and $\sigma_{MCBV,ver,loss} = 3.2$ m. Because the influence of the magnetic field should result in a decrease of beam loss length, it was deduced that the loss in the MQ was more likely.

The final idea of assessing loss patterns resulted in developing the Geant-Quencho-Meter program (GQM, see Chapter 3). Besides, considering user-specified loss patterns, it enables finding the best fitting (to observables) loss patterns. Moreover, this approach is correct only if the correspondence between simulated and measured BLM signals would be 1:1. The program provided iteration over point-like losses to find the best fitting mean value μ of the Gaussian distribution. In addition two other free parameters related to beam loss sizes, σ_l and σ_r , were implemented. This allowed introducing asymmetry of Gaussian shape which could change as the result of strong magnetic field.

Summing up, the presented strategy of assessing loss patterns was based on two main principles:

- a primary beam has a Gaussian distribution,
- the particle loss shape is the effect of the beam shape and the trajectory of the particles.

Therefore, the loss shape can posses a non-Gaussian, asymmetric structure.

5.4.2 Presentation of GQM results

The analysis which is presented in the following part of this chapter rather shows the method of assessing loss patterns than provides final conclusions. This is due to the fact that the case study based on orbit simulations (MAD-X) provided for 2013 FLQT confirmed that Geant4 simulations underestimate BLM signals by a factor of 2-3 (this was previously reported in [95] and [115]). The performed comparison of results (loss distribution, energy distribution in coils, signal in BLMs) obtained using MAD-X loss patterns and those one obtained with GQM showed significant divergence.

The GQM considers loss patterns (determined by the values of μ , σ_l and σ_r , see Section 5.4.1) in user-defined ranges and for each case calculates corresponding BLM signals. The results are compared to the measured values using a simulation-experiment similarity estimator (Eq. 3.5). The minimum of $\Sigma_{\mu, \sigma_r, \sigma_l}^{norm}$, i.e. the squared sum of the normalized differences between simulated and measured BLM signals, determines the most probable loss scenario (assuming perfect correspondence between simulated and measured BLM signals) for the assumed loss location and loss shape. Since the operation of imposing different loss shapes is done on the level of analysis, this approach allows considering thousands of different scenarios in relatively short time (about 2000 cases per hour of PC time).

Fig. 5.13 - Fig. 5.14 show how $\Sigma_{\mu, \sigma_r, \sigma_l}^{norm}$ evolve for a fixed μ and varying σ_l and σ_r factors. For each case only one global minimum exists.

According to the applied algorithm, the location of μ was estimated to be (0.4 ± 0.1) m from the MQ.14R2 centre. For this value, a color map of $\Sigma_{\mu, \sigma_r, \sigma_l}^{norm}$ as a function of beam size σ_l and σ_r is presented in Fig. 5.15. The minimum of the simulation-experiment similarity estimator is marked with a black dot which coordinates were found to be $\sigma_{left} = (1.40 \pm 0.14)$ m and $\sigma_{right} = (1.54 \pm 0.15)$ m. The surrounding region, where $\Sigma_{\mu, \sigma_r, \sigma_l}^{norm} \approx 1.2$, exhibits certain blur with respect to the symmetry line given by the white dotted line. This seems to confirm influence of the magnetic field forces onto the loss shape.

The loss pattern corresponding to the best fitting scenario is shown in Fig. 5.16. Although, these results are given only to present the applied method, such wide spread of lost proton distribution would be in good agreement with observed stable correlation of measured B2E20

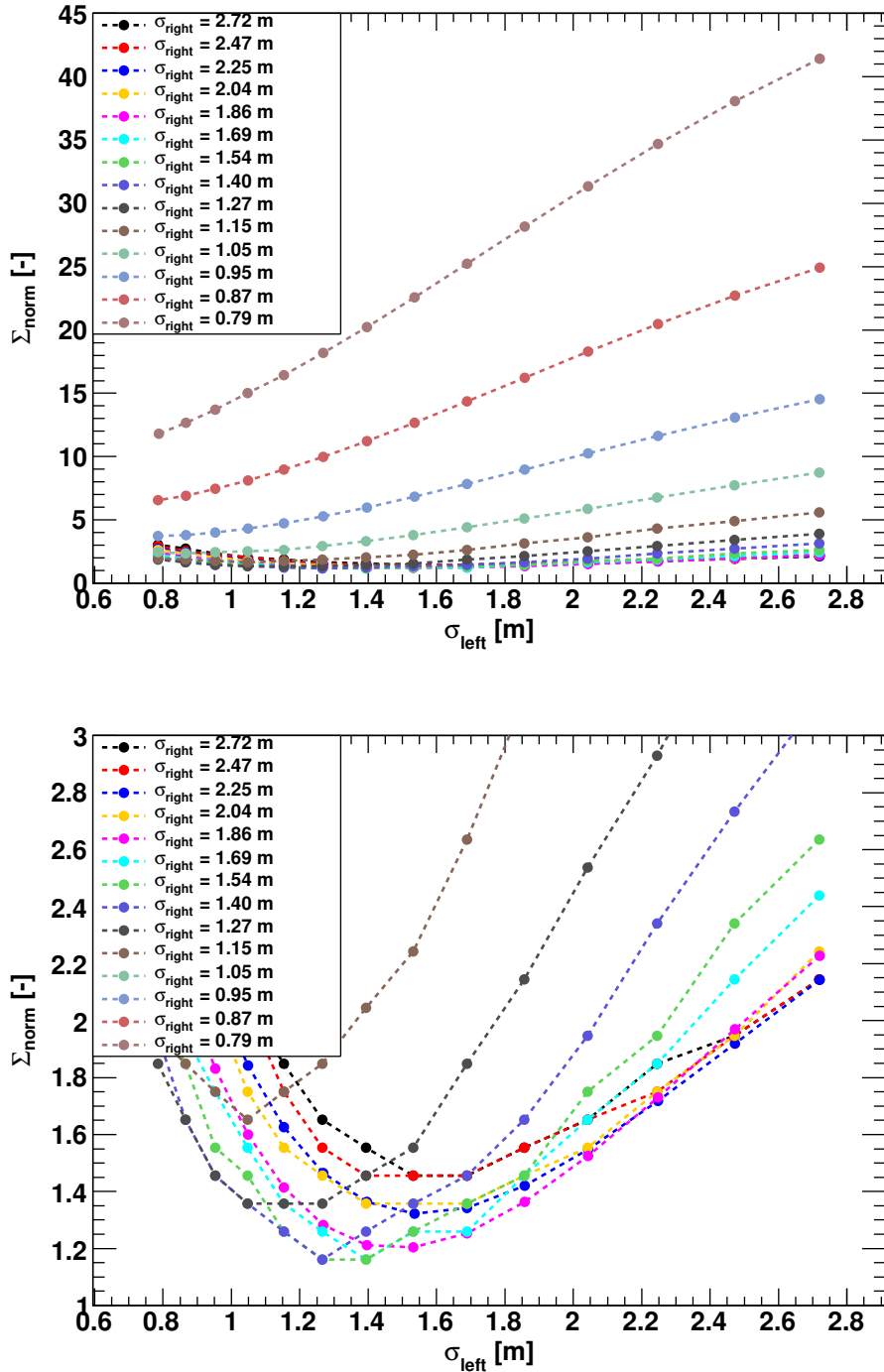


Figure 5.13 – GQM results - Evolution of $\Sigma_{\mu, \sigma_r, \sigma_l}^{\text{norm}}$ as a function of σ_l for varying values of σ_r . For each function only one global minimum exists. The bottom plot shows magnification of the top plot.

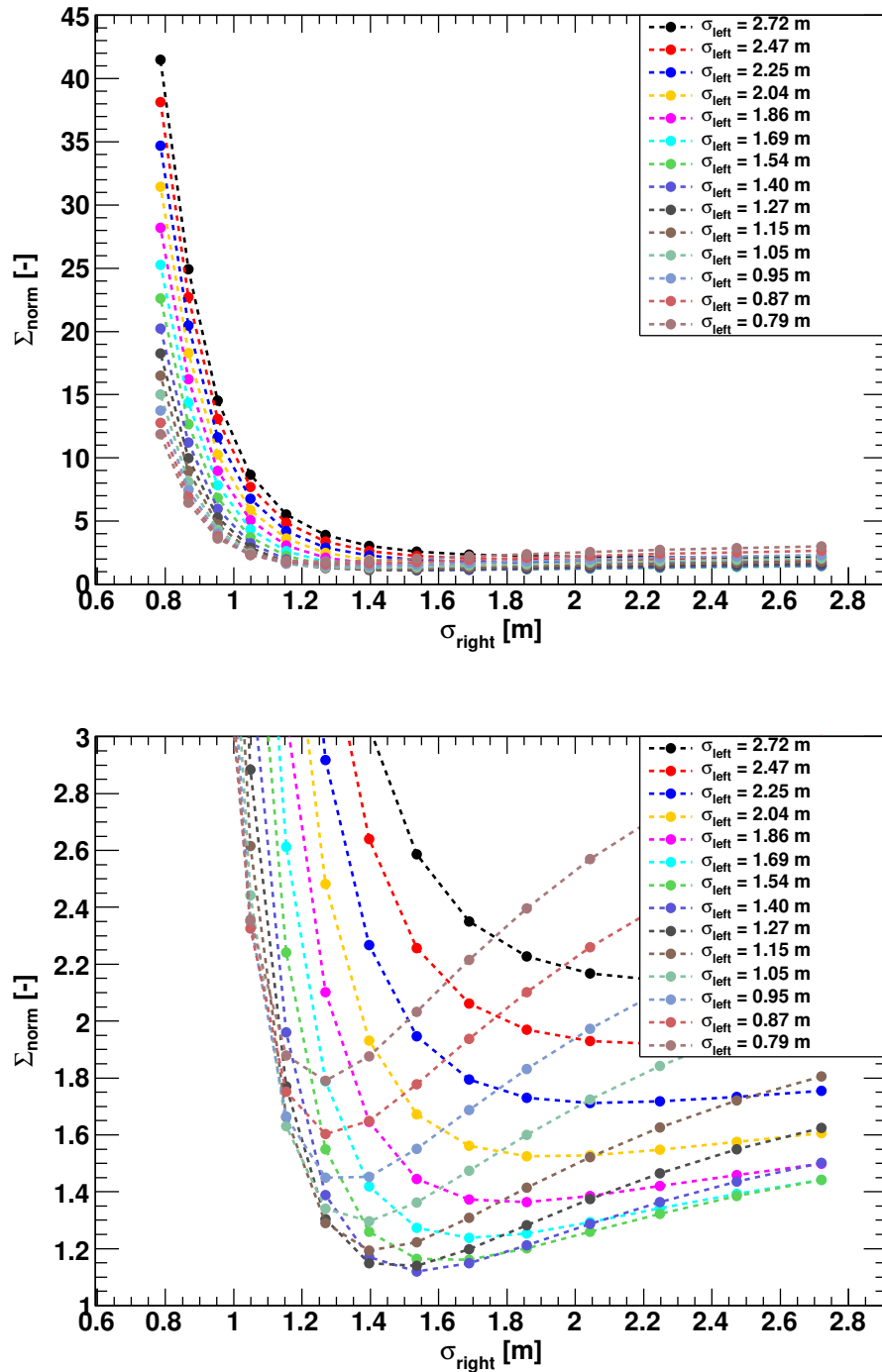


Figure 5.14 – GQM results - Evolution of $\Sigma_{\mu, \sigma_r, \sigma_l}^{norm}$ as a function of σ_r for varying values of σ_l . For each function only one global minimum exists. The bottom plot shows magnification of the top plot.

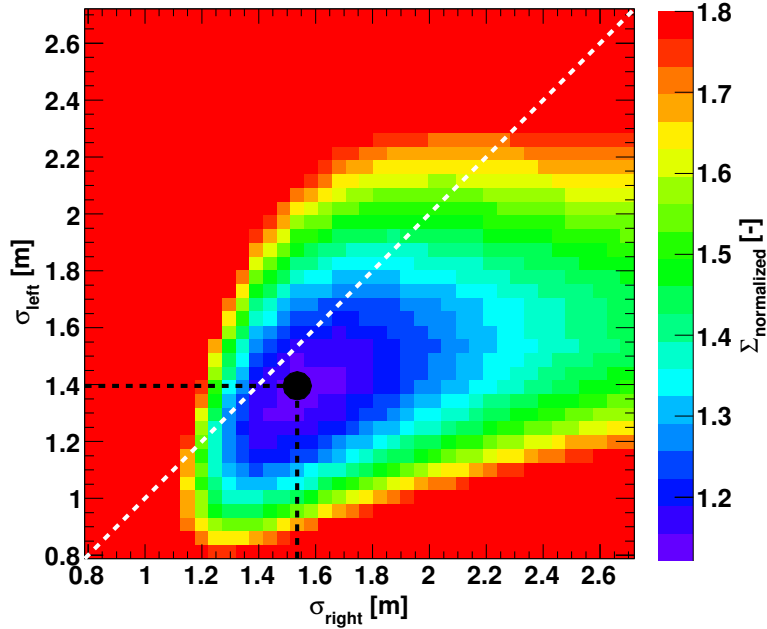


Figure 5.15 – GQM results - distribution of $\Sigma_{\mu, \sigma_r, \sigma_l}^{norm}$ as a function of σ_l and σ_r . White dotted line determines the symmetry boundary. The minimum of the simulation-experiment similarity estimator is marked with a black dot which coordinates are $\sigma_l = (1.40 \pm 0.14)$ m and $\sigma_r = (1.54 \pm 0.15)$ m.

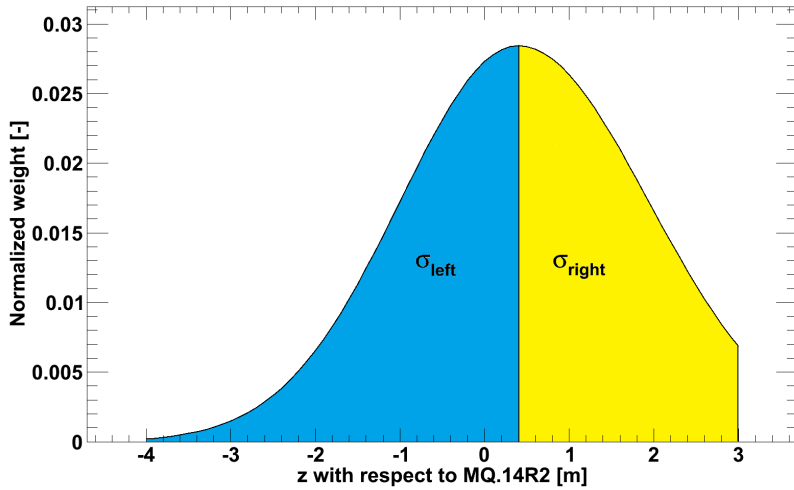


Figure 5.16 – Steady State Quench Test 2010: Loss pattern obtained using GQM. The best fitting (to the measured BLM signals) results, i.e. the smallest $\Sigma_{\mu, \sigma_r, \sigma_l}^{norm} = 1.14$, was obtained for $\mu = 0.4$ m, $\sigma_l = (1.40 \pm 0.14)$ m and $\sigma_r = (1.54 \pm 0.15)$ m.

and B2E30 signals (Fig. 5.10). However, it has to be kept in mind that Geant4 simulations underestimate signals of simulated BLMs.

Fig. 5.17 shows the correlation between the energy density distribution along the most exposed bin of the MQ superconducting coil (the red curve) and the number of secondary particles reaching pseudo-detectors (the black curve) for the estimated loss pattern. The maximum of deposited energy occurred in the second half of the MQ ($z \approx -0.5$ m) with respect to the beam motion (beam 2 coming from the right) reaching the averaged (over the unit cell volume) value of $E_{max} = 0.3 \cdot 10^{-6}$ mJ/cm³/proton. The most numerous population of secondary particles was recorded in the interconnection region between the downstream MB and the MQ. Since this distribution does not provide information on the type, energy and impacting angle of the secondary particles, it cannot be directly used for estimating BLM signals. However, it gives the first estimates of the radiation outside the magnets.

The radial distribution of energy deposited across the most exposed bin is presented in Fig. 5.18. The simulation results were fitted to the power law (Eq. 4.4) in order to calculate the energy deposited in each of 18 stands of the superconducting cable. Therefore, this distribution could be used as an input to the QP3 heat transfer code. Based on these calculations, the average energy density was obtained to be $E_{avg} = 0.16 \cdot 10^{-6}$ mJ/cm³/proton. By multiplying this value by the number of protons impacting the quenching magnet, the quench level could be estimated.

The BLM signals are calculated taking into account a type and energy of secondary particles reaching the monitors (see Section 3.4.2). As the result of using detector response function, the Geant4-based signals are given per proton. Therefore, the population of lost protons on the magnet needs to be known in order to obtain the signal in Gy which is later compared to the measured values. However, in 2010 SSLQT it is not possible to assess the loss intensity. Therefore, for these considerations the total value of $1.1 \cdot 10^{10}$ protons was used. Fig. 5.19 shows the ratios between simulated and measured BLM signals in the case of integrated loss (over the entire loss duration). Since the main task of the GQM was to find the best fitting scenario, these ratios were expected to be around 1 and for the estimated loss scenario indeed varied from ≈ 0.6 to ≈ 1.1 .

By now, the integrated loss was considered. However, to study time-dependent loss evolution a minimum value of $\Sigma_{\mu, \sigma_r, \sigma_l}^{norm}$ has to be found for shorter time windows. Fig. 5.20 shows obtained results for $\Delta t = 1$ s when assuming a number of protons lost at each step proportional to the total loss. This allowed improving the parameter $(\mu, \sigma_r, \sigma_l)$ fitting by at least factor of 2 (for time dependent case $\Sigma_{\mu, \sigma_r, \sigma_l}^{norm}(t) = (0.1-0.5)$). Fig. 5.21 presents how the radiation dose would develop in time if no experiment-simulation errors would affect the GQM results. Based on this approach it would be also possible to investigate the development of resistive volume inside the superconducting coils.

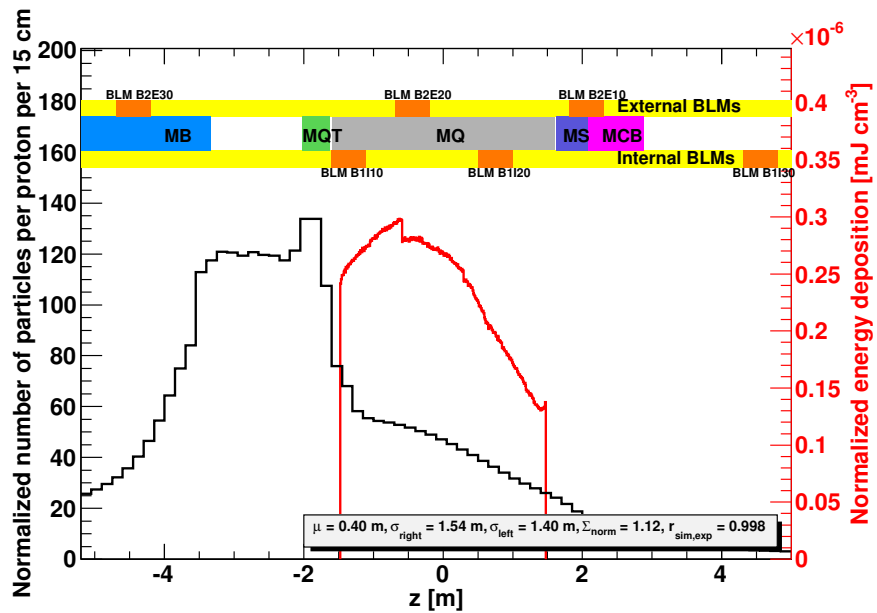


Figure 5.17 – Steady State Quench Test 2010: Energy density distribution in the SC coil and the number of secondary particles reaching the pseudo-detectors.

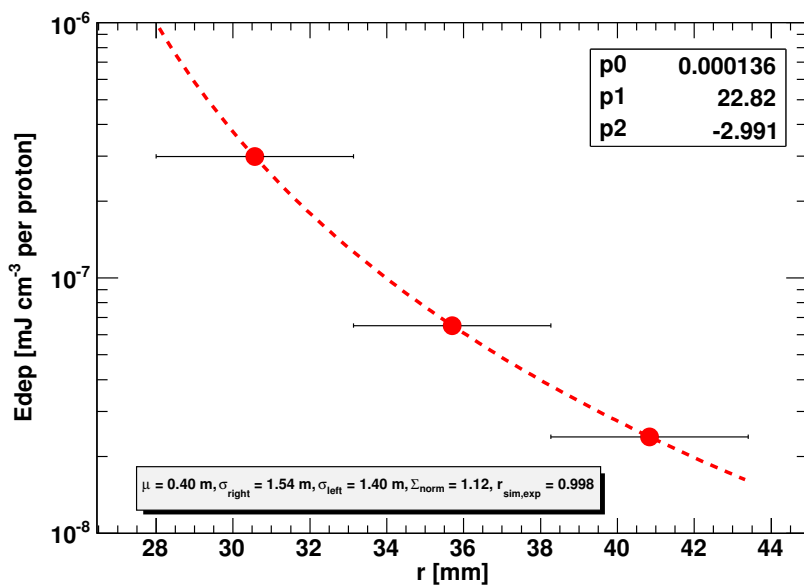


Figure 5.18 – Steady State Quench Test 2010: Radial distribution of energy density along the most exposed bin.

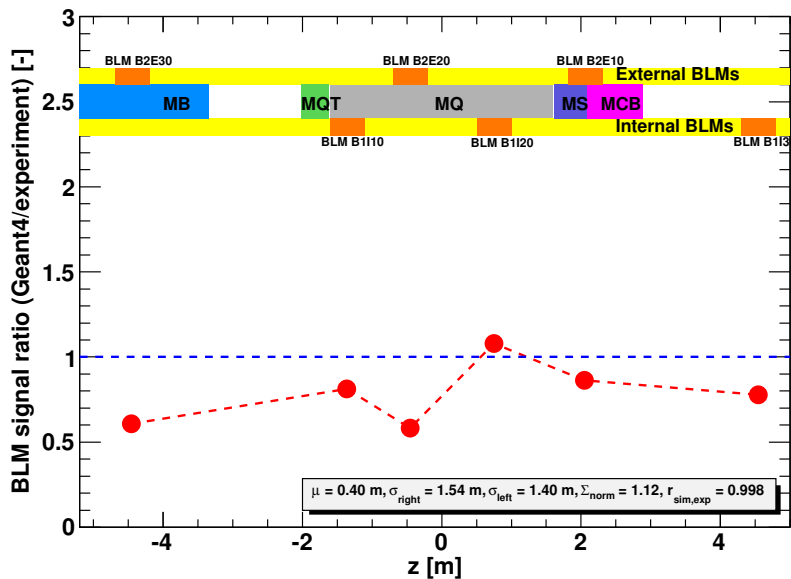


Figure 5.19 – Steady State Quench Test 2010: Ratios between simulated and measured BLM signals for the best fitting scenario. The values oscillate around 1.

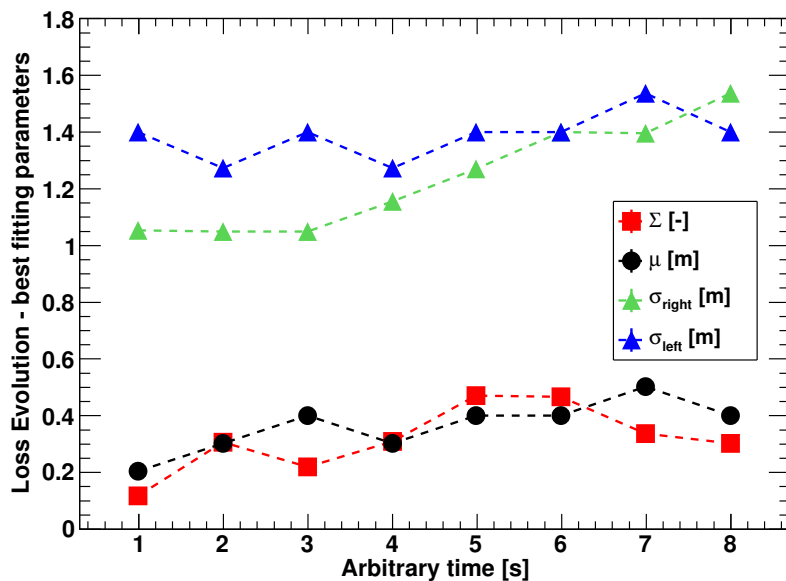


Figure 5.20 – Steady State Quench Test 2010: Time dependent loss pattern evolution. Considering shorter time steps allows lower $\Sigma_{\mu,\sigma_r,\sigma_l}^{norm}$ to be achieved, meaning better agreement between simulated and measured values.

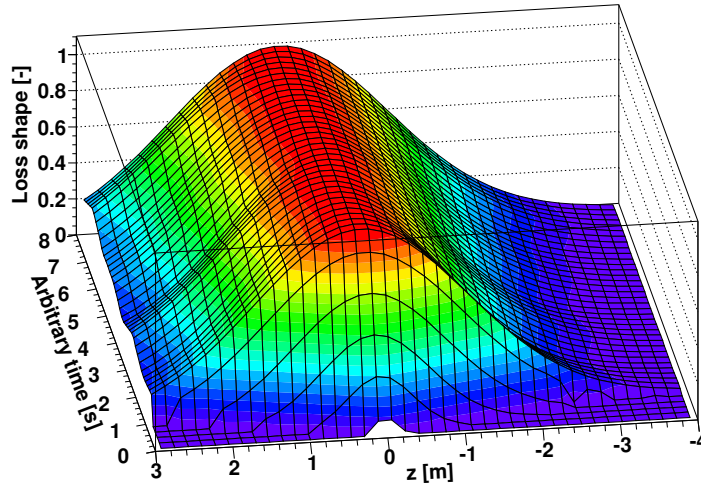


Figure 5.21 – Steady State Quench Test 2010: Although contribution of method uncertainty is dominating (both from the experiment and simulations), this plot shows how the loss shape could evolve in time. The loss shape is determined by the number of protons lost on the aperture.

5.4.3 Summary of assessing quench levels

The data analysis presented in this chapter constitutes a prologue to the 2013 Quench Tests since Steady State Quench Test 2010 was the first such an experiment performed at the nominal energy. The first part of this chapter showed quantitative contribution of two aperture limitations to the total loss of beam intensity. In addition, the analysis of secondary particle shower development was estimated using radiation measurements. The correspondence between BLM and QPS systems was provided. In the second part, the history of different approaches of assessing quench levels was presented.

The summary of 2010 SSLQT results obtained when using different simulation and computation approaches is given in Table 5.1. The maximum energy density deposited on the surface of beam screen was calculated from fitting data to the power law and is represented by E_{max} . The average value of energy density along the entire cable consisting of 18 strands (one of two layers) is given by E_{avg} . Since their values are expressed in $\text{mJ/cm}^3/\text{incident proton}$, in order to estimate the quench level of MQ.14R2 they needed to be multiplied by the total number of protons lost on the magnet. Since this value cannot be accurately calculated, the total loss of $1.1 \cdot 10^{10}$ protons was assumed for estimating Geant4 quench levels, $Q_{L,G4}$. The corresponding values obtained with QP3 heat transfer code are given by $Q_{L,QP3}$ and regardless of the applied method, they are around 0.5 J/cm^3 .

Due to many uncertainties related to both, experimental (losses on collimators, non-constant

5.4. Analysis of the Geant4 simulations

Table 5.1 – Steady State Loss Quench Test 2013: Summary of quench limits obtained with different simulation approaches. E_{max} -maximum energy deposited on the surface of the most exposed cable, E_{avg} -average energy deposited along the cable, $Q_{L,Geant4}$ - quench level calculated from Geant4 data assuming the beam loss of $1.1 \cdot 10^{10}$ protons (overestimated, since losses occurred also on the collimators) and loss duration of 5.6 s, $Q_{L,QP3}$ - quench level obtained using QP3 code.

	E_{max} [mJ/cm ³ /p]	E_{avg} [mJ/cm ³ /p]	$Q_{L,Geant4}$ [mW/cm ³]	$Q_{L,QP3}$ [mW/cm ³]
Point-like loss in the centre of MQ	$3.85 \cdot 10^{-6}$	$0.60 \cdot 10^{-6}$	1082	89
Spread loss with max in the MQ centre	$0.27 \cdot 10^{-6}$	$0.14 \cdot 10^{-6}$	257	98
Spread loss with max in the MCBV centre	$0.22 \cdot 10^{-6}$	$0.11 \cdot 10^{-6}$	213	98
Loss pattern based on GQM results	$0.99 \cdot 10^{-6}$	$0.16 \cdot 10^{-6}$	307	71 – 89

loss rate) and simulation (underestimation of BLM signals) conditions, the accurate quench level could not be obtained. Hence, the analysis of SSLQT 2010 shows rather the structure of possible algorithms than provides the final quench levels. However, the experience collected during this test was crucial when deciding on operational conditions for the next experiment in the steady state regime. This concerned a method providing constant loss rate in time and losses concentrated only within a targeted magnet. The continuation of studies devoted to assessing quench level in steady state regime is presented in the following chapter. The better controlled beam behaviour and two limiting loss cases allowed obtaining conclusive and reliable results.

6 4 TeV Steady State Loss Quench Test 2013

6.1 Motivation

Steady state losses are defined as losses lasting long enough (> 1 s) so that heat transfer from a superconducting coil to the liquid helium bath, in which the conductor is immersed in, and its further flow to the cryogenics system play a crucial role. Efficiency of this process is probably mostly determined by pores in cable insulation which constitute channels for helium. In accelerators, steady state release of energy to magnets is mainly related to slow beam losses originating in beam cleaning, synchrotron radiation, electron-cloud losses, image current losses, beam particle scattering and luminosity losses[145]. This means that they are unavoidable during machine operation and the quench level of superconducting materials has to be specified in this timescale.

A series of Quench Tests were performed in October 2010 at 450 GeV and 3.5 TeV. However, the results were ambiguous. During the experiments at 450 GeV, depending on the beam (beam 1/beam 2) and loss plane (horizontal/vertical), either no transition to the normal conducting state occurred or the development of a resistive volume was observed in one of the Main Dipoles neighbouring to the targeted Main Quadrupole. In addition, in two cases the beam was dumped due to the quenching of bus bars. According to the nominal energy beam tests (3.5 TeV), there was only one event when the Main Quadrupole quenched after distorting beam 2 in the vertical plane (17th October 2010, see Chapter 5). The loss of approximately $1.1 \cdot 10^{10}$ protons in 5.6 s was sufficient to initiate irreversible propagation of resistive zone. Nevertheless, the loss rate was increasing in time (maximum of $4.5 \cdot 10^9$ protons per second) and no constant losses could be ensured.

In 2012, the knowledge on quench level of the superconductors in the steady state loss regime was mainly based on the measurements [95], [104] and only one fully successful experiment at the nominal energy[132],[136]. Therefore, a repetition of the steady state quench test at 4.0 TeV was required in order to revise current thresholds. In addition a developed method of inducing many second losses characterized by a constant loss rate, i.e. a three corrector orbit bump combined with the ADT white noise excitations mode, was provided.

The second motivation of performing this experiment was studying the quench level with respect to the loss scenario. The Collimation Quench Test was expected to deliver approximately the same power to LHC magnets but not in the form of a direct proton beam but in the form of a massive shower of secondary particles originating in a beam hitting the collimators.

6.2 Description of the Steady State Loss Quench Test

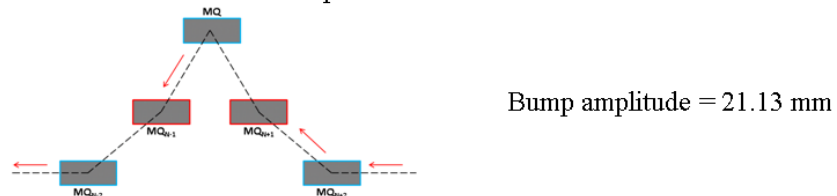
The experiment was conducted on 16th February 2013 as the last test of 48 hour long Quench Test slot. The location of this experiment (cell 12L6) was the same as for the Fast Loss Quench Test (see Chapter 4) due to the safety issues and the fact that seven additional mobile BLM monitors were installed there to increase spacial resolution of radiation measurements.

Since this test directly proceeded the Fast Loss Quench Test (15.02.2013) all BLM thresholds were set to the electronic limit in order to prevent the BLM system to activate the beam dumping process. In other words, beam losses were permitted to provoke quenching and the transition to the normal conducting state was expected to be detected by the QPS system.

1. Injecting three sets of eight pilot bunches with total intensity $< 2.7 \cdot 10^{11}$ protons 0.45 TeV

2. Ramping to the nominal energy 4 TeV

3. Creating the dynamic three corrector orbit bump until losses occur



4. Reducing the bump to 20.36 mm

5. Gating the ADT on only first eight bunches



6. Blowing up the gated bunches in the horizontal plane

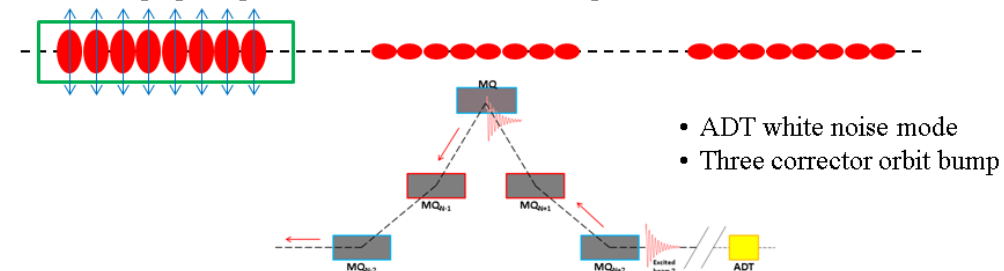


Figure 6.1 – Diagram of the procedure applied during the Steady State Loss Quench Test (16.02.2013).

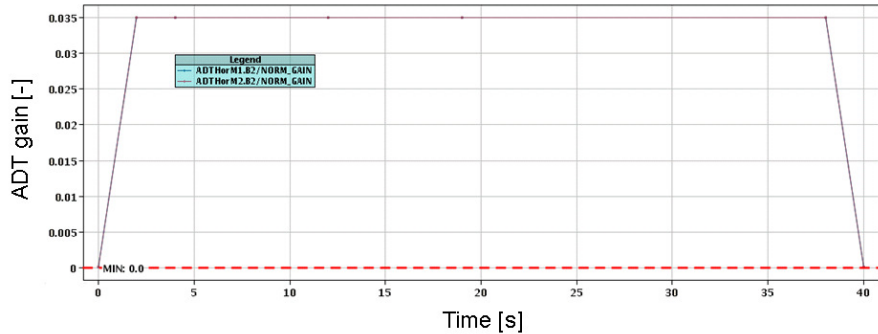


Figure 6.2 – The ADT excitation function used during the Steady State and the Collimation Quench Tests [147]. The total excitation window is 40 s.

The SPS delivered three groups of eight pilot bunches to the LHC (Fig. 6.1). The total beam intensity had to be less than $2.7 \cdot 10^{11}$ protons to fulfill requirements of relaxed Safe Beam Flag (SBF, see Section 4.8). Moreover, it was decided to inject 24 lower intensity bunches (10^{10} protons) instead of a several nominal bunches with 10^{11} protons to minimize the consequences of a potential asynchronous beam dump¹. During the injection to the LHC, each set of bunches consisted of two trains² of fours bunches separated by approximately $1.25 \mu s$ (Injection³ Scheme Single_36b_4_16_16_4bpi9inj). This needed to be applied since the maximum length of the ADT excitation window is $10.5 \mu s$ and all bunches constituting a single set had to be confined in this range. In addition these three sets of bunches were at least $5 \mu s$ apart from each others in order to avoid the bunches from outside the chosen region being affected. Otherwise more than eight bunches could experience excitations due to the ADT field rising and decaying edges. The next step of the test was to increase the beam energy from 450 GeV to 4 TeV. In contrast to the Fast Loss Quench Test, here neither the octupoles were set to zero nor chromaticity changed since the beam oscillations should be naturally dumped in the case of switching off the ADT. Such settings were applied in order to ensure beam stability. A increasing inwards three corrector orbit bump was created until losses were observed (bump amplitude equals 21.31 mm). This was followed by opening horizontal and skew collimators not to have any beam losses there. Further, the bump was reduced to 20.36 mm not only to permit long losses (i.e. not to lose too much beam in too short time) but mostly to prevent other two sets of bunches from being disturbed.

There were two attempts during which eight bunches were gated by the ADT system and blown up using the white noise mode. Combining this with the created three corrector orbital

¹An asynchronous beam dump corresponds to the situation when an activation of an extraction kicker field is not synchronized with a beam abort gap. In this case a large amount of energy would be stored in the matching section and at the beginning of the dispersion suppressor region [61], [146].

²A bunch train is a group of bunches which are injected together to a machine from its pre-accelerator.

³According to the nomenclature of filling schemes [128], Scheme Single_36b_4_16_16_4bpi9inj denotes that 36 single bunches were injected to the LHC and 4 pairs of bunches were expected to collide in IP1 (IP5), 16 pairs of bunches would collide in IP2 and and 16 collision would be provided in IP8. There would be 9 injections from the SPS to the LHC in total. Each transfer would constitute of maximum 4 bunches.

bump, which changed the aperture limitation, allowed the beam to be deposited exactly in the targeted region of Main Quadrupole MQ.12L6.

Fig. 6.2 shows the ADT excitation function which was used during both, the Steady State and the Collimation Quench Tests. After approximately 2 s the excitation level is constant in time. The process terminates after 40 s from its initialization.

6.3 Analysis of the experimental data

6.3.1 Characteristic of the beam losses

Beam intensity evolution in time

The same first eight bunches were excited twice with the same experimental settings (ADT excitation function, bump amplitude) before the Main Quadrupole quenched. The first excitation (Fig. 6.3) resulted in around 37 s long non-linear losses. The loss duration was slightly shorter than the ADT time window (40 s) since very likely parts of initial and final slopes of the excitation functions are below a threshold of inducing losses. In this step the tails of the transverse Gaussian distributions were cut off - around $6.1 \cdot 10^9$ protons in total were lost on the aperture expressing a shape of the polynomial of second degree⁴. Nevertheless, this was insufficient to provoke the magnet transition to the normal conducting state. The second excitation was characterized by the loss of protons almost constant in time (around $3.1 \cdot 10^8$ protons per second). Around 20 s long loss resulted in quenching of the targeted Main Quadrupole (MQ.12L6). Therefore, the obtained results of the Steady State Quench Test are in good agreement with the predictions as it was expected that the threshold loss rate at 4 TeV would be around $(2 - 3) \cdot 10^8$ protons per second.

The Transverse Damper excitation window was very precise and acted only on the specified set of bunches. This is confirmed by the bunch by bunch intensity measurements shown in Fig. 6.4. Three groups of eight bunches are presented at different stages of the experiment: just before the excitations (the green dots), after the first excitation (the blue dots) and just before the beam dump (the red dots). The decrease in bunch intensities can be only observed in the case of the first group of the bunches which were gated by the ADT.

Loss structure and loss duration

The radiation measurements of the BLM which was the most exposed to the radiation of the secondary particles (BLMQI.12L6.B2I20) are shown in Fig. 6.5. Zero on x -axis corresponds to the maximum of the recorded signal. During the first excitation (the green curve) the loss increased linearly in time reaching the maximum radiation dose of 1.8 mGy/s in RS09

⁴During the second excitation beam intensity, I_{beam} , loss in time, t , expressed a shape of the polynomial of second degree, i.e. quadratic function given by $I_{beam}(t) = 8.149 \cdot 10^{10} - 1.619 \cdot 10^9 t - 3.687 \cdot 10^6 t^2$. There is no physical explanation of that - the values are given for the quantitative comparison.

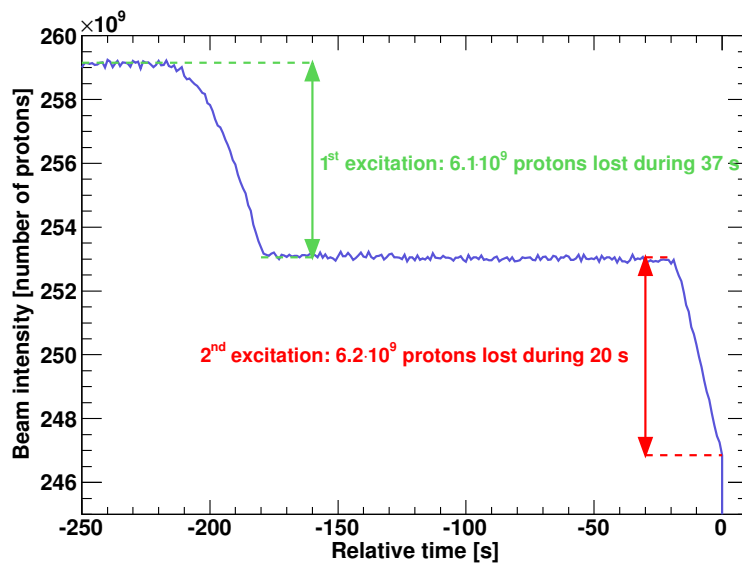


Figure 6.3 – Beam intensity measurements provided by the FBCT (LOBW). Non-linear losses occurred during the first beam excitation. The second beam distortion resulted in the MQ quenching.

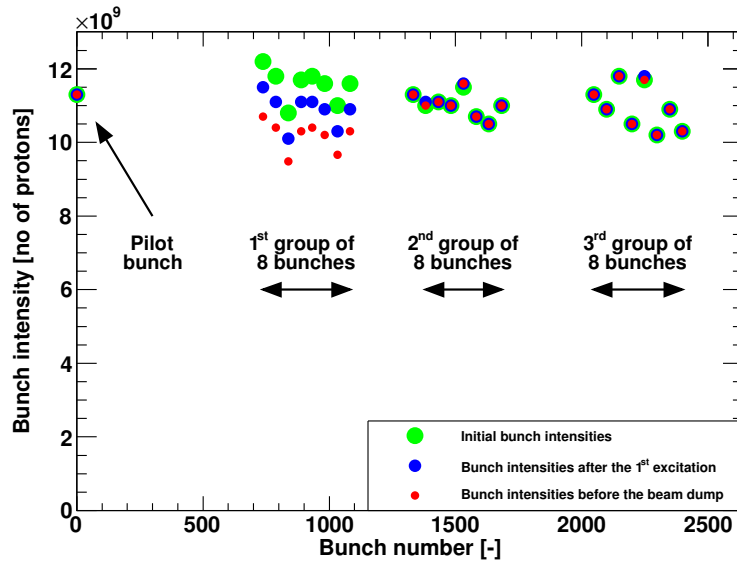


Figure 6.4 – Bunch by bunch beam intensity measurements provided by FBCT. Three groups of eight bunches were injected to the LHC. Their intensities as presented: just after the injection (the green dots), after the first ADT induced excitations (the blue dots) and just before the beam dump (the red dots). Only first eight bunches were manipulated during the experiment.

(integration time of 1.3 s). The loss almost constant in time (the red curve) was achieved during the second attempt - here the peak value was 2.3 mGy/s. The total integrated doses were 52 mGy and 56 mGy correspondingly. The small margin between the obtained safe and critical radiation levels confirms that the BLM signals at quench had been assessed correctly in the steady state regime.

Propagation of secondary particle radiation measured by BLMs

Regarding loss propagation studies, it is important to consider the BLM RS (running sum, i.e. integration time) which is longer than the loss duration in order not to loose part of the signal. Therefore, in these studies (Fig. 6.6) the longitudinal distributions of radiation dose samples probed by BLMs are presented along the magnets in RS12 (83.89 s). The highest signals in the case of both excitations (red line - termination with quench, green line - no quenching) were observed mainly in the second part (with respect to the beam direction) of the MQ and the downstream MB. This loss shape indicates that the losses occurred in the first half of the MQ and very close to the magnet center since usually the peak signal of radiation outside the magnets appears around 1 m from the loss location. Fig. 6.5 shows that during the 1st excitation of the set of eight bunches the induced losses increased non-linearly in time and applying the same ADT excitation function resulted in constant losses during the 2nd attempt. This probably resulted from cutting the transverse Gaussian tails of bunches. In order to verify an impact of this mechanism on the longitudinal loss distribution the BLM signals were normalized to one incident proton (Fig. 6.7, left plot) and the ratios between the corresponding BLM signals were calculated (the right plot). These results indicate that the losses provoked by the ADT white noise mode are spatially repeatable in spite of different time structure of the losses (Fig. 6.5). The temporal loss structure related to the transverse particle population might be the reason of slightly lower signals (around 6%) of the 1st excitation.

In order to compare the influence of the applied excitation modes, i.e. ADT sign flip mode (Fast Loss Quench Test) and ADT white noise excitation (Steady State Quench Test), the BLM signal distributions along the magnets were normalized per impacting proton for the cases of FLQT (Fig. 6.8, left plot, black dots) and SSLQT (red dots). Surprisingly, the results show that regardless on the loss pattern (see Fig. 6.13), the radiation dose measured by the corresponding BLMs located on the downstream MB, interconnection MB-SSS and at the end of the MQ are almost exactly the same and in this region the shape of the cascade is conserved. Only the first half of the MQ is affected by the loss scenario, which results from different excitation methods. As the previous plot shows the consequences (radiation dose of the secondary particle shower) of loosing a single proton, the right plot in Fig. 6.8 shows the comparison of absolute BLM signal distributions. This means that the records were normalized to 1. In this case, the radiation shape seems to be almost the same up to the end of the MQ. Nevertheless, it has to be kept in mind that the data used for the presented comparison was acquired during two different integration times, i.e. RS06 (10.24 ms) was used for FLQT and RS12 (83.89 s) was used for SSLQT. Overall, this aspect also has to be taken into account.

6.3. Analysis of the experimental data

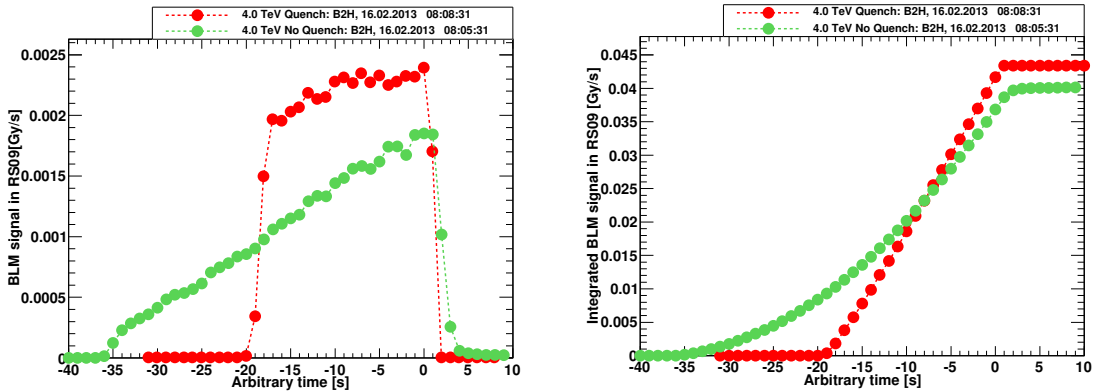


Figure 6.5 – Radiation dose measured by the most exposed BLM (BLMQI.12L6.B2I20) during eight bunch excitations. In both cases the same experimental conditions (ADT excitation function, bump amplitude) were applied. First attempt did not result in the transition to the normal conduction state (green curve). The second ADT excitation caused quenching of MQ.12L6 (red curve).

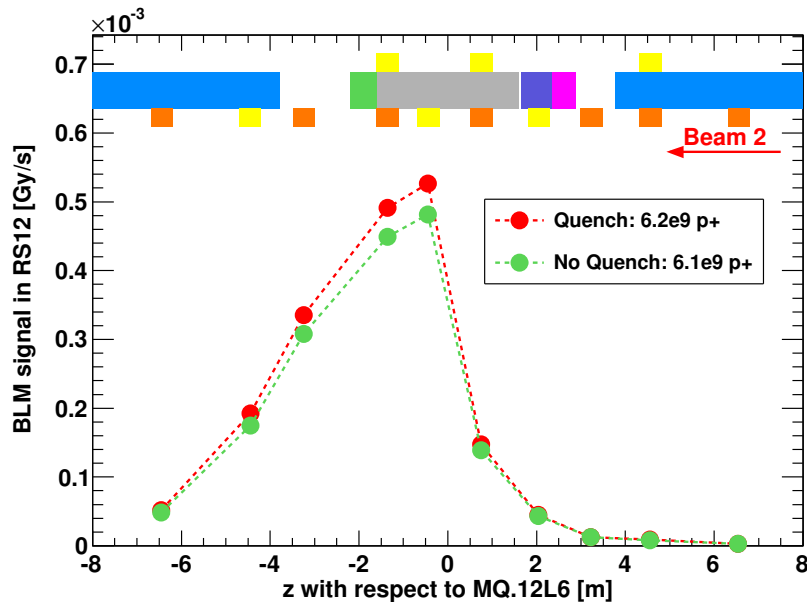


Figure 6.6 – SSLQT 2013: Longitudinal loss propagation measured by BLMs in RS12 for two excitations of the same set of bunches provided by the ADT. The first excitation caused losses of $6.1 \cdot 10^9$ protons (green dots) and was insufficient for inducing magnet quench. The second attempt resulted in losing $6.2 \cdot 10^9$ protons (red dots) which caused magnet transition to the normal conducting state. The difference in signals is very small. Beam 2 comes from the right.

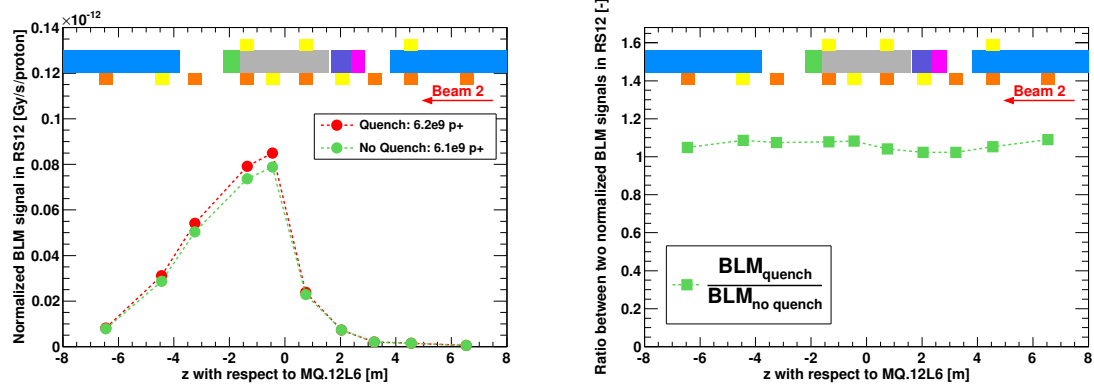


Figure 6.7 – SSLQT 2013: Comparing of longitudinal radiation profiles resulting from two excitations. Left plot: BLM signals normalized to one incident proton. Right plot: ratios between corresponding BLM signals in the case of quenching and were no transition to the normal conducting state occurred. Despite different temporal loss distribution, overall longitudinal shape is conserved. The difference in absolute radiation values of up to 6% was observed. This might come from different transverse population of particles in the excited bunches due to the cut-off of the transverse Gaussian tails.

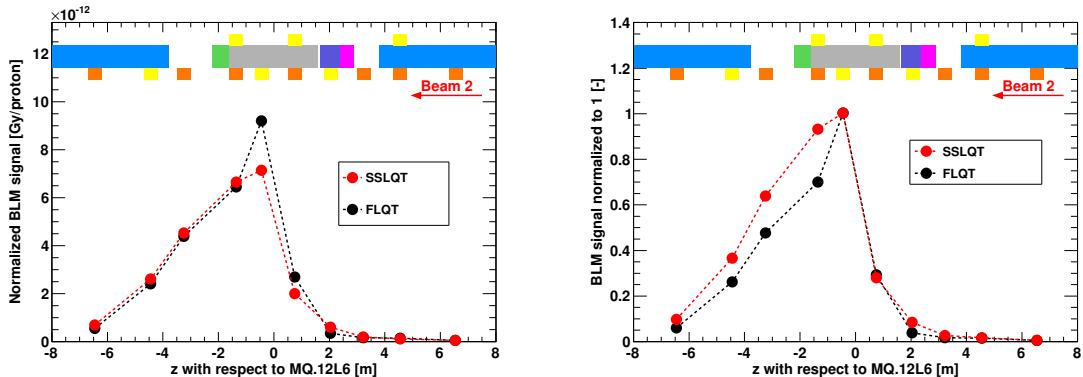


Figure 6.8 – Comparison of longitudinal BLM signals along magnets between SSLQT 2013 and FLQT 2013. Left plot: signals normalized per impacting proton. Right plot: signals normalized to 1. Red dots represent the results of SSLQT when ADT white noise excitation was used and the black dots - results of FLQT with ADT sign flip mode excitation.

6.3.2 Development of the beam loss and onset of the quench

In the case of steady state loss regime the heat transport through superfluid helium plays a dominant role. The energy can be deposited in magnets without quenching them for time in the order of seconds if the loss rate is low enough. Therefore, for example, no quenching occurred during the 1st excitation of the bunch set and did during the second attempt. In this paragraph the correspondence between the developing voltage in the superconductor and radiation dose of secondary particles measured outside the magnet cryostat is presented.

In the case of Steady State Loss Quench Test performed at 4 TeV, the protons hit the aperture for 20 s in total with almost constant loss rate. Fig. 6.9 presents Post Mortem data with high resolution acquisition of BLM and QPS measurements. The last 78 ms of the losses before the beam presence in the LHC was aborted is shown. The peaks in radiation (the green curve) result from tune and other frequency modes present in a beam spectrum. Although at the very beginning of the timescale (about 78 ms before the dump) the BLM signal exceeded 0.009 Gy/s (in RS01), the superconductor remained in its non-resistive state. The quenching

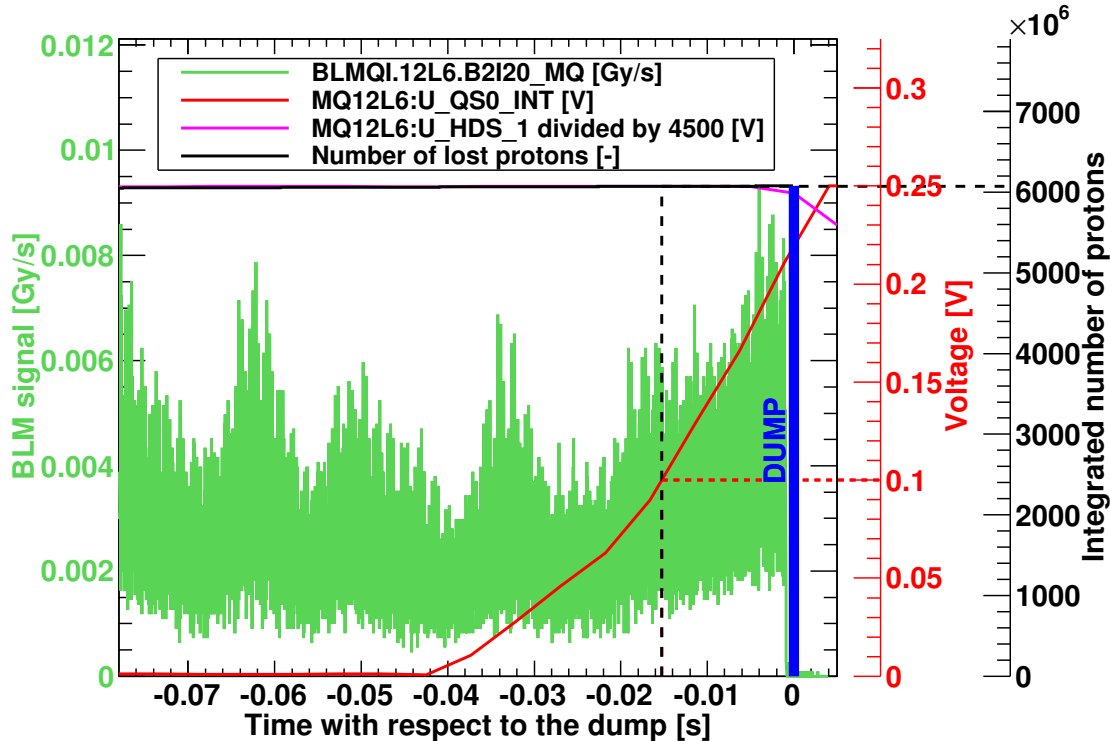


Figure 6.9 – Final Steady State Quench Test results - the correlation between BLM and QPS system measurements. The green line represents the beam losses in the most exposed to radiation BLM monitor, the red line - the voltage difference between two parts of the MQ superconducting coil, the black line - the number of lost protons, the pink line - the voltage on the quench heaters. The black dotted lines point the moment of quenching and indicate the number of lost protons. The red dotted line marks the QPS threshold of 100 mV.

Table 6.1 – Summary of the Steady State Loss Quench Test. The ratios of measured BLM signals compared and the expected BLM signals at quench for different integration times are presented for the same set of eight bunches used during the experiment.

Measured BLM signal/Expected BLM signal at quench [-]									
Excitation	Lost p^+	81.92 $\cdot 10^{-3}$	655.36 $\cdot 10^{-3}$	BLM loss integration time [s]	1.3	5.24	20.97	83.89	Quench
1 st	6.1 $\cdot 10^9$	0.14	0.17	0.29	0.78	1.14	0.48	no	
2 nd	6.2 $\cdot 10^9$	0.19	0.21	0.37	1.01	1.64	0.52	yes	

started around 42 ms before the dump giving the sudden increase in the voltage on the coil (the red line). This corresponds to relatively low instantaneous radiation level (≈ 0.0045 Gy/s). However, in the steady state regime such short variations are not significant. The increase of the voltage function seems to be linear in two separate time steps⁵ ($t \in (-0.037$ s, -0.022 s) and $t \in (-0.016$ s, 0.0004 s)) during which the steepness of the slope increases.

6.3.3 Validation of BLM thresholds

Assessing the BLM signal at quench in the case of performed experiment is very reliable since the loss margin between the safe and critical scenarios was very subtle. The BLM signals for all BLM running sums (from 40 μ s to 83.89 s, the red dots) with respect to the corresponding thresholds (the green dots) are given in Fig. 6.10 and Fig. 6.11. Table 6.1 contains calculated ratios of measured BLM signals to expected BLM signal at quench for RS07 - RS12. Beside two integration times, which actually are the most important ones for this loss duration (5.24 s and 20.97 s), all ratios stay significantly below 1. The quenching occurred when the radiation slightly (by 1%) exceeded the quench level in RS10 (1.01). According to 20.97 s integration time measurements, during both excitations the BLM signals were higher than the expected values at quench. This difference seems to be sufficiently low not to change the thresholds. However, the decision on that will be taken by the Threshold Analysis Working Group, which will be probably launched in spring 2014.

In Section 2.3.3 the description of 4 TeV Collimation Quench Test with protons 2013 was presented. This experiment was conducted at very similar conditions as SSLQT 2013 regarding the ADT excitation function and beam loss duration. The main difference between these two tests was that during 4 TeV Collimation Quench Test the protons hit the collimator jaws instead of the magnet aperture. In contrast to SSLQT 2013, in this case no magnet quenching was observed although the measured radiation dose exceeded the nominal BLM thresholds

⁵The voltage increase in the first time range of $t \in (-0.037$ s, -0.022 s) was fitted with the function $U_{QS0_INT}(t) = 0.56 + 13.70 \cdot t$ and in the second range of $t \in (-0.016$ s, 0.0004 s) the data was fitted with $U_{QS0_INT}(t) = 0.87 + 31.10 \cdot t$.

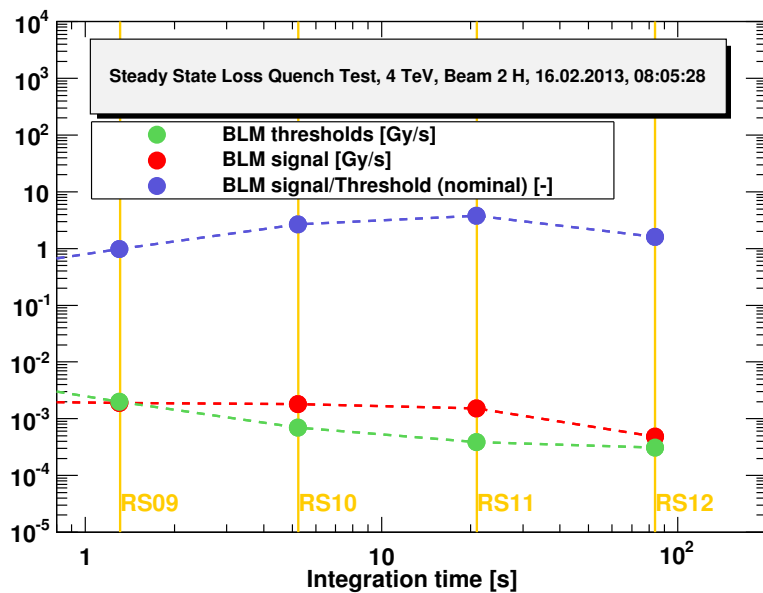


Figure 6.10 – BLM signals (the red dots) vs. thresholds (the green dots) when no quenching occurred. The ratios of the BLM signals to thresholds are presented by the blue dots. Only the signals, which are relevant to the experimental conditions (integration time longer than 1 s), are presented.

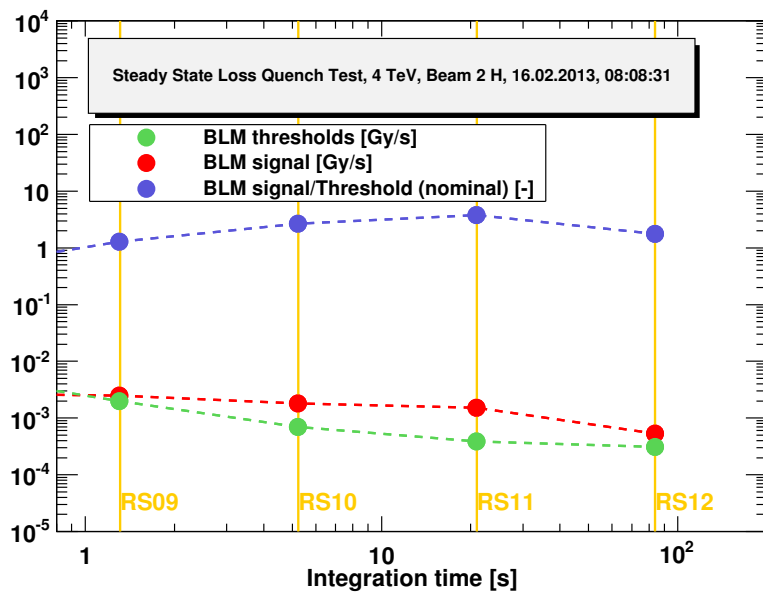


Figure 6.11 – BLM signals (the red dots) vs. thresholds (the green dots) during quenching. The ratio of the BLM signals to thresholds are presented by the blue dots. Only the signals, which are relevant to the experimental conditions (integration time longer than 1 s), are presented.

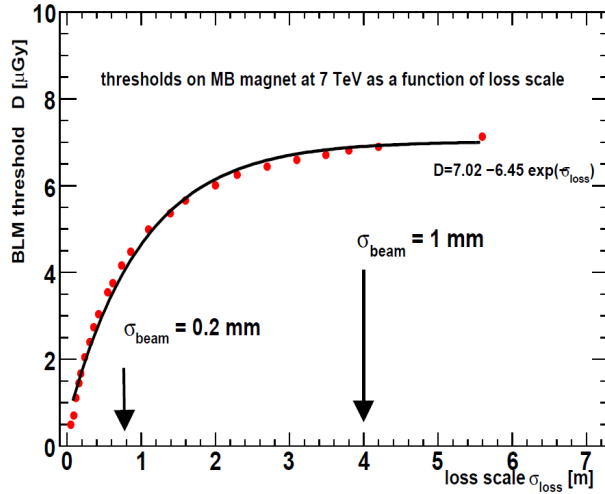


Figure 6.12 – BLM threshold as a function of loss scale [95]. The greater the loss size is, the higher the BLM threshold becomes.

by a factor of 2.3 in RS09 (signal integration time of 1.3 s) and 5.1 in RS10 (signal integration time of 5.2 s). This situation can be explained using the results of the studies dedicated to quench levels of MB magnets [95]. Fig. 6.12 shows the BLM threshold as a function of the beam loss size - the more distributed loss is, the greater the BLM threshold becomes. Therefore, the wide secondary particle shower originating in beam losses on the collimator resulted in higher radiation dose at the location of the downstream magnet. This also indicates that the deposited energy spread was diluted and, thus, insufficient to cause magnet transition to the normal conducting state.

6.4 Results of Geant4 simulations

The methodology of obtaining quench levels in the steady state regime was exactly the same as in the case of the Fast Loss Quench Test (see Section 4.10). According to the estimated loss patterns, results of simulated point like losses were weighted by the corresponding coefficients. Signals in BLMs were calculated by folding various particle spectra with response functions of ionization chambers (for more details see Section 3.4.1).

In this section the analysis of energy deposited inside a superconducting coil is provided. The quench levels were assessed based on both, the Geant4 simulations and QP3 code. Simulated BLM signals were validated by comparing them to the measured observables. The contribution of secondary particles to the total signals was discussed. Besides that, a comparison to the most probable FLQT scenario (Case 73) is presented. This allowed assessing the influence of the applied methodology of inducing beam losses (the ADT white noise excitation and ADT sign flip mode) onto the beam behaviour and development of the secondary particle shower along a magnet complex.

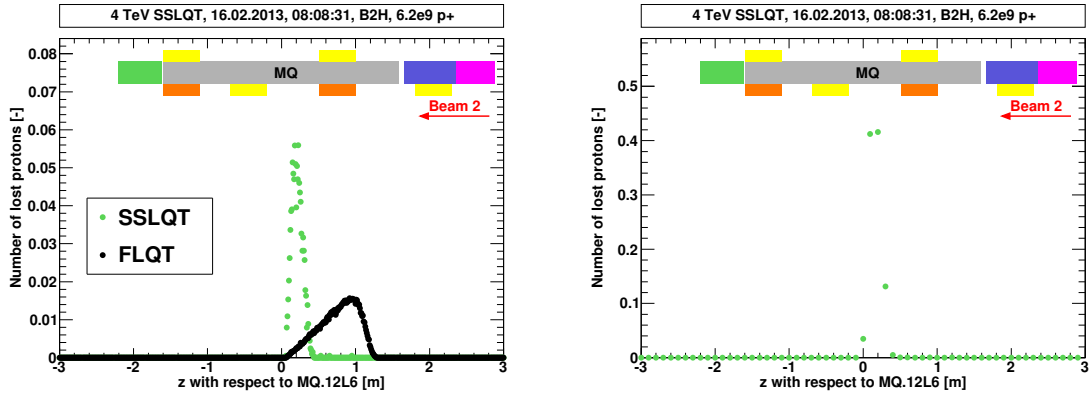


Figure 6.13 – Steady State Loss Quench Test: Loss pattern. Left plot: normalized number of protons lost along the magnets with the simulation step of 0.01 cm (direct data from MAD-X). The green curve corresponds to losses obtained when applying the ADT white noise excitation (SSLQT) and the black curve shows loss distribution resulting from the ADT sign flip mode (FLQT). Right plot: normalized to 1 number of protons with the step of 0.1 cm (recalculated input for Geant4 simulation analysis). Beam 2 comes from the right. Plots based on the data provided by [133].

6.4.1 Loss pattern studies

A loss scenario determines both, the energy deposition distribution inside a superconducting coil and a profile of secondary particle radiation outside a magnet cryostat, so also signals in BLMs. Therefore, implementing the most realistic loss pattern to Geant4 simulations is critical for an appropriate recreation of the processes occurring during the dedicated experiment. In this section the knowledge of loss distribution is based on results of MAD-X simulations [133]. These orbit studies confirmed that the applied method of combining a static three corrector orbit bump⁶ with the ADT white noise excitation provided losses limited only to the region of the central MQ. Moreover, it was revealed that the loss pattern during the SSLQT (the green curve in Fig. 6.13), in contrast to the FLQT (the black curve), was very narrow and concentrated in the middle part of MQ.12L6. In order to quantify the loss spread, the full width at half maximum (FWHM) was computed giving the value of ≈ 0.20 m in the case of slow loss regime and ≈ 0.64 m in the case of short loss duration. Besides being three times more narrow, the steady state loss was also symmetric when the fast loss exhibited significant asymmetry. The most likely, these tendencies resulted from the different principles of the applied ADT modes 1.8.2. During the ADT sign slip mode (FLQT) a beam transverse oscillations were provoked when during the ADT white noise excitation (SSLQT) a beam transverse size was blown-up⁷. In addition, it has to be also kept in mind that the presented loss patterns refer to the losses integrated over different scales of loss durations (milliseconds and seconds, respectively) and

⁶This means that the bump amplitude was kept at the same level.

⁷Precisely, only a part of the beam, which constituted of eight bunches, was affected by the transverse damper due to the chosen length of the excitation window.

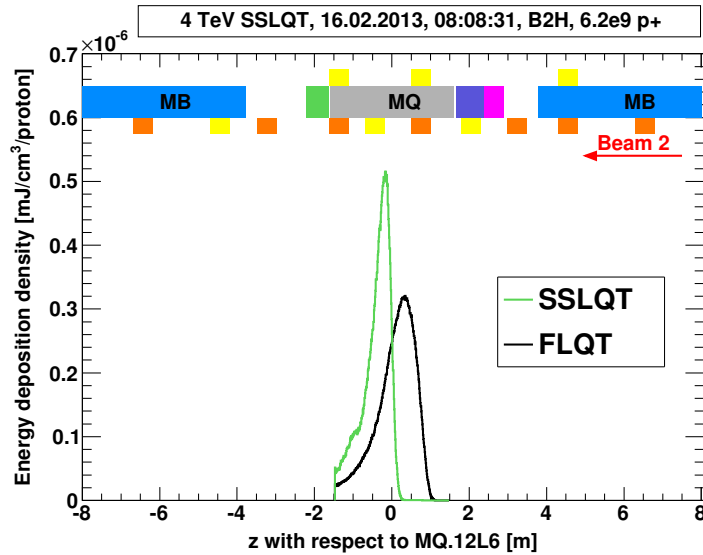


Figure 6.14 – Steady State Loss Quench Test 2013: Geant4 simulations - longitudinal energy density distribution inside a superconducting coil along the most exposed bin.

during the experiments slightly different bump amplitudes were applied (see Sections 4.8 and 6.2). The right plot in Fig. 6.13 presents an input to the Geant4-based data analysis. Due to the differences in binning, only nine (out of 61) loss locations contributed to the final signals.

6.4.2 Energy deposition inside a superconducting coil

A longitudinal energy density distribution along the most exposed bin is presented in Fig. 6.14. The narrow loss pattern of SSLQT also reflected in the the narrow energy density distribution peak. It has reached the highest value of $E_{max} = (5.2 \pm 0.2) \cdot 10^{-7}$ mJ/cm³ per incident proton at $z_{E_{max}} = -0.15$ m, which was approximately 0.3 m from the maximum of the lost proton distribution. A comparison of these values to the FLQT results (Table 6.2) shows that the distance between two peaks ($|z_{L_{max}} - z_{E_{max}}|$) was twice shorter but the value of E_{max} was greater by a factor of 1.6 during the long losses. Although the FWHM of loss distribution in the case of SSLQT was three times smaller than in the case of the FLQT, the FWHM of E_{dep} was smaller only by a factor of 1.4 (0.5 m and 0.7 m respectively).

Considering the steady state loss regime, average energy across an entire cable defines a quench level of a specimen. Therefore, in order to recreate 18-strand situation, the radial energy density distribution coming from the Geant4 simulation data (Fig. 6.15) was fitted to the power law (Eq. 4.4). Based on that, the average energy density was calculated to be $E_{avg} = 2.61 \cdot 10^{-7}$ mJ/cm³/proton and the maximum energy deposited on a surface of the SC coil reached the value of $E_{peak} = 7.92 \cdot 10^{-7}$ mJ/cm³/proton. Multiplying E_{avg} by the number of particles lost on the MQ, i.e. $6.2 \cdot 10^9$ protons, the quench level in the steady state regime was computed to be 1620 mJ/cm³. This corresponds to ≈ 81 mW/cm³ when taking into account

Table 6.2 – SSLQT and FLQT 2013: Maximum energy density in the SC coil: $z_{E_{max}}$ -position of the most exposed cell, $|z_{L_{max}} - z_{E_{max}}|$ - distance between the maximum energy density deposition and maximum in the loss pattern ($z_{L_{max}}$), E_{max} - maximum energy density deposited in a single cell.

	$z_{L_{max}}$	$z_{E_{max}}$ [m]	$ z_{L_{max}} - z_{E_{max}} $ [m]	E_{max} [mJ/cm ³ /proton]
SSLQT	≈ 0.15	≈ -0.15	≈ 0.30	$(5.2 \pm 0.2) \cdot 10^{-7}$
FLQT (Case 73)	≈ 0.92	≈ 0.30	≈ 0.62	$(3.2 \pm 0.2) \cdot 10^{-7}$

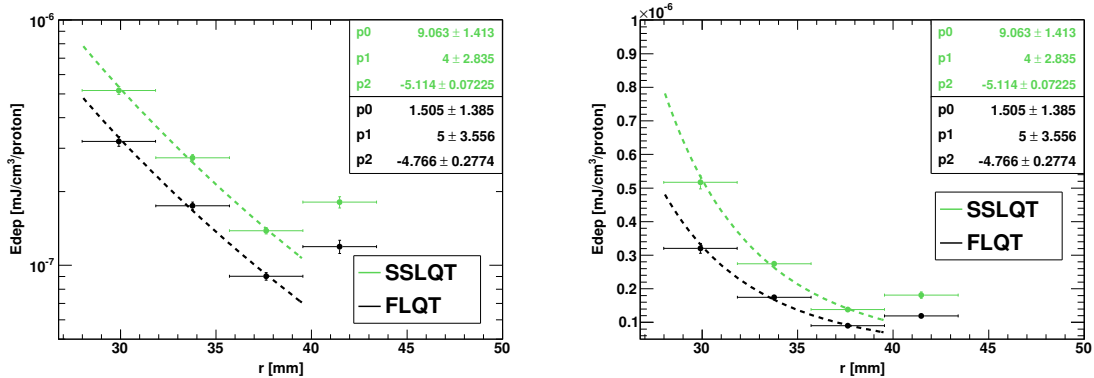


Figure 6.15 – Steady State Loss Quench Test 2013: Geant4 simulations - radial maximum energy density distribution in a SC coil ($\phi = \phi_{E_{max}}$, $z = z_{E_{max}}$). Energy density in the simulated radial bins was fitted to the power law (Eq. 4.4), last bin was neglected due to the simulation artifacts.

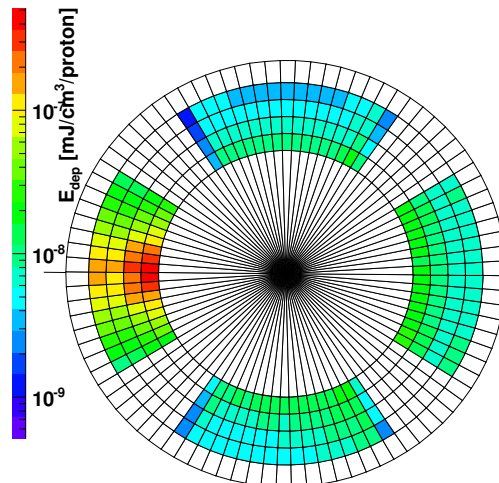


Figure 6.16 – Steady State Loss Quench Test 2013: Geant4 simulations - coil cross-section in the plane where the maximum energy density was deposited.

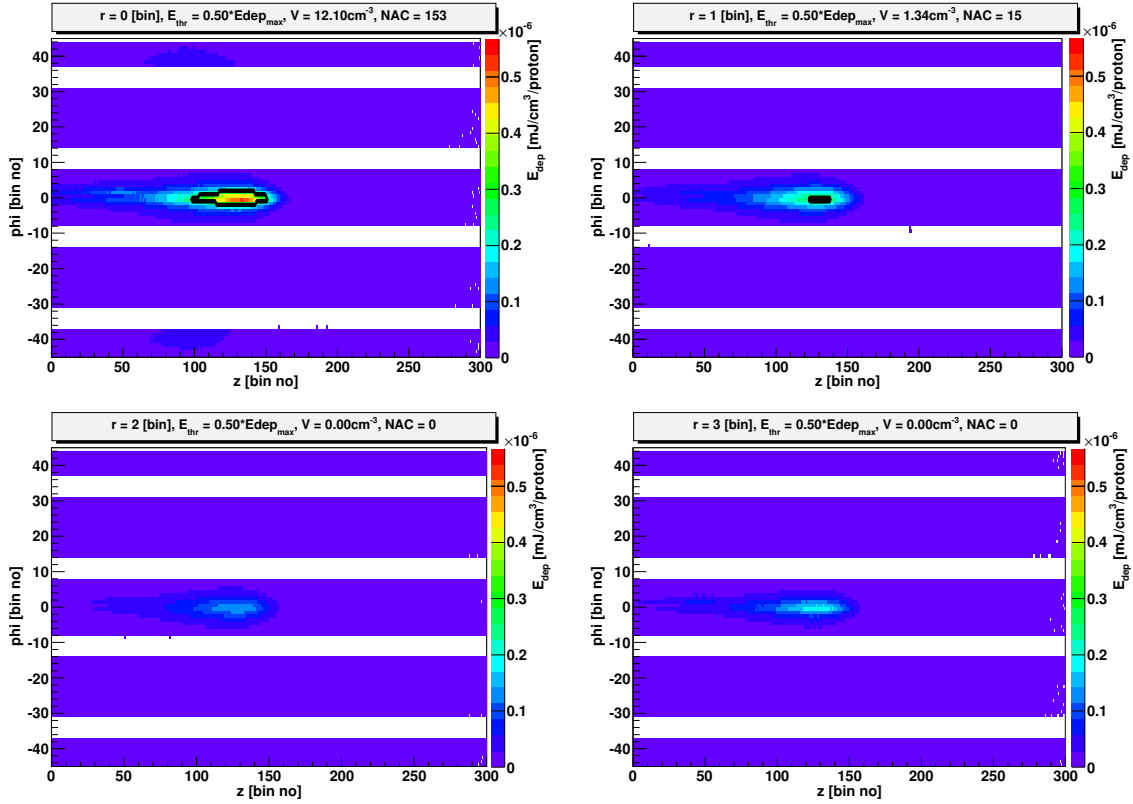


Figure 6.17 – Steady State Loss Quench Test - Geant4 simulations - Color maps of energy density in four simulated coil layers. For simplicity r, ϕ - coordinates are expressed in bin numbers, beam comes from the right. Black lines limit the region defined by the threshold value $E_{thr} = f_{Emax} \cdot E_{max}$. Here $f_{Emax} = 0.5$.

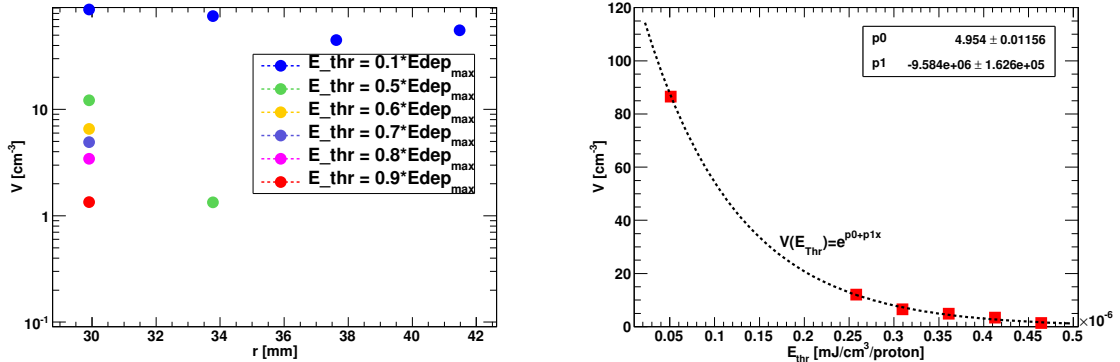


Figure 6.18 – Steady State Loss Quench Test 2013: Geant4 simulations - quenching volume as a function of considered criteria of energy magnitude. Left plot: Above the assumed threshold value of $0.5 \cdot E_{max}$ all energy is confined in the first, the most exposed layer of the coil. Right plot: the volume decreases exponentially as a function of imposed energy threshold, $E_{thr} =$ (results of the first layer).

the loss duration of 20 s. Moreover, it is worth mentioning that the slope of the SSLQT radial energy distribution (green curve) was much steeper than the one of the FLQT (black curve). This means that the strands located closer to the magnet aperture suffered significantly more during long losses than in the case of short losses. However, the quench levels in these two regimes are differently defined due different mechanisms contributing in heat evacuation from a superconductor (see Section 1.4).

Fig. 6.16 shows an azimuthal distribution across the most exposed bin. Similarly to Fig. 4.23, also in this case, the deposited energy is localized within a small region of only one, the targeted, magnet pole. Other magnet poles did not experience high radiation from the backscattered secondary particles.

A spacial resistive volume development can be investigated by observing changes occurring in different cables. However, in the case of Geant4 simulations, one layer represents a transversely integrated energy density over 4.5 strands. This was incorporated to the Monte Carlo code due to the computation time constraints. As it was mentioned in Section 4.10.2 an estimation of a threshold with respect to the E_{max} , which would determine a quenching volume size, requires applying numerical methods and detailed case studies. Therefore, in this section arbitrary thresholds were considered to verify their influence on the three-dimensional quench distribution. Assuming $E_{thr} = 0.5 \cdot E_{max}$ as in Fig. 6.17, only about 0.6% of the superconductor volume in the first layer would undergo the transition to the resistive state. Considering the second layer, this would be reduced to only 0.06%. In this case, simulations indicate that at least nine external strands would not be affected by quenching process. Taking into account other arbitrary threshold values (left plot in Fig. 6.18) suggests that only one to two layers (4–9 strands of a single cable) are involved in the transition to the normal conducting state. The

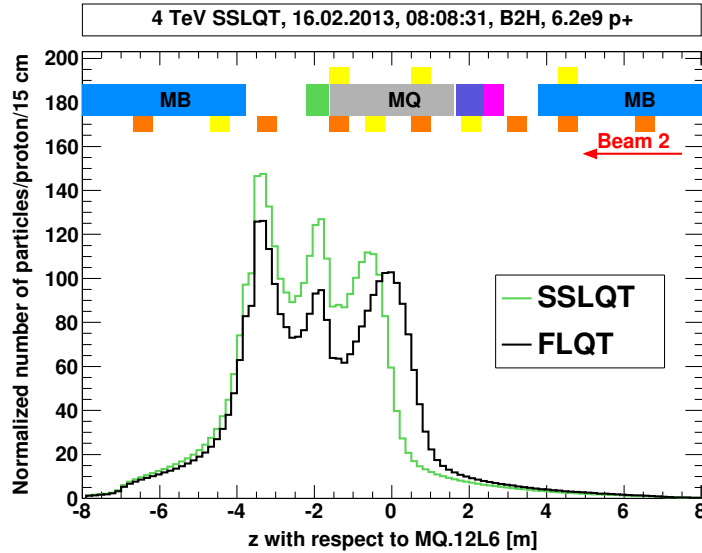


Figure 6.19 – Geant4 simulations - total secondary particle distribution along the magnets. Three peaks are the result of the difference in density of medium which particles pass through. Only the position and width of the first peaks are affected by the loss pattern.

correlation between the volume size contributing in coil quenching as a function of assumed energy threshold is presented in plot in Fig. 6.18. The results of the first layer exhibit an exponentially decreasing tendency.

6.4.3 BLM signals

Substituting exact BLMs, which were installed in the LHC tunnel, with two long pseudo-monitors in Geant4 allowed studying a distribution of secondary particles spread over the entire length of magnets. Fig. 6.19 presents results obtained for the SSLQT (the green curve) and the FLQT (the black curve). Directly from this plot it comes out that only the initial part of the hadronic cascade is determined by the loss location. The remaining part is mostly dominated by the geometrical effects and material properties of the magnet system. The first (with respect to the beam motion) peaks occurred at $z_{SP,SSLQT} = 0.65$ m (SP -secondary particles) and $z_{SP,FLQT} = 0$ m when the second and third peaks were located precisely in the same positions $z_{SP,2} = -1.85$ m, $z_{SP,3} = -3.45$ m regarding the MQ centre. The detailed discussion devoted to the origin of these peaks is presented in Section 4.10.3.

Fig. 6.20 shows angular distributions of all particles reaching BLM detectors (results given only for the standard BLMs, no mobile detectors here). All of them have Gaussian shape but in the case of B1E30 and B2I30 local maxima occur at angles of about 63° and 158° , respectively. This might result from the vicinity of monitors to the MB-SSS interconnection region where many metal-vacuum interfaces can cause accumulated scattering processes. Additionally, particles encounter much less shielding materials in the interconnections than traveling through

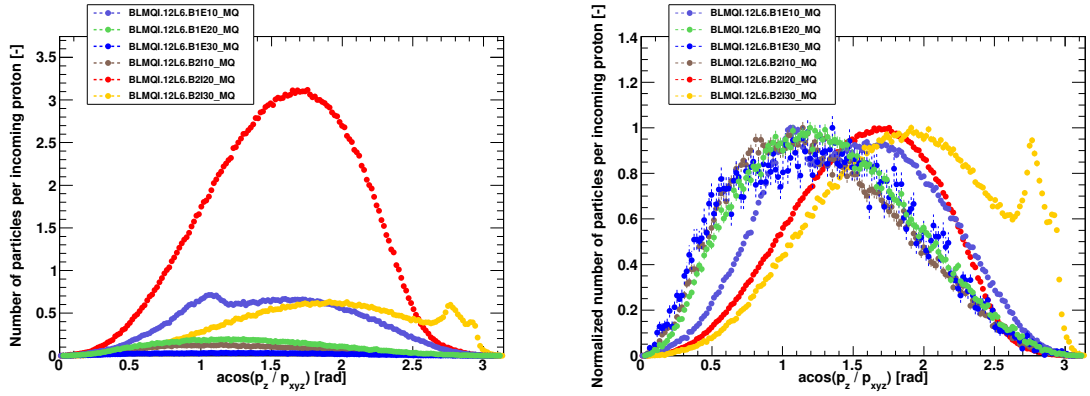


Figure 6.20 – Geant4 simulations - Left plot: angular distributions of particles hitting BLMs (results for only standard monitors are shown). Right plot: normalized to 1 angular distributions of particles hitting BLMs.

the magnets. As it was already mentioned in 3.4.2, a number of available BLM response functions used for calculating the final signals is limited. Therefore, the particles have to be assigned to the closest simulated case. According to this criterion, effectively the most dominant are the particles hitting the ionization chambers with large angles of $60^\circ - 120^\circ$ as presented in Fig. 6.21.

Besides momentum, each particle getting out from a magnet cryostat in Geant4 simulations is recognized by its type and energy. The most significant contribution to BLM signals comes from gammas, neutrons and protons (Fig. 6.22) which is consistent with results presented in [95]. Moreover, in the case of monitors located upstream the loss location ($z > 0$ m), mainly backscattered neutrons and gammas are observed. An impact of protons and positively charged pions starts playing a role already when the number of neutrons and gammas decrease at $z \approx 6.5$ m (Fig. 6.23).

Taking into account all aspects presented above, i.e. type, energy and momentum of the secondary particle shower, the corresponding response functions, and in addition a number of lost protons during the experiment ($6.2 \cdot 10^9$ particles), the BLM signals were calculated. Fig. 6.24 presents a comparison of simulated BLM signals (the green dots) to the measured observables (the black dots) of beam 2 monitors in RS11. This BLM integration time of 20.97 s was used to cover entire loss duration (19 – 20 s). The loss shape was recreated relatively well by the simulations although the absolute values were clearly underestimated. Especially two monitors located close to the loss location ($z \approx 0.8$ m and $z \approx 2.1$ m) exhibit the highest divergence from the measured values. The longitudinal tendency of the calculated ratios of the simulated to the measured values along the magnets represents satisfying agreement (0.4 – 0.7) for downstream monitors. This level of underestimation is very similar to the one obtained for the FLQT (Fig. 4.31). In order to estimate simulation error, a histogram of ratios was created. The results are presented in Fig. 6.25 and confirm previous estimations of simulation accuracy

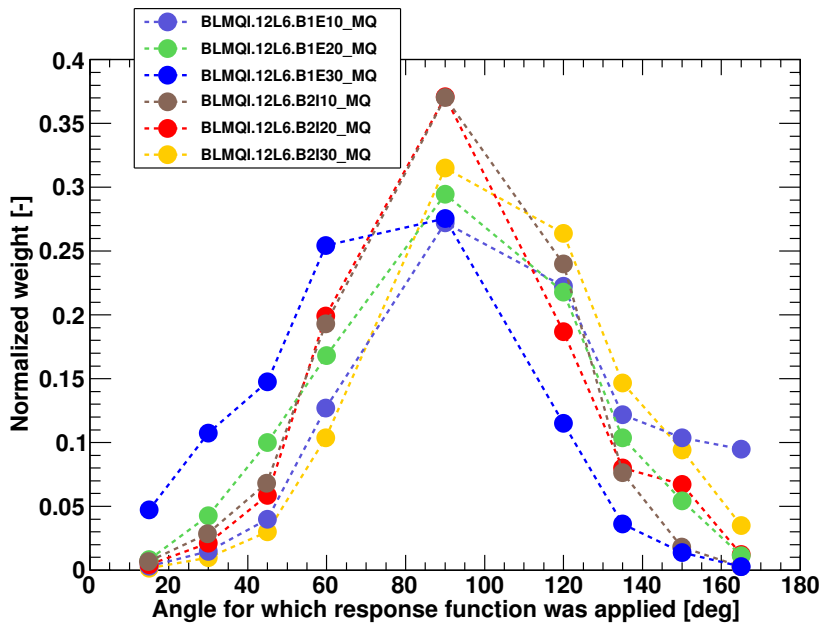


Figure 6.21 – Geant4 simulations - Contribution of different response functions to the total signal.

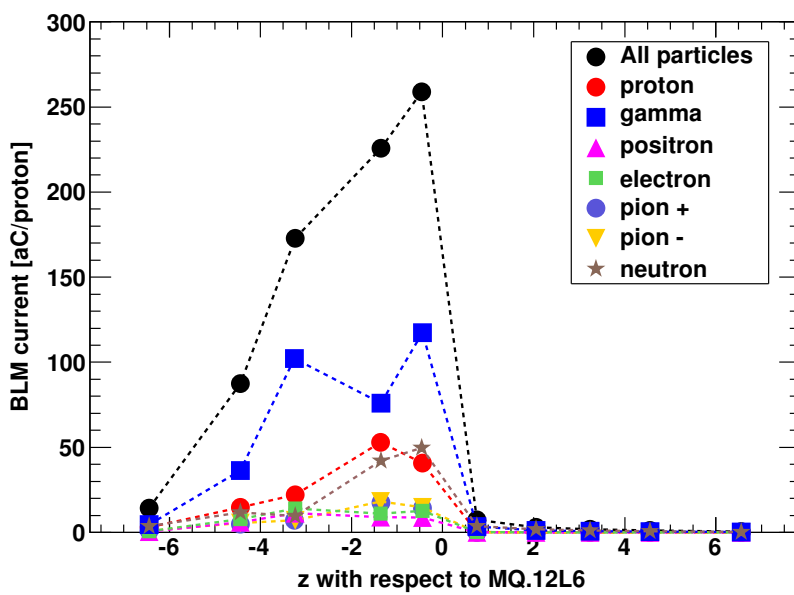


Figure 6.22 – Geant4 simulations - Current generated in BLMs by various secondary particles. Results obtained for beam 2 monitors are presented. Gammas, protons and neutrons play a dominant role in ionizing a gas, which fills a BLM detector.

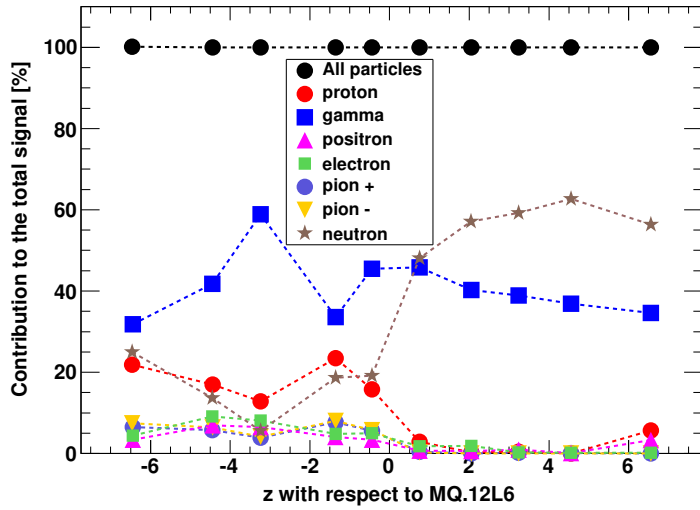


Figure 6.23 – Geant4 simulations - Contribution of secondary particles to the BLM signal.

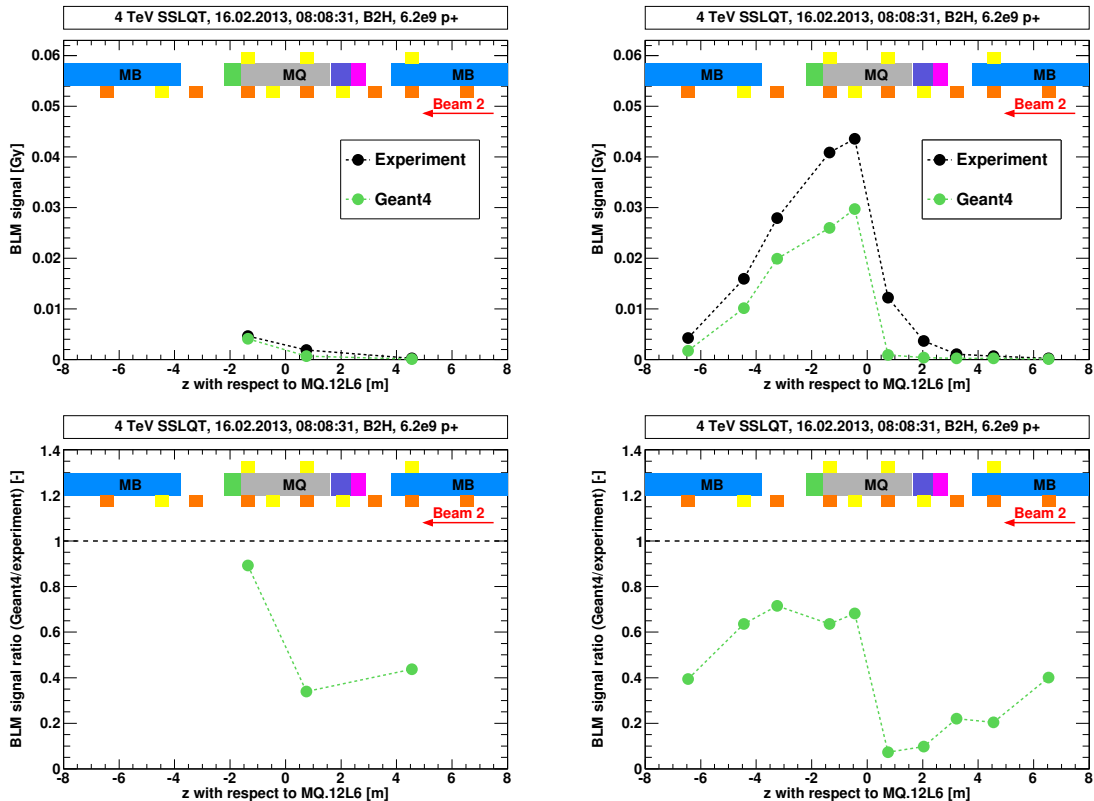


Figure 6.24 – Steady State Loss Quench Test: a comparison of measured and simulated BLM signals. Geant4 simulations underestimate BLM signals by a factor 2-3 in the case of monitors located downstream the loss location and surveying beam 2 losses.

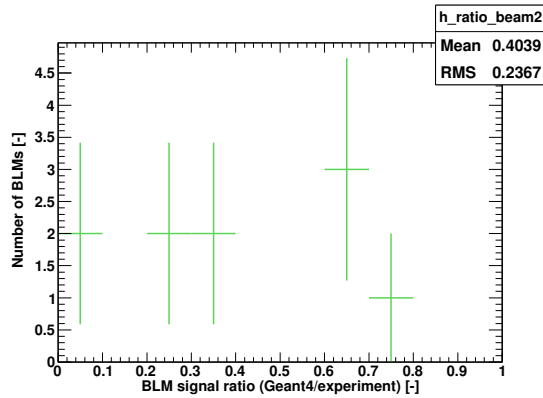


Figure 6.25 – Steady State Loss Quench Test 2013: Geant4 simulations - error estimations of the simulated BLM signals.

$(0.42 \pm 0.13$, Fig. 4.32) giving the mean value of 0.40. However, the RMS is almost twice greater than in the FLQT reaching the value of 0.24. Limiting the number of cases only to the monitors located at $z < 0.5$ m, the value of 0.61 ± 0.11 was obtained.

6.4.4 Quench levels obtained with QP3 heat transfer code

The QP3 heat transfer code was used as a complementary tool for quench level assessment. The inputs to the program are presented in Fig. 6.26. The beam intensity was taken from the logging data base with 1 s resolution since PM data with 20 ms was very noisy. The normalized to 1 radial distribution was derived from Geant4 simulations along the most exposed bin (Fig. 6.15). Based on these data, the computing process delivered the peak value of $E_{peak} = 3806$ mJ/cm³ [114]. In the steady state regime, the average energy deposited along all cable strands $E_{avg} = 1371$ mJ/cm³ has the meaning of the quench level. Expressing this energy as a power needed to induce transition to the resistive state gives the value of ≈ 72 mW/cm³ which is consistent with quench level obtained with Geant4 data ≈ 81 mW/cm³. The assessed results represent good agreement with direct measurements [148] performed using a so-called stack method [149]. During these experiments the quench level of MB inner coil⁸ cables operating at current corresponding to 4 TeV beam (i.e. 6.8 kA) was obtained to be (58-80) mW/cm³.

6.5 Final conclusions

The Steady State Quench Test was performed applying a combination of the static three corrector orbit bump with the ADT white noise excitation mode. This provided losses in

⁸Note that MB inner coil cables differ from MQ coil cables regarding the copper to superconductor ratio, isolation width, number of filaments constituting a cable and filament diameter [20]. The direct measurements with MQ cables are expected in March 2014.

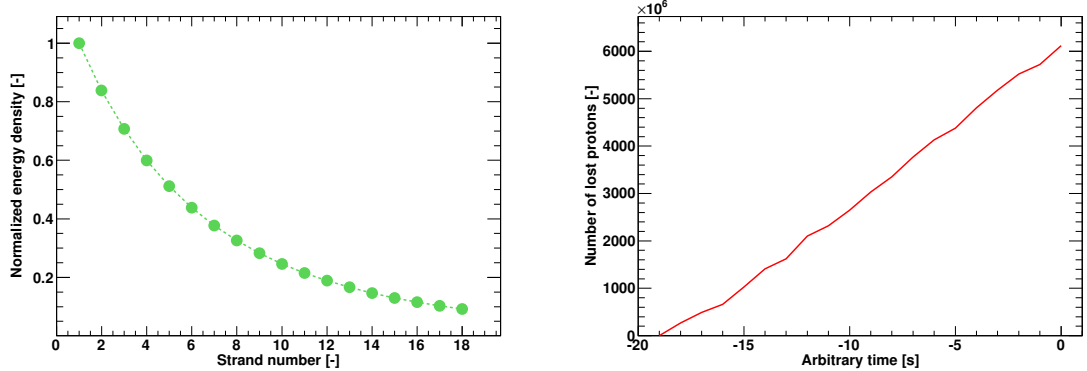


Figure 6.26 – Steady State Loss Quench Test 2013: QP3 input distributions. Left plot: Normalized radial energy density distribution along a cable (18 strands). Right plot: Intensity of lost protons, zero corresponds to the moment of the beam dump.

20 second scale meeting the requirements of a constant loss rate $3.1 \cdot 10^8$ protons per second. During the experiment a set of eight bunches was blown-up. In the first attempt losses were not high enough to cause the transition to the normal conducting state but the second approach terminated with magnet quenching. The corresponding BLM signals in the integration time of 20.97 s (RS11) varied by approximately than 44%. Taking into account that during the first excitation the BLM signal exceeded the expected value by 15% indicates that in this integration time the thresholds could be slightly increased.

The quench test was simulated using Geant4 code. Based on the experimental data (number of lost protons) and loss orbit simulations, the particle loss was simulated using a method of weighting point-like losses with correspondence to the estimated loss pattern. The obtained averaged energy deposited along a cable was $E_{avg} = 2.61 \cdot 10^{-7}$ mJ/cm³/proton. Possessing knowledge of the number of particles lost on the quenched magnet (MQ.12L6), i.e. $6.2 \cdot 10^9$ protons, allowed the quench level to be assessed. The resulting value is 1620 mJ/cm³ which in the case of 20 s long loss corresponds to 81 mW/cm³. In addition, complementary QP3-based computations were provided in order to cross-check the estimated quench level. The obtained value is 1371 mJ/cm³, so therefore ≈ 72 mW/cm³ which is consistent with the calculations based on Geant4 simulations. This proves that the quenching process in the steady state regime is well understood.

Besides, assessing quench levels in the state state regime, the dedicated experiment allowed revising positively the capability of ADT white noise excitation mode as a system of inducing constant loss rates.

7 Summary and final conclusions

The studies presented in this thesis consist of two complementary parts which have allowed the LHC Main Magnet quench levels to be assessed. The first part has involved planning, preparing and finally conducting quench tests varying in the loss timescale and therefore mechanisms of heat transport in a superconducting system. The analysis of the experimental data has included the beam loss characterization in terms of beam trajectory, intensity decay and beam loss monitor signals. The second part was devoted to recreating quench test conditions using Geant4 simulations. Consequently, this has led to the estimation of the distribution of the energy deposited inside superconducting coils and computation of the corresponding BLM signals. Overall, the investigated quench tests have allowed better understanding of the beam behaviour under the influence of external disturbance and of the loss properties.

Although the dedicated quench tests in 2013 were assigned only several hours of the Machine Development time, the entire preparation process lasted for over a year. This was due to the fact that a novel technique of inducing beam losses with very strict specifications was required. Especially the Fast Loss Quench Test was very difficult because of the very low intensity of the beam and very short loss timescale. The idea of combining the three corrector orbit bumps with beam excitation provided by the transverse damper appeared early in 2012 and was followed by a series of tests in order to optimize the settings of the ADT. On top of that, the machine parameters had to be adjusted so that the provoked losses would be able to quench a targeted magnet with well known conditions. Careful investigation resulted in choosing the ADT sign flip mode for inducing beam losses imitating the ones provoked by UFOs. The other 2013 quench test was performed in the steady state regime as a continuation of studies conducted in 2010. However, the loss rate was controlled. In order to achieve constant loss rate, instead of using a dynamic three corrector orbit bump as previously, a bump amplitude was kept on a fixed level and beam blow-up was generated with the ADT white noise excitation mode.

The precise knowledge of all quench test parameters (beam loss intensity, loss duration, loss rate, loss locations) was essential for further Monte Carlo simulations and the accuracy of assessing magnet quench levels. Since it is not possible to measure directly the energy deposited

Chapter 7. Summary and final conclusions

by high energy particles inside LHC superconducting coils, the quench test conditions were recreated using Geant4 code. The outputs of the simulations were the BLM signals, which were compared to the measurements, and the energy deposition inside the superconducting coil.

The preparation of the Geant4 simulations was a very complex process since first of all it required implementing a very detailed magnet representation in the code. All major components of the Short Straight Section (the MQ and its correctors), two neighbouring MBs (with correctors) and the interconnections between magnets (MB-SSS and SSS-MB) have been considered. In the simulations, the BLMs installed in the LHC tunnel were substituted with two long pseudo-detectors for studying the radiation of secondary particle shower also in the regions unattainable directly from the measurements. The BLM signals were calculated by folding particle spectra with the corresponding response functions of ionization chambers. Another demanding part of performing the simulations was related to the implementation of the most realistic way of losing particles along magnets. This part was crucial since the loss scenario determines signals in the BLMs and this data was used for validating the simulations. Moreover, the loss pattern determines the radial energy distribution inside a superconducting coil. This matters when calculating the peak and average energies, which are used for estimating the quench levels. However, in 2010 when the author's studies on the subject began, the knowledge of loss patterns relied only on scientific assumptions. Therefore, a new simulation technique was needed to provide fast and efficient verification of various loss cases. Instead of repeating a very time-consuming process of simulating each loss scenario separately, it was decided to simulate a set of (60-70) point-like losses along a targeted region neglecting the transverse beam size. The final result was obtained by weighting single loss results with the coefficient corresponding to the assumed loss pattern. Such a method allowed considering about 2000 cases per hour of PC time¹.

A C++ based program (ROOT macro) was developed by the author in order to analyze various loss patterns. Besides an option of incorporating pre-defined loss shapes, the Geant-Quencho-Meter also allows finding a loss scenario the most fitting to the measured BLM signals. Using experimental inputs, the GQM provides a full analysis of three dimensional distribution of energy deposited inside a magnet coil, secondary particle shower propagation along pseudo-detectors imitating long BLMs, identification and characterization of particles contributing to BLM signals, calculation of BLM signals and quench levels.

¹This was possible when point-like loss simulations were already prepared. However, simulating and checking them have taken around 2-3 months.

Table 7.1 – Summary of the beam induced Quench Tests 2013. FLQT - Fast Loss Quench Test, SSLQT - Steady State Loss Quench Test, E_b - beam energy, t_l - loss duration leading to the magnet quench, I_l - intensity of beam loss causing quenching, E_{peak} - peak energy at the surface of a superconducting cable, E_{avg} - average energy over 18 strands constituting one layer a MQ superconducting cable, Q_L - assessed quench level, $\frac{BLM_{Geant4}}{BLM_{meas}}$ - ratio between simulated and measured BLM signals, p - protons.

Quench Test	Experimental conditions			Geant4 simulation results		Quench levels			
	E_b [TeV]	t_l [s]	I_l [p]	E_{peak} [mJ/cm ³ /p]	E_{avg} [mJ/cm ³ /p]	Definition	Q_L		
FLQT	4	$(5 - 10) \cdot 10^{-3}$	$(4.0 - 8.2) \cdot 10^8$	$4.87 \cdot 10^{-7}$	$1.65 \cdot 10^{-7}$	$E_{peak} \cdot I_l$	$(200-400)$ mJ/cm ³		
SSLQT	4	20	$\approx 6.2 \cdot 10^9$	$7.92 \cdot 10^{-7}$	$2.61 \cdot 10^{-7}$	$E_{avg} \cdot I_l \cdot t_l^{-1}$	81 mW/cm ³		
Quench Test	$\frac{BLM_{Geant4}}{BLM_{meas}}$ [-] (all beam 2 monitors) (Mean±RMS)			$\frac{BLM_{Geant4}}{BLM_{meas}}$ [-] (beam 2 monitors located downstream the loss location) (Mean±RMS)					
FLQT	(0.42 ± 0.13)			(0.52 ± 0.07)					
SSLQT	(0.40 ± 0.23)			(0.61 ± 0.11)					

The final results of the performed studies are summarized in Table 7.1. The quench levels of MQ.12L6 at the nominal beam energy of 4 TeV in the millisecond and second loss timescales were assessed using the FLQT and SSLQT data, respectively. The loss patterns were obtained from MAD-X simulations [133] and incorporated into the Geant4 data analysis. The beam losses leading to magnet quenching during the FLQT have lasted for (5-10) ms. In this case, a better recognition of the loss duration was not possible due to the resolution of the QPS system. The number of protons inducing the quench of MQ.12L6 was estimated to be $(4.0 - 8.2) \cdot 10^8$. In the considered fast loss regime a quench level (Q_L) is defined by the heat capacity of the cable and liquid helium which the cable is immersed in. Therefore, the maximum energy (E_{peak}) deposited on the surface of the cable was taken into account. The calculated quench level in the millisecond long timescale was $(200 - 400)$ mJ/cm³. This range results from the uncertainty of assessing the number of protons causing magnet quenching. In the case of SSLQT, the constant loss rate of $3.1 \cdot 10^8$ protons per second was achieved over around 20 s. Since in the steady state regime, the efficiency of evacuating heat from the cable by superfluid helium determines the quench level, the average energy over 18 strands was considered. As the result, the quench level in the timescale of seconds was found to be 1620 mJ/cm³. This value corresponds to the power density of 81 mW/cm³.

Additionally to the Geant4 based quench level calculations, the QP3 heat transfer code computations were provided. However, a significant discrepancy between these two methods was observed regarding fast losses where the quench level was computed to be $(40 - 70)$ mJ/cm³. This value is around three times smaller than the quench level coming from Geant4 simulations. The origin of this difference remains under investigation but it most probably results from the fact that the models incorporated to the QP3 code were never validated with experimental data in the fast loss regime. In contrast to the FLQT, the quench levels obtained using Geant4 and QP3 in the steady state regime are consistent, i.e. the QP3 has provided the value of 1371 mJ/cm³ which is equivalent to 72 mW/cm³ for the considered loss duration.

Besides assessing the quench levels of the LHC Main Quadrupoles, the experience gained during the quench test studies leads to a few interesting conclusions:

- Loss patterns are determined by the method of inducing beam losses. The dynamic three corrector orbital bump has provided wide losses along the MQ magnet (SSLQT 2010). Beam excitation with the ADT sign flip mode has resulted in the losses spread over the first half of the MQ (FLQT 2013). The ADT white noise excitation mode has provoked very narrow losses, which were concentrated in the central part of the MQ (SSLQT 2013).
- The beam size plays a crucial role in the temporal loss distribution and the loss duration but its impact on the spacial distribution of the radiation measured by BLMs is negligible.
- Although during FLQT 2013 the same ADT setting were used for exciting various bunches with different intensities, the normalized BLM signals have varied in time. This indicates the influence of the vertical beam size onto the magnitude of beam losses - the smaller a bunch vertical size is, the higher losses occur.

- The synchronization between the BLM and QPS systems is extremely important for assessing quench levels (especially in the fast loss regime). Moreover, the resolution of QPS data acquisition (5 ms) limits estimation of the number of lost protons and therefore the accuracy of the obtained quench level. In the case of FLQT, this has introduced an uncertainty of 50%. Hence, for the future quench tests a reliable method of synchronizing the BLM and the QPS systems has to be provided.
- In order to assess a number of lost protons on a magnet, it has to be assured that no other accelerator components introduce additional aperture limitations or that the losses provoked elsewhere are well controlled. The example of SSLQT 2010 shows that recalculation of losses on collimators to the corresponding values on a cold magnet is not trivial.
- Based on the measurements, the BLM thresholds in low running sums, i.e. with signal integration times from 0.64 ms (RS05) to 10.24 ms (RS06), can be increased even by a factor ≈ 3 and ≈ 6 , respectively (see Fig. 4.3). This will reduce the number of unnecessary beam dumps related to UFO-induced losses and will increase the time available for luminosity production.
- The BLM thresholds in high running sums, i.e. with integration times in the range 1.3 s (RS09) to 83.89 s (RS12) are set adequately to the quench levels. A small difference (see Table. 6.1) between signals recorded in two loss induction attempts during which one has resulted in quenching and the other has not, allows us to come to this judgment. This result is astonishing when taking into account the outcomes of Collimation Quench Test 2013. In that case, although the measured BLM signals were significantly higher than during SSLQT 2013, the magnet located downstream the collimator did not quench. This illustrates that the BLM signal and energy deposition in the coil depend strongly on the loss pattern.
- The radial energy density distribution inside a superconducting coil depends on the longitudinal spread of beam losses on the aperture. Simulations have shown that the more concentrated the loss is, the steeper the radial distribution becomes.
- Geant4 simulations have shown that gammas, protons and neutrons constitute a dominant part of the subsequent secondary particle shower propagating outside the magnets. Moreover, mostly backscattered neutrons and gammas are recorded by BLMs located upstream of the loss location.
- The uncertainty of estimating a loss duration introduces also the uncertainty of an assessed quench level. In the case of FLQT 2013, it was computed that a difference of ≈ 3 ms (from ≈ 5 ms to ≈ 8 ms) is followed by an increase in the MQ quench level by 70% at 4 TeV.
- The approximation method based on weighted point-like losses provides quench levels consistent with Fluka simulations, where a loss pattern was directly incorporated into

the code. Nevertheless, both independent methods applied for computing the BLM signals have underestimated the measured values. The technique used in Geant4 simulations, i.e. BLM response functions, has resulted in the ratio between simulated and measured BLM signals of (0.52 ± 0.07) in the case of the FLQT. Deriving BLM signals directly from energy deposited by secondary particles in a gas detector, as in the Fluka, has provided ratios of (0.85 ± 0.07) .

- The Geant-Quencho-Meter is a very efficient tool for a fast and complete data analysis of quench tests. It allows considering any pre-defined loss pattern as well as finding the scenario which best fits the imposed constraints (for example, BLM signals).

The performed studies have allowed understanding of the loss patterns and the propagation of beam losses along magnets. This has led to assessing the LHC MQ quench levels, which was the main objective of this work. The experience coming from the quench tests will certainly help conducting future quench tests at nominal LHC beam energies.

8 Future perspectives

After LS1, the LHC will operate with beam energy of (6.5 – 7.0) TeV, which certainly will bring new operational challenges. The quench levels assessed in this work at 4 TeV should be extrapolated to the higher beam energies and validated with dedicated experiments. The developed methods of performing quench tests in different timescales are ready and the experience gained by now should allow generating controlled beam losses successfully also in the future. This is necessary to determine performance reach of the machine in the current configuration and prepare upgrades for the era of the High Luminosity LHC.

The quench tests could be improved by incorporating particle detectors to the inside of the magnets, where they would be closer to the loss location and therefore register higher signals. This will enable better probing the transverse loss propagation across a magnet. Such detectors have been already installed in IR7 in the magnet interconnection close to the beam vacuum tubes to be used in the future. Moreover, there are two aspects which are crucial for the future experiments. First of all, the QPS system has to be enhanced so that the high resolution data is synchronized with the BLM signals and acquired in the Post Mortem. Secondly, low intensity beam diagnostics has to be provided.

The strategy of assessing quench levels, which we have developed, can also be used in the studies on new magnets based on Nb₃Sn which will be incorporated to the LHC system. Obviously, these magnets would need to be exposed to beam impact in various timescales. Depending on the location of these magnets (inner triplets or dispersion suppressor), probably the method of inducing losses would require an appropriate adjustment. Based on the experienced gain during the operation with NbTi magnets, quench levels for the superconductor magnets should be assessed relatively fast and efficiently.

The studies on the UFOs shall be continued. The FLQT results show that the BLM thresholds in the millisecond loss regime could be significantly increased but the UFO behaviour at higher beam energies is known only theoretically. Although the loss timescale and loss size achieved during the quench test were adequate to the dimensions of UFO-provoked losses, it has to be kept in mind that the UFO-losses are not pure primary particles but rather they constitute

a combination of various particles. This, in the end determines interactions with magnet materials.

The Geanto-Quench-Meter in its current form, is designed for studying beam loss patterns, their influence onto the propagation of a secondary particle shower along the LHC half-cell, computing BLM signal and calculating quench levels of MQs. This program could be developed so that various loss scenarios and quench levels of different magnet types could be investigated. In addition, an interface preventing a user from changing the core of the code and allowing experimental parameters to be introduced should be provided.

In the previous chapters the simulation method of considering point-like losses and weighting the results by the coefficients corresponding to a loss patterns was presented. Although the obtained quench levels were consistent with those ones coming from the standard simulation procedure provided in Fluka [134], [135], the simulated BLM signals were underestimated with respect to the measured values. Therefore, additional studies should be performed in order to fully understand the origin of this discrepancy. This includes the following steps:

- repeating the process of simulating point-like losses as previously but with BLM signals based directly on energy deposited in a detector gas,
- incorporating an exact loss pattern directly to the Geant4 simulations and investigating its impact onto an energy distribution inside SC coils and signals in BLMs (this should be done for both approaches of simulating BLM signals).

Although time-consuming, these cross-checks would provide information whether an error committed by using the approximation is specific for the method or is related to the Geant4 capability of reconstructing transverse tails of a secondary particles shower. This could be also verified by repeating the performed simulations with new Geant4 versions. If the proposed solutions do not provide the answer to differences in simulating BLM signals, an experiment based on hitting with particles a structure transversely constituting of alternately located blocks of dense matter and BLMs could be done. Comparing measured and simulated detector signals would estimate Geant4 limitations.

Concluding, there is still a lot of space for the future studies on quench levels and investigations on beam loss behaviour in various machine environments. Both, the experimental techniques and simulation methods will develop together with the operational demands of the LHC.

A Technical drawings

In this section the main CDD drawings used for implementation the magnet representation to Geant4 code (see Chapter 3) are given:

- Cross-section of the LHC Main Quadrupole MQ
- Cross-section of the LHC Main Dipole MB
- Interconnection between Short Straight Section SSS and MB
- Interconnection between MB and SSS
- Layout of ARC cell Q12

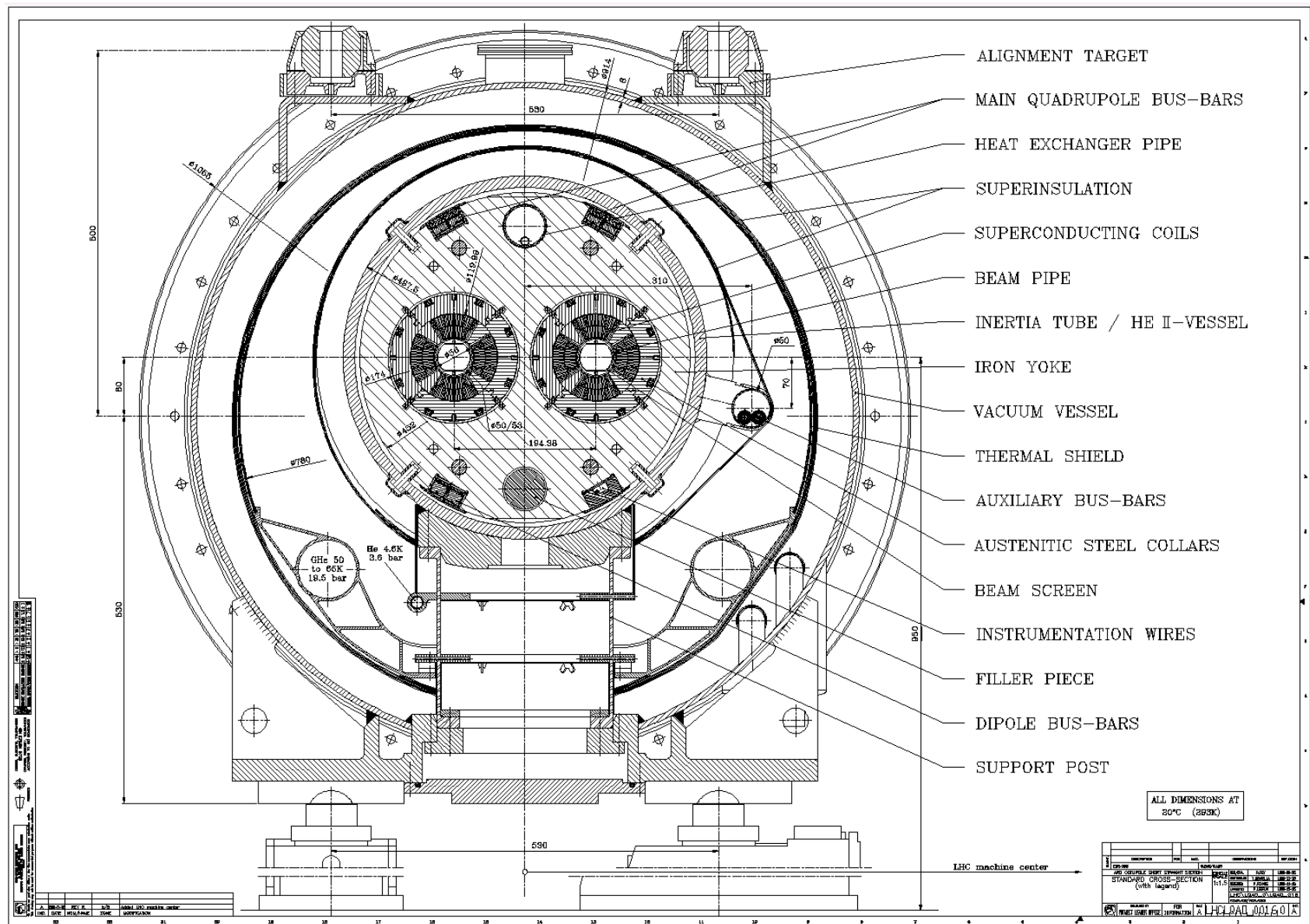


Figure A.1 – Technical drawing: MQ cross-section. CDD drawing: LHCLQAO_0016, [150].

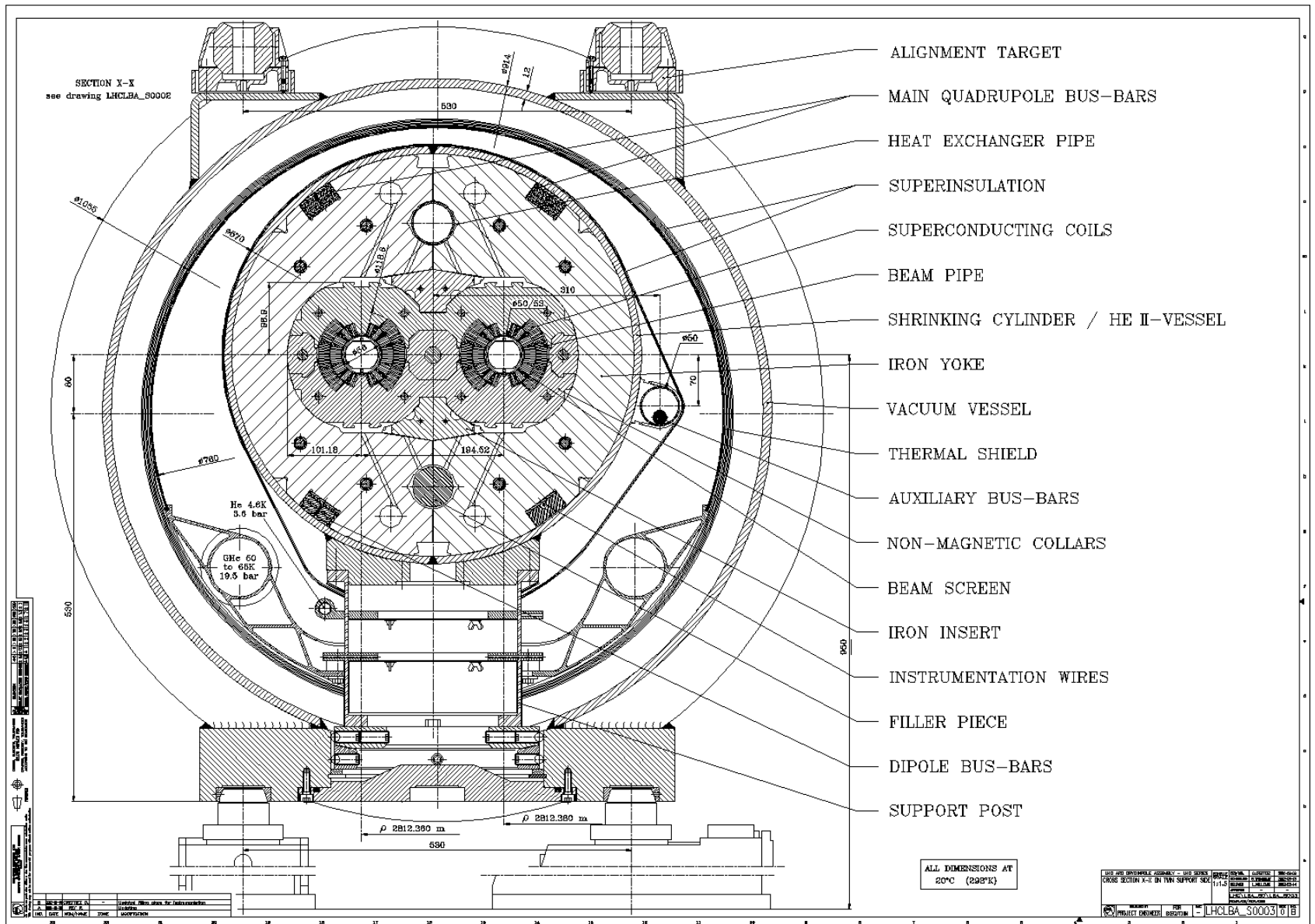


Figure A.2 – Technical drawing: MB cross-section. CDD drawing: LHCLBA_S003, [150].

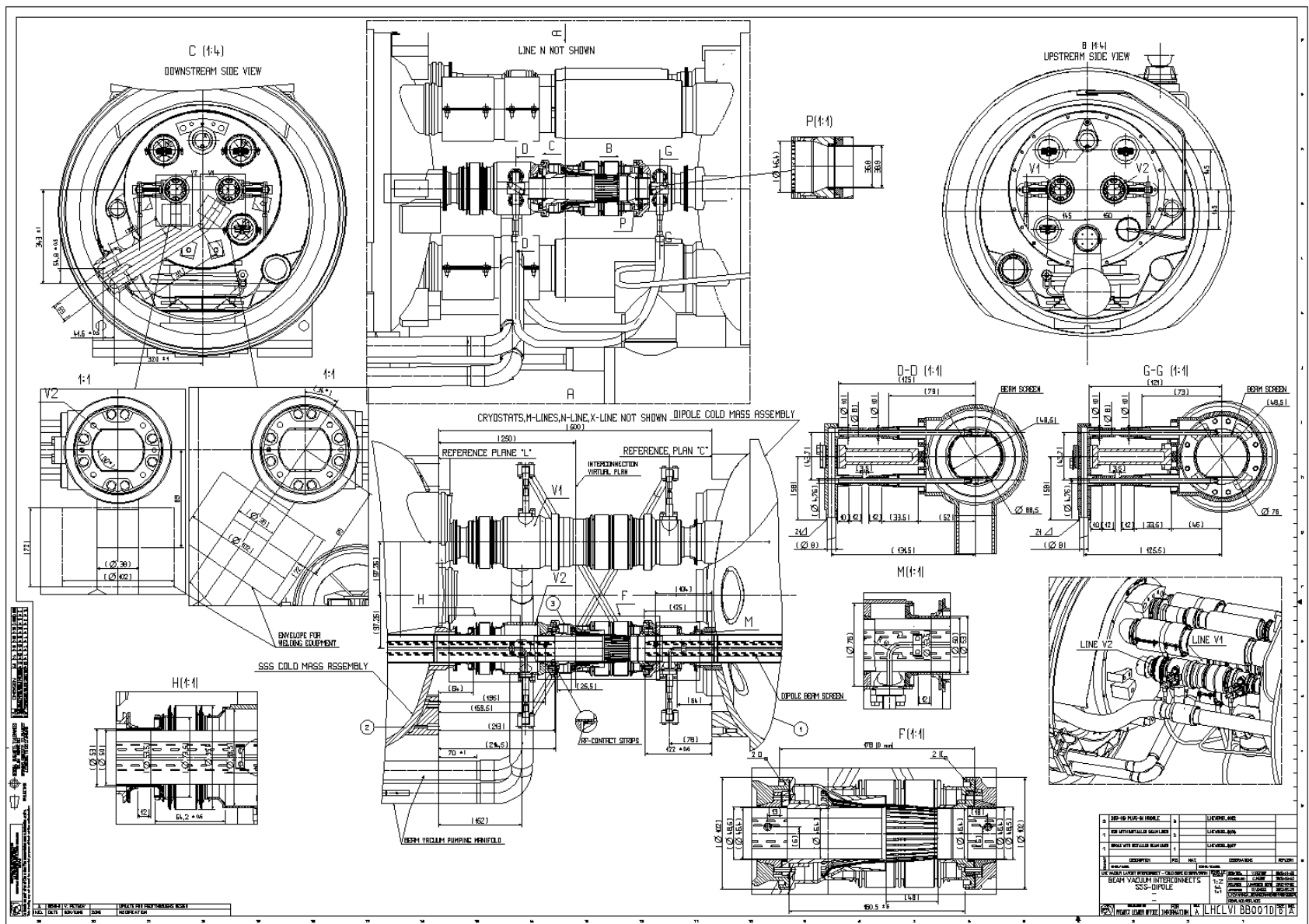


Figure A.3 – Technical drawing: SSS-MB Interconnection. CDD drawing: LHCLVI_BB0010, [150].

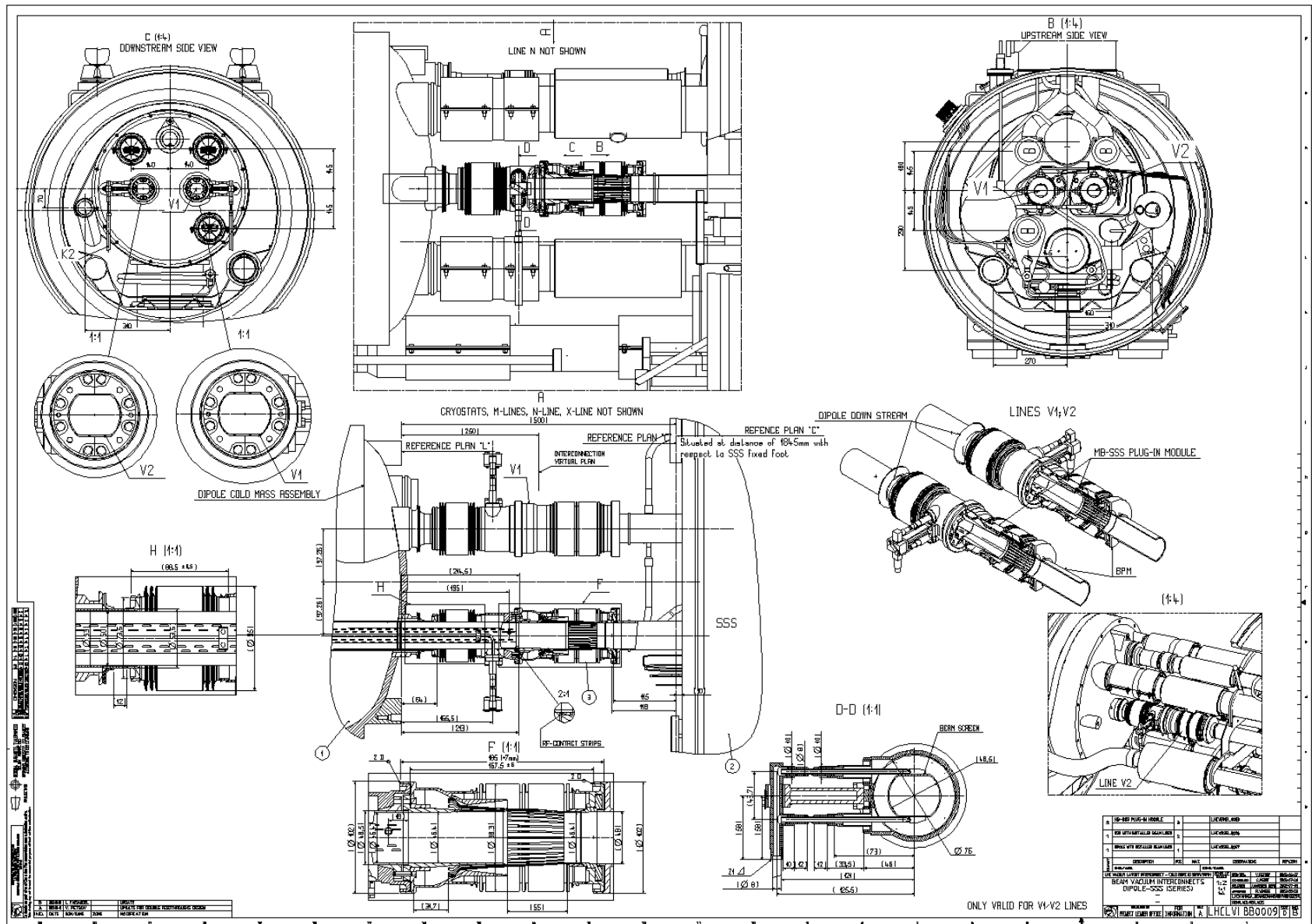


Figure A.4 – Technical drawing: MB-SSS Interconnection. CDD drawing: LHCLVI_BB0009, [150].

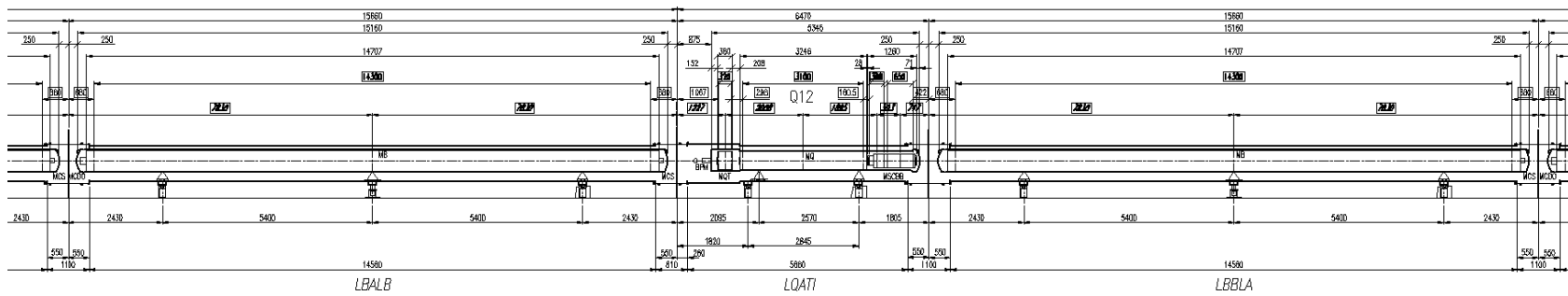


Figure A.5 – Technical drawing: Layout of LHC cell Q12. CDD drawing: LHCLSA_0008, [150].

B Response functions

The methodology of obtaining BLM response functions is presented in Chapter 3. In this section, a comparison of the response function shapes is given depending on impacting angles of various particles (Fig. B.1). Especially in the high energy range, the signals might vary by two orders of magnitude for two extreme cases (0° omitted due to possible simulation artifacts): 15° and 90° .

Appendix B. Response functions

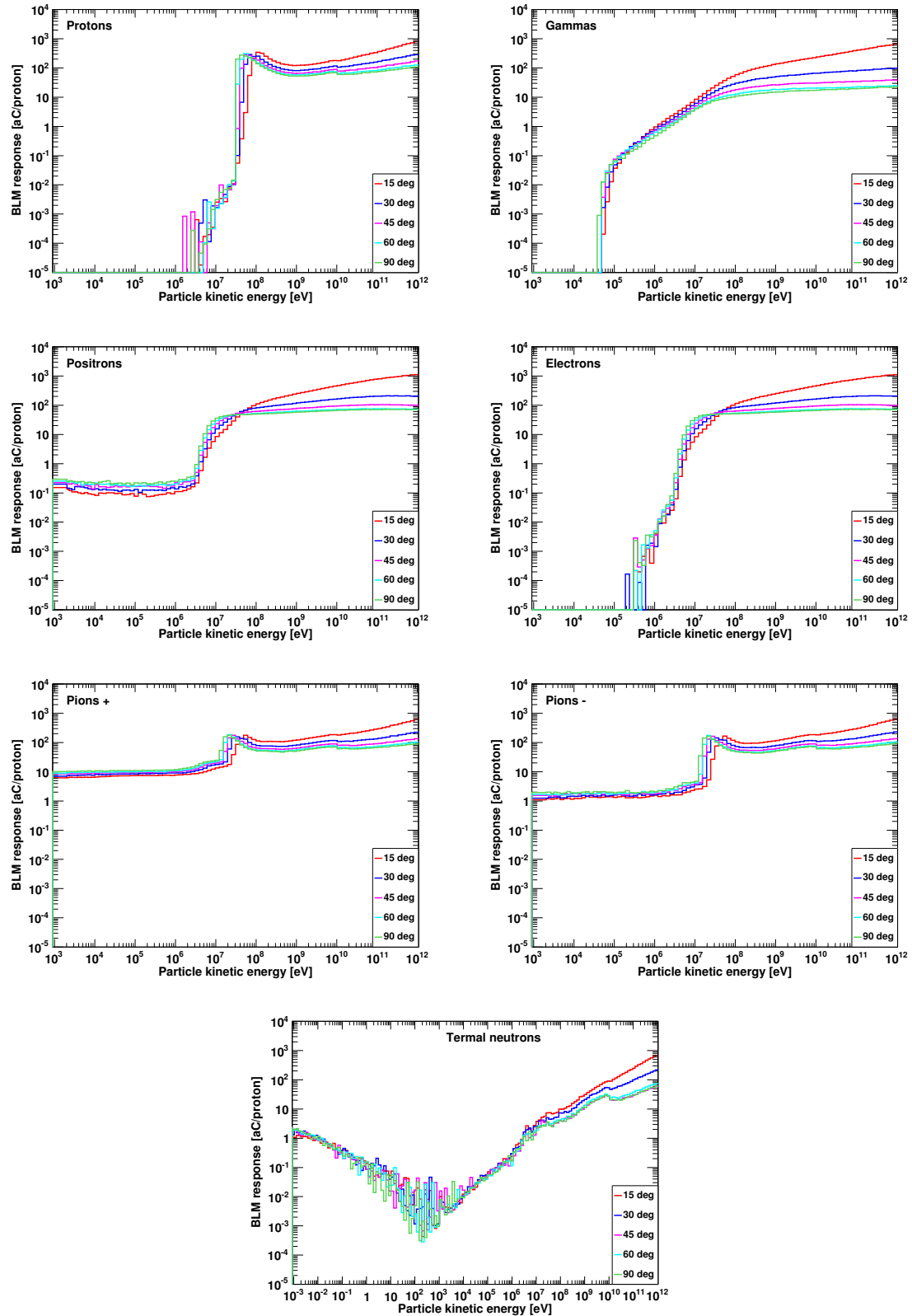


Figure B.1 – BLM response functions for various particle types and impacting angles[115].
176

Bibliography

- [1] C. Lefevre. CERN LHC : the guide, 2008.
- [2] LHC Design Report, Chapter 3: Layout and Performance. Geneva, Switzerland, 2004.
- [3] T. Tortschanoff *et al.* The short straight sections for the LHC. In *Proceedings of 17th Particle Accelerator Conference*, pages 3374–3376, Vancouver, Canada, 1997.
- [4] L. Evans. *The Large Hadron Collider: a Marvel of Technology*. EPFL Press, 2009.
- [5] H. Wiedemann. Particle Accelerator Physics. Basic Principles and Linear Beam Dynamics, 1993.
- [6] LHC Design Report, Chapter 2: Beam Parameters and Definitions . Geneva, Switzerland, 2004.
- [7] CERN-BROCHURE-2006-003-ENG. CERN LHC : the guide, 2006.
- [8] O. Brüning and P. Collier. Building a behemoth. *IEEE Transactions on Applied Superconductivity (IEEE-TAS)*, 448:285–289, 2007.
- [9] *Superconductivity*. DESY Summerstudent programme 2009 lectures.
- [10] M. Tinkham. *Introduction to Superconductivity*. Dover Publications, INC., 2nd edition, 1996.
- [11] D.R. Tilley and J. Tilley. *Superfluidity and Superconductivity*. John Wiley & Sons. Inc., 3rd edition, 2010.
- [12] V.L. Ginzburg. *On Superconductivity and Superfluidity. A Scientific Autobiography*. Springer, 2009.
- [13] P. Schmueser K.H. Mess and S. Wolf. *Superconducting accelerator magnets*. World Scientific, 1996.
- [14] D. Leroy J.B. Jeanneret, L.R. Oberli, and T.Trenkler. Quench levels and transient beam losses in LHC magnets, 1996. LHC Project Report 044.

Bibliography

- [15] M. Sapinski *et al.* Beam Induced Quenches of LHC Magnets. In *Proceedings of IPAC2013*, number 045 in THPEA, Shanghai, China, 2013. CERN-ATS-2013-049.
- [16] M. Sapinski *et al.* Beam-induced quenches of LHC magnets. In *Proceedings of IPAC2013*, number 045 in THPEA, pages 3243–3245, Shanghai, China, 2013.
- [17] H. Wiedemann. Particle Accelerator Physics II. Nonlinear and High-Order Beam Dynamics, 1999.
- [18] L. Rossi. Superconducting Magnets for the LHC Main Lattice. In *IEEE Transactions on Applied Superconductivity*, volume 14, pages 153–158, 2004.
- [19] CERN data base, <http://cds.cern.ch/record/843195>.
- [20] LHC Design Report, Chapter 7: Main Magnets in the Arcs. Geneva, Switzerland, 2004.
- [21] L. Rossi. Superconductivity and the LHC: the early days. *CERN Courier - International Journal of High-Energy Physics*, October 2011.
- [22] R. Schmidt *et al.* Protection of the CERN Large Hadron Collider. *New Journal of Physics*, 290(8), November 2006.
- [23] V. Kain *et al.* Material Damage Test with 450 GeV LHC-type beam. In *Proceedings of the 21st IEEE Particle Accelerator Conference*, Knoxville, TN, USA, 2005. CERN-LHC-Project-Report-822.
- [24] N.A. Tahir *et al.* Impact of 7-TeV/c large hadron collider proton beam on a copper target. *Journal of Applied Physics*, 97(8), April 2005.
- [25] J. Wenninger, R. Schmidt and M. Zerlauth. Machine protection: the key to safe operation. *CERN Courier - International Journal of High-Energy Physics*, 33(7):45–47, September 2013.
- [26] LHC Design Report, Chapter 17: Beam Dumping System. Geneva, Switzerland, 2004.
- [27] M. Ross. Recuperation of ISR Dipole Magnet Yokes for Use as Shielding for the LHC Beam Dumps TDE. Technical Report LHC-PROJECT-NOTE-185, CERN, Geneva, Switzerland, 1999.
- [28] A. Presland *et al.* A Large Diameter Entrance Window for the LHC Beam Dump Line. In *Proceedings of the 21st IEEE Particle Accelerator Conference*, Knoxville, TN, USA, 2005. CERN-LHC-Project-Report-823.
- [29] LHC Design Report, Chapter 9: Powering and Protection. Geneva, Switzerland, 2004.
- [30] D. Hagedorn L. Coull, V. Remondino, and F. Rodríguez-Mateos. LHC magnet quench protection system. In *IEEE Transactions On Magnetics*, volume 30, pages pp.1742–1745, Victoria, Canada, July 1994. CERN-LHC-Note-251.

- [31] K. Dahlerup-Petersen. Protection Systems in the LHC. In *PH/ESE Electronics Seminar of the Superconducting Circuit*, Geneva, Switzerland, November 2011.
- [32] F.Rodríguez-Mateos *et al.* The Protection System for the Superconducting Elements of the Large Hadron Collider at CERN. In *Proceedings of the 1999 Particle Accelerator Conference*, New York, USA, 1999. CERN-LHC-Project-Report-283.
- [33] F. Rodríguez-Mateos and F. Sonnemann. Quench Heater Studies for the LHC Magnets. In *Proceedings of the 2001 Particle Accelerator Conference*, pages 3451–3453, Chicago, USA, 2001. CERN-LHC-Project-Report-485.
- [34] F.Rodríguez-Mateos *et al.* Quench Heater Experiments on the LHC Main Superconducting Magnets. In *Proceedings of EPAC 2000*, pages 2154–2156, Vienna, Austria, 2000. CERN-LHC-Project-Report-418.
- [35] K. Dahlerup-Petersen *et al.* Energy Extraction for the LHC Superconducting Circuits. In *Proceedings of the 2001 Particle Accelerator Conference*, pages pp.3448–3450, Chicago, USA, 2001. CERN-LHC-Project-Report-484.
- [36] A. Siemko. Safeguarding the superconducting magnets. *CERN Courier - International Journal of High-Energy Physics*, 33(7):33–35, September 2013.
- [37] K. Dahlerup-Petersen *et al.* Energy Extraction for the LHC Superconducting Circuits. In *Proceedings of the 7th European Particle Accelerator Conference*, Vienna, Austria, 2000. LHC-Project-Report-421; CERN-LHC-Project-Report-421.
- [38] R. Denz *et al.* Upgrade of the protection system for superconducting circuits in the LHC. In *Proceedings of PAC09*, number 047 in MO6PFP, pages 244–246, Vancouver, BC, Canada, 2009. CERN-ATS-2009-008.
- [39] E. Gschwendtner *et al.* LHC Beam Loss Monitor System Design. In *AIP Conference Proceedings, 10th Beam Instrumentation Workshop*, volume 648, pages 229–236, Upton, New York, USA, May 2002.
- [40] C. Grupen. *Introduction to Radiation Protection. Practical Knowledge for Handling Radioactive Sources*. Springer, 2010.
- [41] G.F. Knoll. *Radiation Detection and Measurement*. John Wiley & Sons. Inc., 2010.
- [42] E.B. Holzer *et al.* Beam Loss Monitoring System for the LHC. In *Nuclear Science Symposium Conference Record, 2005 IEEE*, volume 2, pages pp.1052–1056, Victoria, Canada, October 2005. CERN-AB-2006-009.
- [43] CERN BLM expert E. Effinger. private communication.
- [44] M. Stockner *et al.* Measurements and Simulations of Ionization Chamber Signals in Mixed Radiation Fields for the LHC BLM System. In *Nuclear Science Symposium Conference Record, 2006. IEEE*, volume 3, pages 1342–1345, San Diego, CA, USA, October 2006. CERN-AB-2006-086.

Bibliography

- [45] B. Holzer *et al.* Design of the Beam Loss Monitoring system for the LHC ring. In *Proceedings of EPAC 2004*, pages 2487–2489, Lucerne, Switzerland, July 2004.
- [46] N.V. Mokhov *et al.* Protecting LHC IP1/IP5 Components Against Radiation Resulting from Colliding Beam Interactions. Technical report, Geneve, Switzerland, March 2003. LHC Project Report 633.
- [47] E. Effinger *et al.* The LHC beam loss monitoring system's data acquisition card. In *Proceedings of 12th Workshop on Electronics For LHC and Future Experiments*, pages 108–112, Valencia, Spain, September 2006.
- [48] B. Dehning. Beam loss monitor system for machine protection. In *Proceedings of DIPAC 2005*, number 01 in ITMA, pages 117–121, Lyon, France, June 2005. CERN-AB-2005-062.
- [49] C. Zamantzas. *The Real-Time Data Analysis and Decision System for Particle Flux Detection in the LHC Accelerator at CERN*. PhD thesis, Institute of Physics Publishing, Bristol and Philadelphia, 1990.
- [50] E. Effinger *et al.* The LHC Beam Loss Monitoring System's Surface Building Installation. In *Proceedings of 12th Workshop on Electronics For LHC and Future Experiments*, pages 552–556, Valencia, Spain, September 2006.
- [51] CERN BLM expert Ch. Zamantzas. private communication.
- [52] C. Zamantzas *et al.* An FPGA Based Implementation for Real-Time Processing of the LHC Beam Loss Monitoring System's Data. In *Nuclear Science Symposium Conference Record, 2006. IEEE*, volume 2, pages 950–954, San Diego, CA, USA, November 2006.
- [53] LHC BLM threshold modification reports, http://ab-div-bdi-bl-blm.web.cern.ch/ab-div-bdi-bl-blm/Acquisition_system/Data_acquisition_integration_durations_20100313.htm, May 2013.
- [54] E. Nebot *et al.* Handling of the LHC Beam Loss Monitoring System Abort Thresholds. In *Nuclear Science Symposium and Medical Imaging Conference (NSS/MIC), 2011 IEEE*, pages 477–481, Valencia, Spain, October 2011.
- [55] E. Holzer *et al.* Commissioning and optimization of the LHC BLM System. In *Proceedings of 46th ICFA Advanced Beam Dynamics Workshop on High-Intensity and High-Brightness Hadron Beams*, number 01 in WEO1C, Morschach, Switzerland, October 2010. CERN-BE-2010-031.
- [56] E. Holzer *et al.* Generation of 1.5 Million Beam Loss Threshold Values. In *Proceedings of 11th European Particle Accelerator Conference*, number 147 in THPC, Genoa, Italy, June 2008.
- [57] R. Assmann *et al.* Requirements for the LHC Collimation System. In *Proceedings of EPAC2002*, page 197, Paris, France, 2002. CERN-LHC-Project-Report-599.

- [58] J.B.Jeanneret *et al.* Beam Loss and Collimation at LHC. In *AIP Conference Proceedings*, number 642, pages 189–191, Batavia, Illinois (USA), 2002. CERN-LHC-Project-Report-603.
- [59] I. Baishev, A.Barsukov and J.B. Jeanneret. Radiation heating of primary collimators at ramping. Technical Report CERN-LHC-Project-Report-309, CERN, Geneva, Switzerland, 1996.
- [60] LHC Design Report, Chapter 18: Beam Cleanning and Collimation System. Geneva, Switzerland, 2004.
- [61] B. Goddard R. Assmann, E. Vossenberg, and E. Weisse. The Consequences of Abnormal Beam Dump Actions on the LHC Collimation System, 2002. LHC Project Note 293.
- [62] M. Kramer, F.J.P. Soler. *Large Hadron Collider Phenomenology*. SUSSP Publications and Institute of Physics Publishing, 2004.
- [63] R. Schmidt. How Can We Lose the Beam? Beam Loss Scenarios and Strategies for the Design of Protection Systems. In *LHC Performance Workshop - Chamonix XII*, Chamonix, France, 2003.
- [64] T. Baer *et al.* MKI UFOs at Injection. Technical Report CERN-ATS-Note-2011-065 MD, CERN, Geneva, Switzerland, 2011.
- [65] E. Nebot *et al.* Analysis of fast losses in the LHC with the BLM system. In *Proceedings of IPAC2011*, number 136 in TUPC, San Sebastián, Spain, 2011. CERN-ATS-2011-057.
- [66] T. Baer *et al.* UFOs in the LHC. In *Proceedings of IPAC2011*, number 137 in TUPC, San Sebastián, Spain, 2011. CERN-ATS-2011-051.
- [67] T. Baer *et al.* UFOs in the LHC: Observations, studies and extrapolations. In *Proceedings of IPAC2012*, number 086 in THPPP, New Orleans, LA, USA, 2012. CERN-ATS-2012-100.
- [68] B. Goddard *et al.* Transient beam losses in the LHC injection kickers from micron scale dust particles. In *Proceedings of IPAC2012*, number 092 in TUPPR, New Orleans, LA, USA, 2012. CERN-ATS-2012-219.
- [69] K. Wille. *The Physics of Particle Accelerators: An Introduction*. Oxford University Press, 2000.
- [70] S.Y. Lee. *Accelerator Physics*. World Scientific, 2nd edition, 2004.
- [71] A.W. Chao and M.Tinger. *Handbook of Accelerator Physics and Engineering*. World Scientific, 3rd edition, 2006.
- [72] H. Wiedemann. Particle Accelerator Physics. Basic Principles and Linear Beam Dynamics, 1993.

Bibliography

- [73] J. Wenninger (CERN, BE-OP-LHC), operation expert. private communication, October 2010.
- [74] B. Goddard *et al.* Expected Emittance Growth and Beam Tail Repopulation-From Errors at Injection into the LHC. In *Proceedings of 21st IEEE Particle Accelerator Conference*, pages 1266–1268, Knoxville, Tennessee, 2005. CERN-LHC-Project-Report-814.
- [75] W. Hofle *et al.* Beam Tests of the LHC Transverse Feedback System. In *Proceedings of RuPAC-2010*, number 01 in THCHX, pages 275–279, Protvino, Russia, 2010.
- [76] W. Hofle *et al.* Transverse damping systems for the future CERN LHC. In *Proceedings of the 2001 Particle Accelerator Conference*, volume 2, pages 1237–1239, Chicago, IL, USA, June 2001.
- [77] N. Mounet. *The LHC transverse coupled-bunch instability*. PhD thesis, École Polytechnique Fédérale de Lausanne, 2012.
- [78] E. Gianfelice-Wendt *et al.* LHC Abort Gap Cleaning with the Transverse Damper. In *Proceedings of PAC09*, number 017 in WE6PFP, pages 2519–2521, Vancouver, BC, Canada, 2009. CERN-ATS-2009-016.
- [79] W. Hofle *et al.* Controlled Transverse Blow-up of Highenergy Proton Beams for Aperture Measurements and Loss Maps. In *Proceedings of IPAC2012*, number CERN-ATS-2012-128 in THPPR, pages 4059–4061, New Orleans, LA, USA, 2012.
- [80] L. Vos *et al.* Damping of Coherent oscillations. In *Proceedings of 11th International Advanced ICFA Beam Dynamics Workshop on Beam Cooling and Instability Damping, Festschrift 30th anniversary of Electron cooling*, pages 56–63, Moscow, Russian Federation, 1996. CERN-SL-96-066-AP.
- [81] D. Valuch and P. Baudrenghien. Beam phase measurement and transverse position measurement module for the LHC. In *LLRF07 Workshop*, Knoxville TN, USA, October 2007.
- [82] P. Baudrenghien *et al.* Digital Signal Processing for the Multi-Bunch LHC Transverse Feedback System. In *Proceedings of 11th European Particle Accelerator Conference*, number 122 in THPC, Genoa, Italy, 2008. LHC-PROJECT-Report-1151.
- [83] CERN ADT expert D. Valuch. private communication.
- [84] C. Bracco *et al.* Experiments on the margin of beam induced quenches a superconducting quadrupole magnet in the LHC . In *Proceedings of IPAC2012*, number 004 in MOPPC, New Orleans, LA, USA, 2012. CERN-ATS-2012-209.
- [85] C. Bracco *et al.* Quench Margin at Injection. Technical Report CERN-ATS-Note-2011-067 MD, CERN, Geneva, Switzerland, 2011.
- [86] CERN BLM expert M. Sapinski. private communication, September 2013.

- [87] A. Verweij. QP3: Users Manual.
- [88] M. Sapinski *et al.* LHC magnet quench test with beam loss generated by wire scan. In *Proceedings of IPAC2011*, number 173 in WEPC, San Sebastián, Spain, 2011. CERN-ATS-2011-062.
- [89] CERN Wire Scanner Design, <https://project-wire-scanner.web.cern.ch>, July 2013.
- [90] LHC Design Report, Chapter 8: Insertion Magnets. Geneva, Switzerland, 2004.
- [91] G. Battistoni *et al.* The FLUKA code: Description and benchmarking.
- [92] A. Fass, A. Ferrari, J. Ranft, and P.R. Sala. FLUKA: a multi-particle transport code, 2005. CERN-2005-10, INFN-TC-2005-11, SLAC-R-773.
- [93] G. Battistoni *et al.* The FLUKA code : Description and benchmarking. In *AIP Conference Proceedings*, number 896, pages pp.31–49, Stanford, CA, 2007. SLAC-REPRINT-2007-184.
- [94] A. Lechner *et al.* paper in preparation.
- [95] B. Dehning M. Sapinski and A. Priebe. Simulation of Beam Loss in LHC MB Magnet and Quench threshold test, 2009. CERN-LHC-Project-Note-422.
- [96] Minutes of the Quench Test Strategy Working Group (QTSWG) meeting, 16 March 2012, <http://cern.ch/biq>, 2012.
- [97] S. Redaelli *et al.* Quench Tests at The Large Hadron Collider with collimation losses at 3.5 Z TeV. In *Proceedings of HB2013*, number 245 in MOP, Beijing, China, 2012.
- [98] S. Redaelli *et al.* Collimator losses in the DS of IR7 and quench test at 3.5 TeV. Technical Report CERN-ATS-Note-2011-042 MD, CERN, Geneva, Switzerland, 2011.
- [99] E.B. Holzer. Threshold changes for MD on Collimation Leakage into Dispersion Suppressor IP7 and Magnet Quenching. Technical Report LHC-BLM-ECR-0020 v.2 , EDMS Id: 1143931 v.2, CERN, Geneva, Switzerland, May 2011.
- [100] G. Bellodi *et al.* Pb ions collimator losses in IR7 DS and quench test at 3.5 Z TeV. Technical Report CERN-ATS-Note-2012-081 MD, CERN, Geneva, Switzerland, 2012.
- [101] E.Nebot del Busto. BLM Threshold changes for MD DS Ion quench test. Technical Report LHC-BLM-ECR-0029 v.1 , EDMS Id: 1173323 v.1, CERN, Geneva, Switzerland, November 2011.
- [102] B.Salvachua, S.Redaelli, R.Bruce and D.Wollmann. Quench Test 2013: Quench Margin at 4TeV. Technical Report EDMS Id: 1264646 v.1, CERN, Geneva, Switzerland, February 2013.
- [103] B.Salvachua. First results on proton collimation quench test. In *1st Quench Test Analysis Working Group meeting, 9th April 2013*, Geneva, Switzerland, 2013.

Bibliography

- [104] Ch. Kurfuerst. *Quench Protection of the LHC Quadrupole Magnets*. PhD thesis, Vienna University of Technology, 2010.
- [105] MAD-X webpage, <http://cern.ch/mad>, December 2013.
- [106] W. Herr and F. Schmidt. A MAD-X Primer, 2006. CERN-AB-2004-027-ABP.
- [107] SixTrack webpage, <http://cern.ch/frs>, December 2013.
- [108] S. Agostinelli *et al.* Geant4—a simulation toolkit. *Nucl. Instrum. Methods Phys. Res., A* 506 (2003) 250-303, 2003.
- [109] J. Allison *et al.* Geant4 developments and applications . *IEEE Transactions on Nuclear Science*, 53(1):270–278, Feb 2006.
- [110] J. Apostolakis *et al.* Hadronic Shower Shape Studies in Geant4: Update. Technical Report CERN-LCGAPP-2008-01, CERN, Geneva, Switzerland, 2008.
- [111] L. Bottura *et al.* A general model for thermal, hydraulic and electric analysis of superconducting cables. *Cryogenics*, 40(8-10):617–626, August–October 2000.
- [112] A. Akhmetov *et al.* A continuum model for current distribution in Rutherford cables. *IEEE Transactions on Applied Superconductivity*, 11(1):2138–2141, March 2001.
- [113] Geant4 webpage, <http://geant4.cern.ch>, July 2013.
- [114] B. Auchmann (CERN, TE-MPE-PE), ROXIE and QPS expert. private communication, 2013.
- [115] M. Stockner. *Beam Loss Calibration Studies for High Energy Proton Accelerators*. PhD thesis, Vienna University of Technology, 2007.
- [116] M. Stockner *et al.* Measurements and Simulations of Ionization Chamber Signals in Mixed Radiation Fields for the LHC BLM System. *Nuclear Science Symposium Conference Record, 2006. IEEE*, 3:1342–1345, October 2006.
- [117] M. Sapinski *et al.* Response functions of Ionisation Chamber BeamLoss Monitor. Technical Report EDMS Id: 1055210, CERN, Geneva, Switzerland, March 2010.
- [118] L. Sarchiapone *et al.* FLUKA Monte Carlo simulations and benchmark measurements for the LHC beam loss monitors. *Nuclear Instruments and Methods in Physics Research Section A: Accelerators, Spectrometers, Detectors and Associated Equipment*, 581(1–2):511 – 516, 2007. {VCI} 2007 Proceedings of the 11th International Vienna Conference on Instrumentation.
- [119] M. Brugger *et al.* Measurements and simulations of the BLM response to a radiation field inside the CERF target area. Technical Report ATS/Note/2010/045, CERN, Geneva, Switzerland, November 2010.

- [120] CERN indico webpage: Conferences, Workshops and Events, Workshops, LHC accelerator, LHC accelerator; <http://indico.cern.ch/categoryDisplay.py?categoryId=1537>, 2012.
- [121] CERN ADT expert W. Hofle. private communication.
- [122] A. Priebe *et al.* ADT fast losses MD. Technical Report CERN-ATS-Note-2013-017 MD, CERN, Geneva, Switzerland, 2013.
- [123] A.K. Sharma. *Text book of Correlation and Regression*. DPH Mathematics Series, 2005.
- [124] T.Baer A.Priebe and D.Valuch. MD1-2012 ADT fast losses test at 450 GeV for UFO studies. Technical Report EDMS Id: 1212026 v.1, CERN, Geneva, Switzerland, 2013.
- [125] M.Sapinski A.Priebe, T.Baer and D.Valuch. ADT Fast Losses Test at 450 GeV and 4 TeV for UFO studies. Technical Report EDMS Id: 1225457 v.1, CERN, Geneva, Switzerland, 2013.
- [126] M.Sapinski A.Priebe, T.Baer and D.Valuch. 2012-md3: ADT and MKQ fast loss test for UFO studies. Technical Report EDMS Id: 1244647 v.1, CERN, Geneva, Switzerland, 2013.
- [127] R. Schmidt. Safe LHC Parameters Generation and Transmission (SLPT), 2006. LHC-CI-ES-0004 rev 0.1.
- [128] LHC Filling Schemes; <http://lpc.web.cern.ch/lpc/fillingschemes.htm>, 2013.
- [129] T. Baer (CERN, BE-OP-LHC), operation expert. private communication, May 2013.
- [130] T.Baer W.Hofle, A.Priebe, M.Sapinski, and D.Valuch. Quench Test 2013: Fast Losses Quench Test Using ADT. Technical Report EDMS Id: 1263345 v.1, CERN, Geneva, Switzerland, 2013.
- [131] A. Verweij (CERN, TE-MPE-PE), QPS expert. private communication.
- [132] A.Priebe *et al.* Beam-induced quench test of LHC main quadrupole. In *Proceedings of IPAC2011*, number 172 in WEPC, pages 2388–2390, San Sebastián, Spain, 2011. CERN-ATS-2011-058.
- [133] V. Chetvertkova (CERN,TE-MPE), MAD-X expert. private communication, 2013.
- [134] N.V. Shetty (CERN, EN-STI-EET), Fluka expert. private communication, 2013.
- [135] A. Lechner (CERN, EN-STI-EET), Fluka expert. private communication, 2013.
- [136] M. Sapinski A. Priebe, B. Dehning, M. Q. Tran, and A. Verweij. Investigations of Quench Limits of the LHC Superconducting Magnets. *IEEE Transactions on Applied Superconductivity (IEEE-TAS)*, 23(3), June 2013.
- [137] N. Mounet *et al.* Collimator Impedance Measurements in the LHC. In *Proceedings of IPAC2013*, number 047 in TUPWA, Shanghai, China, 2013.

Bibliography

- [138] G. Valentino *et al.* Beam diffusion measurements using collimator scans in the LHC. In *Phys. Rev. ST Accel. Beams* 16, 021003, 2013.
- [139] B. Dehning A. Araujo-Garcia. Configuration of the Beam Loss Monitors for the LHC arcs. Technical report, Geneve, Switzerland, October 2000. LHC-PROJECT-NOTE-238.
- [140] M. Sapinski, BLM expert, CERN . private communication, September 2013.
- [141] M. Gasior, BPM expert, CERN . private communication, August 2013.
- [142] A. Nosych, BPM expert, CERN . private communication, October 2013.
- [143] Jmad, <https://wikis.cern.ch/display/JMAD/Download>, 2012.
- [144] K. Fuchsberger *et al.* JMAD - Integration of MADX into the Java World. In *Proceedings of IPAC2011*, number 120 in WEPC, San Sebastian, Spain, 2011.
- [145] M. Calvi A. Siemko. Beam loss induced quench levels. 2nd LHC Project Workshop, January 2005. CERN-AB-2005-014.
- [146] B. Goddard R. Versaci, V. Boccone, A. Mereghetti, R. Schmidt, and V. Vlachoudis. FLUKA Studies of the Asynchronous Beam Dump Effects on LHC Point 6. In *Proceedings of IPAC2011*, number 175 in WEPC, San Sebastián, Spain, 2011. CERN-ATS-2011-236.
- [147] LHC eLogbook; <http://elogbook.cern.ch/eLogbook/eLogbook.jsp?lgbk=60>, 2013.
- [148] P.P. Granieri and R. van Weelderen. Deduction of Steady-State Cable Quench Limits for Various Electrical Insulation Schemes With Application to LHC and HL-LHC Magnets. *IEEE Transactions on Applied Superconductivity*, 24(3):1–6, June 2014.
- [149] L.Burnod *et al.* Thermal Modelling of the LHC dipoles functioning in superfluid Helium. In *Proceedings of 4th EPAC*, pages 2295–2297, London, United Kingdom, 1994.
- [150] CERN Drawing Directory (CDD), https://edms.cern.ch/cdd/plsql/c4w.get_in, July 2013.

Curriculum vitae

Personal information

FIRST NAME AND SURNAME: Agnieszka Priebe
EMAIL: agnieszka.priebe@gmail.com
NATIONALITY: Polish
GENDER: Female



Education

IX 2010 - II 2014 Doctoral studies at the European Organization for Nuclear Research - CERN
Beams Department,
Beam Instrumentation Group,
Beam Loss Monitoring System Section,
(Geneva, Switzerland)
and
École Polytechnique Fédérale de Lausanne - EPFL
(Lausanne, Switzerland)
PhD thesis title: *"Quench tests of LHC magnets with beam: studies on beam loss development and determination of quench levels"*

X 2004 – VI 2010 Master studies at Poznan University of Technology - PUT
(Politechnika Poznańska, Poznań, Poland)
Faculty of Technical Physics
Institute of Physics, Solid State Spectroscopy Division
Speciality: Nanotechnology (degree: Master of Science Engineering)
Average of all marks: 4.92 (max is 5.0)
Master thesis subject: *"Investigations the properties and photodegradation of polymer nanocomposites by means of nanotechnological and spectroscopic methods"*

VII-IX 2009 Summer Student Program at Deutsches Elektronen-Synchrotron - DESY
Machine Physics Group (MPY)
(Hamburg, Germany)

X 2007 – IX 2008 Technical Student Program at CERN
Accelerators and Beams Department,
Beam Instrumentation Group,

Beam Loss Monitoring System Section,
(Geneva, Switzerland)

VIII 2007 - IX 2007 Internship at Polish Academy of Sciences
(Polska Akademia Nauk, Poznan, Poland)
Institute of Molecular Physics
Solid State Radiospectroscopy Laboratory

IX 2000 – VI 2004 K. Libelt Secondary School no. 9
(IX Liceum Ogólnokształcące im. K. Libelta w Poznaniu)
Major subjects: Mathematics, Physics, Computer Science
Graduation: National Certificate in Polish, English and Biology

Prizes and achievements

X 2010 Medal for "The Outstanding Graduate of Poznan University of Technology"

VI 2010 2nd place at an institutional stage (in my case: Poznan University of Technology) of 41st edition of the Competition for the best student of the Republic of Poland (organized by Association of Polish Students)

2009/2010 Minister of Science and Higher Education Scholarship for Academic and Scientific Achievements

IV 2008 J.A.Gorecki Scholarship (for scientific performance)

2007/2008 Minister of Science and Higher Education Scholarship for Academic and Scientific Achievements

IV 2007 J.A.Gorecki Scholarship (for scientific performance)

X 2006 Scholarship for scientific performance (PUT)

X 2006 "Scholarship for the outstanding student of Poznan University of Technology" awarded by "Fundacja na rzecz rozwoju Politechniki Poznanskiej" ("Foundation for the Development of Poznan University of Technology")

X 2005 Scholarship for scientific performance (PUT)

VI 2004 "Gold medal for outstanding scientific achievements and the voluntary work" (Secondary School IX LO)

VI 2004 The letter of recognition for contributing to the organization and running the School European Club (Secondary School IX LO)

Courses and participation in workshops

24.04-4.05.2013 CERN Accelerator School (CAS), course on Superconductivity for Accelerators, Erice, Italy

X 2012 –II 2013 English course on writing professional documents

15.-26.01.2013 WAMSDO 2013 - Workshop on Accelerator Magnet, Superconductor, Design and Optimization, CERN, Geneva, Switzerland

4.-5.12.2012 Superconducting Technologies for the Next Generation of Accelerators, CERN, Geneva, Switzerland

7.-12.10.2012 Applied Superconductivity Conference (ASC 2012), Portland, Oregon, USA

18.-30.09.2011 CERN Accelerator School (CAS), course on Intermediate Level Accelerator Physics, Chios, Greece

4.-9.09.2011 *2nd* International Particle Accelerator Conference (IPAC 2011), San Sebastian, Spain

28.06-2.07.2010 The *4th* National Conference on Nanotechnology NANO 2010, Poznan, Poland

VII-IX 2009 German Course (DESY, Hamburg, Germany)

9.-20.03.2009 *40th* IFF Spring School 2009 "Spintronics – From GMR to Quantum Information", Jülich, Germany

11.-12.12.2008 *1st* X-Mas Workshop "Materials Science of Future Semiconductor Technology", Brandenburgische Technische Universität Cottbus, Germany

26.-30.11.2008 *5th* Workshop on Applications of Scanning Probe Microscopy STM/AFM 2008 (under the auspices of the Polish Vacuum Society), Zakopane, Poland

11.03.2008 Course: Radiological Protection, CERN, Meyrin, Switzerland

9.-11.04.2008 Course: C++ Programming Part 1 - Introduction to Object-Oriented Design and Programming, CERN, Meyrin, Switzerland

14.-25.01.2008 US Particle Accelerator School (USPAS), course on the Accelerator Physics, Santa Rosa, California, USA

8.10-14.12.2007 French Course, Level 1, CERN, Meyrin, Switzerland

8-22.09.2007 The Polish – German Summer School “Microsystem Technology”, Fachhochschule Brandenburg, Poznan University of Technology; Brandenburg, Germany; Poznan, Poland

22-29.07.2007 The Polish – German Summer School “Nanoscience”, Leibniz University Hannover, Poznan University of Technology, Adam Mickiewicz University Poznan; Poznan, Poland

26.06-5.07.2007 XXIII Low Temperature Physics Workshop, Summer with Helium 2007 "Nanostructures" , Institute of Molecular Physics, Polish Academy of Sciences; Odolanów, Poland

18-22.09.2006 II Scientific Workshop on Atomic, Molecular and Optical Physics National Laboratory, Nicolaus Copernicus University, Toruń, Poland

2003-2004 Project between Poznan University of Technology and Saginaw Valley State University (USA, Michigan)
Subject: *"Global environment - renewable sources of energy"*

Professional experience

2011-UP TO NOW CERN official guide

2008-2009 Volunteer at Institute of Physics, Solid State Spectroscopy Division, Department of Technical Physics, Poznan University of Technology

2004-2010 Voluntary help in Physics and Mathematics for pupils and students

II 2005-VI 2005 Voluntary help in Physics and Mathematics for pupils and students

Languages

POLISH: native tongue

ENGLISH: upper-intermediate (level of TOEIC) with English for Special Purposes (ESP) - elements of technical vocabulary in the field of modern physics

GERMAN: intermediate

Computer skills

OPERATION SYSTEMS: Windows
Linux

SCIENTIFIC TOOLS: ROOT
Geant4
Autodesk Inventor
Mathematica
Origin
Derive
MAD-X (basics)

PROGRAMMING LANGUAGES: C++
Linux
JAVA
Turbo Pascal

OTHERS: Microsoft Office (Word, Excel, Power Point, Access)
HTML
Internet

Additional information

2007-2010 Postgraduate Pedagogic-Teaching School (2-year long) at Poznan University of Technology, Technical Physics Department
Training at K.Libelt Secondary School no. 9 (IX LO) in Poznan

ACADEMIC YEAR Starościna roku (a representative of students; a mediator between professors

2009/2010 and students) of the 5th year students at Department of Technical Physics, Poznan University of Technology

11.03.09-13.05.09 Course of the proceeding in the emergency and life-threatening states (18 hours; pre-medical rescuer)

Other skills

Driving Licence

Interests connected with the studies

Nanotechnology
Surface Physics
Accelerator Physics
Application of physics in medicine

Spare time activities

Hiking
Traveling
Biking
Skiing
Reading books

List of publications

Main author

1. **A. Priebe**, B. Dehning, M. Sapinski, M. Q. Tran, A. Verweij, "Investigations of Quench Limits of the LHC Superconducting Magnets", *IEEE Transactions on Applied Superconductivity*, vol. 23, no. 3, pp. 4701205-4701205, June 2013
2. **A. Priebe**, K. Dahlerup-Petersen, B. Dehning, E. Effinger, J. Emery, E. B. Holzer, Ch. Kurfuerst, E. Nebot Del Busto, A. Nordt, M. Sapinski, J. Steckert, A. Verweij, Ch. Zamantzas, "Beam-induced quench test of LHC main quadrupole", *Proceedings of IPAC2011*, San Sebastian, Spain, WEPC172, pp. 2388-2390, September 2011
3. **A. Priebe**, T. Baer, B. Dehning, S. Redaelli, B. M. Salvachua Ferrando, M. Sapinski, M. Solfaroli Camillocci, D. Valuch, "ADT fast losses MD", CERN-ATS-Note-2013-017 MD, Geneve, Switzerland, CERN-ATS-Note-2013-017 MD, April 2013
4. **A. Priebe**, M. Nowicki, M. Szybowicz, P. Wojciechowska, "Nanocomposites based on MCAB matrix investigated by means of AFM and Raman microspectrometer", *Proceedings of the 4th National Conference on Nanotechnology NANO 2010*, p.209 (P-Wt-50), Poznan, Poland

Co-author

1. B. Auchmann, T. Baer, M.J. Bednarek, G. Bellodi, Ch. Bracco, R. Bruce, F. Cerutti, V. Chetvertkova, B. Dehning, W. Höfle, E.B. Holzer, A. Lechner, E. N. Del Busto, **A. Priebe**, S. Redaelli, B. Salvachua, M. Sapinski, R. Schmidt, N.V. Shetty, E. Skordis, M. Solfaroli Camillocci, D. Valuch, A. Verweij, J. Wenninger, D. Wollmann, M. Zerlauth, "Testing the beam-induced quench levels of LHC magnets during Run 1", to be submitted to Physics Review Special Topics: Accelerators and Beams (PRSTAB)
2. M. Sapinski, B. Auchmann, T. Baer, W. Bartmann, M.J. Bednarek, S. Bozyigit, Ch. Bracco, R. Bruce, F. Cerutti, V. Chetvertkova, K. Dahlerup-Petersen, B. Dehning, E. Nebot del Busto, E. Effinger, J. Emery, A. Guerrero, W. Höfle, E.B. Holzer, A. Lechner, **A. Priebe**, S. Redaelli, B. Salvachua, R. Schmidt, N. Vittal Shetty, A.P. Siemko, E. Skordis, M. Solfaroli Camillocci, J. Steckert, J. Uythoven, D. Valuch, A. Verweij, J. Wenninger, D. Wollmann, M. Zerlauth, "Beam-induced quench tests of LHC magnets", to be presented in IPAC2014
3. V. Chetvertkova, B. Auchmann, T. Baer, W. Hoefle, **A. Priebe**, M. Sapinski, R. Schmidt, A. Verweij, D. Wollmann, "MadX tracking simulations to determine the beam loss distributions for the LHC Quench tests with ADT excitation", to be presented in IPAC2014

4. N. V. Shetty, A. Lechner, M. Sapinski, **A. Priebe**, V. Chetvertkova, D. Wollmann, A. Verweij, B. Auchmann, "Energy deposition and quench level calculations for millisecond and steady-state quench tests of LHC arc quadrupoles at 4 TeV", to be presented in IPAC2014
5. M. Sapinski, T. Baer, M. J. Bednarek, G. Bellodi, C. Bracco, R. Bruce, B. Dehning, W. Höfle, A. Lechner, E. N. Del Bust, **A. Priebe**, S. Redaelli, B. Salvachua, R. Schmidt, D. Valuch, A. Verweij, J. Wenninger, D. Wollmann, M. Zerlauth, "Beam-induced quenches of LHC magnets", *Proceedings of IPAC2013*, Shanghai, China, THPEA045, pp. 3243-3245, May 2013
6. M. Sapinski, T. Baer, V. Chetvertkova, B. Dehning, W. Höfle, **A. Priebe**, R. Schmidt, D. Valuch, "Generation of Controlled Losses in Milisecond Timescale with Transverse Damper in LHC", *Proceedings of IPAC2013*, Shanghai, China, WEPME044, pp. 3025-3027, May 2013
7. S. Redaelli, R.W. Assmann, G. Bellodi, K. Brodzinski, R. Bruce, F. Burkart, M. Cauchi, D. Deboy, B. Dehning, E.B. Holzer, J.M. Jowett, L. Lari, E. Nebot del Bust, M. Pojer, **A. Priebe**, A. Rossi, R. Schmidt, M. Sapinski, M. Schaumann, M. Solfaroli Camollocci, G. Valentino, R. Versteegen, J. Wenninger, D. Wollmann, M. Zerlauth, "Quench Tests at the Large Hadron Collider with collimation losses at 3.5 Z TeV", *Proceedings of HB2012*, Beijing, China, MOP245, pp. 157-161, September 2012
8. B. Dehning, M. Dabrowski, E. Effinger, J. Emery, E. Fadakis, E. B. Holzer, S. Jackson, G. Kruk, C. Kurfuerst, A. Marsili, M. Misiowiec, E. Nebot Del Bust, A. Nordt, **A. Priebe**, C. Roderick, M. Sapinski, C. Zamantzas, V. Grishin, E. Griesmayer, "Overview of LHC Beam Loss Measurements", *Proceedings of IPAC2011*, San Sebastian, Spain, THOAA03, pp. 2854-2856, September 2011
9. M. Sapinski, F. Cerutti, B. Dehning, E. Effinger, J. Emery, B. Goddard, A. Guerrero, S. Grishin, E. B. Holzer, S. Jackson, Ch. Kurfuerst, A. Lechner, A. Marsili, M. Misiowiec, E. Nebot, A. Nordt, **A. Priebe**, Ch. Roderick, R. Schmidt, A. Verweij, J. Wenninger, Ch. Zamantzas, F. Zimmermann, "Is the BLM system ready to go to higher intensities?", *Proceedings of Chamonix 2011*
10. M. Calviani, M. Brugger, G. Spiez, M. Sapinski, **A. Priebe**, A. Nordt, M. Pojer, "R2E-related MD: slow controlled losses for RadMon/BLM cross-checks", CERN-ATS-Note-2011-070, Geneva, Switzerland, 2011
11. W. Bartmann, C. Bracco, B. Goddard, B. Holzer, M. Bednarek, E. Nebot Del Bust, A. Nordt, **A. Priebe**, S. Redaelli, M. Sapinski, R. Schmidt, M. Solfaroli, A. Verweij, M. Zerlauth, "Quench Margin at Injection", CERN-ATS-Note-2011-067 MD, Geneva, Switzerland, 2011
12. M. Sapinski, B. Dehning, E. Effinger, J. Emery, E.B. Holzer, C. Kurfuerst, **A. Priebe**, C. Zamantzas, "Quench Protection with LHC Beam Loss Monitors", *Proceedings of HB2010*, Morschach, Switzerland, MOPD53, pp. 198-201, September 2010

13. B. Dehning, **A. Priebe**, M. Sapinski, "LHC Beam Loss Measurements and Quench Level Abort Threshold Accuracy", *Proceedings of IPAC2010*, Kyoto, Japan, WEPEB069, pp. 2854-2856, May 2010
14. B. Dehning, T. Bohlen, J. Emery, F. Follin, E. B. Holzer, S. Jackson, D. Kramer, G. Kruk, P. Le Roux, J. Mariethoz, M. Misiowiec, L. Ponce, Ch. Roderick, M., Ch. Zamantzas, M. Stockner, D. Bocian, V. Grishin, H. Ikeda, **A. Priebe**, "First Experience with the LHC Beam Loss Monitoring System", *Proceedings of PAC09*, Vancouver, Canada, TH5RFP034, pp. 3522-3524, May 2009
15. M. Sapinski, B. Dehning, **A. Priebe**, "Simulation of Beam Loss in LHC MB Magnet and Quench threshold test", CERN-LHC-Project-Note-422, Geneva, Switzerland, 2009
16. E.B. Holzer, D. Bocian, T.T. Böhlen, B. Dehning, D. Kramer, L. Ponce, **A. Priebe**, M. Sapinski, M. Stockner, "Generation of 1.5 Million Beam Loss Threshold Values", *Proceedings of EPAC08*, Genoa, Italy, THPC147, pp. 3333-3335, June 2008
17. A.Wykrota, **A. Priebe**, B.Broda, M.Nowicki, "AFM and nanoindentation investigations of PPS+BaTiO₃ composites", *Proceedings of the 5th Workshop on Applications of Scanning Probe Microscopy STM/AFM 2008*, Zakopane, Poland